Design of Multivalent DNA Nanomaterials for use in Cancer Diagnostics and Therapeutics

A thesis submitted to the Board of Mathematical, Physical and Life Sciences Division, Department of Chemistry in partial fulfilment for the degree of

Doctor of Philosophy

At the

University of Oxford

Liyiwen Yuan

Exeter College, Michaelmas Term 2021



Design of Multivalent DNA Nanomaterials for use in Cancer Diagnostics and Therapeutics

Liyiwen Yuan

Doctor of Philosophy, Exeter College, Michaelmas Term 2021

Abstract

Cancer is one of the major causes of mortality nowadays, owing to the lack of accurate diagnostic and therapeutic techniques. DNA-based nanomaterials show extraordinary performance in cancer diagnosis and have applications in therapy, owing to their predictable secondary structures, small sizes, excellent biocompatibility, and programmability.

Rolling circle amplification (RCA) has been identified as a promising technique to make DNA nanomaterials, including DNA hydrogels, origami, nanoribbons, nano-scaffolds and DNA nanoflowers (DNFs). These DNA nanomaterials have potential in a wide variety of applications, involving drug delivery, *in vivo* imaging, electronic circuit fabrication and therapeutics. However, there was a lack of chemistry to expand their functionality, which greatly limited their applications. To address this, we developed a strategy involving commercially available modified nucleoside triphosphates in RCA, resulting in densely modified products. The modified RCA products can then be

functionalised by targeting moieties such as aptamer and peptide, which enhance their binding ability towards specific cancer cells.

The size of the RCA generated particles can be tuned through reaction time, Mg^{2+} concentration and the addition of polymers such as PLL and PEG. The PEGylated products can be labelled using the abovementioned method, leading to condensed fluorescent particles with better cellular uptake.

Additionally, a nanocarrier system based on cyclic DNA was designed and evaluated for mRNA detection in cells. The untemplated cyclisation of DNA through CuAAC chemistry was efficient, and the multivalent system showed an improved binding towards target cancer cells. However, the internalisation of the system by cells needs to be improved. Entrapment of the system in subcellular compartments was observed, which significantly increased the background signal.

Declaration of Authorship

I, Liyiwen Yuan, declare that this thesis and the work presented in it are my own and have been generated by me as the result of my own original research.

I confirm that:

• This work was done wholly while in candidature for a research degree at this University;

• Where I have consulted the published work of others, this is always clearly attributed;

• Where I have quoted from the work of others, the source is always given. With the exception of such quotations, this thesis is entirely my own work;

• I have acknowledged all main sources of help;

• Where the thesis is based on work done by myself jointly with others, I have made clear exactly what was done by others and what I have contributed myself;

Acknowledgements

First and foremost, I want to express my gratitude to Prof. Tom Brown for providing me with the opportunity to conduct research in the group. Thank you for being such a patient and supportive mentor. Also, a huge thank you to Prof. Afaf El-Sagheer for all your advice, inspiration, and, most importantly, encouragement, which always cheered me up.

Thanks to Dr. Ysobel R. Baker and Dr. Jinfeng Chen for their contributions in the RCA and DNA ring work. Thanks to Dr. Arun Shivalingam, Dr. Lapatrada Taemaitree and Dr. Nicolò Z. Fantoni, for their invaluable assistance and advice throughout these years. Additionally, huge thanks to Prof. Tom Brown, Prof. Afaf El-Sagheer, Dr. Lapatrada Taemaitree, Dr. Nicolò Z. Fantoni and Dr. Jinfeng Chen, for their patience in revising this thesis. I also appreciate the company of all the brownies, Arun, Ellia, Pui, Jack C, Nicolò, Sarah, Ashley, Piotr, Yssy, Cam, Sara, Jack H, Sven, Josh, Yutong, Lynda, Pawan, Chunsen, Thanishta, Cheng, Lilian and Jerry. Thank you for all the fun and support, which has made this such a cherished and memorable experience. To my good friends, Arun, Ellia, Pui, Grant, Dennis, Jack, Thanishta, Nico, Yun, Shuai, Yan, Ke, Jing and Pengyu, my 'girl gang' Weiyi, Carrie and Norma. Thank you for always being there for me through the lows and highs. I cannot express how grateful I am to have you as my friends.

Many thanks to Prof. Robert Carlisle (The Institute of Biomedical Engineering, University of Oxford) for helping me with tissue culture and flow cytometry. Thanks to all the PTCL and CRL building and facility service staff for their kind help.

I would also like to acknowledge the University of Oxford, PAG and the China Scholarship Council for funding my study and research during the DPhil.

Finally, and most importantly, I am very thankful to my mum, dad, boyfriend, and family members for their endless love, trust, and understanding.

Abbreviations

A/dA/dATP	Adenine/deoxyadenosine/deoxyadenosine triphosphate
Å	Ångstrom
Ab	Absorbance
Apt	Aptamer(s)
aq	Aqueous
AMP/ ATP	Adenosine monophosphate/ triphosphate
BCN	Bicyclo[6.1.0]nonyne
BSA	Bovine serum albumin
c	Molar concentration
C/dC/dCTP	Cytosine/deoxycytidine/deoxycytidine triphosphate
°C	Degrees Celsius
con.	Concentration
CuAAC	Copper-catalysed azide-alkyne cycloaddition
Cy3	Trimethine cyanine dye
Cy5	Pentamethine cyanine dye
DCM	Dichloromethane
DIBO	Dibenzocyclooctyne
DMF	Dimethylformamide
DMSO	DMSO Dimethyl sulfoxide
DMT	4,4′-Dimethoxytrityl
DNA	Deoxyribonucleic acid
DNAR	DNA ring
DNF(s)	DNA nanoflower(s)

DTT	Dithiothreitol
dsDNA	Double-stranded DNA
DPBS	Dulbecco's phosphate-buffered saline
EDTA	Ethylenediaminetetraacetic acid
ESI	Electrospray ionisation
eq	Equivalent (s)
FAM	Carboxyfluorescein
FDA	Food and Drug Administration
FISH	Fluorescence *in situ* hybridisation
FRET	Fluorescence resonance energy transfer
g	Gram
G/dGTP	Guanine/deoxyguanosine triphosphate
h	Hour (s)
HPLC	High-performance liquid chromatography
K_d	Dissociation constant
J	Coupling constant
L	Litre(s)
l	Light path length in cm
M	Molar concentration
MB	Molecular beacon
min	Minute(s)
mRNA	Messenger RNA
MS	Mass spectrometry
MUC1	Mucin 1
MW	Molecular weight

m/z	Mass/charge
NF	Nanoflower(s)
NHS	*N*-hydroxysuccinimide
NMR	Nuclear magnetic resonance
NTP/dNTP	Nucleoside/deoxynucleoside triphosphate
nt	Nucleotide(s)
OD	Optical density
ODN	Oligonucleotide
O/N	Overnight
PAGE	Polyacrylamide gel electrophoresis
PBS	Phosphate-buffered saline
PCR	Polymerase chain reaction
PPi	Pyrophosphate
pH	Potential of hydrogen (-log H^+)
RCA	Rolling circle amplification
RCT	Rolling circle transcription
RNA	Ribonucleic acid
RNase	Ribonuclease
RP-HPLC	Reversed-phase high-performance liquid chromatography
RT	Room temperature
R_f	Retention factor
SDS-PAGE	Sodium dodecyl sulphate–polyacrylamide gel electrophoresis
SELEX	Systematic evolution of ligands by exponential enrichment
SEM	Scanning electron microscopy
siRNA	Small interfering RNA

SNA	Sphere nucleic acid
SPAAC	Strain-promoted azide-alkyne cycloaddition
ssDNA	Single stranded DNA
T/dT/dTTP	Thymine/deoxythymidine/deoxythymidine triphosphate
TAMRA	Carboxytetramethylrhodamine
TBE	Tris-Borate-EDTA (buffer)
TBDMS	*Tert*-butyldimethylsilyl (protecting group)
TEAB	Triethylammonium bicarbonate (HPLC buffer)
TEMED	Tetramethylethylenediamine
THPTA	Tris(3-hydroxypropyltriazolylmethyl)amine
TLC	Thin layer chromatography
T_m	Melting temperature
Tz	Triazole linkage
U/UTP/dU/dUTP	Uracil/uridine triphosphate/deoxyuridine/deoxyuridine
UV	Ultraviolet
V	Voltage
v	Volume
w	Weight
W	Watt(s)
δ	Chemical shift in parts per million
ε	Extinction coefficient
$\lambda_{ex}/\lambda_{em}$	Excitation/emission wavelength

Chapter 1. General introduction

1.1 Nucleic acids

1.1.1 Primary structure of nucleic acids

Nucleic acids are linear, polymeric macromolecules that store and carry genetic information. These polymers are formed by nucleotide building blocks composed of a pentose sugar (2′-deoxy-D-ribofuranose in DNA, 2′-D-ribofuranose in RNA) that covalently attached to a 5'-phosphate group and a 1′-heterocyclic base. The sugar and base together are referred to a nucleoside. From a chemical perspective, those nucleobases are divided into purines (adenine and guanine) which possess two heterocyclic rings and pyrimidines (cytosine, thymine and uracil), which consist of a single ring. RNA contains three bases found in DNA (adenine, guanine and cytosine), but thymine is replaced by the related base, uracil, which lacks a methyl group at the C5 position of the sugar ring (Figure 1.1).[1]

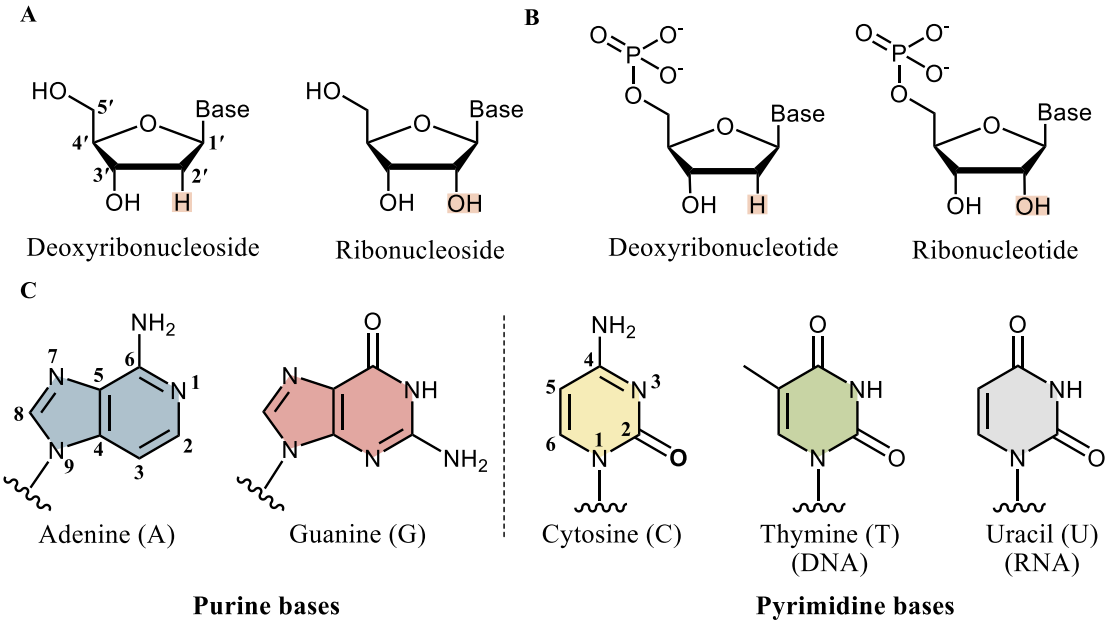


Figure 1.1. Chemical structure of **A**. nucleosides, **B**. nucleotides, and **C**. heterocyclic bases of nucleic acids. Purine bases include adenine (A) and guanine (G); pyrimidine bases include cytosine (C), thymine (T, in DNA) and uracil (U, in RNA).

Purine bases (A and G) are attached to the C1′ of the sugar by their N9 atom, while pyrimidine bases (C, T and U) are attached to the C1′ of the sugar by their N1 atom. The bond formed is called a glycosidic bond. This bond is rotatable, and as a result, the base can exist in two distinct orientations, giving rise to *syn*- and *anti*-conformations (Figure 1.2). Usually, the *anti*-conformation is favoured partly due to the steric effects.[1]

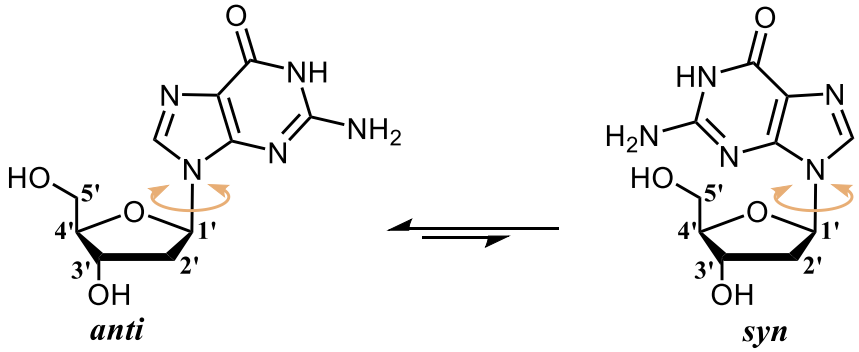


Figure 1.2. Chemical structure of *anti*- and *syn*-conformations of a purine nucleoside, using deoxy-guanosine as an example.

The nucleobase is *cis* with respect to the 4′-hydroxymethyl group, which is known as the β-configuration. When the base is *trans* to the hydroxymethyl group, it is known as the α-anomer (Figure 1.3), which is very rare in nature.

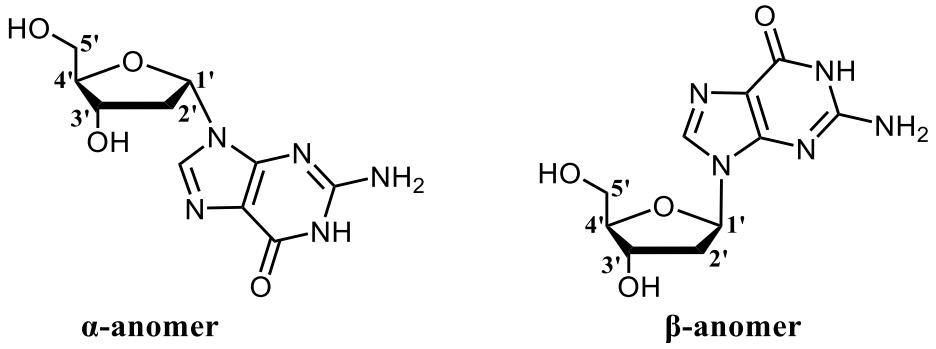


Figure 1.3. Chemical structures of nucleoside α- and β-anomers, using deoxy-guanosine as an example.

To form a dinucleotide (dimer), the phosphate group of one nucleotide is covalently linked to the 3′-hydroxyl group of another, forming a phosphodiester linkage. The end that has a free 5′-phosphate is called 5′ end, and the other end with a 3′-hydroxyl group

is called 3′ end (Figure 1.4). The repetition of this arrangement forms the extended polymeric structure of oligonucleotides. The sequences of DNA and RNA are conventionally read in the 5′ to 3′ direction because they are enzymatically synthesised in this direction in cells. The phosphate groups are negatively charged, contributing to an overall negative charge of nucleic acids at physiological pH. This charge is neutralised *in vitro* and in cells by cations such as Na^{+}, Mg^{2+} and some proteins containing positively charged amino acids.

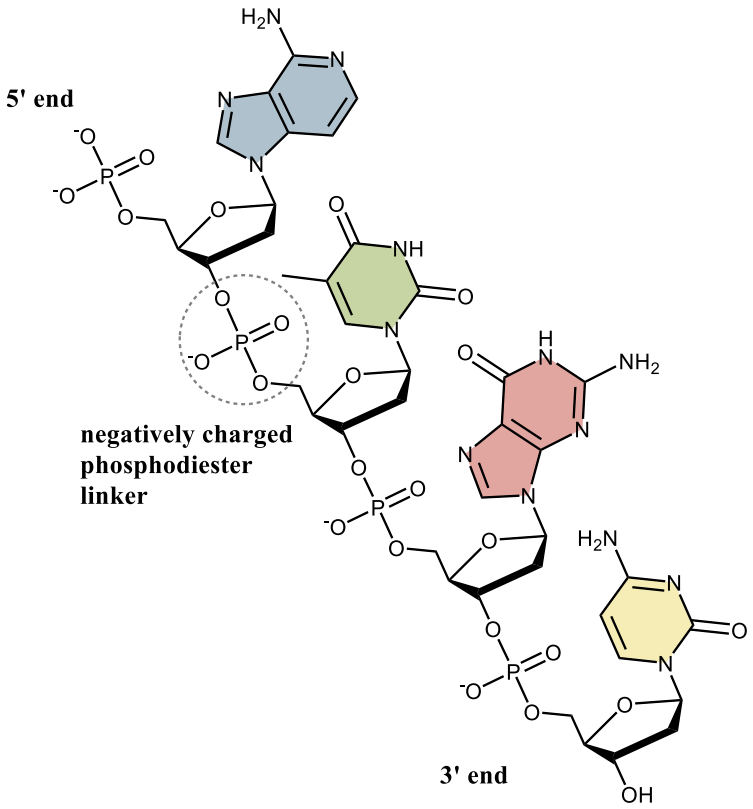


Figure 1.4. Chemical structure of oligonucleotide 5′-ATGC-3′. The monomers are linked by negatively charged phosphodiester bonds.

1.1.2 Secondary structures of nucleic acids

1.1.2.1 Nucleic acid duplexes

The 3D structure of DNA was intensively studied in the late 1940s to early 1950s. In 1950, Erwin Chargaff first discovered that purines and pyrimidines pair in a 1:1 ratio in DNA, the ratio of adenine: thymine and guanine: cytosine is always 1:1.[2] Based on this and the X-ray studies on DNA by Maurice Wilkins and Rosalind Franklin,[3] in 1953, James D. Watson and Francis Crick proposed the secondary structure of DNA. According to their model, DNA exists as a double helix composed of two antiparallel nucleic acid chains. The 5' end of one chain held close to the 3' end of another. The phosphate and sugar backbones face the outside of the helix, while the purine and pyrimidine bases face the inside. The bases are held together via intermolecular hydrogen bonds and A pairs with T (U in RNA) whereas C pairs with G (Figure 1.5.A).[4]

The helical conformations of DNA vary depending on the sequence composition, protein binding, and the ionic or hydration environment. Early X-ray diffraction studies first revealed two conformations of DNA helix, A- and B-form, which are both right-handed (Figure 1.5.B).

The B-form DNA, which exists at high humidity, represents an average conformation of DNA at neutral pH and physiological conditions. In B-form DNA, the two strands

are wound up around the axis of the helix. The distance between adjacent stacked base pairs is 3.32 Å, and a full turn of the double helix is formed every 10.5 base pairs (Figure 1.5.B). The axial rise is mainly determined by the sugar puckers. In B-form, the pucker of the deoxyribose sugar ring is C2'-*endo*, leading to a larger axial rise (Figure 1.6). All the glycosidic bonds in B-form are in *anti*-conformation. The resulting DNA double helix has a wide, deep major groove and a narrow, deep minor groove. The size of the grooves enables the accommodation of large molecules such as proteins in the major groove and small molecules such as dyes and drugs in the minor groove.

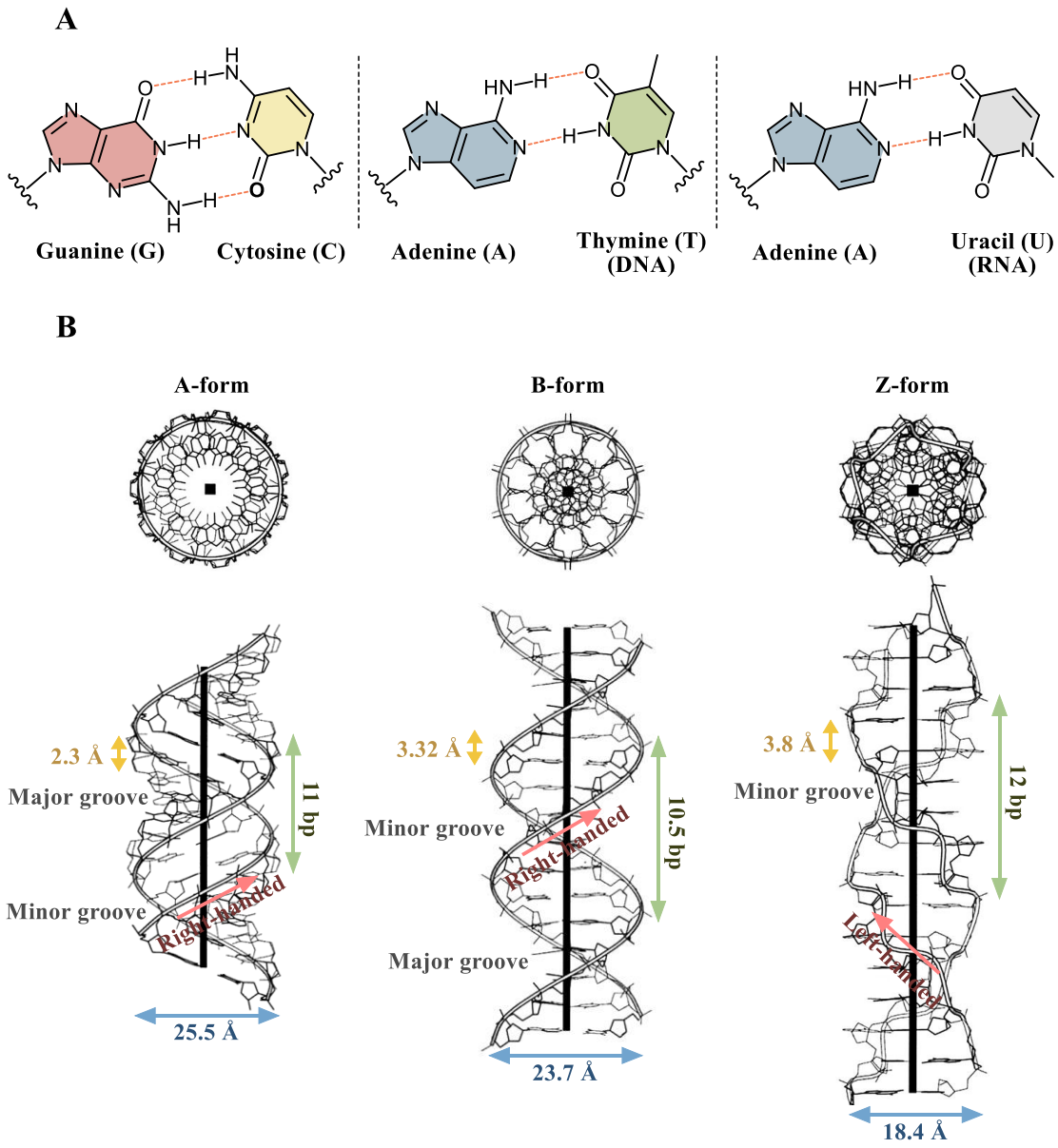


Figure 1.5. A. Watson-Crick base pairing: GC, AT, and AU pairs. C forms three hydrogen bonds with G, while A forms two hydrogen bonds with T (or U in RNA). Hydrogen bonds are presented as dashed lines. **B**. Top and side views of major duplex conformations in DNA (A-, B- and Z-forms) with parameters. Yellow arrows indicate the axial rise. Blue arrows indicate the helix diameter. Green arrows indicate the helical turn,

A-form is also a common right-handed conformation and is commonly found in RNA-

DNA and RNA-RNA duplexes. In contrast to B-form, the furanose sugar is in C3'-endo conformation in A-form, which brings the 5' and 3' hydroxyl groups closer than in B-DNA (Figure 1.6), resulting in a more compact conformation with 11 base pairs per turn (Figure 1.5.B). Similar to B-form, all glycosidic bonds in A-form are in the *anti*-conformation. As a result, the A-form has a deep major groove and very a shallow minor groove.

DNA can also adopt the Z-form. Different from A- and B-form, Z-form is a left-handed helix in a zigzag pattern. Z-form has the least compacted structure among the three forms, with a helical turn of 12 base pairs and an inter-base distance of 3.8 Å. The major groove is absent in Z-form, while the minor groove is narrow (Figure 1.5.B). The formation of Z-form is generally unfavourable, making it challenging to study.

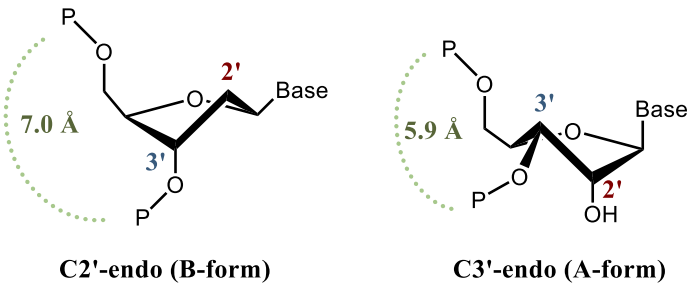


Figure 1.6. Sugar puckers in A- and B-form, which explains the difference in inter-base distance.

Which conformation a helix would adopt depends on the ionic and hydration environments, the sequence of the helix and sometimes the presence of other particles such as DNA binding proteins.

1.1.2.2 Hairpin loop

Watson-crick base pairing can also occur intramolecularly. When two regions of the same strand are complementary in opposite directions, they can hybridise and form a double helix region separated by a single-stranded loop. The resulting structure is called a hairpin loop. Hairpin loops are a common type of secondary structure, especially in RNA molecules. For example, tRNA, which carries amino acids to the ribosome during translation, is formed by three hairpin loops, giving it the shape of a three-leafed clover. In some prokaryotes, hairpin loops also play a role in gene expression by terminating transcription. DNA hairpin loops are also commonly used as probes for sequence detection in qPCR and *in vitro* studies. The simplest structure of this kind of probe is a molecular beacon, which is a 20 to 25 nt single-stranded DNA labelled with a reporter and a quencher molecule at 5' and 3' ends (Figure 1.7). More examples of these probes are discussed later in Section 1.5.

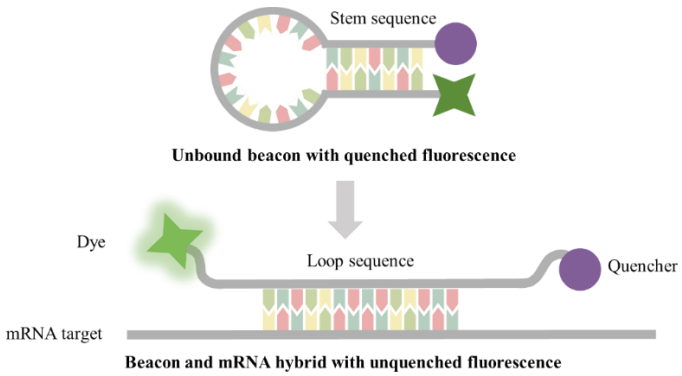


Figure 1.7. A Molecular Beacon binds to its specific DNA or mRNA target sequence, opening the hairpin loop to separate the reporter dye from the quencher.

1.1.2.3 Nucleic Acid Triplexes

Beyond the Watson-Crick base pairing, polypurinic sequences can host additional hydrogen bond interactions through Hoogsteen base pairing.[5] In a Hoogsteen base pair, the N7 (as a hydrogen bond acceptor) and C6 amino group (as a hydrogen bond donor) of the purine base bind to the pyrimidine base on the N3–C4 face (Figure 1.8.A). Instead of *anti*-conformation in Watson-Crick base pairing, the glycosidic bond in the purine in a Hoogsteen base pair is in *syn*-conformation, which reduces the size of the minor groove. This base pairing occurs when a third DNA strand bind to a DNA duplex, forming a DNA triplex. There are two combinations of the Watson-Crick-Hoogsteen triplex (Figure 1.8.B). When the third strand binds in the same orientation with the purine strand in the duplex, the triplex formed is called parallel, otherwise antiparallel. When C is involved in the Hoogsteen base pair, low pH (<6) is required to protonate the N3.

Hoogsteen base pairs are less stable than canonical Watson-Crick base pairs. As mentioned, *syn*-conformation of the glycosidic bond, which is required for Hoogsteen base pairing, is less favoured due to the steric hindrance. Also, the repulsion between the negatively charged backbones massively hinders the formation of triplexes; thus, a high concentration of bivalent cations is typically required to stabilise the structure.[6,7]

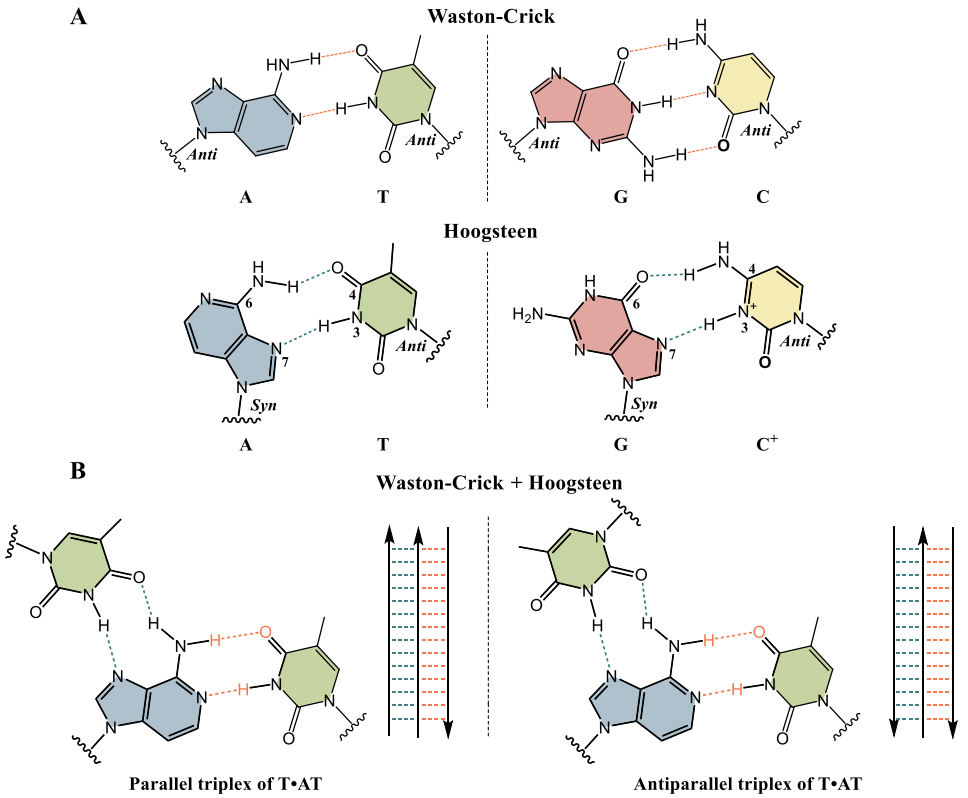


Figure 1.8. A. Comparison between Watson-Crick and Hoogsteen base-pairing; **B**. Examples of parallel and antiparallel triplexes formed by A and T. Parallel and antiparallel refer to the direction of the third strand relative to the purine-rich strand of the duplex.

1.1.2.4 G-quadruplex

Hoogsteen base pairing makes the formation of some important secondary structures possible. For example, when four guanine bases associate through Hoogsteen hydrogen bonding, a square planar structure called G-tetrad is formed.[8] When two or more G-tetrads stack together, the structure formed is called a G-quadruplex. G-quadruplexes can be formed intra- or intermolecularly by guanine-rich strands in different orientations, including parallel,[9] anti-parallel[10] and the mixture of both.[11–13] Presence

of a monovalent cation largely determines the formation and stability of a G-quadruplex. The cation interacts with the O-6 carbonyl oxygens of the G-tetrad, screening the electronic repulsion, making the formation of the G-quadruplex less electronically unfavourable (Figure 1.9.A).[14] Depending on the size, the ions can position along or between the G-tetrad planes. The most commonly studied ions for G-quadruplex stabilisation are Na^+ and K^+ as they are physiologically relevant. They both stabilise G-quadruplexes, although K^+ is reported to stabilise this type of structure to a greater extent.

G-quadruplexes have attracted much attention for their physiological significance. For example, human telomeric DNA contains tandem G-rich (TTAGGG) repeats which can form different G-quadruplex structures (Figure.1.9.D).[9–11,13,15,16] In normal somatic cells, the telomere shortens by 50 to 200 bases after each cell replication, leading to cell apoptosis after specific numbers of replication.[17] However, the presence of telomerase in cancer cells prevents this process by extending telomeric sequences at the chromosome ends. The formation of intramolecular G-quadruplex in human telomeric DNA has been shown to stop the extension by telomerase, reactivate the apoptosis of cancer cells.[18,19] Hence these structures have been used as targets for anti-cancer drugs in the past few decades. Compounds that target these sequences have been reported, while a few have been trailed for clinical use.[20,21]

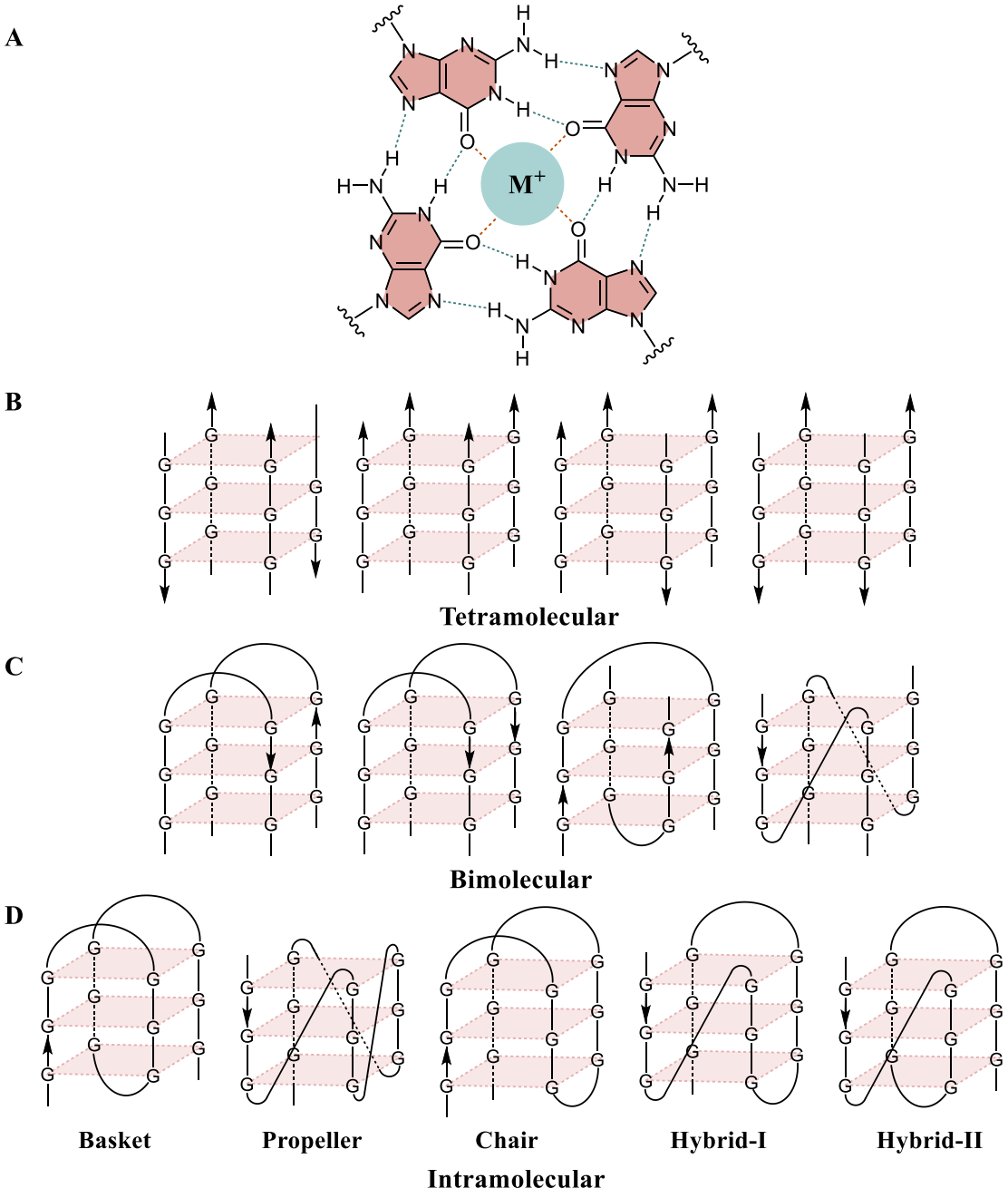


Figure 1.9. Different topological variants of G-quadruplexes; **A**. Chemical structure of the G-tetrad. Four guanosines are hydrogen-bonded by Hoogsteen base pairing, and the monovalent cation M^+ interacts with O6 atoms; **B-D**. Some examples of G-quadruplex arranged intermolecularly and intramolecularly. The intramolecular G-quadruplexes showed can be formed by human telomeric repeats. All illustrated using a 3-tiered G-quadruplex.

1.1.3 Solid-phase synthesis of oligonucleotides

Oligonucleotides are short strands of DNA or RNA, usually up to around 100 nucleotides in length. Chemical synthesis of oligonucleotides is beneficial in current laboratory practice as it provides rapid and inexpensive access to customised oligonucleotides of desired sequences and modifications.

Phosphoramidite chemistry, developed in the 1980s by Marvin Caruthers, and later enhanced with solid-phase supports and automation, is the most prevalent chemical method to assemble oligonucleotides.[22–24] Whereas biosynthesis of DNA and RNA proceeds from 5′ to 3′, the oligonucleotides are chemically synthesised on solid support from the 3′-end to the 5′-end. The 3′-end is bound to a solid support during synthesis, and one nucleotide is added in each synthesis cycle. Each cycle consists of a few steps, namely activation, coupling, capping, oxidation, and detritylation. When the synthesis is completed, oligonucleotides are cleaved from the solid support and deprotected (Figure.1.10).[22–24]

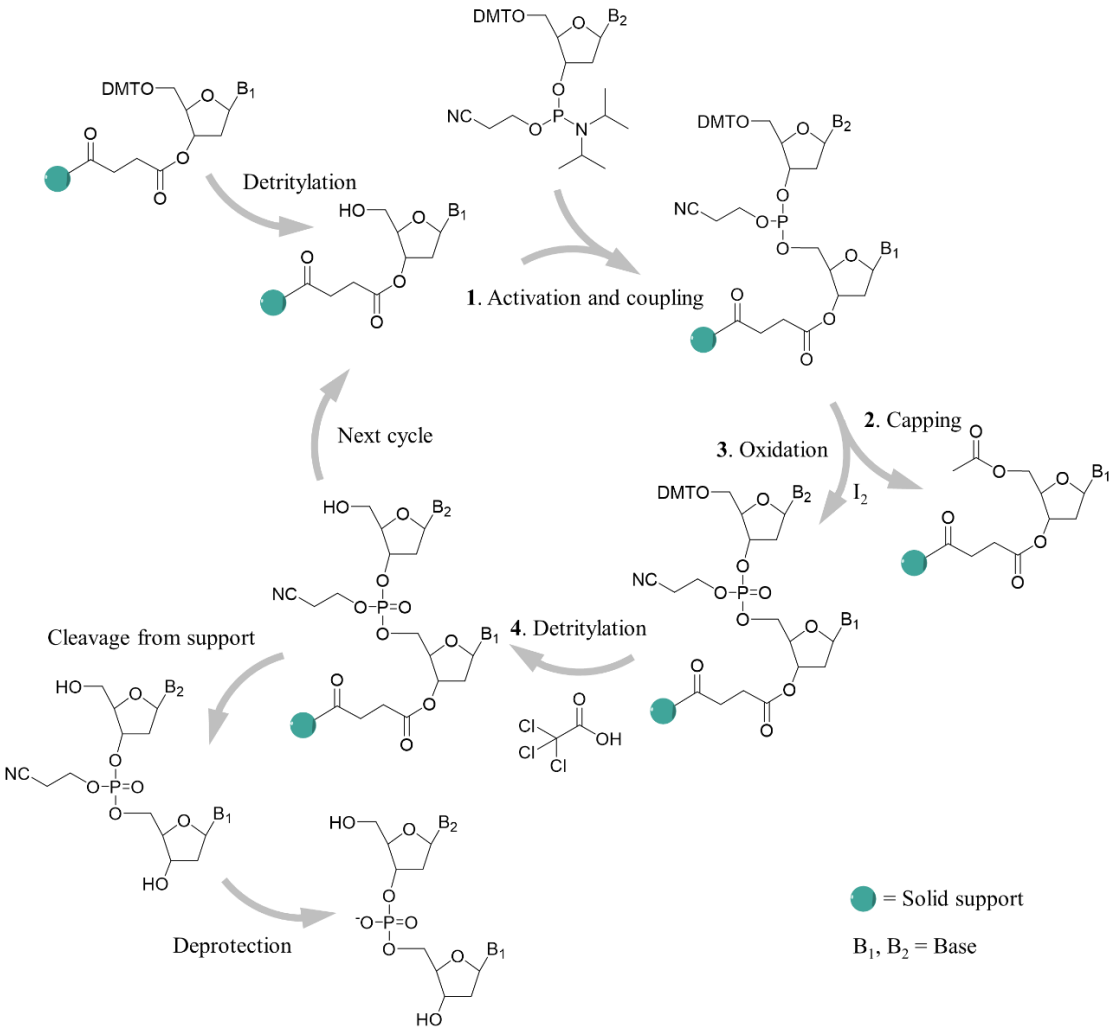


Figure 1.10. Schematic of automated solid-phase oligonucleotide synthesis. The addition of each monomer occurs in four steps, and the cycle is repeated until the whole sequence has been completed.

Each phosphoramidite monomer has a 2-cyanoethyl protecting group, a diisopropylamine group on the 3′-phosphite moiety, and a 4,4′-dimethoxytrityl (DMT) protecting group on the 5′-hydroxyl moiety. For the nucleobases, the exocyclic primary amino groups of adenine (A) and cytosine (C) are protected; the heterocyclic base of guanine (G) is protected to improve solubility, whereas no protection is required for thymidine (T) (DNA) and uridine (U) (RNA) (Figure.1.11).[25,26]

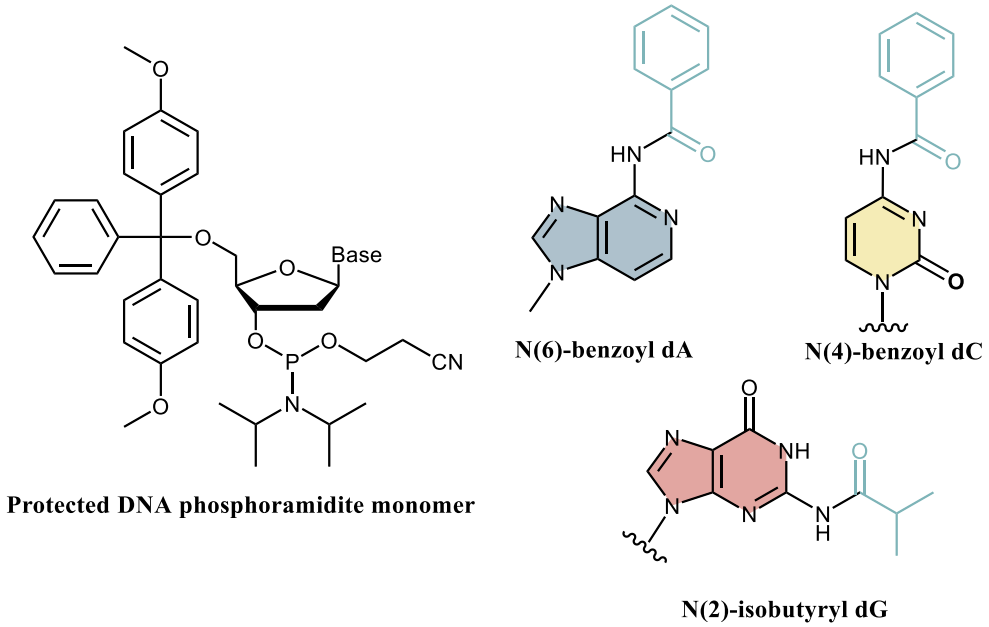


Figure 1.11. Protected DNA phosphoramidite monomer and protected bases for solid-phase synthesis. dT does not require protecting groups on the base.

In the first step, detritylation, the DMT group of the growing oligonucleoside is removed with trichloroacetic acid (TCA), forming active 5′-hydroxyl. In the coupling step, the incoming phosphoramidite monomer is activated by tetrazole, a weak acid, by protonating the diisopropylamine group. This activated phosphoramidite monomer then reacts with the deprotected 5′-hydroxyl group of the support-bound nucleoside, forming a phosphite triester linkage. The diisopropylamine group of the monomer leaves and is washed away with excess monomers and reagents. While the coupling usually is very efficient, it is not possible to achieve 100% efficiency. When the 5′-hydroxyl groups that fail to couple are further elongated, the resulting oligonucleotides would contain base deletion on different positions, leading to impure products. Hence,

the uncoupled 5′-hydroxyl groups need to be blocked using a mixture of acetic anhydride and N-methylimidazole acetylates. In the oxidation step, the phosphorus atom of the newly formed phosphite triester linkage is converted from an unstable P(III) to a stable P(V) state, with iodine, pyridine, and water. The cycle repeats until the desired sequence is completed, then the oligonucleotide is cleaved from the solid support with concentrated aqueous ammonia at 55 °C. The cyanoethyl protecting groups on the phosphates and the protecting groups from the nucleobases are also removed in the step.

RNA chemical synthesis is similar to the synthesis of DNA. The major difference is that the 2′-hydroxyl group of RNA must be protected throughout the solid-phase synthesis cycles to prevent 5′ to 2′ coupling of monomers and 3′ to 2′ backbone migration or chain cleavage. Due to the steric bulk of the 2′-hydroxyl protecting group, coupling efficiency during RNA synthesis is lower than DNA, limiting the length of synthesised RNA oligonucleotides at approximately 75 nt. The most commonly used 2′ protecting group is tert-butyldimethylsilyl (TBDMS), which is removed with a source of fluoride such as triethylamine trihydrofluoride (Figure.1.12).[27]

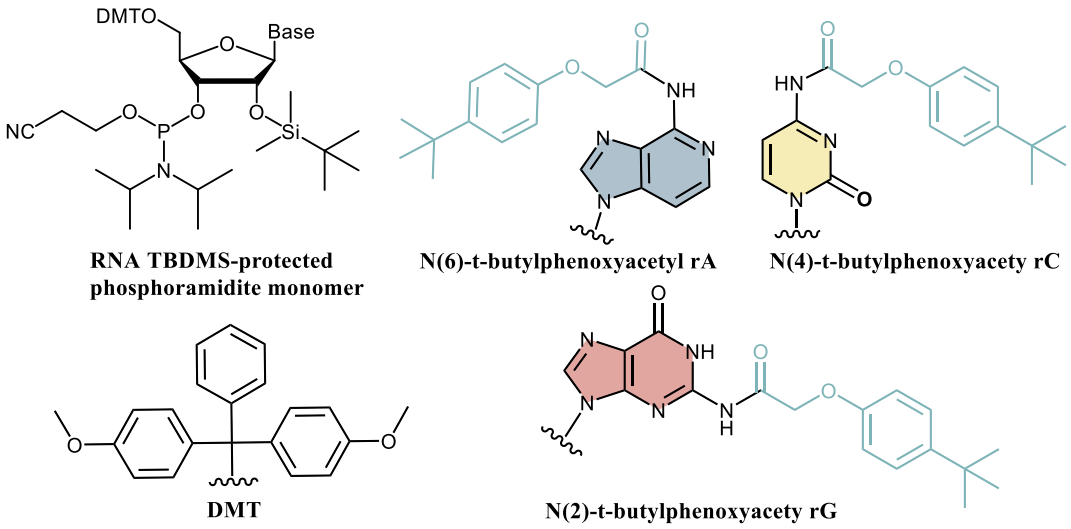


Figure 1.12. 2'-TBDMS-protected phosphoramidite monomers used in solid-phase RNA synthesis.

After synthesis and deprotection, oligonucleotides are purified by high-performance liquid chromatography or gel electrophoresis to remove truncated strands and incompletely deprotected molecules and then characterised by mass spectrometry.

1.2 Aptamer

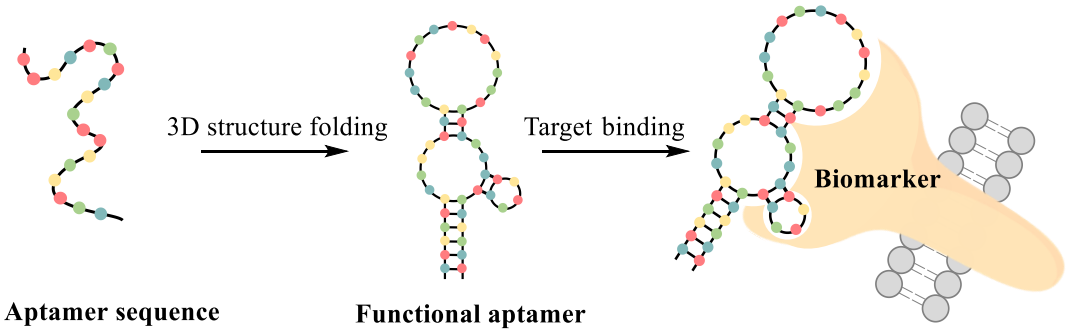


Figure 1.13. Schematic illustration of aptamer folding and binding to its target.

Aptamers are short synthetic single-stranded DNA/RNA molecules that bind to their targets with specific three-dimensional structures (Figure 1.13). Aptamers are typically isolated *in vitro* from synthetic nucleic acid libraries via a selection procedure called systematic evolution of ligands by exponential enrichment (SELEX).[28,29] During SELEX, the sequences in the library are exposed to the target, and non-binding sequences are removed by affinity chromatography or target capture on paramagnetic beads. The bound sequences are expanded by PCR and used as substrates for next round selection, with the stringency of the elution conditions increased to identify the tightest-binding sequences. Through the iterative process, tight-binding aptamer sequences can be isolated (Figure 1.14).

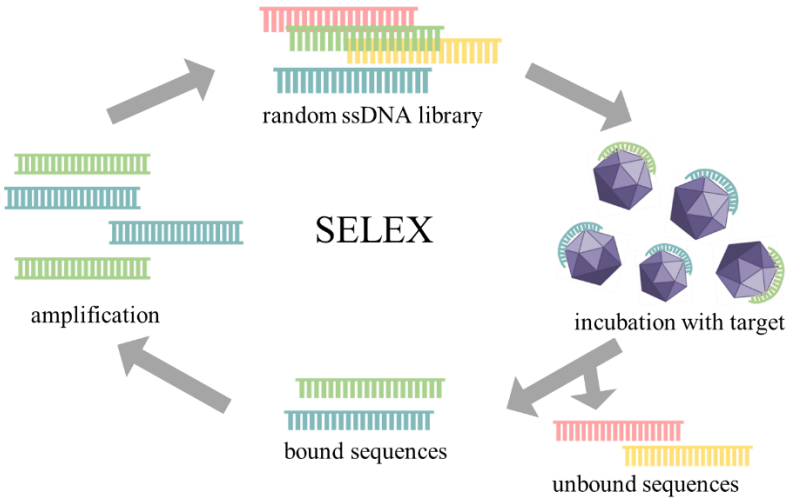


Figure 1.14. Schematic illustration of SELEX aptamer selection.

Aptamers have high affinity and specificity to small organic and inorganic molecules, such as ATP, cocaine and lead, and large protein complexes and cells.[30] The selectivity

of aptamers is originated from their unique three-dimensional structure, which allows them to bind their target through non-covalent interactions, including hydrogen bonding, hydrophobic or electrostatic interactions, base stacking, van der Waals forces, and shape complementarity.[31] A large number of aptamers display G-quadruplex structures which enable various folding topologies that recognise their targeting ligands.

1.2.1 Aptamers vs Antibodies

Antibodies have been successfully targeting agents in biological and clinical applications. Up to date, at least 570 therapeutic monoclonal antibodies have been approved for clinical trials, and 79 have been approved by FDA.[32] Though antibodies have been regarded as an ideal choice for many applications, instances appeared where they fail to work as anticipated. Aptamers have overcome many shortages of antibodies, hence are widely considered as an attractive alternative to antibodies.[33–35] Some of the key differences between antibodies and aptamers are listed below.

	Antibody	Aptamer
Stability	• Sensitive to temperature, easily denatured when heated. • Once denatured, cannot refold or restore function	• Stable at room temperature. • Can denature and fold repeatedly without losing function. • Stability can be further enhanced by the incorporation of modified nucleotides. • Sensitive to nuclease degradation
Storage and handling	• Limited shelf life (6 months) • Cold-chain transport, refrigeration/freezing storage needed	• Very long shelf life (several years if frozen) • Stable at ambient temperature, no cold-chain transport required.
Production	• Produced through *in vivo* procedures • Requires months to years • Low batch to batch reproducibility • Expensive to produce • Only in small scale	• Isolated *in vitro* through SELEX • Can be produced in several weeks • Chemically synthesised, giving high batch to batch reproducibility • Cost-effective • Scalable
Immunogenicity	• Significantly immunogenic	• low-immunogenic and low-toxicity
Size	• Large molecules (~160 kDa) hence low tissue penetration	• Small molecules (5 to 15 kDa) therefore high tissue penetration
targets	• Targets must produce an immune response	• Varies from inorganic ions, small molecules, peptides, proteins to complicated cells and tissues

1.2.2 Applications of Aptamers

Due to the development of SELEX, studies on aptamers have progressed substantively, and many applications of aptamers have emerged. Aptamers have been widely researched as recognition groups in biosensor, drug, bio-imaging, analytical and diagnostic applications.[33,34,36,37,] In 2004, a vascular endothelial growth factor (VEGF)-

specific aptamer (Macugen) was approved by FDA for the treatment of age-related macular degeneration.[38] However, since then, no other aptamer-based drug has entered the market, whereas several aptamer-mediated drugs failed clinical trials.[36,37]

1.3 Rolling circle amplification

Rolling circle amplification (RCA) is an isothermal enzymatic process that amplifies short DNA primers to long repeating sequences. During this process, a small cyclic oligonucleotide acts as the template. Nucleic acid polymerases (such as phi29, Bst, and Vent *exo*-DNA polymerase for DNA, and T7 RNA polymerase for RNA) keep adding nucleotides to the primer annealed to the cyclic template, resulting in the production of long, single-stranded DNA/RNA with tandem repeats complementary to the template (Figure 1.15). Unlike polymerase chain reaction (PCR), RCA does not require heating/annealing cycles. The amplification occurs under mild conditions at a constant temperature, making it possible to be conducted *in vitro* and in living systems.

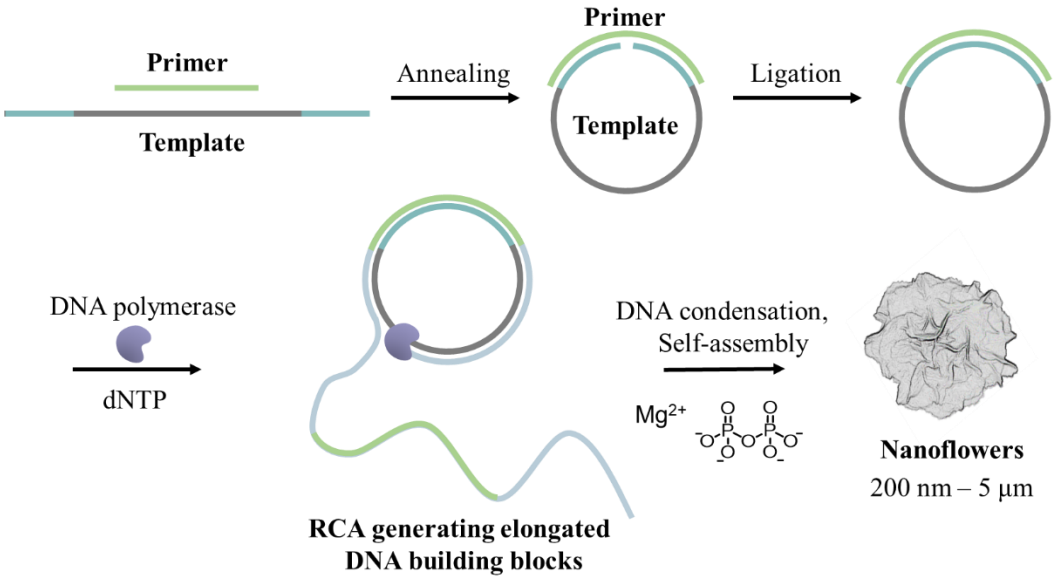


Figure 1.15. Enzymatic preparation of DNFs. A linear DNA template with a 5' phosphate is annealed to a DNA splint and cyclised using T4 DNA ligase. The splint is extended using a DNA polymerase with strand displacement activity to give long ssDNA formed of repeating units. The DNA then co-crystallises with the pyrophosphate by-product and with Mg^{2+} ions present in the amplification buffer to give DNFs.

Four components are required for RCA: (1) a cyclised DNA template; (2) a short DNA primer; (3) a DNA polymerase with a suitable reaction buffer; and (4) deoxynucleoside triphosphates (dNTPs) as building blocks.

1.3.1 Cyclisation of single-stranded oligonucleotides

1.3.1.1 Enzymatic cyclisation using T4 ligase

Cyclised DNA templates can be obtained from both enzymatic and chemical strategies.

DNA ligase is an enzyme that can join two strands of DNA together by forming a

phosphodiester bond between the phosphate group of one strand and the deoxyribose group of another. It is required by all organisms as it plays essential roles during DNA replication, DNA repair, and DNA recombination.[39,40] T4 DNA ligase, derived from the bacteriophage T4, is one of the most commonly used ligases in laboratory research. To initiate the reaction, the lysine residue of the ligase is adenylated by reacting with the cofactor adenosine triphosphate (ATP). The adenyl group is then transferred to the 5'-phosphorylated end of nucleic acid, forming a pyrophosphate group. Lastly, the adenylated end reacts with the adjacent 3'-hydroxyl group on another nucleic acid strand, forming the phosphodiester bond and releasing adenosine monophosphate (AMP) (Figure. 1.16).[41,42]

The optimal reaction temperature for T4 ligase is 37 °C.[43] However, the interaction between the two strands that require ligation is also a critical parameter. Although high temperature reduces the ligation efficiency by denaturing the annealed DNA ends, low temperature diminishes the activity of the enzyme. Typically lower temperatures (4°C to room temperature) with longer reaction times are used to get the best results.[43–45]

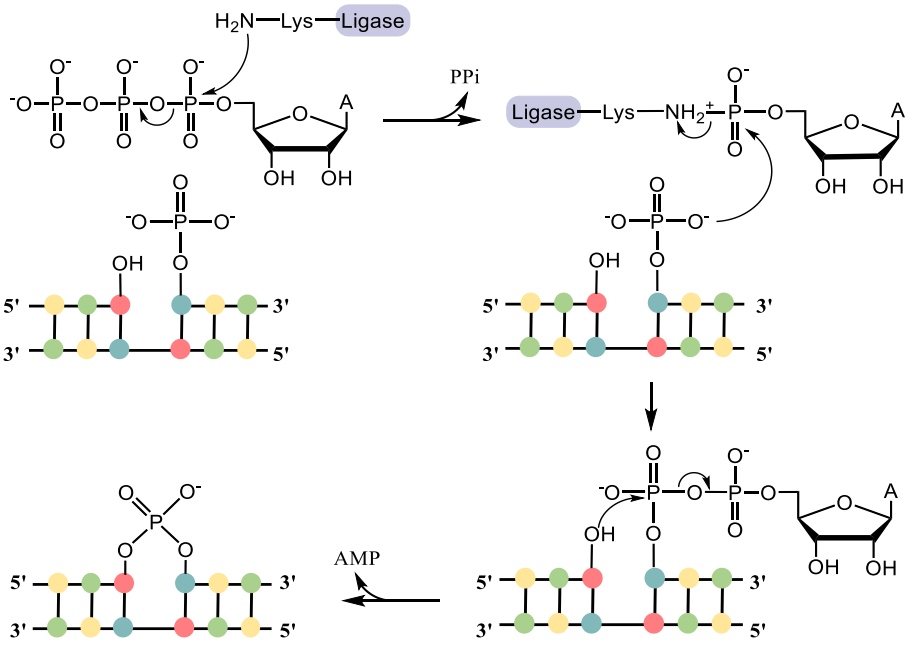


Figure 1.16. Reaction mechanism for T4 DNA ligase. 'A' denotes an adenine base.

1.3.1.2 Chemical cyclisation using copper(I)-catalysed azide-alkyne cycloaddition reaction (CuAAC)

By introducing artificial backbone linkages to DNA, cyclisation can be achieved without enzyme catalysis. Compared to enzymatic methods, chemical cyclisation is more economical and easier to conduct on a large scale. Different chemical routes to DNA cyclisation, including 5′-amine/3′-phosphate and 5′-amide/3′-carboxylate di-imide coupling and copper(I)-catalysed azide-alkyne cycloaddition (CuAAC), have been demonstrated in our group. In this study, CuAAC was used.

The term click chemistry was first coined by K. B. Sharpless *et al.* in 2001.[46,47] The reaction benefits from fast reaction rate, stereospecificity, high-yield, aqueous reaction

conditions, and little or no side products. The copper(I)-catalysed azide-alkyne cycloaddition (CuAAC), discovered in 2001,[48,49] represents a good example of click chemistry and has since been expanded to applications in diverse fields.[50] In this reaction, Cu(I) species catalyses the regioselective formation of 1,4-disubstituted triazoles from alkynes and azides (Figure 1.17.A). The catalytically active Cu(I) can be directly generated by reducing Cu(II) ($CuSO_4$) with ascorbate. Water-soluble ligand tris(3-hydroxypropyltriazolylmethyl)amine (THPTA) is normally present to protect Cu(I) centres from oxidation and to accelerate the reaction. To further minimise the oxidation of Cu(I), the reaction is normally performed in anaerobic conditions by degassing the reaction mixture using argon.[48,51–53]

One significant benefit of click chemistry is bio-orthogonality. The reaction can proceed fast in living organisms without interacting with the biological system or producing cytotoxic by-products. Additionally, the reaction happens under mild conditions in aqueous media at room temperature. Moreover, the reaction is highly selective, and the triazole linkage formed is exceptionally stable and nontoxic. These features make the method favourable for engineering biomaterials such as nucleic acids for cell culture applications.[54–56]

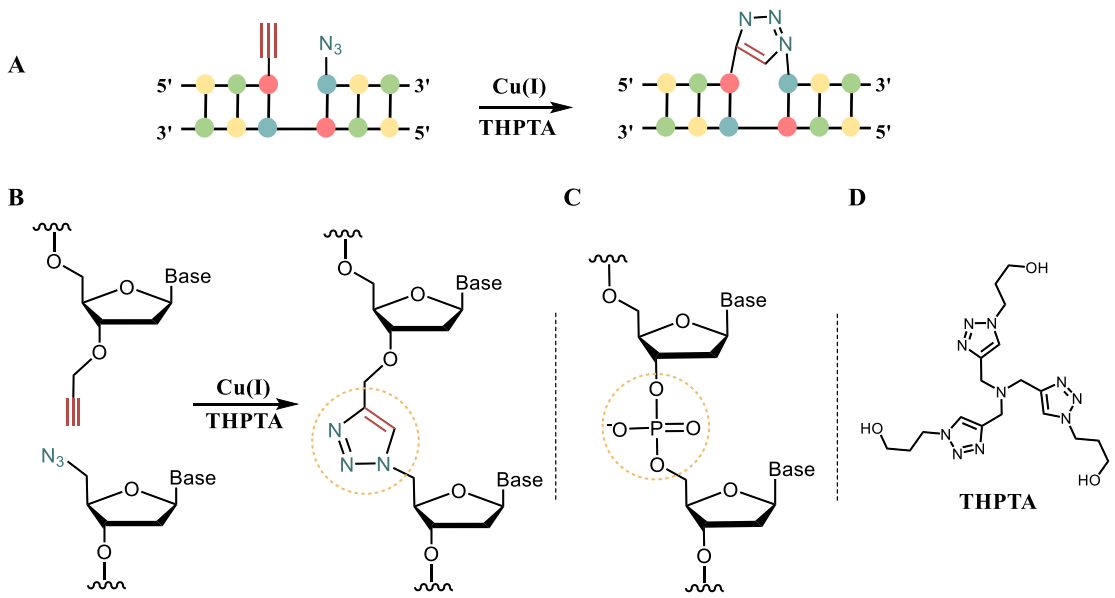


Figure 1.17. CuAAC cyclisation of linear DNAs containing 5′-azide and 3′-alkyne to generate a biocompatible triazole linkage. **A**. Schematic illustration of templated ligation; **B**. Chemical structure at ligation point; **C**. Structure of natural phosphodiester linkage; **D**. Structure of ligand THPTA.

A biocompatible triazole linkage that mimics native phosphodiester bond was proposed in our group in 2010 (Figure. 1.17.B).[57–59] Compared to previously reported triazole linkages, this new triazole has better flexibility and allows readily read through by DNA and RNA polymerases both *in vitro* and *in vivo*. Several click-linked genes containing this linkage were successfully transcribed and translated into functional proteins, further validating their biocompatibility.[60,61] Another recent study in our group demonstrated using this linkage to cyclise single-stranded DNA without templation. The cyclised product can then be used as the template for RCA.[62]

1.3.2 Primer

Primers, which can be both DNA and RNA, can also be used as a bridge splint to cyclise DNA templates. By employing different designs of the primer, applications of RCA can be broadly expanded. A few examples are presented here.

Functionalities such as reporting groups and binding moieties have been introduced into RCA-generated DNA by attaching them to the 5′ end of the primer. When the primer is linked to a solid support, the resulting RCA products can be easily isolated.[63,64] This process, termed solid-phase RCA, localises the amplification signals, enabling multi-target detection with high sensitivity.[65,66]

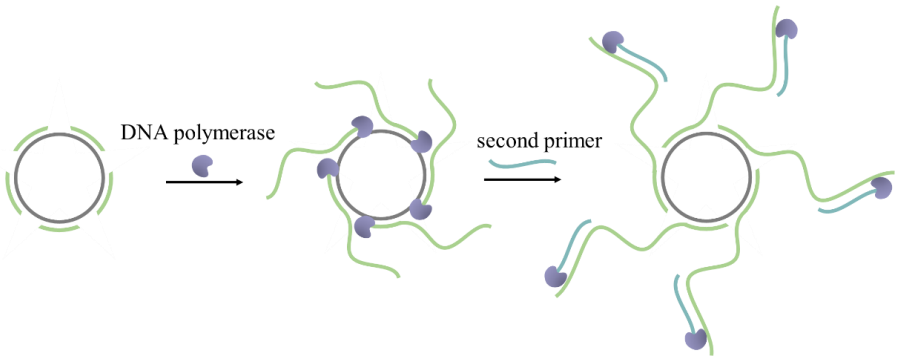


Figure 1.18. A combination of multiprimed RCA and hyperbranched RCA in the presence of multiple primers.

When additional primers are used to hybridise to the same template, multiple RCA can occur simultaneously, producing multiple ssDNAs.[67] When a second primer complementary to the amplicon is used, the RCA generated DNA is further amplified,

termed hyperbranched RCA (Figure 1.18).[68] This method amplifies DNA in an exponential way since it is helpful in detecting targets in low abundance.

1.3.3 Polymerase

Various polymerases have been used in RCA, including phi29, Bst, and Vent DNA polymerase for DNA amplification and T7 RNA polymerase for RNA amplification. These polymerases have high processivity, strand displacement ability, and good stability. Among all the polymerases, phi29 is most frequently used for DNA amplification as it shows the best performance. It is reported that phi29 DNA polymerase can bind strongly to single-stranded DNA and promote replication over 70 kb in 40 min.[69] However, under different circumstances, other polymerases are preferred. For example, when 2′-OMe RNA modification presents in cyclised templates, Bst DNA polymerase has shown higher efficiency of RCA than phi29.[70]

1.3.4 Nucleoside triphosphates

The enzymatic incorporation of modified nucleoside triphosphates during PCR amplification and primer extension has been widely applied as a facile strategy for generating modified nucleic acids. This method has also been developed to introduce functionalities into RCA products. For example, nucleoside triphosphates bearing fluorescent tags on the bases (Cy3-dCTP and Cy3-dUTP) have been used to generate

fluorescently labelled RCA products for detection purposes.[71] Biotinylated dN*TPs have also been incorporated during RCA to be captured by streptavidin-conjugated particles.[72] Other modifications reported include modified phosphate group such as α-thio-[73] and α-borano-dNTPs,[74] modified sugar such as LNA, 2-OMe-NTPs, and 2-fluoro-NTPs (Figure 1.19).[70] Combining with modified nucleoside triphosphates, RCA can potentially engage in potent applications, including but not limited to drug delivery, biosensing, and nanomaterial fabrication.

1.3.5 Applications of RCA

As a simple and isothermal enzymatic method, RCA has been used to generate periodic DNA on a large scale. Integrating it with various techniques has provided opportunities for ultrasensitive detection of nucleic acids,[75–79] small molecules, [80,81] proteins,[82,83] viruses[84] and cells.[75,85–87] RCA is also regarded as a powerful tool to prepare DNA building blocks for nanomaterial construction. With careful engineering, highly ordered nanostructures including origami,[88,89] nanoribbons,[88] nanotubes,[90–92] nano electronic circuits, and hygrogels[84] can be formed from RCA products and applied as diagnostics, therapeutics, and bioelectronics.

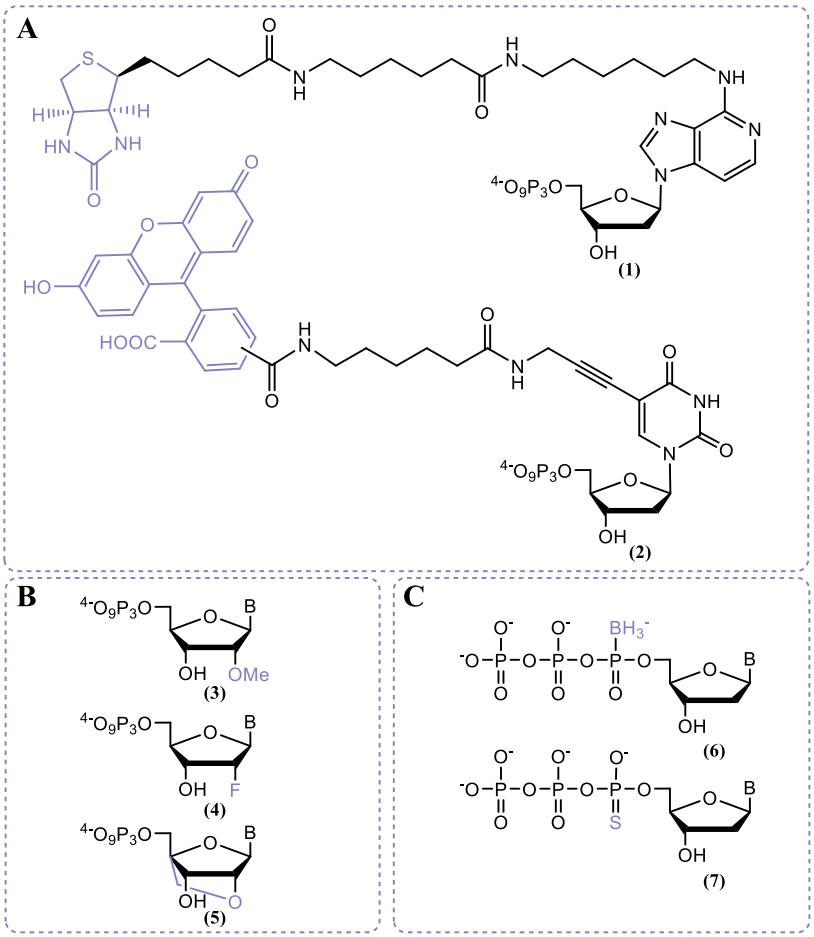


Figure 1.19. Examples of some modified nucleoside triphosphates reported in RCA. **A**. Base modifications: (**1**) Biotin-dATP; (**2**) Cy3-dUTP; **B**. Sugar modifications: (**3**) 2-OMe (**4**) 2-fluoro (**5**) LNA; **C**. Phosphate modifications: (**6**) α-borano (**7**) α-thio.

1.4 Cellular uptake of nanoparticles

Nanoparticles are usually defined as a particle with diametre between 1 and 100 nm. The term is sometimes used for particles with sizes up to 500 nm. Nanoparticles usually present unique physical and chemical properties, including increased hardness, mobility, catalytic activity, electric and magnetic properties. Therefore, nanoparticles

have been widely studied for applications in a variety of areas, such as materials, electronics, catalysis, energy, and drugs.[93–95] When coming to diagnostic and therapeutic applications, the dimension of nanoparticles is comparable with sub-cellular components, making them good candidates for bio-tagging, bio-labelling and delivery.[93,94,96,97]

However, it remains a big challenge to achieve efficient delivery of these particles to desired cell populations and subcellular targets. To better predict the transportation and biological impact of nanoparticles *in vivo*, it is critical to understand their interactions with the cell surface and their trafficking pathways in the cellular environment.[98–100]

To penetrate the cell, particles need to cross the cell membrane. The cellular membrane is a bilayer of phospholipids with hydrophilic heads and hydrophobic tails. The amphiphilic lipids give the cell membrane an overall negative charge. The hydrophobicity/hydrophilicity of the membrane allows small biomolecules to enter the cell by passive diffusion.[101,102] Differently, bigger molecules such as nanoparticles enter the cell through a mechanism mediated by channels, receptors, or transporters.[103] This is referred to as endocytosis. In this process, the particles to be uptaken are surrounded by the localised area of the cell membrane, which then folds in to form a vesicle. The vesicle transports the particles to different intracellular locations before fusing with intracellular or cell membranes and getting recycled. Endocytosis is

generally divided into two categories, which are phagocytosis and pinocytosis.[104] The processes are shown in Figure 1.20.

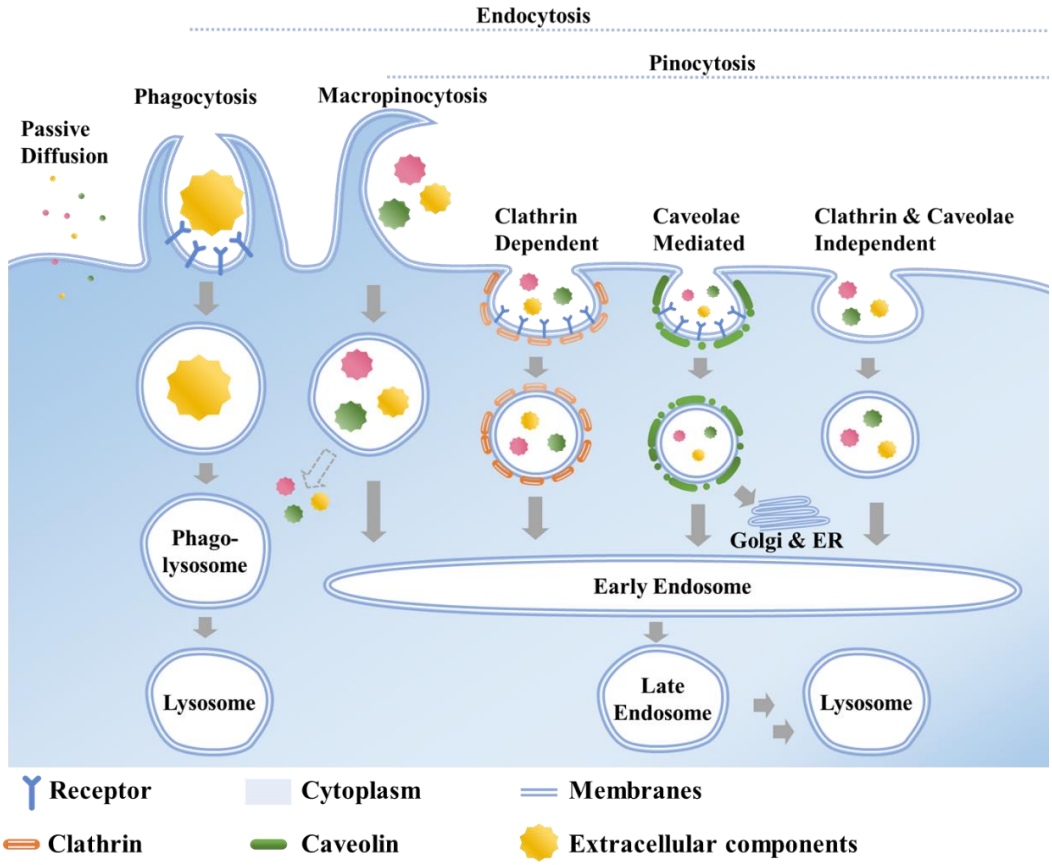


Figure 1.20. Schematic overview of extracellular particles internalisation pathways. While small molecules enter via passive diffusion, multiple different pathways exist for cellular entry of larger nanoparticles via endocytosis mechanisms, including phagocytosis, micropinocytosis, clathrin-dependent, caveolae-dependent, and clathrin- and caveolae-independent pathways. The pathway by which nanoparticles get uptaken determines their intracellular destination and biological response. Golgi & ER = Golgi apparatus and Endoplasmic reticulum. The vesicles are not scaled to actual size.

Phagocytosis is usually restricted to occur in phagocytes such as macrophages. It is at

the base of cellular defence mechanisms such as the elimination of apoptotic cells.[105–107] This process requires a specific ligand-receptor interaction, which triggers the formation of a vesicle called phagosome to engulf and transport the particle.[108] Phagocytosis can mediate the uptake of particles larger than 0.5 μm, and the event takes from 30 min to a few hours, depending on the cell type and the type of particles being delivered.[100]

Different from phagocytosis, pinocytosis happens in almost all cell types. It can be categorised into at least four mechanisms: macropinocytosis, clathrin-mediated endocytosis, caveolae-mediated endocytosis, and clathrin- and caveolae-independent endocytosis. The size of particles delivered through pinocytosis is much smaller than phagocytosis, varying from a few to hundreds of nanometres except for macropinocytosis where vesicles up to 5 μm can be formed.[100]

Macropinocytosis is a non-specific internalisation pathway characterised by the entrapment of surrounding components into cell membrane protrusion.[109] The vesicles formed, called macropinosomes, are stabilised by actin, and their size ranges from 0.5 to 1.5 μm, allowing the transportation of large particles.[110] Macropinosomes have been reported to be porous, which may allow their contents to escape lysosomal degradation.[109,110]

Clathrin-mediated endocytosis is the primary mechanism for the cellular uptake of nutrients and plasma membrane components. This mechanism occurs in domains enriched in clathrin protein, which is 0.5-2% of the total area on the cell membrane.[111] With the aid of other proteins, clathrin can polymerise, forming a coated pit in size of 120-150 nm, trapping the extracellular component inside. This process can be either mediated specifically by ligand-receptor interactions or non-specific through hydrophobic or electrostatic interactions.[112] However, the receptor-mediated process is reported to be 1000 times more selective with less extracellular fluid internalised. Upon the scission of the cell membrane, the vesicles transport to endosomes and end up fusing with lysosomes, resulting in vesicular contents breakdown.[113]

Caveolae-dependent endocytosis is mainly mediated by a dimeric protein, caveolin. The plasma membrane invaginations stabilised by caveolin are called caveolae, typically with a size of 50−60 nm.[114,115] Upon activation by specific signals, caveolae vesicles get pinched off from the membrane and transported into the cytoplasm. The destinations for these vesicles and their contents are other caveolin-based compartments, including the Golgi apparatus and the endoplasmic reticulum.[98,116–120] Therefore, caveolae-dependent endocytosis provides a pathway for nanoparticles to avoid lysosome degradation. Similar to clathrin-mediated endocytosis, in this mechanism, ligand-receptor recognition can occur. Targeting ligands such as albumin

and cholesterol have been used to deliver nanoparticles through this pathway.[121]

Clathrin- and caveolae-independent endocytosis takes place in cells deprived of clathrin and caveolae. Folate-modification has been widely used for cancer cell targeting as the growth of cancer cells requires an increasing amount of folic acid.[104,122] Internalisation of folic acid has been found to undergo this mechanism.[99] Nanoparticles functionalised with folate can therefore be delivered using this strategy without being destructed and might be released directly into cytoplasm without entering lysosome.[104]

Direct cellular internalisation of nanoparticles without any assistance is very rarely observed. However, alternative pathways can significantly increase the delivery efficiency of transfection to the cytoplasm (Figure 1.21).

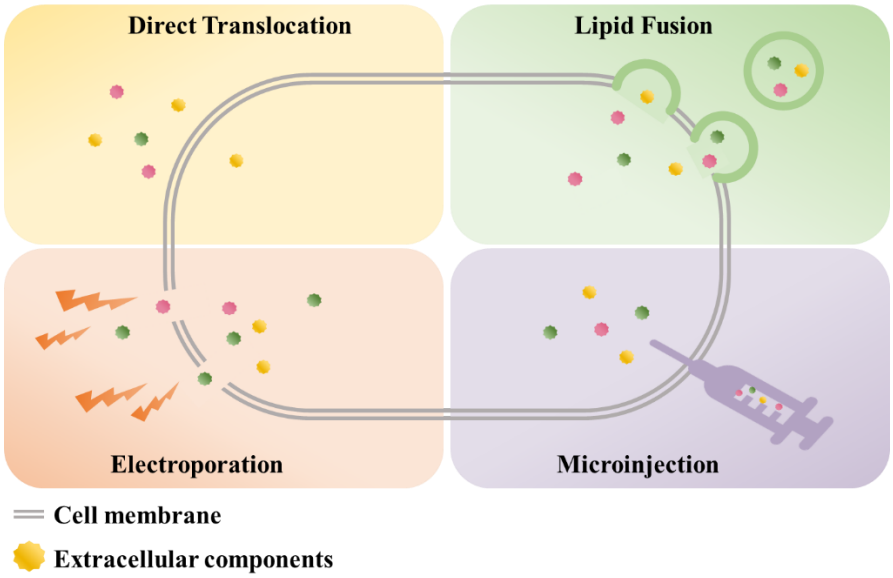


Figure 1.21. Schematic overview of direct cytoplasmic delivery strategies of nanoparticles. These include direct translocation, lipid fusion, electroporation, and microinjection. Direct translocation and lipid fusion rely on the physicochemical properties of the nanoparticles and reagents used. Electroporation uses electrical pulses to disrupt the plasma membrane to allow internalisation. Microinjection punctures the cell plasma membrane with a microscopic needle to inject nanoparticles directly into cells.

Direct translocation of nanoparticles to the cytoplasm can be achieved by modifying nanoparticles with membrane-disruptive agents such as cell-penetrating peptides (CPP). CPPs are short amino acid sequences (typically 5–30 amino acids) that translocate across the cell membrane. They are generally classified into cationic CPPs, amphipathic CPPs, and hydrophobic CPPs.[123] Different mechanisms have been proposed to explain the direct translocation of CPPs across the lipid bilayer of the cell membrane, including inverted micelle formation,[124] pore formation,[125] adaptive

translocation[126] and the membrane thinning model,[127] but the understanding of this process is still evolving. Up to date, more than 25 CPP-conjugated drugs have entered preclinical and clinical trials in applications as diagnostics and therapeutics for inflammation,[128,129] pain,[130–132] cancer,[133] heart diseases[134–136] and ageing.[137] However, none has been approved by FDA.

Lipid fusion uses some types of lipids to achieve cytoplasm delivery. These lipids share similar properties with the plasma membrane and fuse with the membrane when they join.[138] After fusion, the entrapped contents get released directly to the cytoplasm. This approach is commonly used for protein and nucleic acid delivery.[139,140,]

Electroporation is a strategy to disturb cell membranes physically using electrical pulses. Upon applying an electrostatic field, cell membranes will break down temporarily, leaving pores large enough for nanoparticles to pass through. When correct conditions are used, electroporation efficiently transfects nanoparticles into the cytoplasm without apparent cell damage.[141–143]

Microinjection is a direct method to introduce nanoparticles into the cytoplasm or nucleus with the help of a precision positioning tip.[144] Using this method, all intracellular and cellular membrane barriers can be penetrated easily on a cell-per-cell basis. When it comes to single-cell transfection, microinjection presents advantages

over other techniques, including precise delivery, defined dosage, and host-range independence.[145]

1.5 RNA detection in live cells

Over the past decades, RNA molecules have been proved to play important roles in cellular functions. They are responsible for transporting and interpreting genetic information and regulating gene expression and catalysis of essential biochemical processes. These functions are achieved through temporal-spatial expression and stability of specific RNAs in cells. To better acquire the dynamics of RNA molecules in live cells, many imaging approaches have been developed.

1.5.1 Protein-based probes

One of the most widely used methods is the genetically encoded RNA reporter system (Figure 1.22). In this method, a coat protein of MS2 bacteriophage (MS2CP), is used which binds strongly to a unique RNA hairpin (MS2-binding site (MBS)).[146] Two plasmids are used to transcribe these sequences in cells. On one of them (plasmid 1), which encodes the MS2CP, the sequence of GFP is fused as reporting tags. The second one (plasmid 2) expresses RNA sequences of interest, bearing repetitive MBSs. As MS2CP does not interact with any component in mammalian cells, this system enables easy observation of target RNA with high affinity and specificity. Detection sensitivity

can be further improved by inserting additional copies of MBS.[147] Other protein-RNA modules have also been identified, which makes orthogonal tracking of multiple RNAs possible.[148,149] This strategy provides a way to observe the movements of mRNA in cells directly. However, limitations to this technique include high background noise, complicated cloning, and multistep transfection.

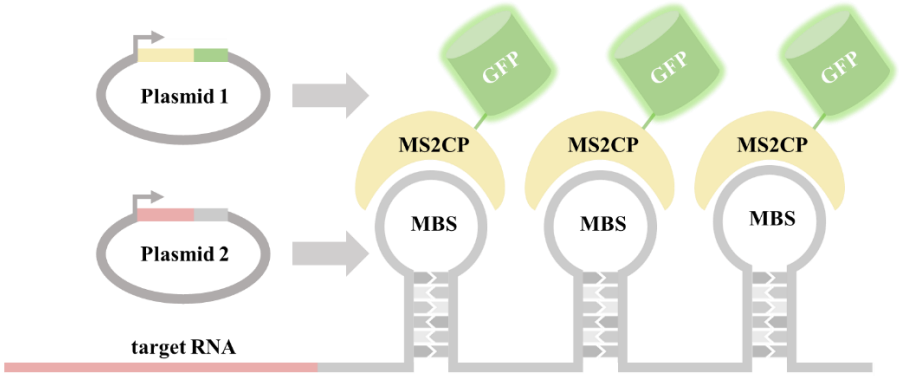


Figure 1.22. Illustration of MS2-GFP imaging of target RNA. Two components are required. MS2CP-GFP fusion is encoded by plasmid 1 while MBS along with target RNA is encoded by plasmid 2. MS2CP binds specifically to MBS hence anchors the GFP reporting groups on the target RNA sequence. Arrow marked as the position of the promoter.

1.5.2 Oligonucleotide-based probes

1.5.2.1 linear oligonucleotide probes

Based on Watson-Crick base pairing, oligonucleotide-based probes are also commonly used for RNA detection in living cells.

Fluorescently labelled linear oligonucleotide probe is one of the simplest designs for real-time RNA localisation despite poor specificity and significant background noise (Figure 1.23.A).[150,151] By using the fluorescence resonance energy transfer (FRET) dual-probe system, relatively better results can be obtained.[150,151] In this system, two probes binding to adjacent regions on the target RNA are labelled with two fluorophores at their 5′ and 3′ end that forms a FRET pair. Only when both probes hybridise to the same RNA sequence the acceptor fluorophore gets excited, producing a signal of detection (Figure 1.23.B). Therefore, the background noise can be differentiated from the actual signal. However, the specificity is limited for single and dual linear probes as they hardly distinguish targets that differ by only a few bases.[152]

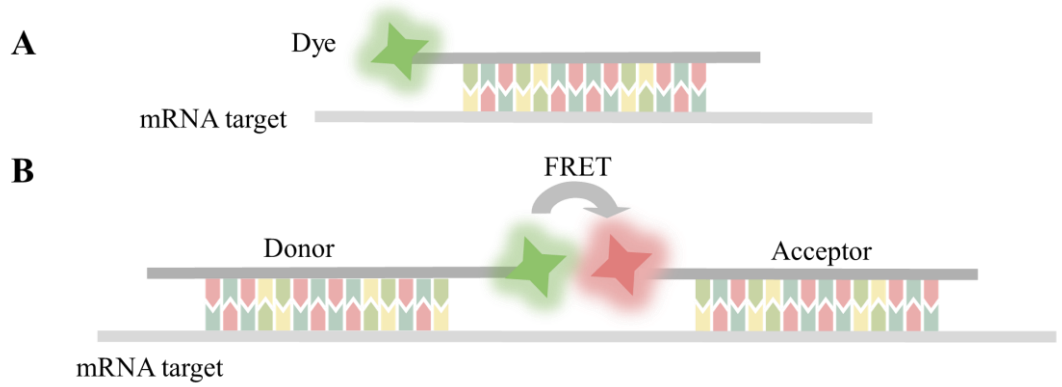


Figure 1.23. Illustration of linear oligonucleotide probes for RNA detection. **A**. Fluorophore functionalised linear probe; **B**. FRET linear probe.

1.5.2.2 Molecular beacons

The most commonly adopted class of probes for live-cell RNA detection is the

molecular beacon (MB), which is formed by hairpin oligonucleotides. The loop is formed by the targeting sequence, which is normally 15-25 nt. It is designed to have a unique antisense sequence and appropriate thermal stability. The stem is constructed by two complementary sequences, with a fluorophore and a quencher respectively conjugated at the 5' and 3' ends. In the absence of target RNA, the fluorescence is quenched as the fluorophore and the quencher stay in proximity. Binding to the target sequence opens up the stem, separating the fluorophore and the quencher, restoring the fluorescence emission (Figure 1.24.A). This enables molecular beacons to detect with low background in the presence of free probes.[153–155] The signal-to-background ratio can be up to 200 folds under optimal conditions.[153] The hairpin loop works as an activation energy barrier which significantly improves the specificity as low as one mismatch can be recognised. However, false-positive signals are observed in living cells due to degradation by nucleases and binding by nucleic acid-binding proteins. Chemical modifications could be introduced into the sequences to improve stability in the subcellular environment. To further enhance the specificity, FRET molecular beacons were demonstrated.[156,157] Similar to linear FRET probes, the two beacons which hybridise to neighbouring sites on the target are labelled with a FRET pair. Only when they are both hybridised to the target, the FRET occurs (Figure 1.24.B). The FRET signal can be discriminated from false signals caused by degradation and non-

specific loop opening.

One major challenge of the methods demonstrated above is the cellular delivery of the probes. Generally, oligonucleotides are prevented from penetrating the cell membrane. To deliver them, extra measurements are normally required. These include microinjection, transfection, cell-penetrating peptide, and electroporation. However, some of these methods might cause issues like cell stress and cell damage.[158–161] Also, the quenching efficiency of quenchers is affected by different factors and sometimes can be lower than expected.[162] This can be improved by using inorganic quenchers such as gold nanoparticles or by conjugating several quenchers into the same MB.[163–165]

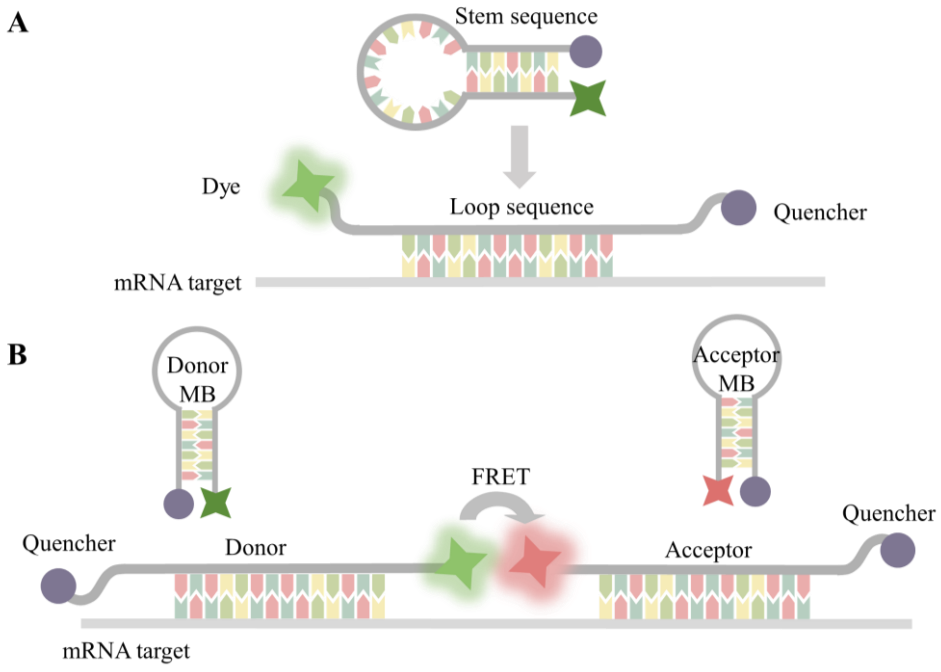


Figure 1.24. Illustration of hairpin oligonucleotides probes for RNA detection. **A**. Molecular beacon; **B**. FRET molecular beacon.

1.5.2.3 light-up aptamers

Another valuable tool for RNA detection in living cells is light-up aptamers, which consist of in vitro selected RNA sequences and their cognate fluorogens.[166] The fluorogens are cell-permeable small molecules that are fluorescent only upon binding with the corresponding RNA sequences (Figure 1.25).

The light-up aptamer system has some distinct properties. The fluorogen can be chemically synthesised and engineered, and the corresponding RNA sequences can be selected via SELEX, meaning the entire system can be programmed as needed. In addition, some light-up aptamers have shown outstanding stability against pH and photo bleach.[167–169] These together attribute to the detection and imaging of various targets under different conditions.

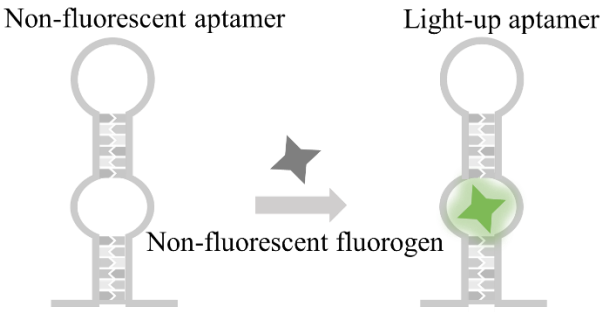


Figure 1.25. Illustration of a light-up aptamer. A non-fluorescent fluorogen can be excited once tightly bound to an aptamer, leading to an increase in fluorescence.

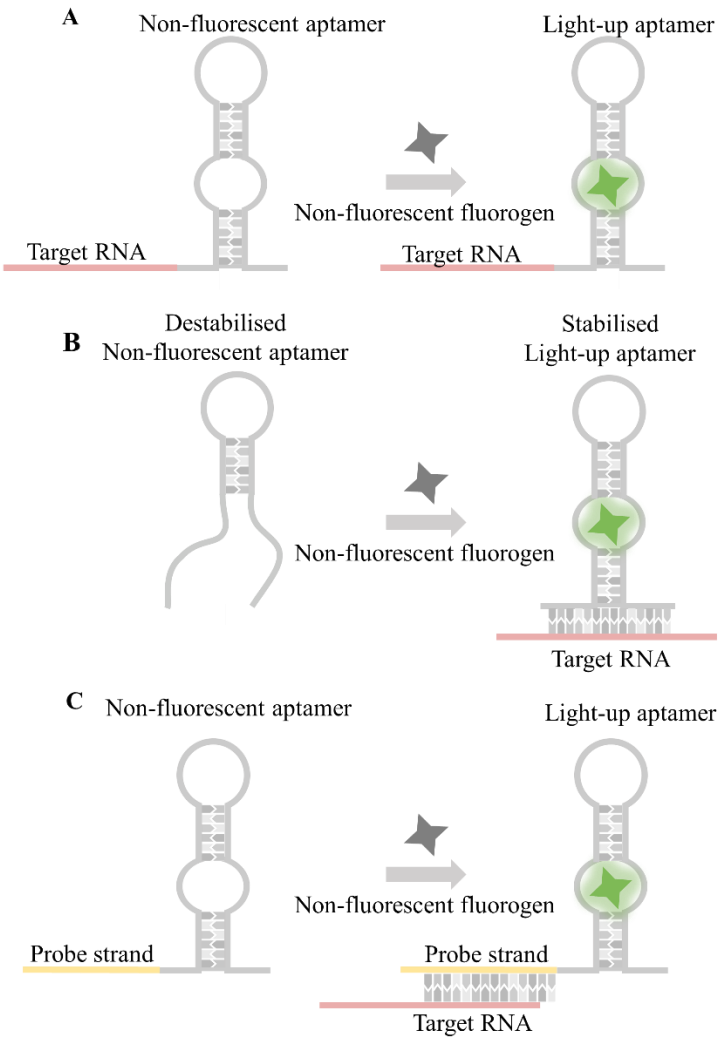


Figure 1.26. Illustration of some designs using light-up aptamer for RNA detection. **A**. light-up aptamer is tagged to an exogenous RNA sequence for its tracking in living cells; **B**. Light-up aptamer is designed as a probe for RNA detection. The structure is only stabilised and becomes fluorescent upon binding to its target molecule; **C**. Light-up aptamer is combined with other probes for localised detection of target molecules.

By tagging the light-up aptamer sequences to endogenous RNAs, their spatiotemporal dynamic in cells can be mapped. Additionally, the aptamers can be used as an alternative to standard fluorophores, providing a high signal-to-background ratio and

easy programmability. With careful design, the structure of light-up aptamers can be facilitated by the target RNA, which enables the release of fluorescent signals upon recognition.

However, limitations exist for applying light-up aptamers in cellular and in vivo imaging. The spectral coverage of light-up aptamers is still narrow, requiring further development. Orthogonality is another pursuit for multiplex imaging and detection in living cells, as most of these aptamers form G-quadruplex, leading to potential crosstalk between them.[170] Still, light-up aptamers represent a good alternative for fluorophore and fluorescent proteins, and their utilisation in combination with other imaging and detection method is worth exploring.

1.5.2.4 Sticky flares

Spherical nucleic acids (SNA) are a class of 3D DNA structures that have been applied in biological and biophysical research. They are constructed by a spherical inorganic core with linear oligonucleotides covalently attached to its surface. The densely packed structure gives it enhanced cellular uptake without the employment of transfection agents. Based on this structure, sticky flare is reported to monitor and quantify target RNA in live cells. Sticky flare is formed by a 13 nm gold nanoparticle core and a coat of oligonucleotides. A fluorescently labelled oligonucleotide probe termed flare

sequence is used. The flare sequence has a hanging tail that is antisense to the target RNA, while the rest is complementarily hybridised to the coating sequences, holding the fluorophore close to the gold core. In the absence of targets, the fluorescence is effectively quenched by the gold nanoparticle. When entering the cells, the flare sequence captures the target and escapes from the SNA surface. Consequently, the fluorescence of the fluorophore gets recovered, which enables the localisation of the target RNA spatiotemporally (Figure 1.27).[171,172]

However, problems emerged, including endosome accumulation and degradation after cellular uptake, which led to non-specific signals.[173,174]

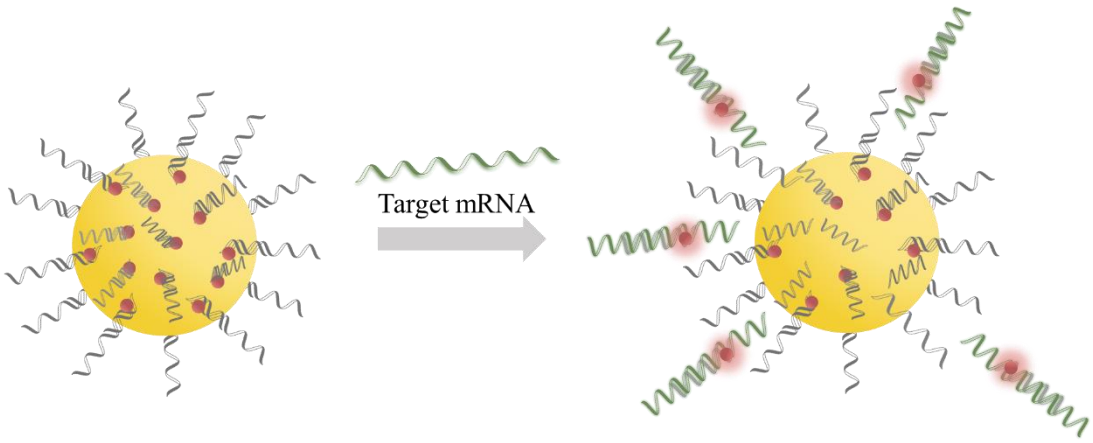


Figure 1.27. Illustration of sticky flares for mRNA detection. Fluorophore modified flare sequence is quenched by the gold core in the absence of the target. When encountered with the mRNA target, the flare sequences are released from the particle, restoring the fluorescence.

All these approaches have advantages and disadvantages. By conjugation with other

techniques, it is possible to gain precise information of target RNA in live cells. Yet, an ideal detection system still needs to be developed.

1.6 Aims and objectives

The biocompatibility, water-solubility, structural programmability by Watson-Crick base pairing, and complementary target recognition properties of DNA make it an excellent foundation for fabricating novel nanomaterials. Due to their high target specificity, extended half-life, and potential eukaryotic cell uptake, DNA-based nanostructures are expected to impact the biomedical and diagnostic fields significantly.

The overall goal of this study is to develop aptamer-functionalised DNA nano and microstructures that can be used for cancer cell recognition, intracellular imaging, drug delivery, and mRNA detection.

The specific aims of this work are to:

Chapter 2

Develop a generic method to attach functionalities to RCA-generated materials, which expands the possible applications of the technique.

Chapter 3

Develop methods to condense RCA generated DNFs studied in Chapter 2 to improve

their properties for biological applications.

Chapter 4

Develop a DNA nanocarrier system for mRNA detection in live cells, with improved cellular recognition and uptake.

Chapter 2. Preparation, characterisation and application of chemically modified DNA nanoflowers

2.1 Introduction and aims

Nanostructures made from DNA molecules have many advantages over other exogenous organic and inorganic nanomaterials. For example, they have good biocompatibility, high water solubility, are easily programmed through Watson-Crick base pairing rules, and potentially target complementary nucleic acids.

Among them, DNA nanoflowers (DNFs) generated from rolling circle amplification (RCA) are excellent candidates for diagnostic and therapeutic applications. During RCA, a primer hybridising to a cyclised DNA template is amplified by a highly processive polymerase, generating elongated non-nicked DNA concatemer.[175,176] The DNAs produced then assemble into densely packaged, petal-like structures through crystallisation with inorganic magnesium pyrophosphate ($Mg_2P_2O_7 \bullet 3.5H_2O$, *MgPP*), generating precipitated material DNFs.[177] By including an aptamer complementary sequence into the RCA template, DNFs can recruit a specific aptamer, allowing them to recognise particular biomarkers.[170] Different functionalities such as imaging agents and drugs have been loaded onto DNFs by incorporating dye- or drug-labelled nucleoside triphosphates (dNTPs) during RCA, and the covalent incorporation of the functionalities was shown to be stable.[170] The densely packed structure allows DNFs to resist nuclease degradation and enables slow drug release under extreme conditions.[175,176]

Nevertheless, only limited strategies have been developed to modify DNA components in DNFs.[175,178] As mentioned in Section 1.3.4, several modified dNTPs have been used during RCA to construct DNFs. However, DNA polymerases such as phi29 do not incorporate bulky dNTPs efficiently, significantly restricting the application of this approach.[71,179] For example, incorporating fluorophore-labelled dUTP has been attempted in RCA, with only 2.5% of total dTTP substituted.[175] When biotinylated dATP was used, DNA production dramatically reduced when the ratio of biotinylated dATP went beyond 25%.[72] In another recent study, several dUTP analogues with different modified side chains at the C5 position (hydroxymethyl, COOH, allylamine, propynyl, aminopropargyl, and hydroxypentynyl dUTP) were used during RCA.[180] The results demonstrated that increasing the size of the modified side chains remarkably suppresses the production of DNA.

To address these obstacles, the work aimed to develop a generic method to introduce functional groups to RCA products efficiently. This was achieved by incorporating reactive dNTP analogues in RCA, followed by post-reaction attachment of the functional groups to these reactive positions through a labelling reaction (Figure 2.1**)**. The chemistry to modify RCA fabricated nanomaterials was vastly expanded, making the applications of these materials more versatile.

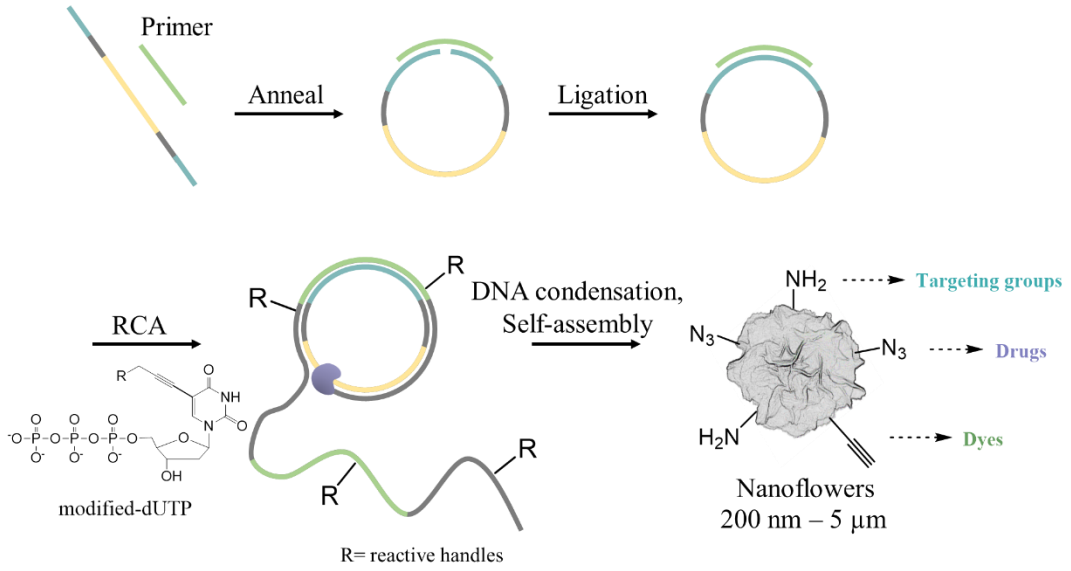


Figure 2.2. Scheme of enzymatic preparation of functionalised DNFs. A linear DNA template is annealed to a DNA primer and cyclised using T4 DNA ligase. The primer is then amplified by a DNA polymerase with strand displacement activity to give long ssDNA. During this process, modified dNTPs (here dUTP) are used to introduce reactive handles into the ssDNA formed. The DNA then co-crystallises with the pyrophosphate by-product and Mg^{2+} ions to give compact DNFs. These DNFs can be further modified to carry different functionalities for diverse applications.

2.2 Choice of oligonucleotide sequences

Several templates and splints were used in this study. Template **1** encoded an aptamer sequence specifically targeting the mucin 1 (MUC1) glycoprotein; overexpression of MUC1 in the cells is associated with a range of epithelial cancers, making it an attractive biomarker and therapeutic target for cancer.[181] Template **2** encoded to a trimeric G-quadruplex aptamer that recognises human epidermal growth factor receptor 2 (HER2);

overexpression of transmembrane receptor tyrosine kinase HER2 is found in approximately 15–30% of breast cancers and is associated with reduced survival. Therefore, it has drawn people's interest as a therapeutic target for breast cancer treatment.[182,183] Template **3** is a control containing a scrambled sequence that does not bind to any known receptors on cell surfaces. For Section 2.4-2.6, template **1** was used, while for Section 2.7, template **2** and **3** were used. The secondary structures of the templates are shown in Figure 2.2.

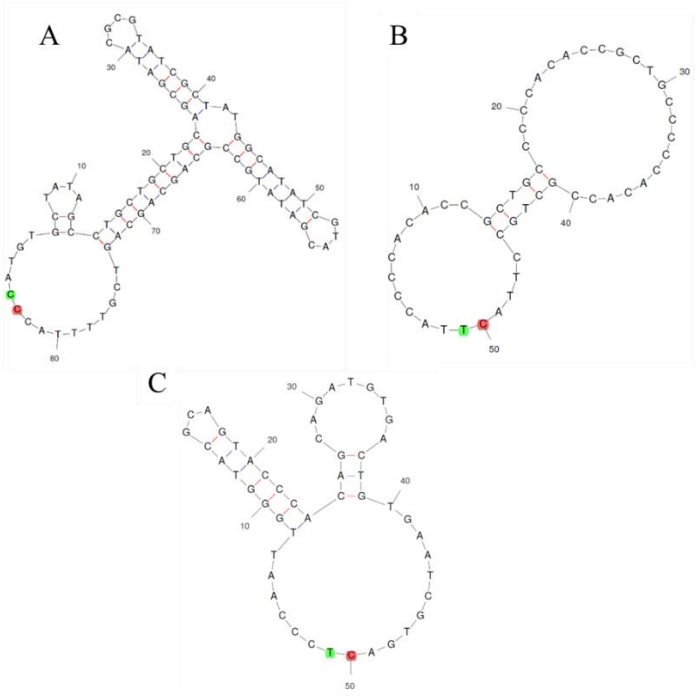


Figure 2.2. Secondary structures of cyclised templates used in the study. Predicted by Mfold web server software.[184] **A**. template **1**; **B**. template **2**; **C**. template **3**. The highlighted bases represent the point of ligation.

Fluorophore-labelled anti-MUC1 (sequence 7), anti-HER2 aptamers (sequence

9), and their randomised versions (sequence 8, 10) were made for cell binding tests. A FAM-modified HER2 aptamer was synthesised with a 5′-alkyne that can be covalently attached to azide-decorated DNFs via a CuAAC reaction (sequence 11). Their chemical structures are shown in Figure 2.3.

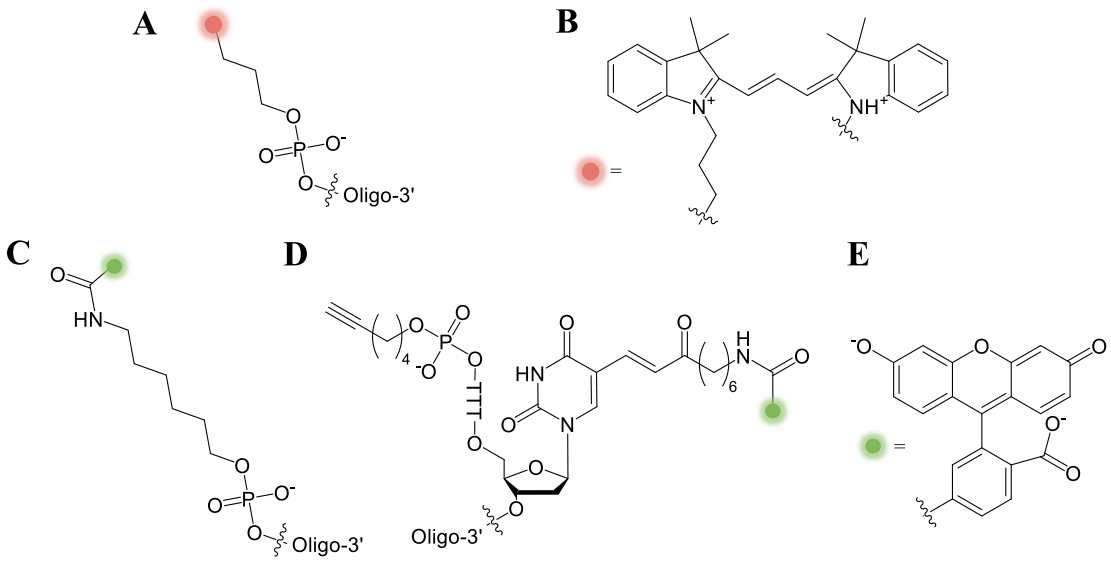


Figure 2.3. Chemical structures of fluorescent oligonucleotides used in the study. **A**. Chemical structure of 5'-Cy3 oligonucleotide with a simplified illustration of Cy3; **B**. Chemical structure of Cy3; **C**. Chemical structure of 5'-FAM oligonucleotide with a simplified illustration of FAM; **D**. Chemical structure of 5'-alkyne-FAM oligonucleotide; **E**. Chemical structure of FAM.

	Oligonucleotide	Sequence (5′→3′)	Length (nt)
1	Template **1** (anti-MUC1 aptamer)	[P]CATGTGCTATAGCCTGCTGCTGCAGCGATAC GCGTATCGCTATGGCATATCGTACGATATGCC GCAGCAGCAGTCGTTTTACC P = 5′-PO_4	83
2	Template **2** (anti-HER2 aptamer)	[P]TTACCCCACACCGCTGCCCCCACACCGCTG CCCCCACACCGCTGCCTTAC P = 5′-PO_4	50
3	Template **3** (control)	[P]TCCCAATTGGGTACGCAGTACCCACAGCAG ATGTGACTGTGAATCGTGAC P = 5′-PO_4	50
4	Splint **1** (anti-MUC1 aptamer)	GGCTATAGCACATGGGTAAAACGAC	25
5	Splint **2** (anti-HER2 aptamer)	TGGGGTAAGTAAGGCA	16
6	Splint **3** (control)	CAATTGGGAGTCACGATT	18
7	5′-Cy3 anti-MUC1 aptamer	[X]GGCTATAGCACATGGGTAAAACGAC X = 5′-Cy3	25
8	5′-Cy3 scrambled MUC1 aptamer	[X]GCACATGGGCTATAAACGACGGTAA X = 5′-Cy3	25
9	5′-FAM anti-HER2 aptamer	[X]GCAGCGGTGTGGGGGCAGCGGTGTGGGGG CAGCGGTGTGGGG X = 5′-FAM	42
10	5′-FAM mutated anti-HER2 aptamer	[X]GCAGCAGTGTGAGGGCAGCAGTGTGAGGG CAGCAGTGTGAGG X = 5′-FAM	42
11	5'-alkyne-FAM-HER2 aptamer	[X]TTTYGCAGCGGTGTGGGGGCAGCGGTGTG GGGGCAGCGGTGTGGGG X = 5′- hexynol modification, Y = amino C6-dT modifier labelled with FAM-NHS ester.	46

Table 2.1. Sequences of oligonucleotides used in this study. Template **1** and splint **1** have been reported previously.[185] Templates **2** and **3** have been reported previously in the group.[62]

2.3 Cyclisation of templates via T4 ligation

To perform RCA, linear templates were first converted to their cyclised version. To enable cyclisation using the T4 DNA ligase enzyme, linear oligonucleotides bearing

5′-phospate/3′-hydroxyl modifications were synthesised using automated solid-phase phosphoramidite chemistry. The purified linear templates were then annealed with a short bridging oligonucleotide (primer). The primer brings the two reactive ends of the linear template close, enabling the formation of a natural phosphodiester backbone linkage between the ends by the ligase.

In previous reports, the ligated templates were generally used for the subsequent RCA reaction without purification.[175,178,185,186] However, when the resulting ligated products were analysed on denaturing PAGE, more than one band was observed, including unreacted templates and ligated products in different sizes (Figure 2.4). This indicated that further purification by PAGE was necessary.

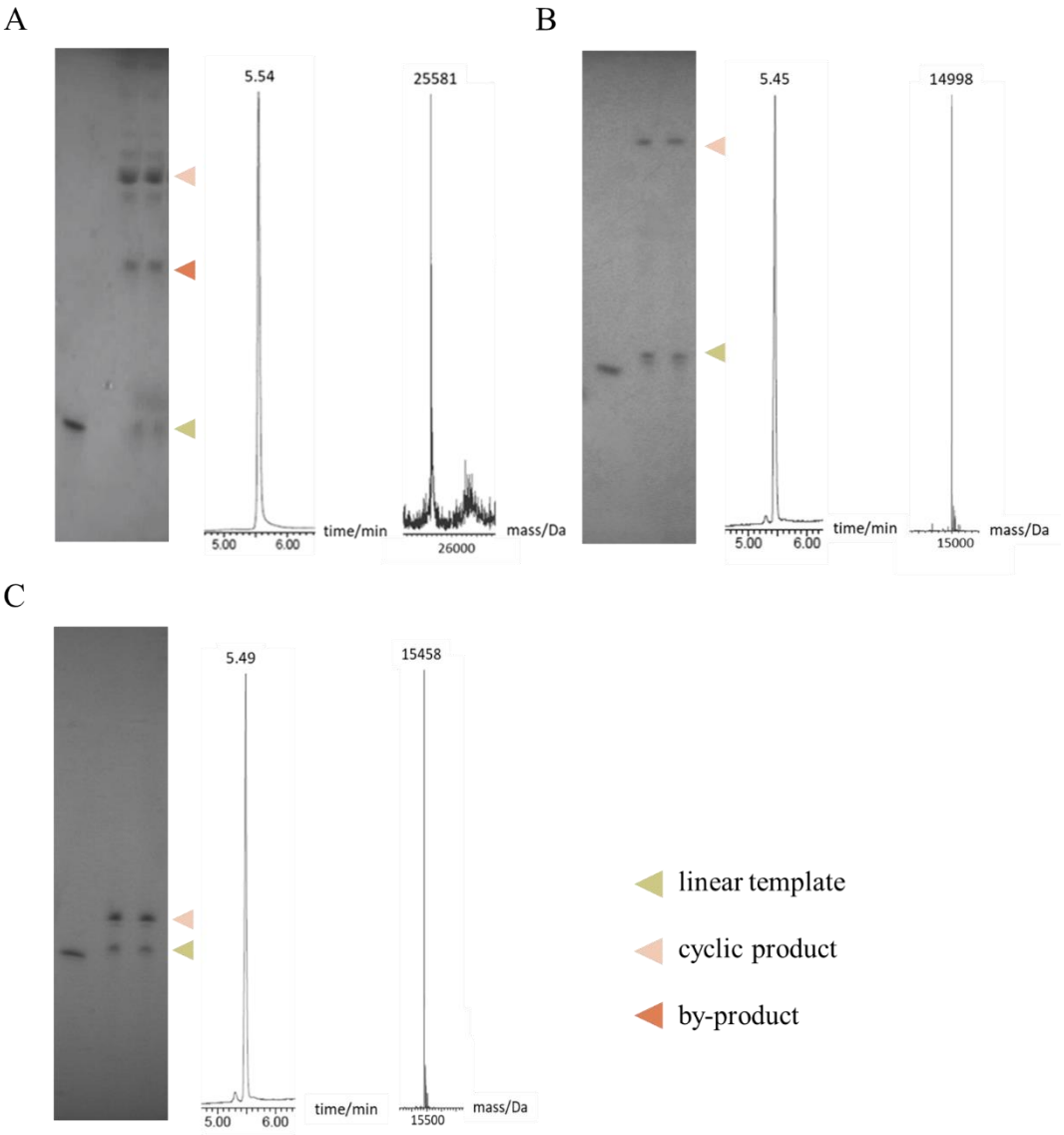


Figure 2.4. The splint-mediated enzymatic cyclisation of **A**. linear template **1** on 8% PAGE. After gel extraction, reverse-phase UPLC (UV abs at 260 nm) and mass spectrum (ES^-) of the cyclic product were obtained (calculated mass: 25579 Da, found mass: 25581 Da); **B**. linear template **2** on 15% PAGE. Reverse-phase UPLC (UV abs at 260 nm) and mass spectrum (ES^-) of the cyclic product were indicated (calculated mass: 14994 Da, found mass: 14998 Da); **C**. linear template **3** on 12% PAGE. Reverse-phase UPLC (UV abs at 260 nm) and mass spectrum (ES^-) were shown. (Calculated mass: 15456 Da, found mass: 15458 Da).

For template **1**, the cyclisation reaction gave multiple bands on PAGE, which were mainly polymeric ligated by-products. The most intense band was excised and extracted from the gel. This was a ligated cyclic product as confirmed by mass spectrometry. Compared with templates **2** and **3**, polymeric products were only observed for template **1**, possibly due to its long and highly self-templated sequence.

As the enzymatic ligation occurs between the 5′-phosphate and 3′-hydroxyl groups, various combinations could lead to the formation of by-products with different sizes and topologies (Figure 2.5).

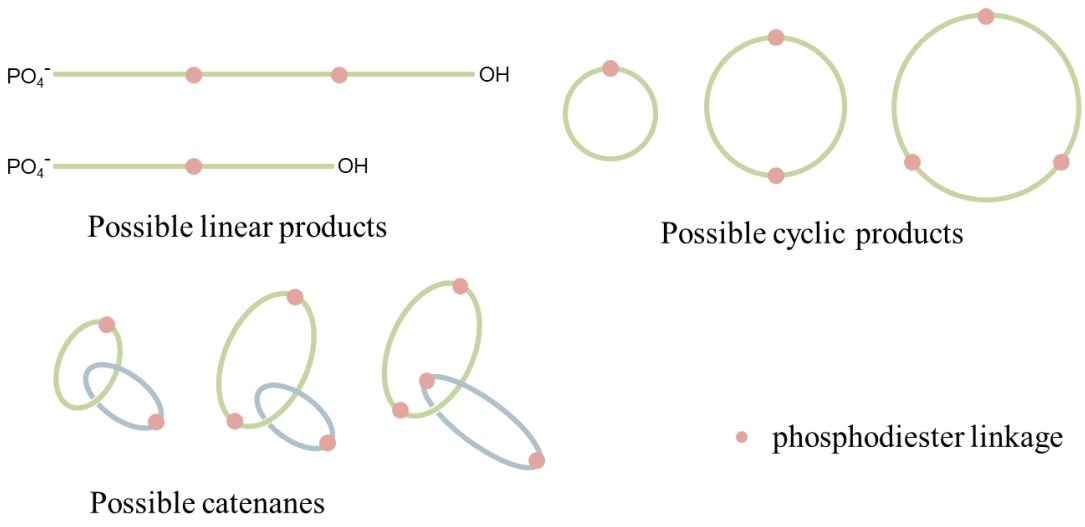


Figure 2.5. Possible linear and cyclic products formed during T4 cyclisation reaction. For linear by-products, the 5′-phosphate and 3′-hydroxyl groups are available for further ligation. Once polymeric cyclic products and catenanes are formed, no unreacted 5′-phosphate and 3′-hydroxyl are in presence.

To investigate the composition of the ligated products in template **1**, exonuclease

digestions were performed (Figure 2.6). Only unreacted linear template and linear by-products possess the terminal 5′ and 3′ ends after ligation. Therefore, Exonuclease (Exo) I and III, which digest the single-stranded DNA and double-stranded DNA (self-hybridisation and primer-template hybridisation sites) respectively from the 3′-hydroxyl groups (Figure 2.6.A), were used to remove linear oligonucleotides in the products. As shown by PAGE (Figure 2.6.B), only the linear precursor was eliminated after nuclease treatment. This indicated that the other bands showed on the gel were cyclic products of different sizes, coming from intra- and intermolecular ligation.

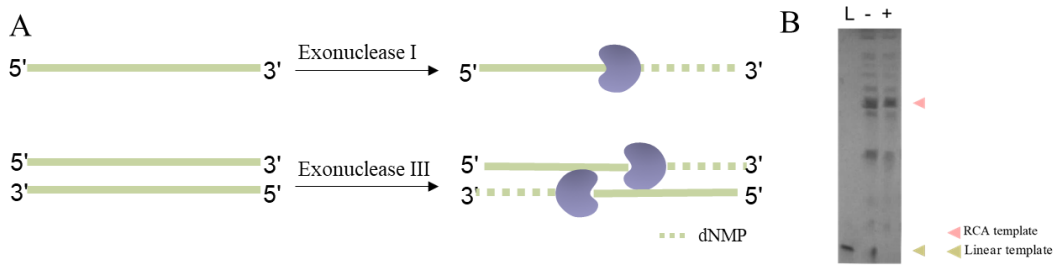


Figure 2.6. A. Digestion of linear DNAs in a 3' to 5' direction by Exo I and III. Exo I digests ssDNA, while Exo III is specific to dsDNA, where a primer is hybridised to a template. **B.** Ligation products of template **1** before and after digestion by Exo I and III, analysed on 8% denaturing PAGE. Lane **L**: Linear template. Lane –: without treatment of nucleases. Lane +: with the addition of nucleases.

Generally, low reaction concentration prevents intermolecular reaction as the reactive sites on different molecules have less chance to combine. To investigate the impact of reaction concentration on the generation of by-products, the ligation was conducted in different concentrations, with the concentration of template varying from 0.15 μM, 0.3

μM, 0.6 μM to 1.2 μM and 3 μM. After ligation, the reaction mixtures were analysed on denaturing PAGE (Figure 2.7). The gel showed that although varying the concentration, polymeric ligation was still present, emphasising the importance of purification before the next step.

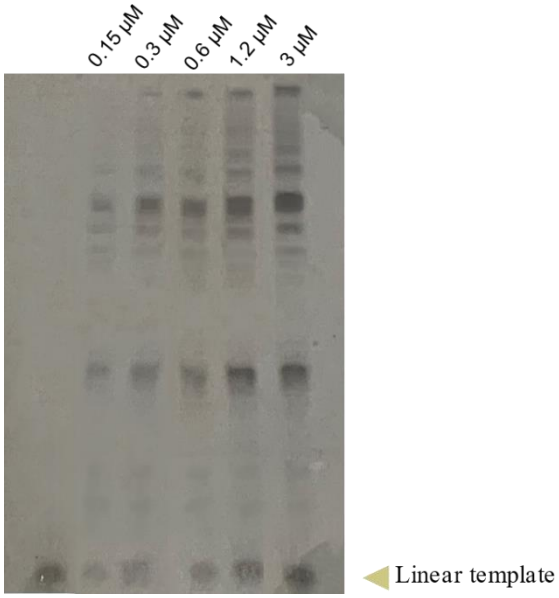


Figure 2.7. Analysis of T4 ligation of template **1** at different template concentrations, on 8% denaturing PAGE.

To ensure the consistency of the study, T4 ligated products of all templates were always purified by denaturing PAGE, and the bands interested were excised, extracted and desalted by NAP columns before use in RCA. HPLC traces showed that the gel-purified templates were in high purity (Figure 2.4).

2.4 Optimisation of RCA by phi29 DNA polymerase

The production of DNFs consists of two steps: production of long DNA strands by DNA polymerase, followed by crystallisation of the resulting DNA with inorganic components MgPP. To obtain the best results, various reaction conditions, including reaction temperature and different reaction buffer components, were investigated using unmodified dNTPs.

2.4.1 Reaction temperature

The optimal reaction temperature for phi29 polymerase is 30 °C. Elevated reaction temperature could benefit the amplification of DNA with high G/C content and improve amplification efficiency. Reaction temperature up to 40 °C reportedly does not significantly compromise the enzymatic activity of phi29.[187] In order to determine the optimal reaction temperature for RCA, reactions were carried out at a gradient temperature (33.2 °C, 30.9 °C, 30.2 °C, 30 °C), and the products were loaded on a 0.8% agarose gel for analysis (Figure 2.8). As RCA products are extremely long, they have poor mobility on the gel and remain at the top. The results showed a significant reduction in long DNA production when the temperature was higher than 31 °C. Therefore 30 °C was used in all the following experiments.

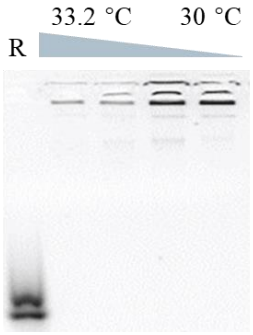


Figure 2.8. A 0.8% agarose gel showing RCA products when incubated at different temperatures. Lane **R**: linear template **1** and splint **1.**

2.4.2 Addition of dithiothreitol (DTT)

Dithiothreitol (DTT) is frequently added to enzyme reaction buffers as a protective reagent for the cysteine residues in proteins. It acts as a potent reducing agent which prevents intramolecular and intermolecular disulfide bridge formation via air oxidation between the SH groups of the cysteine residues.[188]

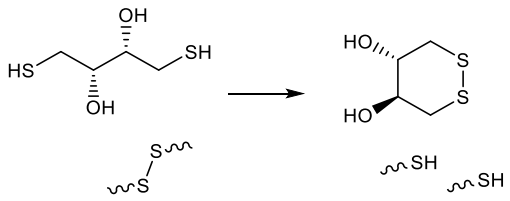


Figure 2.9. Reduction mechanism of disulfide bond cleavage by DTT.

The reaction buffer of phi29 DNA polymerase was supplemented with DTT. However, DTT is not very stable in solution. After repeating thaw and freeze, it precipitates and loses its potency. Non-reversible precipitation of DTT from the reaction buffer after thaw and freeze cycles was observed during our study. To test if the presence of DTT

was essential for efficient RCA, the reactions were performed in the buffers with and without DTT. The RCA products were analysed by 0.8 % agarose gel electrophoresis (Figure 2.10). No apparent decrease in long DNA production was shown, meaning precipitation of DTT should not cause any issue.

2.4.3 Addition of BSA

Addition of 0.1 mg/mL BSA is usually recommended for enzymatic reactions, as it prevents enzyme loss in tube and pipette tip surfaces and stabilises the enzyme. However, adding BSA to our reaction is not ideal. It has been reported that proteins in the reaction mixture can be encapsulated and trapped within the DNFs generated during RCA.[189] This could introduce undesirable reactive sites such as primary amine to the structure, leading to non-specific attachment of functionalities.

To see if the absence of BSA impairs the efficiency of RCA, the reactions with and without BSA were carried out using the general procedures. From analysis on 0.8 % agarose gel, no significant reduction in DNA production was observed (Figure 2.10), indicating that the addition of BSA is not imperative for the reaction. A second band with higher mobility was observed, which has been reported in other studies as a double-stranded DNA product.[190] More details about the band are demonstrated in Section 2.5.3.

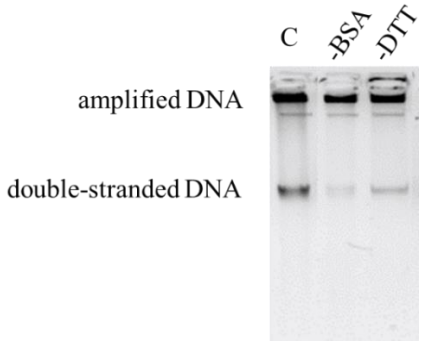


Figure 2.10. A 0.8% agarose gel showing RCA products with different components in a reaction buffer. Lane **C**: a control with the presence of both BSA and DTT.

2.4.4 Amplification time

It has been reported that amplification time substantially contributes to the size and morphology of RCA products.[175] When the reaction is performed for a longer time, the size of the resulting particles increases from 150 nm to a few micrometres, and the structures bloom from petals to flowers.[175,178,191] To investigate the effect of amplification time on DNA production and particle structure, reactions were carried out for different times (1, 2, 4, 6, 8, and 20 h). After incubation for the desired period, the reactions were inactivated by heating at 65 °C for 10 min. The precipitated products were isolated by centrifugation and loaded onto a 0.8% agarose gel to compare RCA efficiency. While long DNA was generated in all cases, an increase in DNA yield was observed with increasing reaction time. For the reactions with incubation time shorter than 4 h, most of the DNA products were soluble and found in the supernatant. As the incubation time increased, more DNA was crystalised with Mg^{2+} and pyrophosphate,

forming precipitated products. The morphology of the particles generated was analysed using scanning electron microscopy (SEM).

SEM imaging showed that flower-like structures started to form after 2 h and the size of the particles grew slowly over time. When the incubation time increased to 20 h, the diameter of the DNFs formed reached around 2.2 μm. In addition, the size of DNFs was uniform at the beginning of the amplification but was significantly more dispersed after 20 h (Figure 2.11). The trend is consistent with previous studies;[175] however, an earlier 'blossom' of DNFs was observed, possibly due to the different templates and enzymes used.

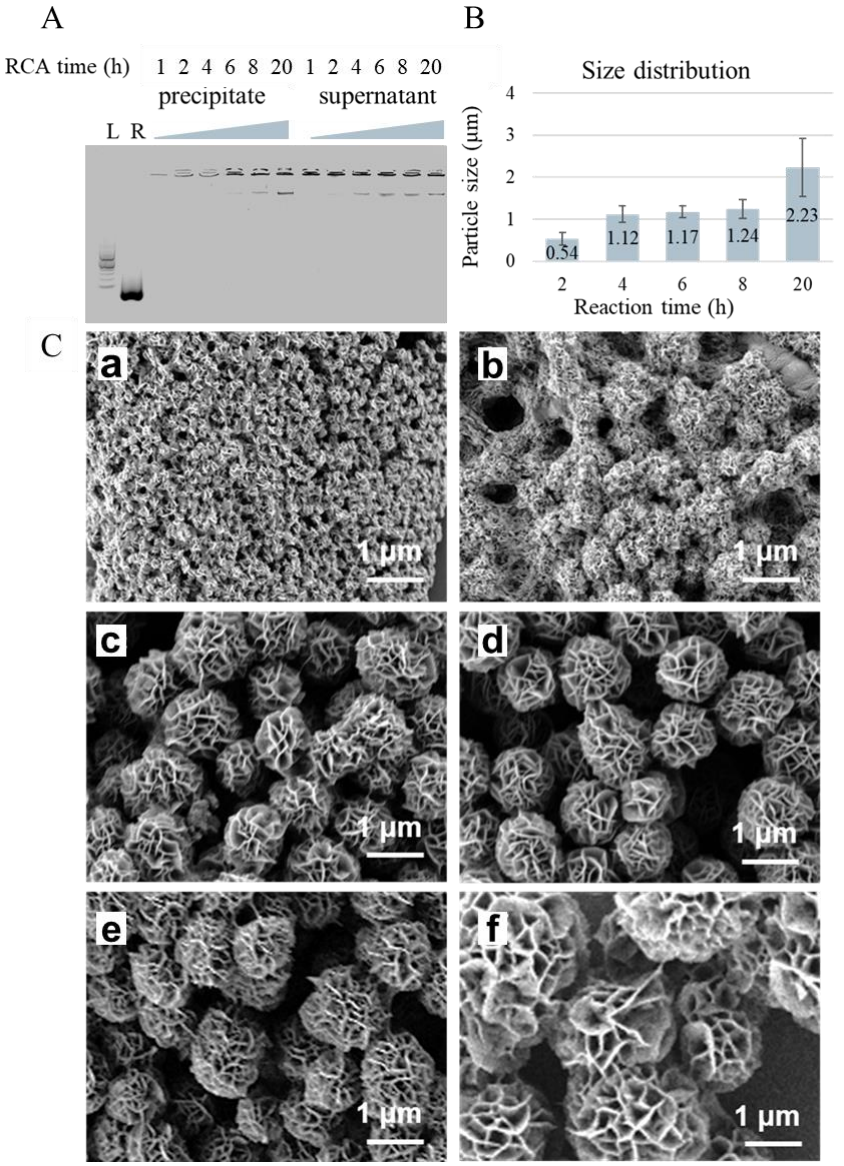


Figure 2.11. Effects of reaction time on RCA. **A**. Agarose gel analysis of RCA products with different amplification times; Lane **L**: 100 bp DNA ladder; Lane **R**: linear template **1**; **B**. Size distribution of DNFs obtained after different amplification times. Size measured from SEM images. Error bars represent the standard deviation of 50 particles measured. **C**. SEM images of DNFs with **a**. 1 h; **b**. 2 h; **c**. 4 h; **d**. 6 h; **e**. 8 h and **f.** 20 h incubation.

2.4.5 Concentration of Mg^{2+}

Mg^{2+} in the reaction buffer contributes to the formation of the inorganic scaffold of DNFs and plays an essential role in the enzymatic process. It serves as a cofactor for DNA polymerases, facilitating the interaction between DNA polymerase and the substrate. Moreover, positively charged Mg^{2+} stabilises negative charges on phosphate backbones, promoting the primer's hybridisation to the template. Therefore, we investigated the effect of Mg^{2+} concentration on RCA efficiency by adding different concentrations of Mg^{2+} (from 10 mM to 22.5 mM) to RCA reactions. The precipitated DNFs were isolated by centrifugation, and the precipitate and the supernatant were loaded onto a 0.8% agarose gel to compare RCA efficiency (Figure 2.12).

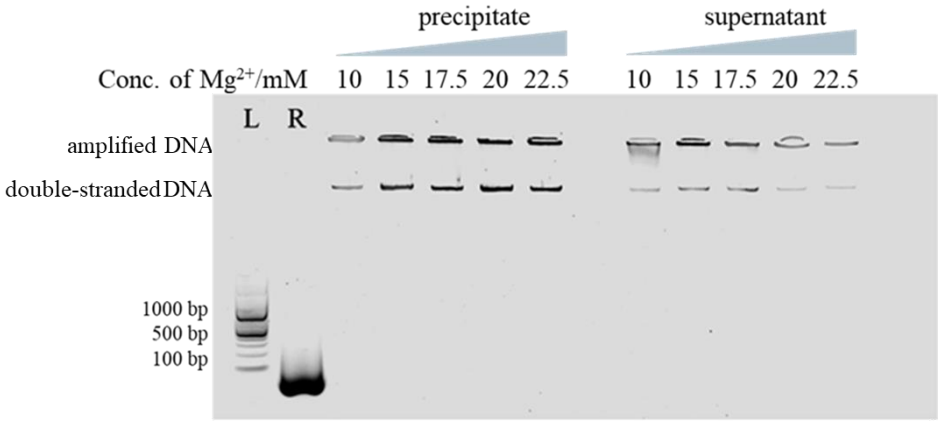


Figure 2.12. A 0.8% agarose gel of the precipitate and supernatant from RCA reactions with different Mg^{2+} concentrations. RCAs were carried out for 20 h using phi29 DNA polymerase. Lane **L**: 100 bp DNA ladder; Lane **R**: linear template **1**.

The agarose gel showed that with Mg^{2+} concentrations above 15 mM, RCA proceeded

efficiently. Less DNA was observed when 10 mM of Mg^{2+} was used, suggesting that the amplification was slightly impaired. This was also reflected in the size of the precipitate obtained after centrifugation. The pellet formed with 10 mM Mg^{2+} was smaller and harder to collect by centrifugation than the others. Moreover, with a higher concentration of Mg^{2+}, less DNA was observed in the supernatant. This can be attributed to the increased amount of MgPP formed, which settled down DNA. In the latter studies, 15 mM of Mg^{2+} was used, which was the minimal amount needed for well-performed reactions, unless otherwise stated.

2.5 Modified nucleotide triphosphates

2.5.1 Choice of modified nucleotide triphosphates

Advantages of using modified triphosphates in RCA include elevated stability against nucleases and more diverse applications in medical and biological fields. However, only a limited number of modified triphosphates have been successfully incorporated into RCA to generate DNA products with chemical modifications (section 1.3.5).[71,73,178,179,186] Some of them have been shown to impede the production of long DNA products.[73] Besides, the use of resulting modified RCA products was not well explored.

With reaction conditions optimised, the compatibility of six modified nucleoside

triphosphates with RCA was investigated. Each triphosphate has a chemically reactive handle – either an amine, alkyne, or azide. These groups are small, potentially to be tolerated by DNA polymerases. They contain chemical groups that can be subsequently labelled, allowing post-synthesis modification with commercially available bio-tags and dyes. Labelling reactions used for these chemical handles include N-hydroxysuccinimide (NHS) ester coupling (for amines) or copper catalysed alkyne-azide cycloaddition/strain-promoted alkyne-azide cycloaddition (for azides and alkynes).

Triphosphates **1**–**5** are mimics of dTTP, whereas **6** is a mimic of dCTP (Figure 2.13). Triphosphates **1**, **2**, **4,** and **6** are commercially available, whereas triphosphates **3** and **5** were prepared according to literature procedures and converted to the corresponding sodium salts before use.[192,193]

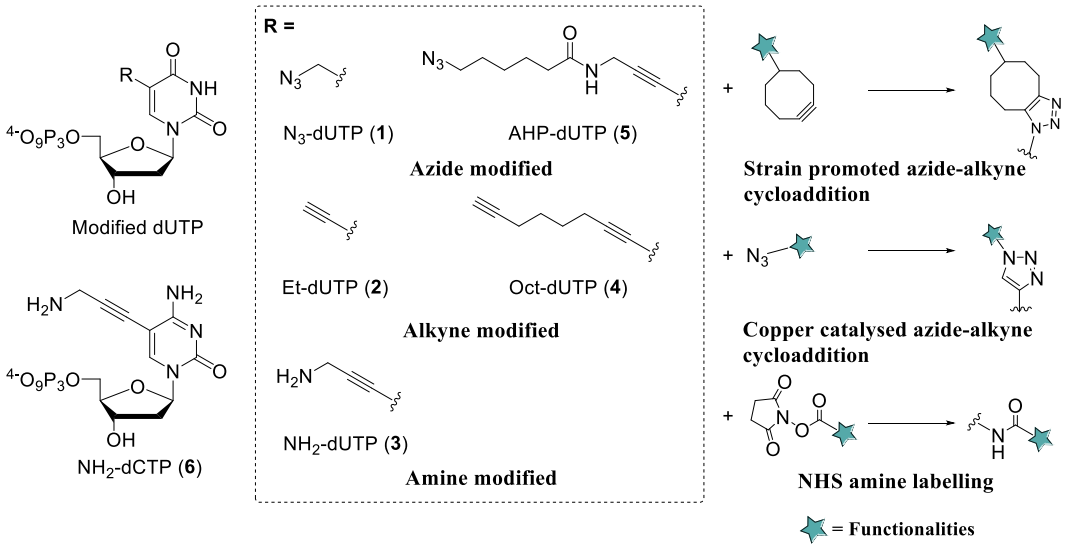
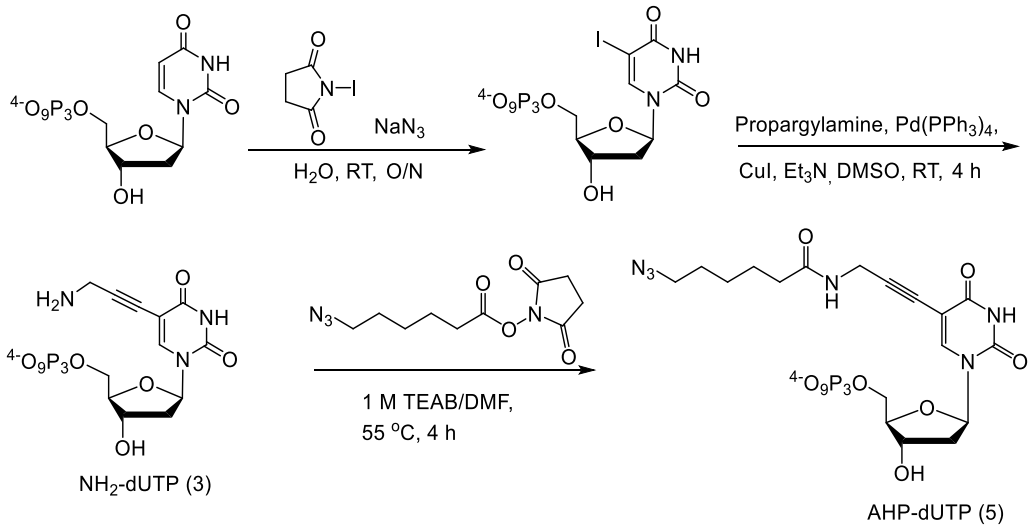


Figure 2.13. Modified triphosphates and corresponding labelling methods investigated in this study. Triphosphates **1**–**5** are mimics of dTTP, whereas **6** is a mimic of dCTP. The reactive chemical handles can subsequently be labelled via SPAAC (for azide), CuAAC (for azide and alkyne), or NHS (for amine) labelling reactions.

2.5.2 Synthesis of modified nucleotide triphosphates 3 and 5

2'-deoxyuridine-5'-O-triphosphate (dUTP) has been extensively used to introduce functional groups to nucleic acids, as it is one of the easiest nucleotide triphosphates to chemically modify.[194–196] Importantly, a functional group attached at the 5-position on the uracil base protrudes into the major groove of DNA double helix, which is distant from Watson-Crick base-pairing sites. Therefore, introducing modifications at this position ensures minimal disruption and destabilisation to the B-DNA duplex formed.



Scheme 2.1. Synthesis of NH_2-dUTP (**3**) and AHP-dUTP (**5**) from dUTP.

Starting from a commercially available dUTP, iodination was carried out at room temperature, using N-iodosuccinimide and sodium azide in water. The reaction is highly regioselective, giving only one regioisomer of iodo-dUTP intermediate. The crude iodo-dUTP was first purified by HPLC, then coupled with propargylamine through the Sonogashira reaction using $Pd(PPh_3)_4$ and CuI as the catalysts.[192] The product NH_2-dUTP (**3**) was purified by HPLC and was further labelled with 6-azidohexanoic acid NHS ester to generate AHP-dUTP (**5**). Characterisations of the triphosphates are listed in Section 6.6.

2.5.3 Incorporation of modified triphosphates in RCA

The generation of DNFs, as mentioned before, involves two stages: elongation of DNA strands by DNA polymerase followed by crystallisation of DNA strands with inorganic

components MgPP in the reaction buffer. To investigate the performance of triphosphates **1**–**6** in the generation of DNFs, both steps were evaluated. For general RCA, the concentration of each dNTP was kept at 2 mM. When a modified triphosphate was used, the concentration of the triphosphates remained 2 mM while the ratio between modified and canonical triphosphate varied. RCA with various ratios of triphosphates **1**–**6** was carried out for 20 h.

2.5.3.1 Length analysis of DNA products by agarose gel electrophoresis

The length of RCA products was analysed by agarose gel electrophoresis. After RCA, the precipitated products were isolated by centrifugation, and both precipitate and supernatant were loaded on a 0.8% agarose gel. For all modified triphosphates, long DNA products with low mobility were observed at the top of the gel, indicating continuous amplification of DNA strands by the polymerase (Figure 2.14).

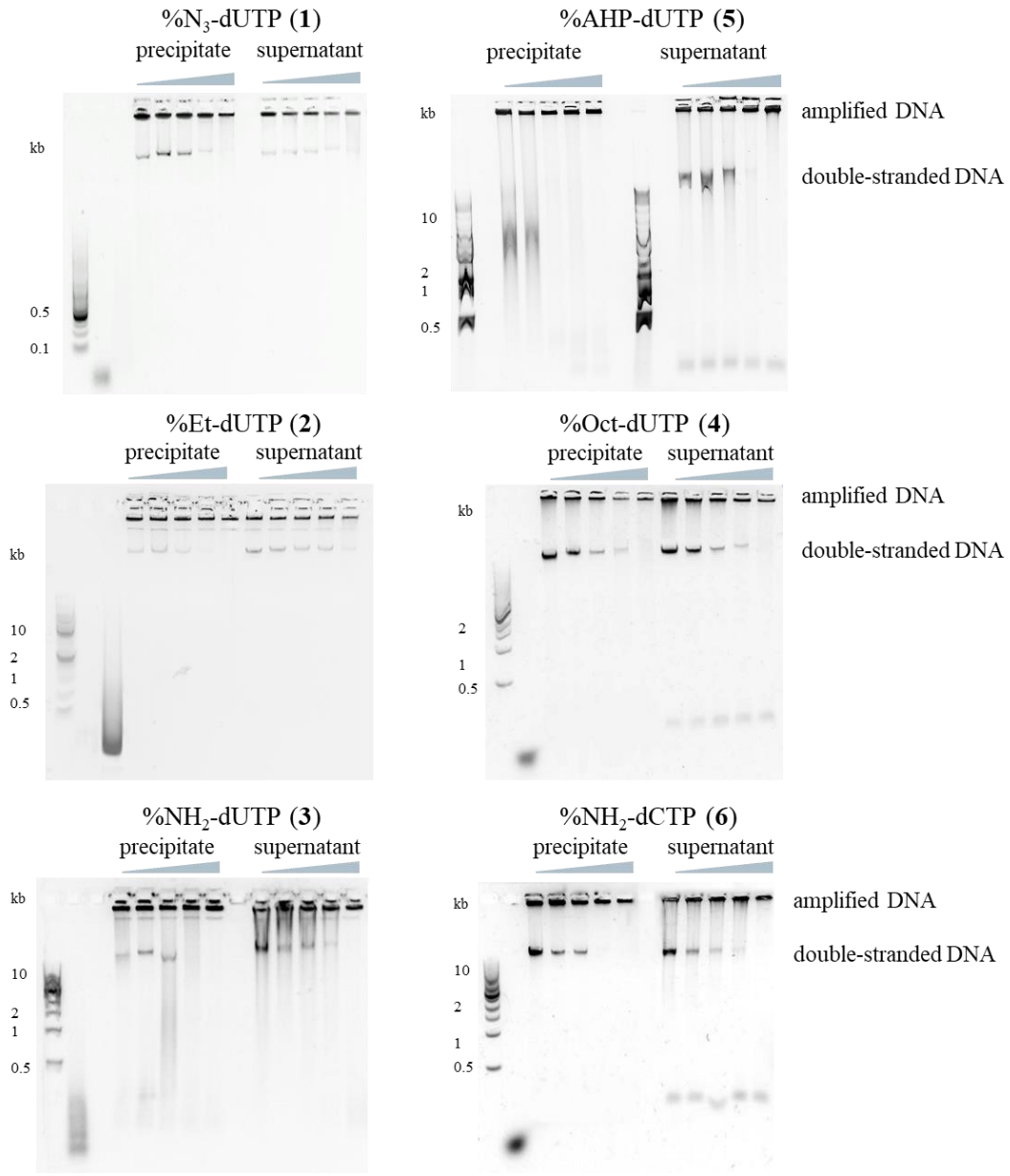


Figure 2.14. Agarose gel electrophoresis analysis of RCA reactions when dTTP was substituted with 0–100% modified triphosphates indicated above the lanes. The total dNTP concentration was kept at 2 mM in all cases.

In some cases, a second band with higher mobility was observed. This band has been observed in previous studies, which was confirmed to be a double-stranded DNA

product.[190] It has been proposed that single-stranded DNA products could self-hybridise to form double-stranded DNA, hindering the production of longer DNA and eventually stopping the amplification. This can be avoided by adding single-strand binding (SSB) proteins which block self-hybridisation (Figure 2.15). When RCA is used to generate long single-stranded DNA, adding SSB proteins is a helpful strategy to ensure efficient DNA production. However, to avoid the introduction of undesirable reactive sites, such as amine, to DNFs, SSB was not used in our study.

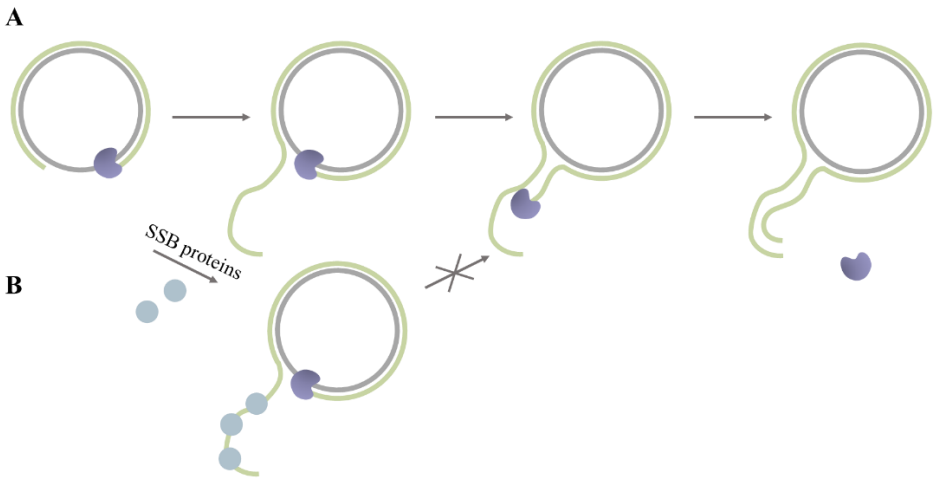


Figure 2.15. A proposed mechanism of **A.** how double-stranded products are formed during RCA and **B.** how SSB proteins prevent double-stranded product formation.

2.5.3.2 Quantification of DNA produced by fluorometric plate reading assay

While agarose gels provide a qualitative understanding of the RCA reaction products,

quantification was also sought when employing modified triphosphate. SYBR^{TM} Gold, a fluorescent dye that binds both single- and double-stranded DNA, was used in a fluorometric plate reading assay.

DNFs are complex structures formed by DNA and MgPP. The structures have shown to be highly stable against nucleases and do not dissociate easily upon dilution.[175] To quantify the DNA contents in DNFs, the compact structures needed to be disrupted to ensure complete binding with SYBR^{TM} Gold. To achieve this, after RCA, precipitated DNFs were isolated by centrifugation and incubated with chelating reagent EDTA overnight. EDTA chelates Mg^{2+}, consequently solubilising the inorganic core of the DNFs and releasing the absorbed DNA. Scanning electron microscopy imaging confirmed the collapse of the DNF structure after EDTA incubation (Appendix 7.32). The supernatant from centrifugation was also collected. Both precipitate (blue bars) and supernatant (green bars) were mixed with SYBR^{TM} Gold, and the fluorescence was measured using a BMG Labtech CLARIOstar microplate reader (Figure 2.16). The combination of the DNA in the precipitate and the supernatant gave the total DNA generated during RCA.

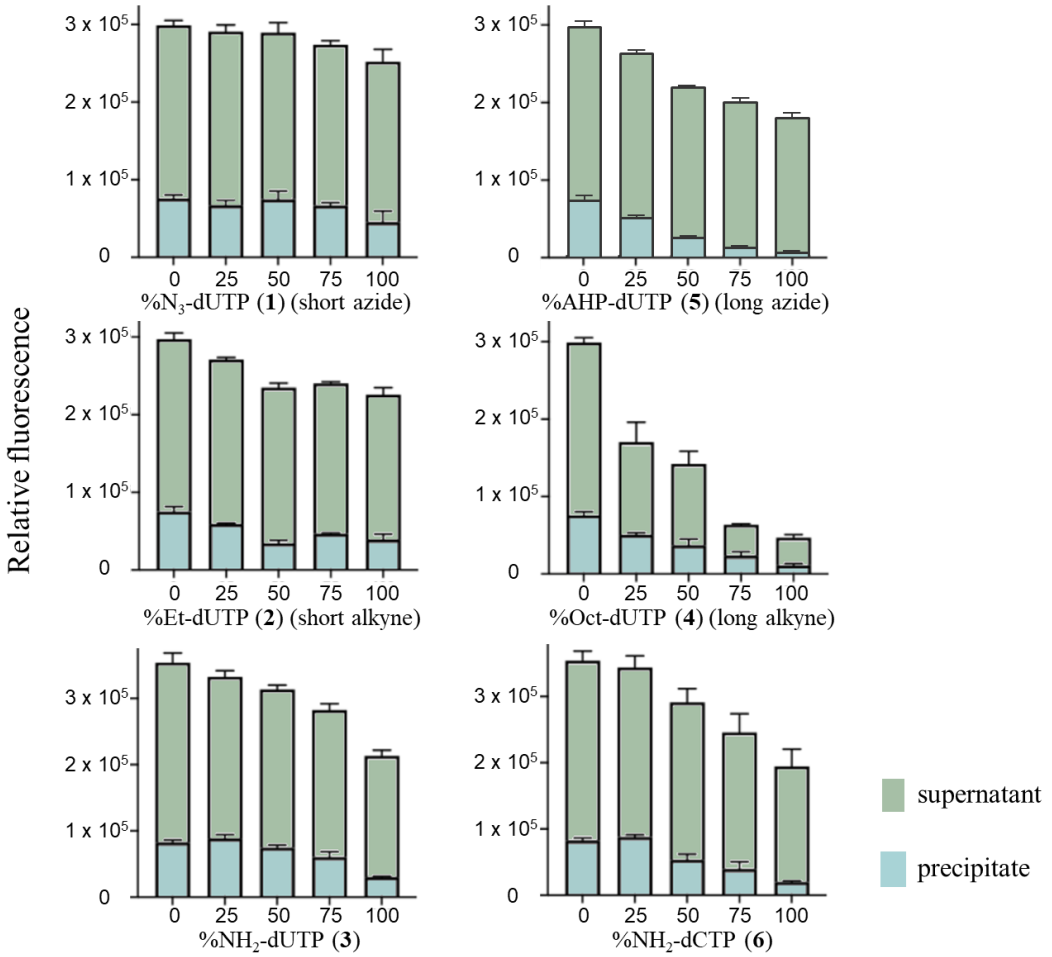


Figure 2.16. Fluorescence-based analysis comparing DNA produced during RCA when modified triphosphates were used in the amplification step. The x-axis indicates the percentage of modified triphosphates substitution. The y-axis is the relative fluorescence intensity which is approximately proportional to DNA concentration. Unmodified reaction (0%) is used as a reference for direct comparison. Green bars represent the 'free' DNA in the supernatant, and blue bars represent DNA precipitated as DNFs. Error bars represent the standard deviation of three different RCA reactions.

DNA was produced in all cases. However, as the ratios of modified triphosphates increased, the amount of overall DNA generated decreased. Some modified

triphosphates caused significantly lower yield than the others (e.g. Oct-dUTP).

For azide-modified triphosphates, N_3-dUTP (**1**) and AHP-dUTP (**5**), a considerable amount of DNA was produced during RCA, even when the canonical dTTP was fully substituted. In comparison with unmodified RCA (0% substitution), 100% substitution by N_3-dUTP (**1**) slightly reduced the overall amount of DNA produced by 16%. While for AHP-dUTP (**5**), 34% less DNA was yielded. This is in agreement with other reports where nucleobases with smaller modifications were tolerated better by phi29 DNA polymerase.[71,72,179,180,190] When looking at the amount of DNA entrapped in precipitated DNFs, much less DNA was observed when AHP-dUTP (**5**) was used due to less efficient amplification. Similarly, for alkyne-dUTPs used in this study, Et-dUTP (**2**) with a shorter linker on the 5-position showed a greater amount of DNA production during RCA than bulkier Oct-dUTP (**4**). When substituting dTTP completely with Et-dUTP (**2**), overall DNA yield decreased by 20%, while Oct-dUTP (**4**) resulted in 76% reduction. One possible explanation for the poorly yielded reaction with Oct-dUTP (**4**) is that the highly hydrophobic linker makes the resulting DNA product aggregate easily, preventing the DNA chain from further extending. For amine-modified triphosphates, NH_2-dUTP (**3**) and NH_2-dCTP (**6**), similar trends were observed. With the substitution of modified triphosphates increasing, the amplification of DNA slowed down. DNA was produced at 100% substitution for all triphosphates used, indicating the modified

dNTPs were actually incorporated during RCA.

2.5.3.3 Structural analysis of DNFs by Scanning electron microscopy (SEM)

Scanning electron microscopy (SEM) is one of the most useful instrumental methods for solid nanoparticle imaging. Here, SEM was used to study the structure of DNFs bearing different modifications. From SEM images, for N_3-dUTP (**1**) and Et-dUTP (**2**), the structure of DNFs was not affected even at high substitution levels (Figure 2.17). However, for AHP-dUTP (**5**) and Oct-dUTP (**4**), small-sized particles were observed with 100% modified triphosphate substitution. This correlates with the results from the plate reading assay, where less DNA was precipitated at high modification levels when these two triphosphates were used. Similarly, the size of DNFs formed with amine-modified triphosphates NH_2-dUTP (**3**) and NH_2-dCTP (**6**) became smaller when higher percentages of modified triphosphates were used. This is in agreement with a reduction in the amount of DNA produced (Figure 2.14). Another possible cause of the decrease in size is that the cationic amine interacted with the anionic phosphate backbone in DNA, lessening the repulsion and compacting the structure. SEM demonstrated that by altering the type and dose of modified triphosphates, the size and morphology of DNFs can be controlled. With tunable size, the applications of these particles as biomedical agents can be potentially expanded.[197]

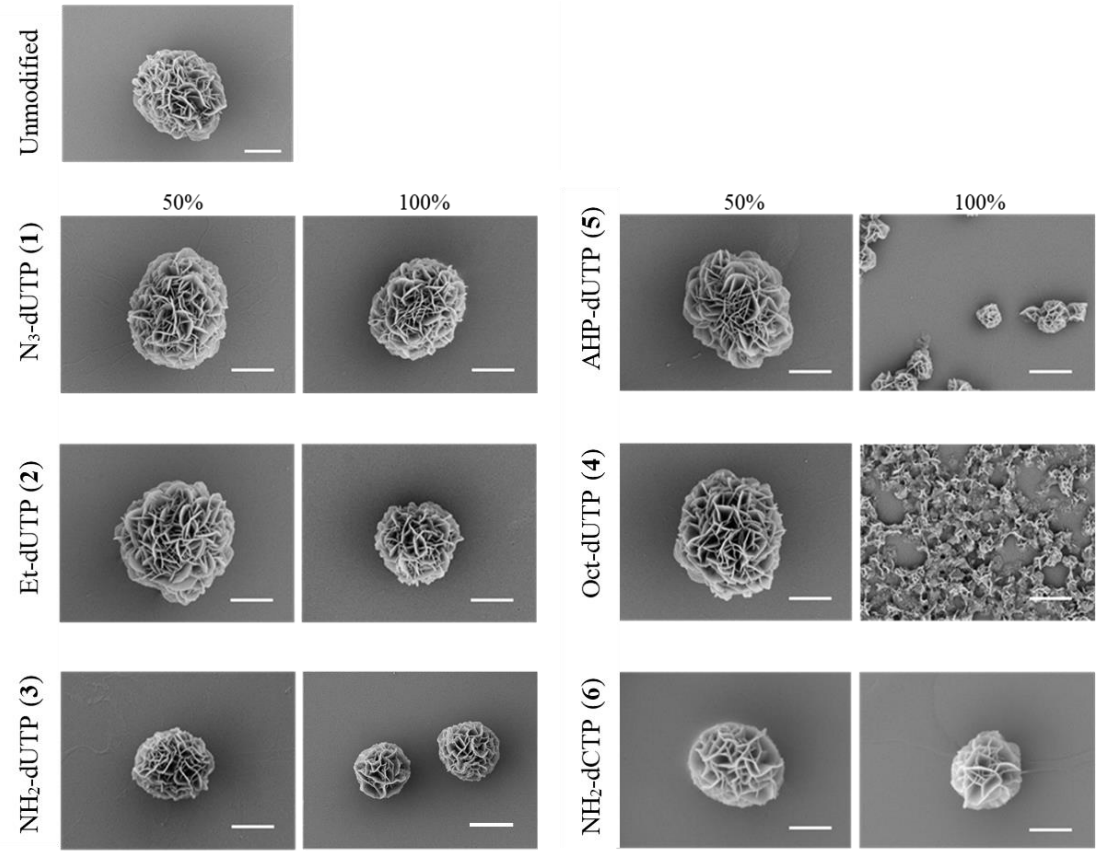


Figure 2.17. SEM images of DNFs with different modified triphosphates. Only 50% and 100% modified triphosphate substitutions are shown here. Other percentages are shown in Section 7. A scale bar represents 1 μm.

2.6 Labelling of modified DNFs

It has been demonstrated that the introduction of modified triphosphates **1**, **2**, **3,** and **6** did not significantly affect DNA yield or DNF morphology. Therefore, subsequent labelling on these chemical handle-containing DNFs was investigated. For the preliminary studies, fluorescent dyes were chosen as they can be visualised and quantified easily.

2.6.1 Labelling of amine-modified DNFs with NHS ester

DNFs produced with amine-modified triphosphates were labelled with a fluorophore-NHS ester. Coupling between NHS ester and amine requires a pH between 7.2 to 9. Organic solvents such as DMSO and DMF are sometimes needed to provide better solubility for hydrophobic dyes such as non-sulfonated fluorescent dyes. For labelling of DNFs, it is crucial to ensure that the labelling condition does not disrupt the DNA encapsulation and the DNF structure. In this study, a labelling buffer consisting of 10 mM HEPES, 10 mM Mg^{2+}, 50% DMSO with pH 8.0 was used. Compared to bicarbonate buffers commonly used for such labelling reactions, the buffering capacity of HEPES is not affected by the CO_2 concentration, making it more suitable for long term storage and applications in the open atmosphere. 10 mM Mg^{2+} was included in the buffer to stabilise the structure of DNFs, by preventing the dissociation of the inorganic skeleton MgPP. To investigate the stability of DNFs in this labelling environment, unmodified DNFs were incubated in the buffer overnight in contrast to different aqueous environments. The stability of DNFs in labelling buffers was analysed by agarose gel electrophoresis and SEM.

After incubation, DNFs were isolated by centrifugation. The precipitate and the supernatant were run on agarose gel separately. The results showed that including 10 mM Mg^{2+} in the HEPES buffer (10 mM HEPES, 50% DMSO, pH=8.0) prevented the

DNA from leaching into the supernatant (Figure 2.18.A). In contrast, PBS and water led to the escape of DNA from the DNFs to the supernatant. This is an important observation, given that many DNF protocols utilise PBS and water for long-term DNF storage. In our latter studies, all samples were prepared fresh before use to avoid loss of DNA from DNFs.

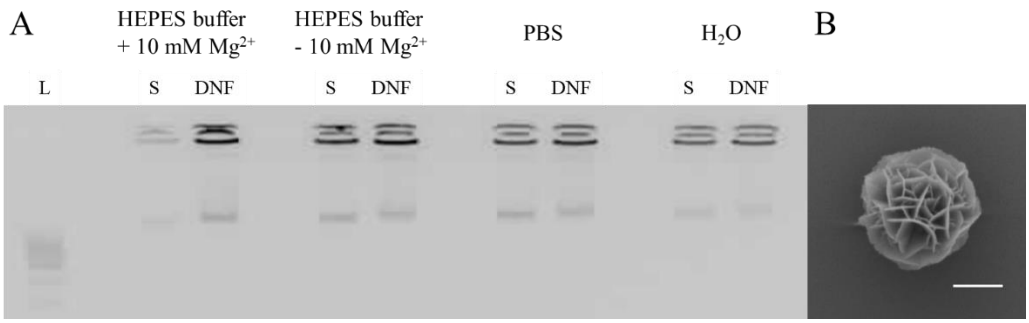


Figure 2.18. Stability of DNFs in different aqueous environments. **A**. The DNA present in the DNFs (noted as DNF) and the supernatant (noted as S) after incubation in 10 mM HEPES, 50% v/v DMSO with/without 10 mM Mg^{2+}, PBS and water overnight, analysed by 0.8% agarose gel electrophoresis. The addition of Mg^{2+} prevents DNA leaching from DNFs. Lane **L**: 1kb DNA ladder; **B**. SEM image of DNF incubated in 10 mM HEPES, pH 8.0, 50% v/v DMSO with 10 mM Mg^{2+}. Scale bar represents 1 μm.

From the SEM image, no change in the morphology was seen after incubating DNFs in the Mg^{2+}-supplemented HEPES buffer (Figure 2.18.B). This buffer was used for all subsequent labelling reactions unless otherwise stated.

DNFs generated with various ratios of NH_2-dUTP (**3**) were labelled with FAM-NHS

ester in the HEPES labelling buffer. The excess unreacted dye was washed away by centrifugation, and the FAM-labelled DNFs were imaged by fluorescence microscopy (Figure 2.19.B). The bright field was used to observe the actual DNF and the FAM channel to detect FAM dye (Figure 2.19.C). From the imaging, bright green spots were observed which overlapped with the DNFs in the bright field, indicating successful labelling of the DNFs with the fluorophore (Figure 2.19.D). To get a relative quantification of the labelling, the fluorescence of DNFs was measured using a fluorometric plate reading assay. The isolated DNFs were first incubated in EDTA to break down their compressed structures, followed by fluorescence measurement by the plate reader under the FAM channel. As expected, the fluorescence intensity of DNFs increased as the ratio of modified triphosphates used increased. This suggested that by altering the amount of modified dNTP used in RCA, the extent of labelling on DNFs can be controlled. However, a small amount of non-specific labelling was also observed in unmodified DNFs (Figure 2.19.F), which is considered to occur on the DNA polymerases encapsulated in DNFs. The source of this non-specificity is discussed in Section 2.6.4. The SEM image of labelled DNFs showed minimal disruption in morphology after labelling (Figure 2.19.E).

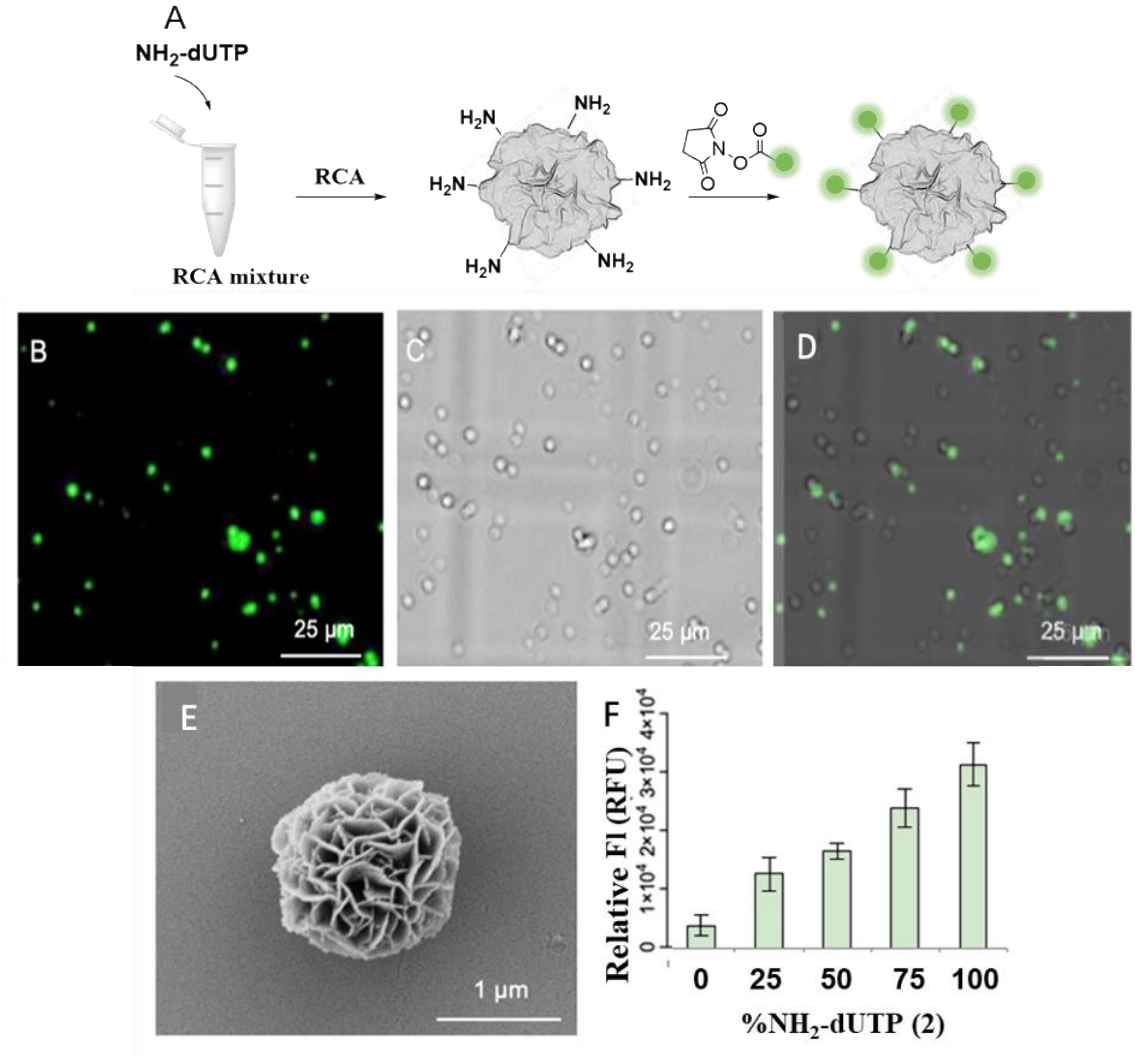


Figure 2.19. NHS-ester labelling of H_2N-DNFs. **A**. Schematic diagram of the method; **B**. Fluorescence image of FAM-labelled H_2N-DNFs under 475 nm excitation. The DNFs were prepared with 50% of NH_2-dUTP (**3**); **C**. Bright field image of the sample shown in B; **D**. Overlay of fluorescence and bright field. Some particle migration occurs as the samples are in water; **E**. SEM image of DNFs after labelling; **F**. Relative fluorescence intensity (RFU) of FAM-NHS labelled DNFs containing varying modification levels. Error bars represent the standard deviation of three repeat reactions.

2.6.2 Labelling of azide-modified DNFs by BCN dyes through SPAAC

Azide modified DNFs (N_3-DNFs) were prepared using different percentages of N_3-dUTP. The modified DNFs with the addition of 50% N_3-dUTP (**1**) were first labelled with Cy5-BCN through SPAAC reaction. Unmodified DNFs were also labelled with the same dye as a negative control. However, a fluorescent signal was observed in both cases, indicating non-specific interaction between the DNFs and the Cy5-dye (Appendix 7.34). At the same time, unmodified DNFs were also treated with less hydrophobic FAM-BCN dye, where little fluorescent signal was detected after the reaction. This suggested that the significant amount of non-specific fluorescence observed for hydrophobic Cy5-BCN was due to physical interactions rather than covalent labelling. Therefore, when conducting labelling on DNFs, it is necessary to consider the hydrophobicity of the labelling agents.

DNFs with different levels of azide-modification were then treated by FAM-BCN and the labelled DNFs were imaged by fluorescence microscopy under the bright field and the FAM channel. From the imaging, bright green spots were observed under the FAM channel (Figure 2.20.B), which overlap with DNFs in the bright field (Figure 2.20.C), indicating successful labelling. Fluorometric plate reading assay showed a correlation between the fluorescence intensity of DNFs and the ratios of modified triphosphates used in RCA (Figure 2.20.F). The trends were consistent with what was observed from

the previously demonstrated amine-NHS labelling. In contrast to the NHS labelling, little non-specific labelling was observed in unmodified DNFs. SEM confirmed that the labelling step did not impact the DNF structure (Figure 2.20.E).

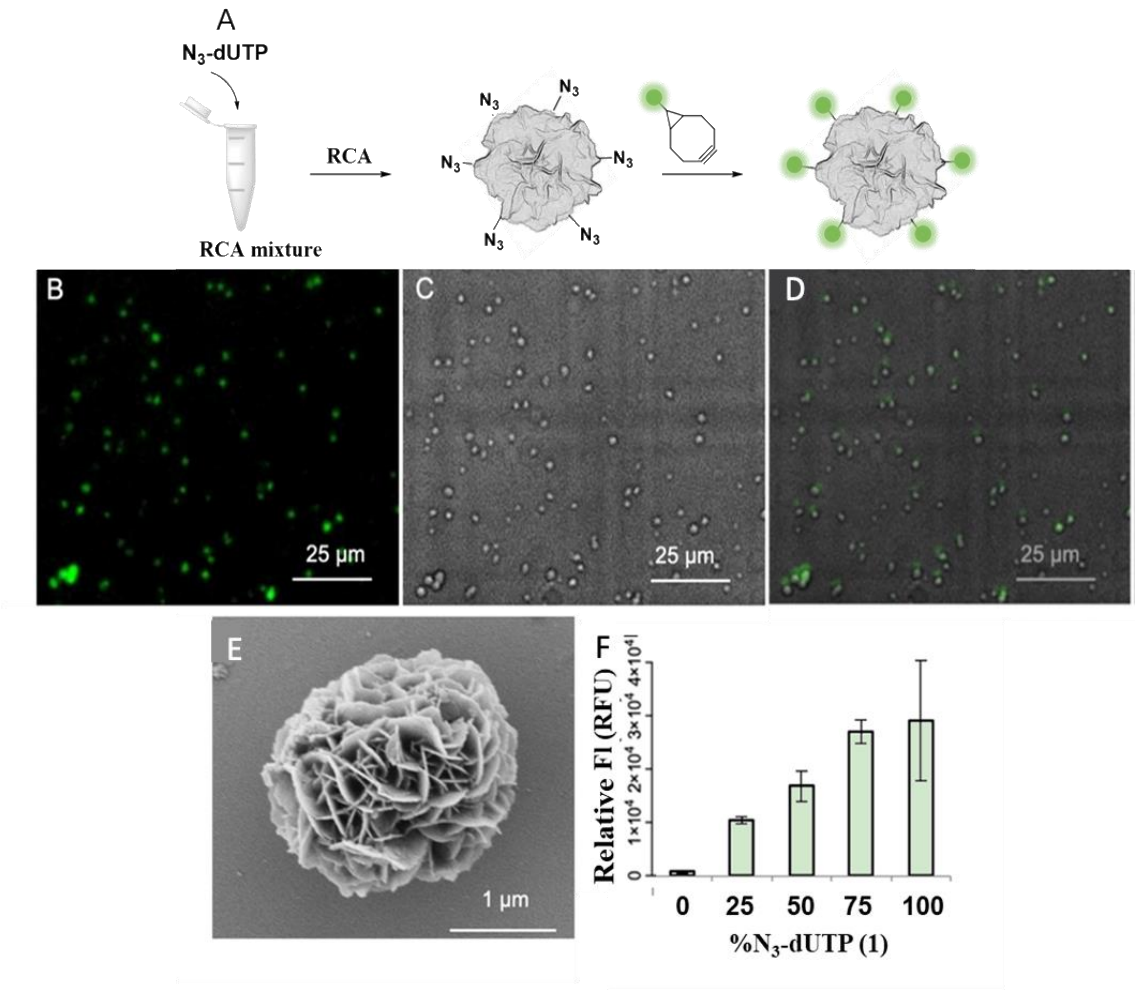


Figure 2.20. SPAAC labelling of N_3-DNFs. **A**. Schematic diagram of the method; **B**. Fluorescence image of FAM labelled N_3-DNFs under 475 nm excitation. The DNFs were prepared with 50% of N_3-dUTP (**1**); **C**. Bright field image of the sample shown in B; **D**. Overlay of fluorescence and bright field. Some particle migration occurs as the samples are in water; **E**. SEM image of DNFs after labelling; **F**. Relative fluorescence intensity (RFU) of FAM-BCN labelled DNFs containing varying levels of modification. Error bars represent the standard deviation of three repeat reactions.

2.6.3 Labelling of alkyne-modified DNFs by azide dye through CuAAC

Alkyne modified DNFs prepared with various ratios of Et-dUTP (**2**) were labelled with 3-azido-7-hydroxycoumarin (N_3-coumarin) through CuAAC. Coumarin is not fluorescent until it reacts with alkyne, allowing detection of the conjugation process. To perform the labelling, alkyne-modified DNFs were incubated with N_3-coumarin, $CuSO_4$, tris-hydroxypropyltri azolylmethylamine ligand (THPTA), and sodium ascorbate reductant (NaAsc) for 2 h in the HEPES labelling buffer (Figure 2.21.A). The labelled products were then isolated by centrifugation, followed by the fluorescence measurement with the fluorometric plate reading assay. The fluorescence signal was observed to increase correspondingly with the amount of Et-dUTP used during RCA (Figure 2.21.C). The use of Cu(I) during CuAAC raised concern on DNF structure alteration, as the cationic Cu ion could replace Mg^{2+} in the DNF structures. SEM showed no structure change after CuAAC labelling (Figure 2.21.B). These results confirmed that the labelling reaction specifically occurred by forming covalent bonds on DNFs instead of non-specific physical interactions.

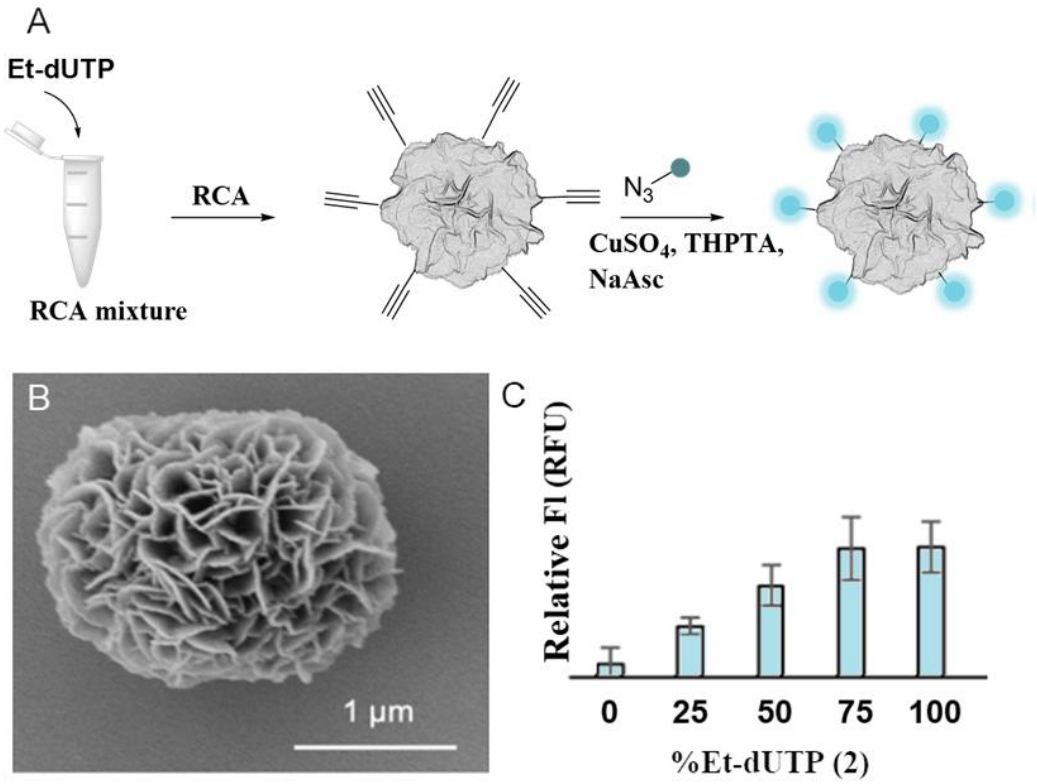


Figure 2.21. CuAAC labelling of alkyne-DNFs. **A**. Schematic diagram of the method; **B**. SEM image of N_3-coumarin-labelled DNFs prepared with 50% Et-dUTP (**2**); **C**. Relative fluorescence intensity (RFU) of N_3-coumarin labelled DNFs containing varying levels of modification. Error bars represent the standard deviation of three repeat reactions.

2.6.4 Non-specificity of NHS-ester labelling

In Section 2.6.1, when unmodified DNFs was treated with an NHS-ester fluorophore, an increase in fluorescent signal was observed. This non-specific labelling was not observed for the click-mediated labelling methods.

The inorganic core of DNFs is formed by MgPP, which has been reported to have a

flower-like structure.[198] To rule out the non-specific interactions of the fluorophores with the inorganic skeleton, MgPP precipitate was incubated with TAMRA NHS-ester, similar in hydrophobicity with FAM. Compared to unmodified RCA products labelled under the same conditions, no noticeable colour change was seen for MgPP, indicating that the non-specificity did not occur on MgPP (Figure 2.22.A, B).

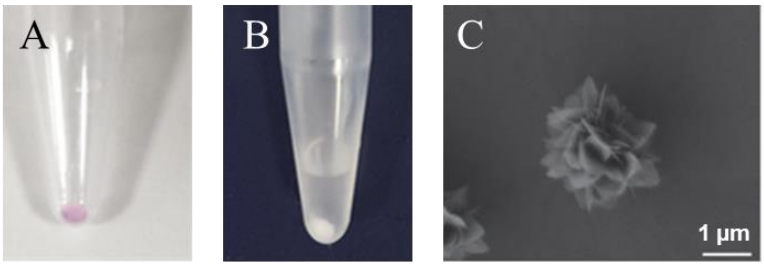


Figure 2.22. A. Unmodified RCA product after labelling with TAMRA-NHS. **B**. MgPP after labelling with TAMRA-NHS. **C**. SEM image of MgPP.

Previously studies demonstrated encapsulation of particles such as proteins in porous DNF structures during the amplification (Figure 2.23).[189] We hypothesised that the lysine-abundant DNA polymerase used for RCA, phi29, was encapsulated during RCA, introducing extra amines into DNFs. To confirm this, unmodified DNFs were labelled with TAMRA NHS-ester and compared with TAMRA-labelled phi29 on SDS-PAGE. The DNA and protein components of DNFs separated on the gel, and the fluorescence was observed on the protein instead of the DNA. This indicated that the non-specific labelling occurred on the phi29 DNA polymerase incorporated during RCA (Appendix

7.33). Washing repeatedly after labelling did not eliminate the non-specific fluorescence, suggesting that encapsulation of proteins was well preserved under the washing conditions. Labelling on the proteins allows the preparation of functionalised DNFs without altering the DNA components. The reactive groups to CuAAC and SPAAC click reactions do not occur in nature or RCA reaction conditions, making them beneficial over NHS-labelling when orthogonal labelling is required.

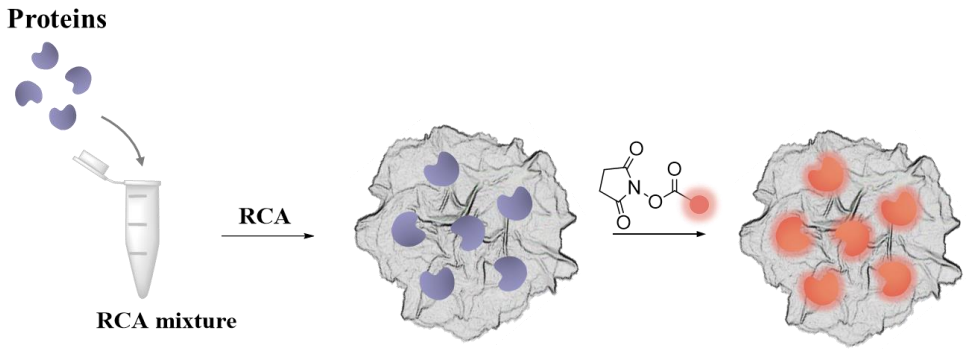


Figure 2.23 Schematic of non-specific labelling of proteins such as phi29 encapsulated in DNFs.

2.6.5 Dual labelling of DNFs

It has been demonstrated that modified triphosphates could be introduced into DNFs efficiently, and the chemical handles are available for successive labelling with other reactive groups. Next, we investigated the generation of more complex modified DNFs by including two different modified triphosphates to the same RCA reaction using the developed methods. Dual labelling on these DNFs was then performed. We also used lysine-rich protein as an alternative source of amine as it was proved stable.

2.6.5.1 Dual labelling using two modified triphosphates

DNFs were prepared with 25% N_3-dUTP (**1**) and 25% H_2N-dCTP (**6**), which were then simultaneously labelled by FAM-BCN and TAMRA-NHS ester (Figure 2.24). The labelled particles were observed by fluorescence microscopy under corresponding channels. Fluorescent imaging of the DNFs under FAM (475 nm) and TAMRA (550 nm) excitation wavelengths confirmed successful labelling of the particles. Colocalisation of the two channels suggested labelling of the two fluorophores occurring on the same constructs. SEM imaging demonstrated that the labelling step did not impact the DNF structure.

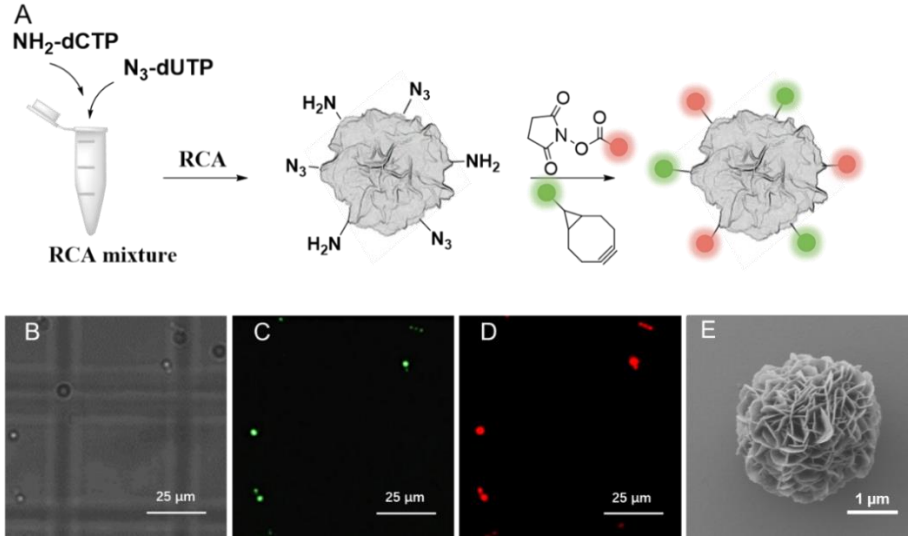


Figure 2.24 Dual labelling of DNFs prepared using 25% N_3-dUTP (**1**) and 25% H_2N-dCTP (**6**), labelled with FAM-BCN and TAMRA-NHS ester. **A**. Schematic of the method; **B**. Bright field image of dual labelled DNFs; **C**. Fluorescent image under 475 nm excitation confirming attachment of the FAM dye; **D**. Fluorescent image under 550 nm excitation confirming attachment of the TAMRA dye; **E**. SEM image showed no alteration in the structure.

To show the versatility of the method, a fluorescent peptide was used for DNFs labelling. DNFs were prepared using 25% Et-dUTP (**2**) and 25% H_2N-dCTP (**6**), followed by simultaneous treatment with a TAMRA-labelled peptide and FAM-NHS ester. The peptide contained an N-terminal azide, allowing reaction with the alkyne handles on the DNFs through CuAAC. The labelled particles were then observed by fluorescence microscopy under corresponding channels. Fluorescent images of DNFs under FAM (475 nm) and TAMRA (550 nm) excitation wavelengths confirmed successful labelling of both the peptide and the fluorophore on the DNFs. Overlapping of the two channels suggested labelling of the two moieties occurring on the same DNFs (Figure 2.25). Instead of simultaneous labelling, the labelling was also performed step-wise. After treatment of each chemical label, DNFs was washed thoroughly, and similar labelling results were obtained. By conducting the peptide labelling after the NHS labelling, orthogonality within DNFs can be achieved without modifying the amines on the peptide. The results showed the feasibility of the labelling method, which could immensely expand the functionalities carried by DNFs.

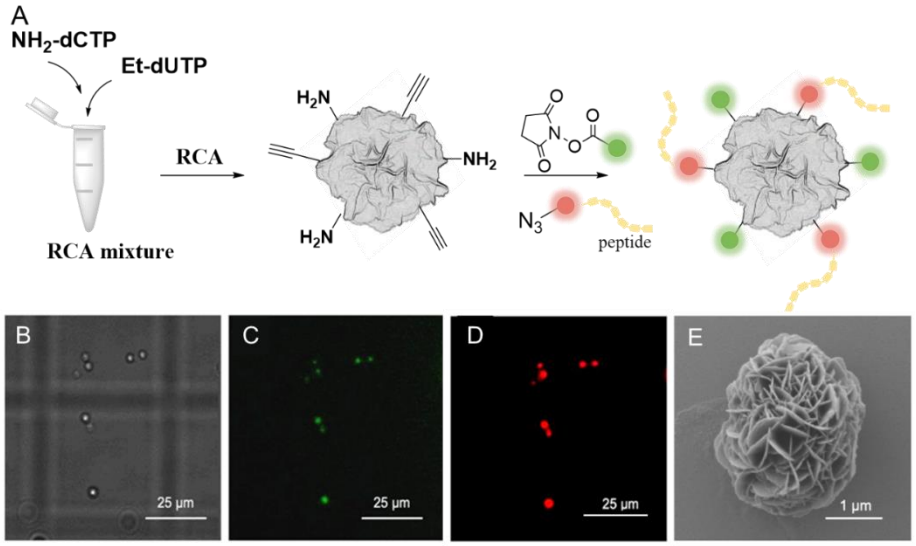


Figure 2.25 Dual labelling of DNFs prepared using 25% Et-dUTP (**2**) and 25% H_2N-dCTP (**6**), modified with TAMRA labelled peptide with N-terminal azide and FAM-NHS ester. **A**. Schematic of the method; **B**. Bright field image of dual labelled DNFs; **C**. Fluorescent image under 475 nm excitation confirming attachment of the FAM dye; **D**. Fluorescent image under 550 nm excitation confirming attachment of the TAMRA labelled peptide; **E**. SEM image showed no alteration in the structure.

2.6.5.2 Dual labelling of protein-encapsulated DNFs

According to Section 2.6.4, when proteins are added to RCA, they are steadily encapsulated in the DNF structures. This enables the use of the trapped proteins as a stable source of amine for NHS ester labelling. Here, BSA was used for a few reasons: BSA was confirmed to have no adverse effect on the amplification process of RCA; BSA contains abundant lysines (60 lysine sites), providing reactive sites for efficient labelling; BSA is cheap and widely available in chemistry and biology laboratories. At the same time, N_3-dUTP (**1**) was also used to introduce reactive azide sites to achieve

dual labelling. DNFs were prepared with 1 mg/mL of BSA and 25% N_3-dUTP (**1**), which were then treated simultaneously with TAMRA-NHS ester and FAM-BCN. The labelled particles were observed by fluorescence microscopy under corresponding channels. Fluorescent imaging of DNFs under FAM (475 nm) and TAMRA (550 nm) excitation wavelengths confirmed the successful attachment of both dyes. Overlapping of the two images suggested labelling of the two fluorophores occurring on the same construct (Figure 2.26). SEM imaging demonstrated that the labelling step did not impact the DNF structure.

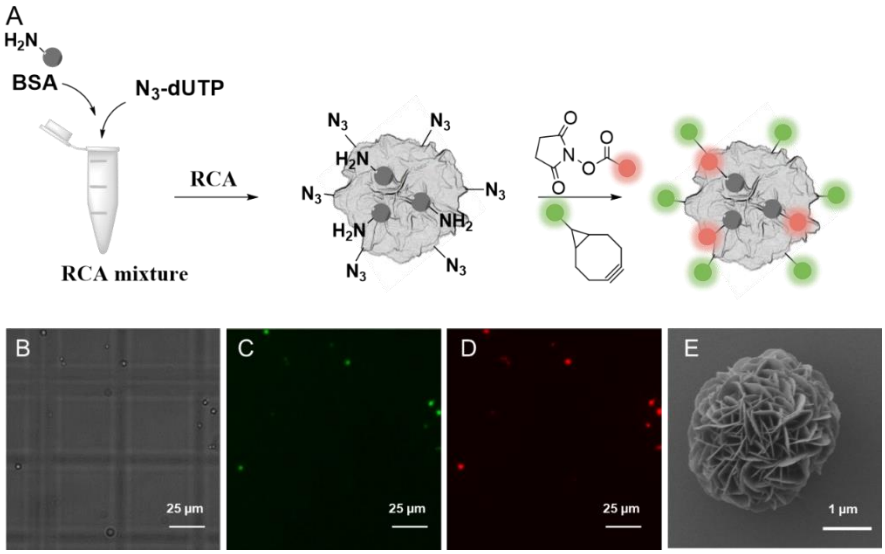


Figure 2.26 Dual labelling of DNFs prepared using 25% N_3-dUTP (**1**) and 1 mg/mL of BSA, modified with FAM-BCN and TAMRA-NHS ester. **A**. Schematic of the method; **B**. Bright field image of dual labelled DNFs; **C**. Fluorescent image under 475 nm excitation confirming attachment of the FAM dye on the azide group introduced; **D**. Fluorescent image under 550 nm excitation confirming attachment of the TAMRA dye on BSA; **E**. SEM image showed no alteration in the structure.

2.7 Binding of DNFs to cell surface receptors

By including therapeutic aptamer sequences in the template, DNFs can be endowed with multivalent binding properties for selective cell recognition. This can be useful in cancer cell detection, intracellular imaging, and cell-specific drug delivery. Aptamers such as KK1B10 to target leukaemia cancer cells,[186] sgc8 to target breast cancer cells,[186,191] and MUC1 to target mucins on epithelial cells[185] have been used to encode DNFs for recognition and delivery purposes. It has shown that DNFs with embedded aptamer sequences bind to specific cells efficiently without undesired binding to non-target cells. Inspired by this, the reported MUC1 and HER2 aptamers targeting MUC1 and HER2 biomarkers were chosen for this study. The MUC1 aptamer (encoded by template **1**) has already been included in DNFs for cell targeting,[185,199] while the HER2 aptamer (encoded by template **2**) has never been studied for cellular application.

2.7.1 Binding of the anti-MUC1 aptamer to MUC1 positive cells

We first investigated the binding of the MUC1 aptamer to adenocarcinomic human alveolar basal epithelial cell A549 and human breast cancer MCF-7, which are known to express abundant MUC1. Between the two cell lines, MCF-7 has been reported to express a higher level of MUC1.[199] We made two Cy3-modified DNA sequences: one

with reported MUC1 aptamer sequence and the other with a scrambled sequence that does not bind to any cell surface receptors. Before the binding experiments, cells were dissociated from the culturing flasks at 37 °C by incubating with trypsin-free cell dissociation buffer instead of trypsin which is commonly used for cell detachment. This is to avoid any possible degradation of the cell-surface proteins by trypsin, which could be detrimental to the study.

The cells were then incubated in 1%(w/v) BSA/DPBS blocking buffer for 10 min at 37 °C to minimise non-specific binding. Labelled aptamers were then added to the cells at a concentration of 5 μM, followed by incubation in the dark at 37 °C for 40 min with agitation. After incubation, the cells were washed 5 times with DPBS to remove any unbound aptamer before fluorescence measurement by flow cytometry. The results showed no fluorescence increase in either of the cells used, suggesting no aptamer binding to the target (Figure 2.27). Due to the poor binding, this aptamer was not further studied.

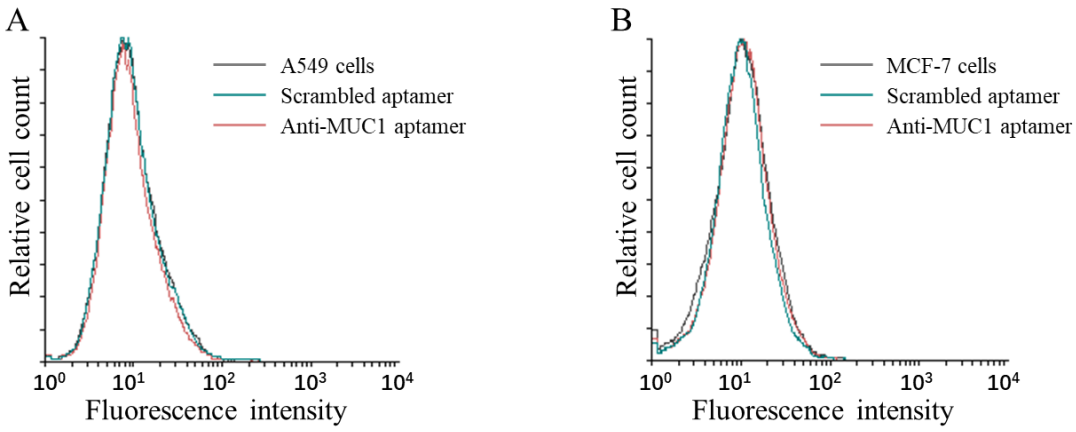


Figure 2.27 Assessment of the binding of the anti-MUC1 aptamer to its target by flow cytometry. **A**. A549 and **B**. MCF-7 cells were incubated with Cy3 labelled anti-MUC1 aptamer for 40 min at 37 °C in the dark. Each experiment was repeated three times.

2.7.2 Binding of anti-HER2 aptamer to breast cancer cells

To investigate the binding properties of the reported trimerised anti-HER2 aptamer towards breast cancer cells, the sequence was made with a 5' amine for attachment of fluorophore.[200] The G-rich anti-HER2 aptamer was confirmed within our group to form G-quadruplex at the presence of K^+, which is fundamental for its binding ability. Based on this, a mutated sequence was reported by altering two bases on each aptamer repeat.[201] This is assumed to interfere with the interactions between the aptamer and the receptor by bringing structural modifications to the G-quadruplex. To assess the binding affinity of the aptamer to HER2 biomarker, breast cancer cells SK-BR3, which is HER2+, and MCF-7 and MDA-MB-468, which are HER2-, were used. HER2 expression level in different cell lines was evaluated by commercially available FITC-

labelled anti-HER2 antibody or affibody (antibody mimetics).

The aptamers were slowly annealed in 100 mM K+ solution to form the G-quadruplex structure before binding experiments. Anti-HER2 aptamer and the mutated aptamer were added to dissociated cells to a final concentration of 5 μM, and the cells were further incubated in the dark at 37 °C for 40 min with agitation. After incubation, the cells were washed before fluorescence measurement by flow cytometry. To confirm the level of HER2 expression in each cell line, HER2 specific antibody (2 μL) or affibody (5 μL) were added to the cells.

In the presence of antibody and affibody, SK-BR3 cells showed strong fluorescence, indicating a high level of HER2 protein expression. In contrast, MCF-7 and MDA-MB-468 showed a low level of HER2 expression. This is in agreement with other publications.[202–204]

For SK-BR3, which is highly HER2+, a significant increase in fluorescence was observed with the addition of the aptamer, indicating binding between the cells and the aptamer. In contrast, for MCF-7, which expresses a low level of HER2, only a slight increase in fluorescence was observed, indicating a low degree of binding. However, the fluorescence signal after adding aptamer did not always correlate with the HER2 expression level in the cell lines. When the affibody was used, a weak fluorescence

signal was observed in MDA-MB-468, suggesting low expression of HER2. However, the addition of the aptamer gave a significant shift of fluorescence, which indicated that binding of the aptamer occurred. This suggested that apart from HER2, the aptamer was bound to other components in MDA-MB-468. For MCF-7, the fluorescence signal with the addition of the aptamer was stronger than it with the affibody and antibody. This did not agree with what was observed for SK-BR3 cells, where aptamer showed the weakest signal. This also suggested the existence of other targets on the cells.

When adding the mutated aptamer to all three cell lines, the fluorescence signal of the cells reduced significantly. However, there was still some fluorescence observed in SK-BR3 and MDA-MB-468. This was because the mutations introduced in the sequence did not entirely distract the G-quadruplex structure, giving a reduced binding to the targets (Figure 2.28).

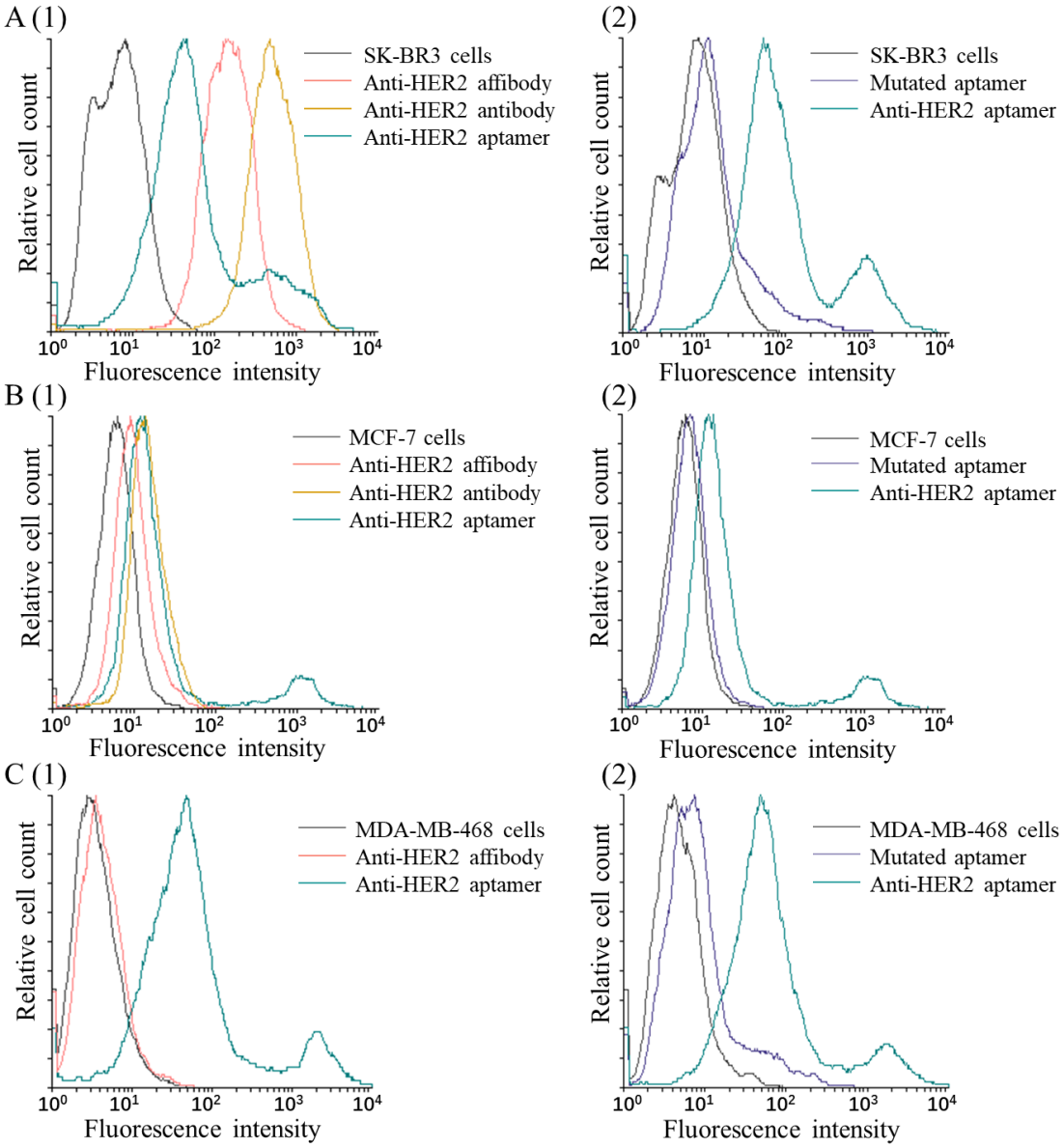


Figure 2.28 Assessment of the binding ability of anti-HER2 aptamer to breast cancer cells by flow cytometry. **A**. SK-BR3 cells, **B**. MCF-7 and **C**. MDA-MB-468 cells were incubated with FAM-HER2 aptamer, (**1**) FITC-labelled affibody or FITC-labelled antibody; (**2**) FAM-mutated HER2 aptamer for 40 min at 37 °C in the dark. Each experiment was repeated three times.

2.7.3 Binding of anti-HER2 peptides to breast cancer cells

Two breast cancer cell-binding peptides were used in this study as targeting agents. Peptide **1** was reported to exhibit specific binding to breast cancer cells,[205] while peptide **2** was known to specifically bind to HER2 receptors on breast cancer cells (Figure 2.29).[206] Both peptides were labelled with fluorescent dyes for visualisation. Peptide **1** was labelled with TAMRA, and peptide **2** was labelled with FAM. To assess the binding affinity of the peptides, they were incubated with breast cancer cells SK-BR3 (HER2+) and MCF-7 (HER2-), followed by fluorescence analysis with flow cytometry.

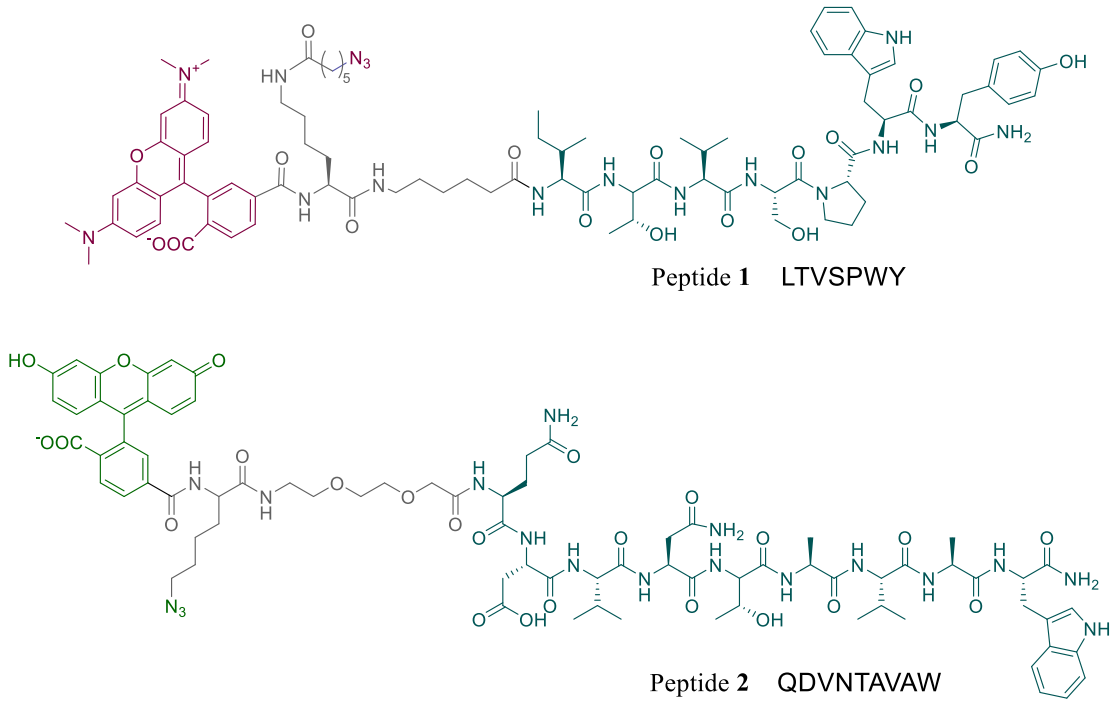


Figure 2.29. Structures of TAMRA labelled azide-functionalised peptide **1** and FAM labelled azide-functionalised peptide **2** used in the study.

Prior to the binding experiments, harvested cells were blocked by 1%(w/v) BSA/DPBS blocking buffer, as mentioned before. Labelled peptides were then added, and the cells were incubated in the dark at 37 °C for 40 min, followed by washing procedures before fluorescence measurement by flow cytometry.

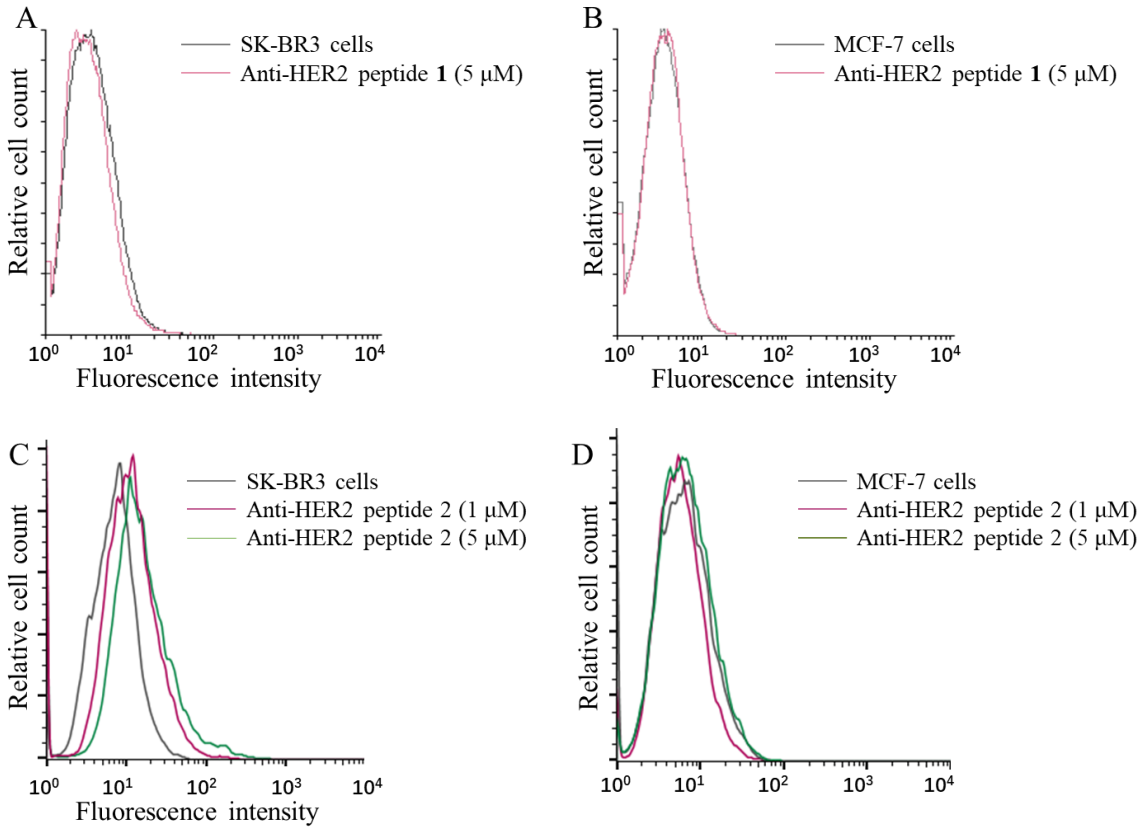


Figure 2.30. Assessment binding of the peptides to HER2 receptor by flow cytometry. SK-BR3 cells and MCF-7 cells were incubated with 5 μM of TAMRA-labelled peptide 1 (**A**, **B**) and FAM-labelled peptide 2 (**C**, **D**) for 40 min at 37 °C in the dark. Each experiment was repeated three times.

From flow cytometry results, peptide **1** did not show binding to either of the cells, which is inconsistent with the literature (Figure 2.30).[205] This could be due to the

modification on the C-terminus. The target biomarker of this peptide was not specified previously, making it hard to validate its binding ability. Therefore, this peptide was not further studied. For peptide **2**, an increase in fluorescence was observed after incubating HER2+ SK-BR3 cells, indicating binding occurred. In the HER2- MCF-7 cells, no evident binding was seen at the concentrations used. Therefore, peptide **2** was used in the following study.

2.7.4 Construction and binding of HER2 targeting DNFs

When a sequence complementary to an aptamer is encoded within the RCA template, the resulting DNA product will contain tandem repeats of the aptamer. Ideally, this aptamer concatemer could bind to multiple targets simultaneously, giving the particle an enhanced affinity. Meanwhile, it is worth considering that targeting molecules such as aptamers bind to their targets through structural recognition. The multiple aptamer sequences within the same DNF structure are likely to interact, preventing them from folding into the 3D structure required for target recognition. One solution to this is to attach the aptamer to the outer surface of DNFs through the labelling method we demonstrated. This method could reduce intermolecular aptamer interactions within the condensed DNF structure and better expose the aptamer to the target. To attach aptamers to DNFs, RCA was carried using a randomly sequenced template (Table 2.1. template **3**) and N_3-dUTP (**1**). The DNA generated from this sequence did not bind to

any known biomarker on cells. The introduced N_3 linkers were labelled with alkyne and FAM-modified HER2 aptamers (Table 2.1. 5'-alkyne-FAM-HER2 aptamer) through CuAAC. The labelled DNA products were visually coloured, indicating the successful attachment of the fluorescent aptamer. These DNFs were then treated with FAM-BCN in case any unreacted N_3 remained. The resulting DNFs carried anti-HER2 aptamer on the surface, therefore, were termed as Apt-DNFs.

As a comparison, another batch of DNFs was made with HER2 aptamer templated sequence (Table 2.1. template **2)** and N_3-dUTP (**1**). The products were subsequently labelled with FAM-BCN. The DNFs obtained carried HER2 aptamer sequence within the DNF structure, termed as Tem-DNFs. Control DNFs were made using the randomly sequenced template (template **3)** and N_3-dUTP (**1)** followed by labelling with FAM-BCN. These DNFs did not contain any targeting units and were termed as Con-DNFs.

An overall 25 mM of Mg^{2+} was used for RCA in this section to condense the size of DNFs (Section 3.3) for better binding performance. The binding of these DNFs to HER2+ SK-BR3 cells was assessed by flow cytometry.

In the previous binding experiments, cells were dissociated before incubation with aptamers and peptides. In this study, the cells remained attached to the culturing plate when incubated with DNFs. The reason to do this is that DNFs are insoluble materials

and cannot be separated from cells by centrifugation. To remove unbound DNFs, the cells were washed with DPBS when attached to the plate, then scraped off the plates gently before flow cytometry measurement.

The flow cytometry results showed that after incubation with Con-DNFs, cells exhibited a minor increase in fluorescence, indicating a low degree of binding. The result was consistent with our expectation as Con-DNFs did not contain any targeting sequence. With both Apt-DNFs and Tem-DNFs, an increased fluorescence signal was observed. When comparing them, cells incubated with Apt-DNFs showed a more significant fluorescence signal, implying enhanced binding to the HER2 biomarkers (Figure 2.31.A). The elevated binding is possibly due to the better-preserved structures of the aptamer and their improved exposure towards the target. This labelling strategy allows the attachment of structure-dependent ligands and targeting groups on DNFs without compromising their functions.

To demonstrate another potential application, we made peptide-modified DNFs (Pep-DNFs) by attaching azide modified FAM-peptide **2** to the surface of DNFs using CuAAC chemistry. The DNFs were prepared using the random template (template **3**) and Et-dUTP (**2**). Flow cytometry suggested that the Pep-DNFs also had a significant affinity towards SK-BR3 cells (Figure 2.31.B). While the peptide alone exhibited moderate binding towards the cells, Pep-DNFs showed greatly improved binding to

HER2+ cells. An explanation for the enhanced binding observed in Pep-DNFs is their multivalency. Multiple peptides on the same DNF construct simultaneously bind to the HER2 proteins on the same cell, drastically increasing the affinity.

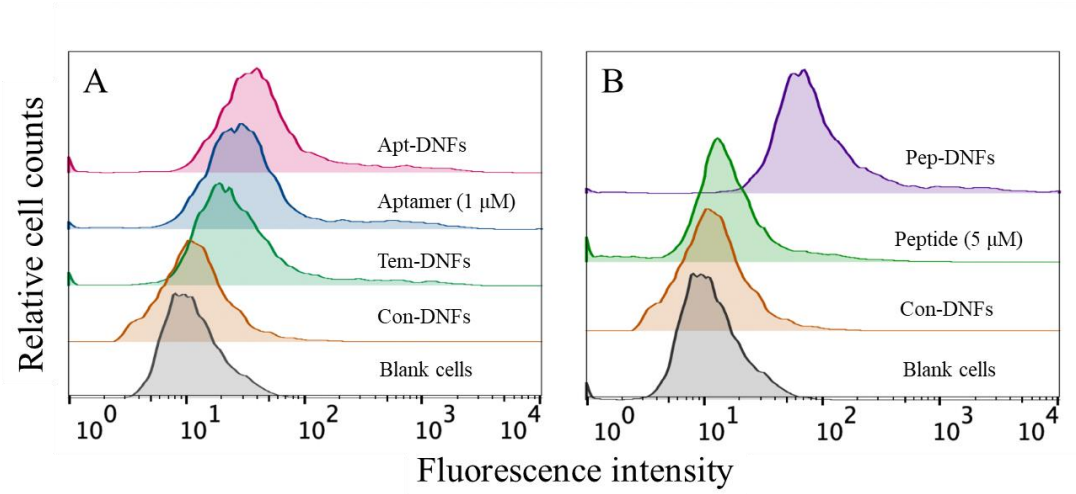


Figure 2.31. A. Flow cytometry studies comparing the binding of Apt-DNFs with Tem-DNFs to SK-BR3. Apt-DNFs showed improved binding to the cells, indicating that covalently attaching the aptamer to DNFs leads to better affinity. **B**. Flow cytometry studies show that Pep-DNFs efficiently bind to SK-BR3 cells. All experiments were done in duplicate.

2.8 Conclusions and future work

Nanostructures and materials generated by RCA have shown great potential in biomedical and clinical applications, including bioimaging, biosensing, cancer therapy and protein engineering. This chapter found a simple approach for preparing heavily functionalised DNFs with a range of modifications. Chemically modified nucleoside triphosphates, some commercially available, with small reactive handles were

incorporated during RCA. The efficiency of this process was shown to be dependent on the length of the chemical handles. The triphosphates play an essential role in controlling the production of ssDNA and the morphology of the DNFs produced. By carefully utilising the triphosphates, DNFs carrying modified handles can be obtained without compromising RCA efficiency and DNF structure.

We have developed approaches to label modified DNFs under mild conditions efficiently. Fluorescent labels, peptides and DNA aptamers have been used for labelling without altering the structure of DNFs. Orthogonal labelling has been achieved, which endowed multiple functions to the same construct, expanding the possible application of the materials. Moreover, entrapped proteins have been used as labelling sites for NHS ester, which maintains the integrity of DNA components.

Targeting groups, including aptamers and peptides, have been covalently attached to DNFs using the methods developed. Improved binding relative to conventional DNF suggested potential in diagnostic and therapeutic applications.

A key advantage is that the approach uses commercially available nucleoside triphosphates, which avoids multi-step organic synthesis. Reactive biological labels for these chemical handles are also readily available, making it a facile strategy to conduct in different labs.

Incorporation of some modified triphosphates with long chemical handles (for example, AHP-dUTP (**5**) and Oct-dUTP (**4**) in this chapter) leads to the production of DNFs in small size. Although not discussed here, these DNFs can be beneficial in applications such as cellular and subcellular delivery. How the properties of the side chains, such as hydrophobicity and charge, affect the amplification efficiency and the DNF structure need to be better understood. In addition, the composition of the labelled DNFs needs to be further studied by techniques such as XRD. For example, although no alteration in the structure was observed, it is worth investigating if the usage of Cu in CuAAC labelling changes the inorganic components of DNFs.

Moreover, it is essential to know the precise loading of functionalities on DNFs for a predictable outcome in some applications. Furthermore, the attachment of other functionalities is awaited to be explored. Except for fluorophore, DNA aptamer, and peptide demonstrated in this study, attachment of functionalities such as drug, polymer, and antibody can be helpful and need to be explored in the future.

Chapter 3. Condensation of DNA nanomaterials generated by rolling circle amplification

3.1 Introduction and aims

DNA nanotechnology has produced an extensive range of structures that can be used in numerous biological applications, including imaging, biological sensing and targeted delivery of drugs, proteins and genes. These structures benefit from the biocompatibility and structural programmability of DNA, making them better for biomedical applications than other exogenous nanomaterials. However, challenges for their applications remain to be addressed, including enzymatic hydrolysis, immune recognition, degradation and low cellular uptake. To perform their therapeutic roles, DNA nanomaterials must be taken up by cells and tissues to a high concentration. The hydrophilicity and negative charge of DNA nanomaterials prevent them from passing the amphiphilic, negatively charged cell membrane, making their uptake by mammalian cells consistently poor.

The size of DNA nanostructures also determines their internalisation pathway to cells. Large particles are known to enter cells via non-specific endocytosis pathways such as phagocytosis and micropinocytosis, while receptor-mediated endocytosis only allows the internalisation of small particles because the vesicles involved in these processes are small.[207]

DNFs generated from RCA have shown potential as therapeutic and diagnostic agents,

owing to their cell targeting ability, drug loading capacity and stability against extreme conditions. In chapter **2**, we developed a methodology to chemically modify DNFs, which expanded the functions and potential applications. However, the size of DNFs we studied was usually bigger than one micrometre, which could limit their applications in cells. We observed that the size of DNFs grew over time. In addition, the choice of modified nucleoside triphosphate also affected the size of DNFs generated.

Other strategies have been reported to impact the size of DNFs generated by RCA, including varying the concentration of Mg^{2+} in reaction buffer[62] and condensing the particles using cationic polymers such as Poly-L lysine (PLL).[208] With tuneable size, DNFs can be designed with improved cellular uptake, which benefits cellular and subcellular applications.

In this chapter, we first investigated the existed methods for altering the size of HER2-aptamer templated DNFs. In addition, we demonstrated the use of biocompatible polyethylene glycol (PEG) as a condensing agent for DNFs, which has not been studied before.

3.2 Effects of reaction time on DNF size

It has been discussed in Section 2.4.5 how reaction time affects DNA production and

the size of DNFs generated. When the reaction was performed for a short period, less DNA was produced, with small size of DNFs generated. It is known that the formation of DNFs involves the amplification of DNA and the crystallisation of DNA with the by-product pyrophosphate anion ($P_2O_7^{4-}$) and Mg^{2+} in the amplification buffer. In short reaction times, low quantities of DNA and pyrophosphate were produced, resulting in small crystal sizes. As previously described in Chapter 2, using template **1** (MUC1 aptamer templated, Table 1.1), the diameter of DNFs with defined structures can be as small as 1.1 μm after 4 h reaction. It was observed that the size of the DNFs did not increase much in the first few hours. An explanation for this is that more nucleation sites are generated in the solution instead of large crystals as the reaction begins. Here, HER2 aptamer encoded template **2** was used to perform time-coursed amplification and particles produced were studied using SEM. When the amplification was carried for 4 h, DNFs with a diameter around 600 nm were produced (Figure 3.1), which was much smaller than those generated by template **1 (**1.1 μm). It was possibly due to the G-rich sequence generated using this template, which led to more compact structures. This suggested template sequence dramatically influenced the size of DNFs.

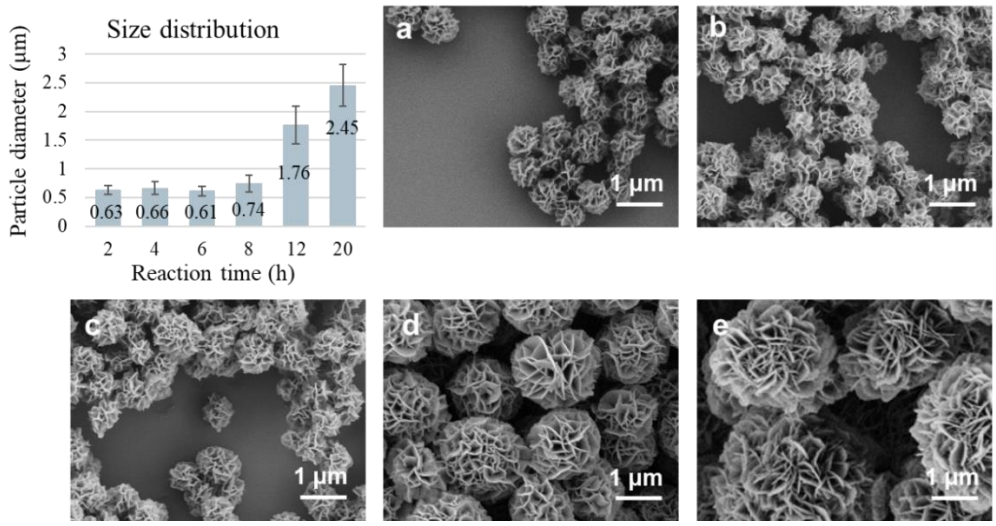


Figure 3.1 Size distribution of DNFs obtained after different amplification times using template **2** in chapter **2**. Size measured from SEM images. Error bars represent the standard deviation of 50 particles measured. **a-e**. SEM images of DNFs generated after **a**. 2 h; **b**. 6 h; **c**. 8 h; **d**. 12 h and **e**. 20 h incubation with 10 mM Mg^{2+}. Scale bars represent 1 μm.

3.3 Effects of Mg2+concentration on DNF size

Mg^{2+} concentration was found to affect the formation of DNFs. Higher concentrations of Mg^{2+} accelerates DNA amplification by facilitating the interactions between DNA polymerase and the substrate DNA and promoting the binding between primer and template. Mg^{2+} also forms the inorganic core of DNFs, which induces DNA precipitation. In addition, the concentration of Mg^{2+} has been found to play a critical role in the size of DNFs. By increasing the concentration of Mg^{2+} present in the reaction buffer, a decrease in the size of DNFs was observed by SEM. With 25 mM Mg^{2+} in the reaction, the size of DNFs went down significantly from an average of 2.5 μm at 10

mM Mg^{2+} to less than 500 nm. In addition, with more $Mg^{2+,}$ the DNFs exhibited a more even size distribution, with less defined structures (Figure 3.2).

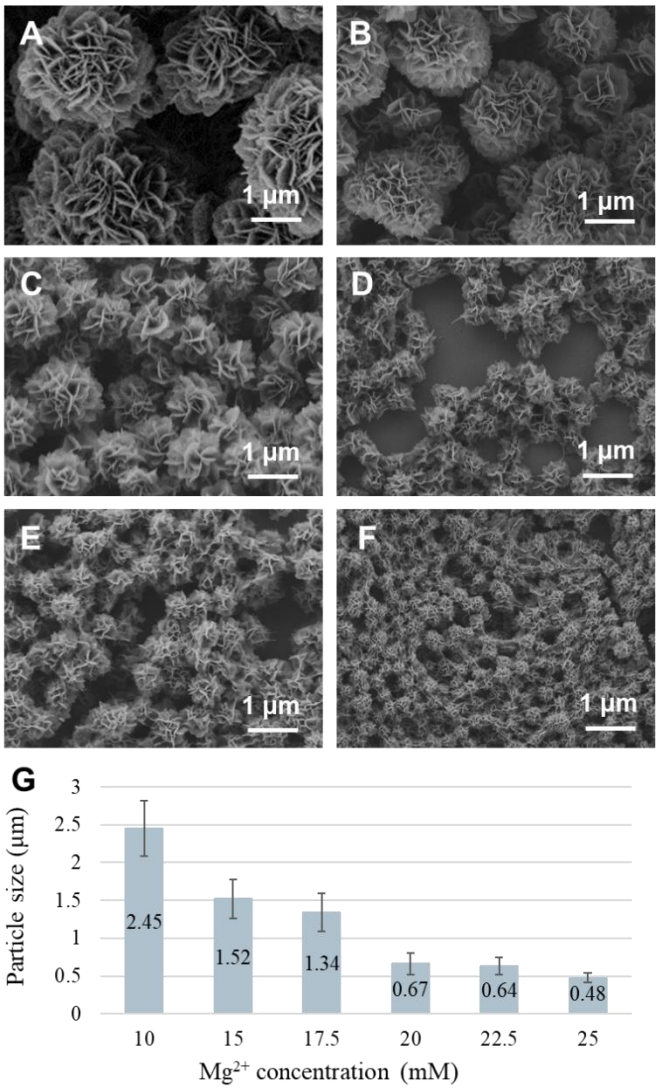


Figure 3.2 SEM images of the DNFs formed in the presence of **A**. 10 mM; **B**. 15 mM; **C**. 17.5 mM; **D**. 20 mM; **E**. 22.5 mM and **F**. 25 mM of Mg^{2+} after 20 h incubation. Scale bars represent 1 µm. **G**. Size distribution of DNFs formed with different Mg^{2+} concentrations after 20 h incubation. Size measured from SEM images. Error bars represent the standard deviation of 50 particles.

Although the reason is not immediately obvious, one possible explanation for the

tendency observed is that abundant Mg^{2+} accelerates the nucleation of the MgPP crystals, producing a large number of crystals with small crystal sizes.

When shorter amplification times were combined with high Mg^{2+} concentration, the diameter of particles could be reduced further. When RCA was carried for 6 h with 25 mM Mg^{2+}, the size of DNFs generated reduced by 1/3 compared with those generated with less Mg^{2+} (10 mM), from 600 nm to 400 nm (Figure 3.3).

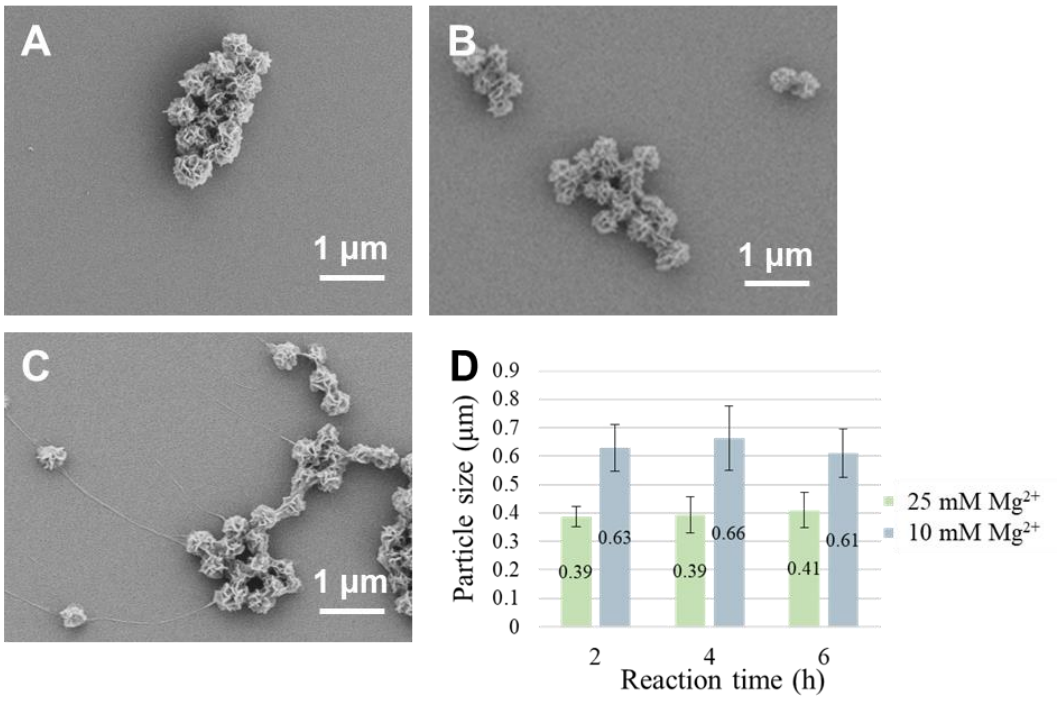


Figure 3.3 SEM imaging of the DNFs formed in the presence of 25 mM of Mg^{2+} after **A.** 2 h; **B**. 4 h and **C**. 6 h incubation time. Scale bars represent 1 μm. **D**. Size distribution of the DNFs formed with 10/ 25 mM Mg^{2+} after different incubation times. Size measured from SEM images. Error bars represent the standard deviation of 50 particles measured.

3.4 Effects of cationic polymer Poly-L lysine (PLL) on DNF size

Positively charged polymers are generally used as condensation and transfection reagents for DNA and RNA.[209–211] These polycations bind and package DNA into sub-micron particles, neutralise the negative charge of DNA, readily interact with and pass through the negatively charged cell membrane.[212,213] Poly-L lysine (PLL) has been reported to condense DNFs efficiently. After reaching a certain threshold concentration (0.4 mg/mL), cationic PLL promptly binds to DNFs, exchanges and releases Mg^{2+} cations in the inorganic core, destructing the MgPP crystal structure and inducing a dramatic reduction in particle size. The composition of the condensed complex was characterised by XRD, which indicated the absence of Mg^{2+}, confirming the suggested mechanism.[208]

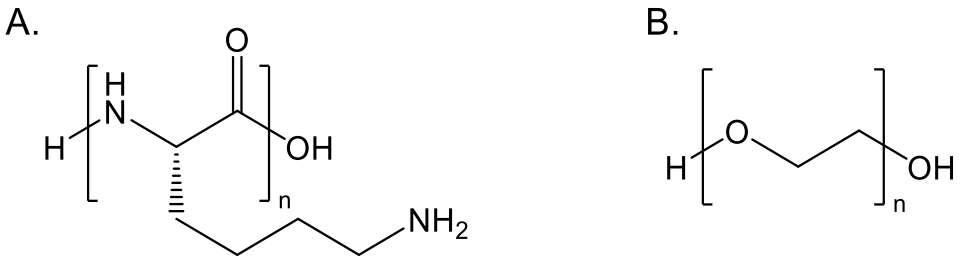


Figure 3.4 Chemical structures of **A**. PLL and **B**. PEG.

Here, we incubated RCA products with various amounts of PLL and analysed the structure change by SEM. A final concentration of 0.2 – 5 mg/mL PLL was added to RCA products, and the mixture was incubated for 4 h at room temperature. The flower-

like structure was observed to deform with the increasing amount of PLL, which was consistent with the previous study (Figure 3.5).[208]

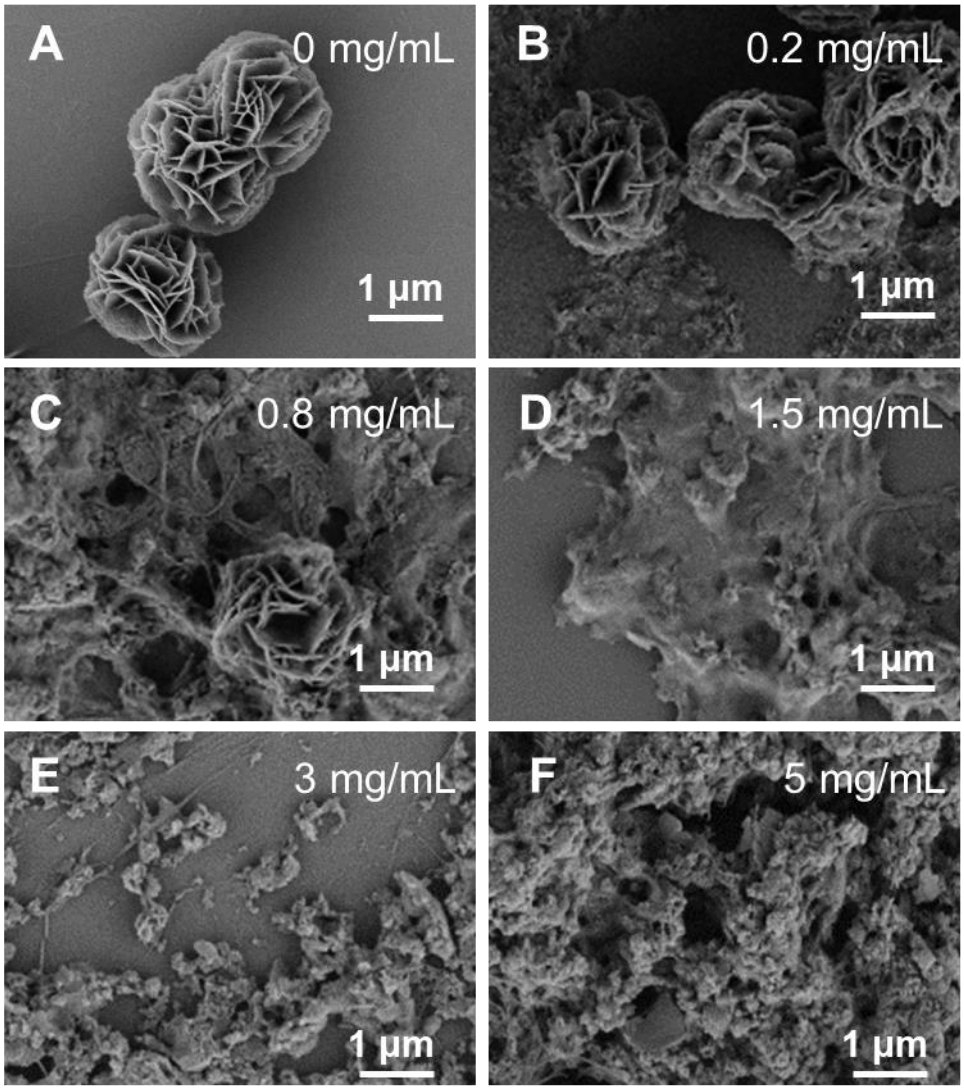


Figure 3.5 SEM images of DNFs **A**. before condensing process and **B-F**. after condensation with increasing concentrations of PLL. Scale bars represent 1 µm. SEM images show the deformation of flower-like structures with the addition of PLL.

As the defined particle structures were devastated, it was hard to measure their size

from SEM images. Hence, dynamic light scattering (DLS) was used to evaluate the size of the resulted structures. DLS measures particle sizes by illuminating samples with a laser and analysing the light scattered by particles. It can be used to measure particles from a few micrometres to less than 1 nm scale.

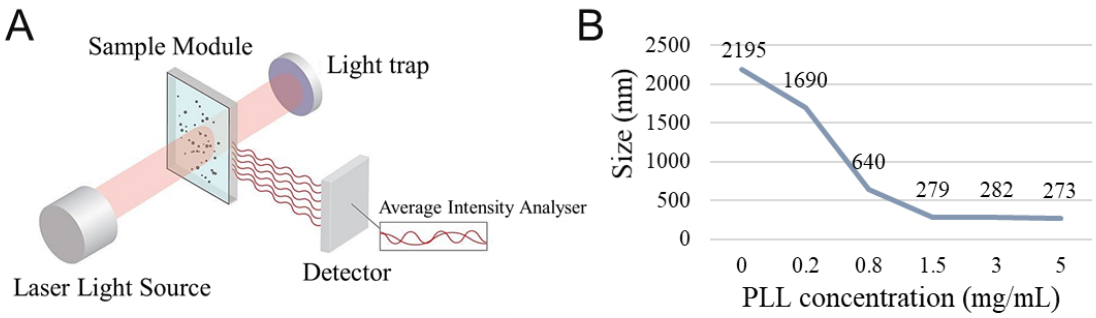


Figure 3.6 **A**. Representation of DLS principle. A single-frequency laser is directed to the sample. The incident laser light gets scattered by the particles in the sample in all directions. The scattered light is detected over time, and the signal is interpreted to determine the particle size. **B**. Size of condensed particles at different concentrations of PLL, detected by DLS.

From the measurement, by mixing 1.5mg/mL of cationic PLL with DNFs, the size of particles significantly decreased to about 280 nm. No further decrease in the particle size was observed when more than 1.5 mg/mL PLL was added, indicating the exchange between PLL and Mg^{2+} to completion.

The approach has been confirmed useful for RCA product condensation. However, PLL is known to have potent cytotoxicity and can initiate cell apoptosis, which prevents it

from being widely utilised in *in vivo* applications.[214,215] Another polycation used for DNFs condensation, polyethylenimine (PEI), was also reported to be cytotoxic and induce cell apoptosis.[216] The cationic polymers tend to interact with negatively charged cellular components, interfering with the normal cellular process and causing toxicity. Despite their outstanding ability as transfection and condensation reagents, drawbacks of cationic polymers also include their multimolecular aggregation under physiological environments and rapid clearance from the bloodstream.[212,213]

3.5 Effects of neutral polymer polyethylene glycol (PEG) on DNF size

PEGs are neutral, water-soluble, biocompatible polymers that do not hydrolyse or decompose upon storage. Conjugation of PEG can effectively improve the water-solubility and circulation half-life of medicines, leading to improved safety and therapy outcomes.[217,218] Hence, PEGs of different molecular weights have been widely applied in a variety of biomedical applications.[219,220]

PEGylated PLL has been used to compact DNA for gene transfer *in vivo*. It was reported to be more secure than typical viral vectors and more efficient than non-PEGylated PLL DNA polyplexes.[221,222] PEG grafted in the polyplexes prevents polyplexes aggregation and promotes DNA transfection without affecting the condensed structure.[223] When coordinating with monovalent and divalent salt at high

concentrations, PEG could induce DNA condensation.[224,225] This can be explained by the crowding effect of PEG and the electrostatic screening of the negative charge by PEG and the cations. In our study, we used PEG in RCA for the first time to investigate its condensing effect on the resulted DNA products.

3.5.1 Condensation of DNF by PEG

PEGs with small sizes were discovered to have a poor condensation effect on DNA.[226] To get optimal results, we used PEGs with relatively large MW, 3000, 4000 and 8000 Da, to investigate if the polymer length influenced DNA condensation. Different concentrations (10% to 40% w/v) of these PEGs were added to RCA reaction mixtures, and the reaction was carried out for 20 h. The products were washed by centrifugation before being analysed by 0.8% agarose electrophoresis.

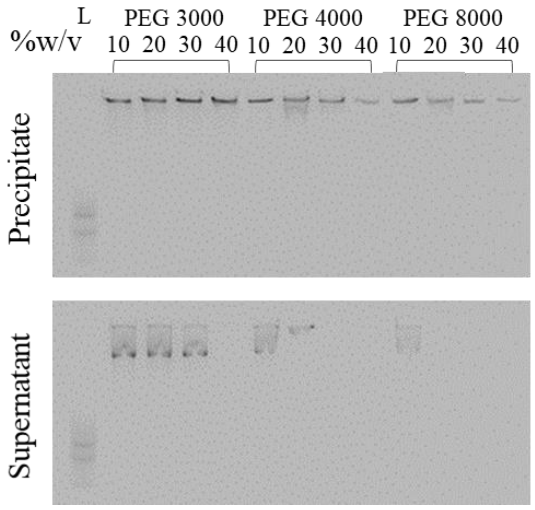


Figure 3.7 Agarose gel analysis of RCA products with different % w/v PEG in various sizes; **L**. 100 bp DNA ladder. 15 mM Mg^{2+} was used for all reactions. The lack of DNA observed in supernatant indicated better precipitation of DNA by larger/more concentrated PEG.

The gel indicated that the addition of high concentration and MW PEGs retarded amplification, leading to low DNA yield (Figure 3.7). Compared to PEG 3000, when PEG 4000 and 8000 were used, less DNA was generated after RCA. When higher concentrations of PEG were added to the reaction, less DNA was produced. As a crowding agent, PEGs have been reported to improve the efficiency of PCR by increasing the binding affinity between the substrate and the polymerase.[227–229] However, these agents can also impair the catalytic activity of the polymerase at high concentrations and MW, which is consistent with what we observed.[230–233] This effect can be caused by the dehydration of the polymerase-DNA substrate complex by PEGs, which affect the structure and the function of the polymerase.[230–233]

The impact of PEG on the size and structure of RCA generated materials were analysed by SEM. Compared to DNFs formed without PEG, with the addition of 10% PEGs in different sizes, the particle size decreased by 43%-50%. PEG 8000 showed a slightly better condensing effect than the other two shorter polymers. When higher concentrations were used, the diameter of the particles further decreased to smaller than 300 nm. This can be attributed to the better crowding and charge-shielding effect of large and concentrated PEGs. However, as high concentrations of PEG hamper the amplification, no obvious structure was observed in samples with 40% PEG 4000 and 8000.

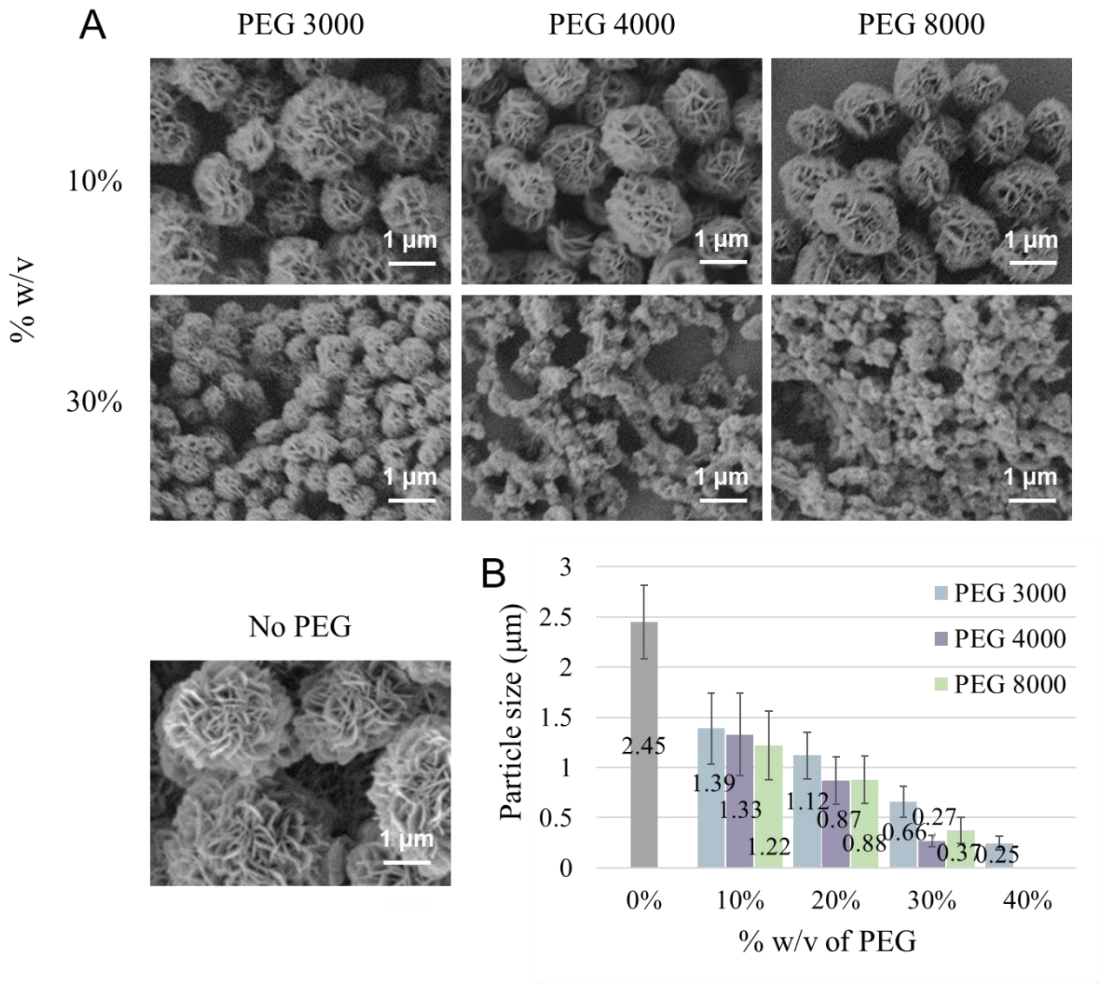


Figure 3.8 **A**. SEM images of DNFs formed with different % w/v PEG in different sizes. 15 mM Mg^{2+} was used for all reactions. Scale bars represent 1 µm. SEM images show the reduced size of condensed DNA nanoparticles. **B**. Size distribution of the DNFs formed with different PEG concentrations. Size measured from SEM images. Error bars represent the standard deviation of 50 particles measured. SEM images of particles formed with other % w/v are shown in the appendix.

3.5.2 Stability of PEGylated DNA particles

To see if the structure of PEGylated RCA products was stable, precipitate produced by RCA with 20% PEG 3000 were incubated in different solutions for 48 h. The

precipitate was then isolated by centrifugation, and the DNA contents were analysed by agarose electrophoresis. RCA products without the addition of PEG were treated under the same conditions for comparison. According to the gel, the PEG-containing particles showed good stability in most of the solutions, with a small amount of DNA leaching into the solution (Figure 3.9). However, in the presence of 10 mM chelating agent EDTA, an increased DNA loss was observed, indicating destruction of the structure. This suggested that Mg^{2+} played an essential role in maintaining the structural integrity of the particles.

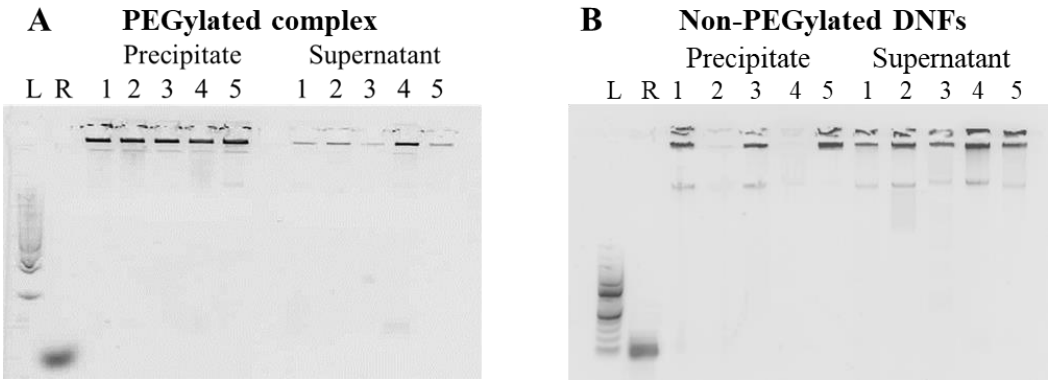


Figure 3.9 0.8% agarose gel analysis of the stability of **A**. RCA products with 20% PEG 3000 and **B**. Non-PEGylated RCA products, in different solutions; **L**. 100 bp DNA ladder; **R**. linear template; Particles incubated in **1**. 1x PBS buffer; **2**. 1x TBE buffer (2 mM EDTA); **3**. 50 mM Tris, pH 8; **4**. 10 mM EDTA; **5**. water for 48 h.

For the PEGylated products, insoluble materials remained even after 48 h incubation in 10 mM EDTA, showing better stability against EDTA than conventional DNFs,

which entirely deformed in 2m EDTA after 48 h. The stability may be because PEG participated in the formation of the particle, which is not affected by EDTA. In addition, it is possible that the PEG provided a coating outside of the particles, shielding the external environment and providing extra stability. The particles with improved stability can be used where extreme experimental conditions are required and are more suitable for long term storage and transportation if needed.

3.5.3 Labelling of PEGylated DNA particles

To explore the applications, labelling the PEGylated DNA particles with fluorescent dye was achieved, by labelling on the PEG and the DNA components.

FAM-modified PEG 3000 was used in the RCA reaction, and the resulting particles were imaged using fluorescence microscopy. The imaging of the particles showed intensive fluorescence, indicating the successful inclusion of fluorophores. This also confirmed that PEG was involved in the particle structure. Moreover, different amounts of amine-modified PEG 3000 (10%, 20%, 30% and 40% w/v) was used in RCA to generate products with amines. These particles were subsequently labelled with FAM NHS ester. The labelled products were analysed by 0.8% agarose gel (Figure 3.10). The gel showed an increasing intensity of fluorescence as the amounts of NH_2-PEG used increased, indicating the modification level of the particles can be tuned by

altering the quantity of PEG. By attaching chemical labels on PEG, the DNA components in the particles remain intact, allowing them to function in subsequent applications.

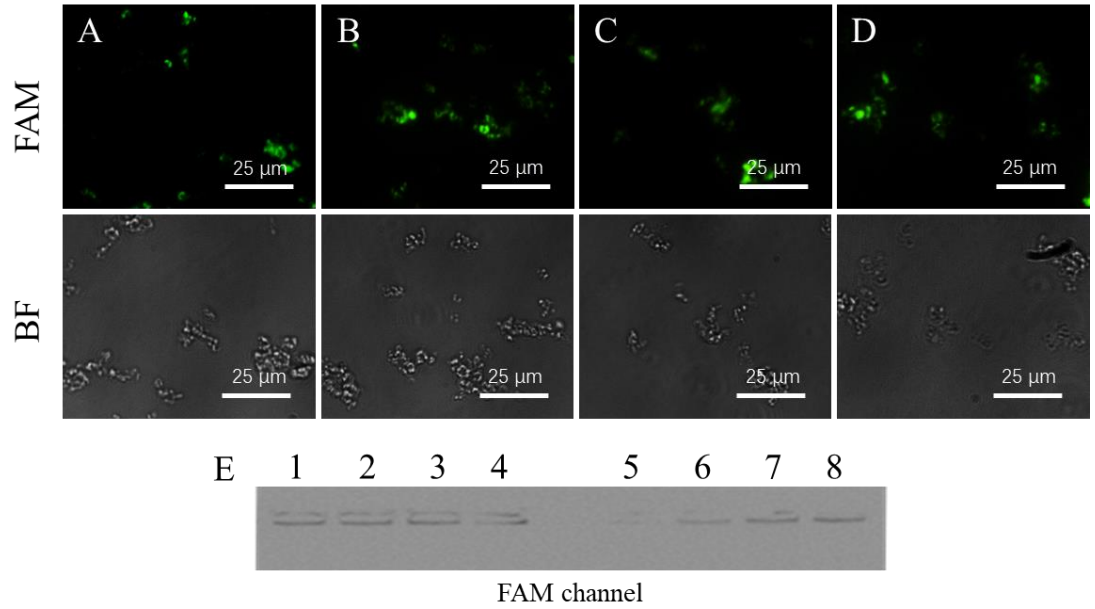


Figure 3.10 Fluorescence and bright-field (BF) imaging of FAM-labelled PEG-condensed DNFs. The DNFs were prepared with **A**. 30% FAM-labelled PEG 3000; **B**. 30% amino-PEG 3000, labelled by FAM NHS ester; **C**. 30% PEG 4000 and 50% NH_2-dUTP, labelled by FAM NHS ester; **D**. 30% PEG 8000 and 50% NH_2-dUTP, labelled by FAM NHS ester. Some particle migration occurs as the samples are in water. Fluorescence images were taken under 475 nm excitation **E**. Agarose gel analysis (0.8%) of FAM-labelled products made with **1**. 30% NH_2-PEG 3000 ; **2**. 30% PEG 3000, 50% NH_2-dUTP; **3**. 30% PEG 4000,50% NH_2-dUTP; **4**. 30% PEG 8000, 50% NH_2-dUTP; **5**. 10% NH_2-PEG 3000; **6**. 20% NH_2-PEG 3000; **7**. 30% NH_2-PEG 3000; **8**. 40% NH_2-PEG 3000.

Using the method described in section **2.6.1**, NH_2-dUTP was incorporated to introduce reactive handles into DNA in PEGylated RCA products. 30% PEG 4000 or 8000 was

used with 50% NH_2-dUTP during RCA, and the resulting materials were labelled with FAM-NHS ester, using the conditions developed in Chapter 2. Fluorescence imaging showed successful labelling of the particles, suggesting the PEG condensation can be combined with the previously described labelling method, therefore expanding the applications of the particles (Figure 3.10).

3.5.4 Cellular uptake of PEG-condensed DNFs

PEG has been widely used as a coating for nanoparticles, providing protection against enzymatic degradation and aggregation. When conjugated with DNA nanomaterials, neutrally charged PEG can form a dense shield, lessening unfavourable repulsion between DNA and the negatively charged cell membrane, promoting cellular uptake. In our study, RCA products generated with PEG showed smaller sizes, making them more likely to internalise cells via endocytosis pathways. Therefore, we expected to see a more efficient cellular internalisation for the PEGylated RCA products than DNFs generated by the conventional method.

To evaluate the cellular internalization, RCA was carried out using HER2 aptamer encoding template **2**, with 50% NH_2-dUTP and PEG with different MW. The products were later labelled with FAM NHS ester using the conditions developed previously. The fluorescent particles were incubated with HER2+ cell line SK-BR3 and HER2-

cell line MCF-7 in the dark at 37°C for 40 min. The cells were then washed and imaged using fluorescence microscopy (Figure 3.11).

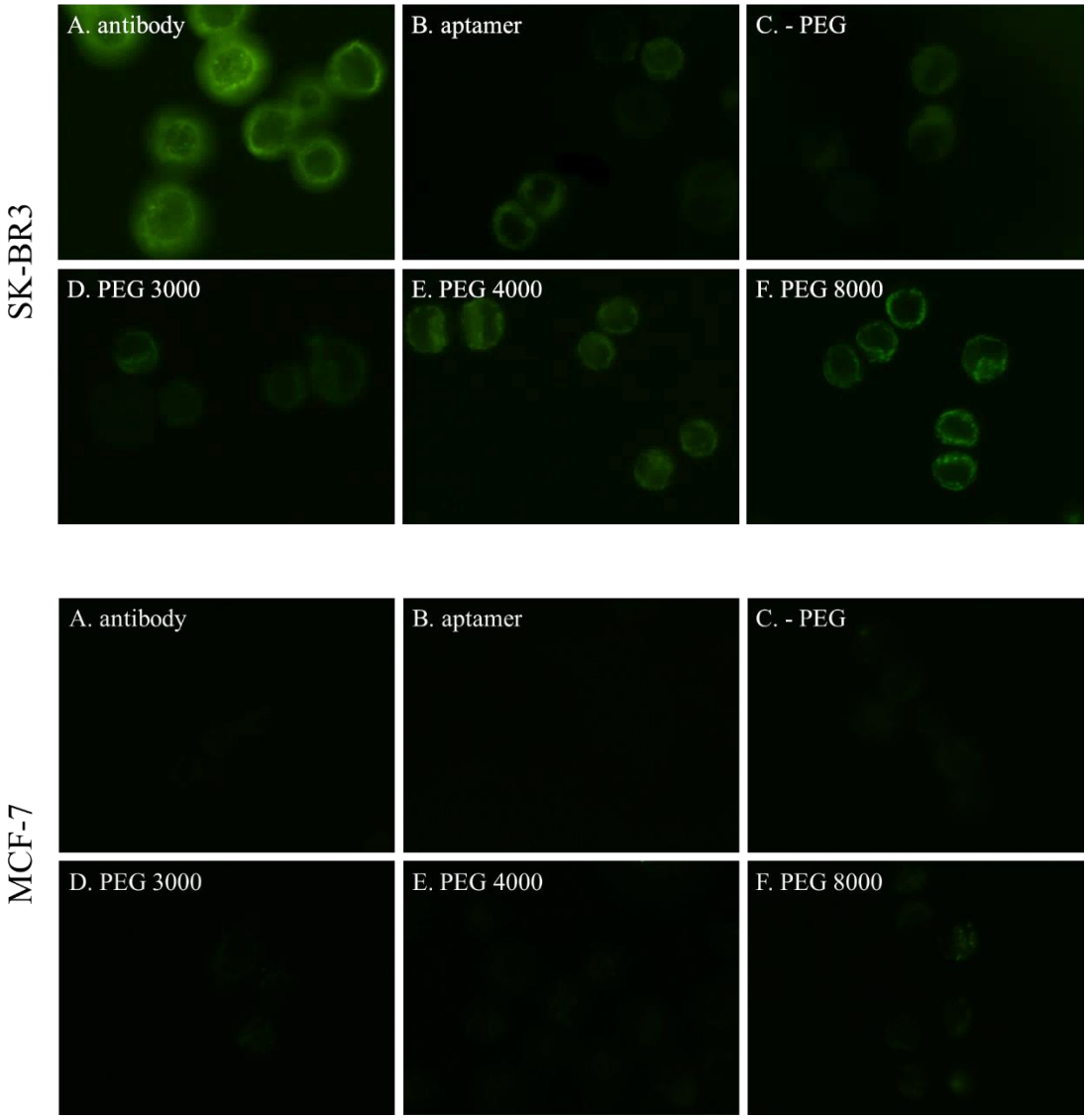


Figure 3.11 Fluorescence imaging of HER2+ SKBR3 and HER2- MCF7 cells after incubation with **A**. anti-HER2 antibody; **B**. anti-HER2 aptamer; **C**. FAM-labelled DNFs made with 25 mM Mg^{2+}; **D**. FAM-labelled PEGylated DNA particles made with 30% PEG 3000; **E**. FAM-labelled DNFs condensed with 30% PEG 4000; **F**.FAM-labelled DNFs condensed with 30% PEG 8000.

From the imaging, with anti-HER2+ antibody SK-BR3 showed bright fluorescence, indicating its expression in HER2. When non-PEGylated DNFs were added, the cells showed a weak fluorescence, suggesting minor binding and internalisation of these particles. For the PEGylated DNA particles, the fluorescence of the cells increased as the size of PEG increased, indicating enhanced affinity. While the particles made with PEG 3000 showed a similar level of fluorescence with non-PEGylated particles, cells incubated with PEG 4000 and 8000-particles exhibited stronger fluorescence. This could be because the larger PEGs better screened the negative charge on DNA, minimising their repulsive static interactions with the cell membranes. Also, the particles made with larger PEGs were smaller in size, making them bind to and internalise the cells more readily. For HER2- cells MCF-7, no noticeable fluorescence was observed, indicating the binding was specific.

3.6 Conclusion

For in cell and *in vivo* applications, it is important to keep the size of DNA nanomaterials within the limit for cellular uptake. In this chapter, we demonstrated several methods for condensing the size of RCA generated materials. By controlling the reaction time and Mg^{2+} concentration, RCA generated DNFs can be obtained with sizes as small as 400 nm without obstructing their defined flower structure. By adding cationic polymer PLL, the particle size dramatically dropped to below 300 nm, with

the flower-like structure fell apart. Cationic polymers condense DNFs by neutralising the negatively charged DNA backbones, reducing the charge repulsion, and by replacing the Mg^{2+} in the MgPP core, which leads to the structure collapse. The primary concern of using the cationic polymers in condensing DNFs is their inherent cytotoxicity, limiting their employment in biological applications.

Neutrally charged polymer PEG has been reported to increase stability, cellular uptake, and circulation time of nanoparticles when grafted. Here, we used PEG with different sizes during RCA to get condensed DNA particles. It was shown that the presence of PEG effectively reduced the size of the RCA generated particles. Compared to non-PEGylated DNFs, these particles had a more compact structure and showed better resistance against chelating agents. Modifications on these condensed particles can be introduced on both PEG and the DNA components, making them applicable for diverse purposes. The PEGylated particles showed a better affinity to cells than the non-PEGylated DNFs, possibly due to the screening of the negative charge on DNA. However, the condensation process is not well understood. To get a more comprehensive understanding, PEG with a broader range of size and concentration should be used, and the composition of the particles formed needs to be further analysed by techniques such as XRD.

Chapter 4. Preparation of DNA nanocarrier systems and their applications in mRNA detection

4.1 Introduction and aims

Approaches for specific RNA quantification in cells typically rely on cell lysis to isolate RNA or cell fixation; both damage the cells and impact further studies.[234–237] These methods only provide the average expression level of an individual gene for a given cell population and cannot be used to study RNA at a single-cell level.

Oligonucleotide-based probes such as linear probes and molecular beacons have been developed for live-cell mRNA detection by *in situ* hybridisation (Section 1.5.2).[151,154–157] However, the major challenge for these probes is cellular delivery.

To address these problems, Mirkin *et al*. developed spherical nucleic acids (SNAs) based probes known as Nanoflares and SmartFlare^{TM} to detect RNA levels in single living cells.[165,172,233] In contrast to the traditional methods, these probes do not require cell fixation or lysis, enabling subsequent assays requiring undamaged cells. SmartFlare^{TM} consists of a 13 nm gold nanoparticle conjugated with single-stranded oligonucleotides designed to recognise specific RNA transcripts (‘capture’ strands). The capture strand is hybridised with a short oligonucleotide functionalised with a fluorophore at the 5' end (‘reporter’ or ‘flare’ strand). In the bound state, fluorescence of the reporter strand is quenched due to its proximity to the gold nanoparticle core. When the target RNA is present, it binds to the capture strand and displaces the reporter

strand, whose fluorophore is restored. The increased fluorescence intensity is proportional to RNA target concentrations.

However, recent literature has reported the limitations of these probes.[239] It was found that (i) fluorescence intensity of SmartFlare^{TM} probes failed to correlate target mRNA levels within cells; (ii) SmartFlare^{TM} fluorescence intensity is potentially dependent on the efficiency of the probe uptake; (iii) fluorescence intensity of SmartFlare^{TM} is linearly proportional to the probe concentration used instead of mRNA level; (iv) most SNAs are trapped within endosomes which hinders their binding to the targets.[173]

To circumvent the above limitations of current mRNA probes, we developed a DNA nanocarrier system to detect the levels of target mRNA in single cells. In our design, DNA nanorings (DNARs), which are cyclic DNA, are used to carry fluorophore-labelled complementary oligonucleotides (termed as signal strand) (Figure 4.1). Upon hybridisation, the fluorophore of the signal strand is quenched by the quencher embedded in the DNA ring. An aptamer sequence is attached to the signal strand to allow specific recognition of target biomarkers on cells. Once the signal strand encounters the target mRNA, it should be released from the DNA ring and hybridise with the target, resulting in a fluorescence signal that is proportional to the target level.

Survivin is a member of the inhibitor of the apoptosis protein family, which inhibits

caspases and blocks cell death. Its expression is observed in most human tumours and malignant tissues but generally undetected in normal cells.[240] Therefore, survivin has become an important intracellular target for tumour diagnostics and anti-cancer therapies. In our proof-of-principle study, we used human breast cancer cells (SK-BR3, MCF-7 and MDA-MB-231) as models for survivin mRNA targeting due to different levels of survivin transcripts in these cells.[241,242] These breast cancer cells also express different levels of cell surface receptors HER2, which enables specific recognition by anti-HER2 DNA aptamer conjugated to the signal strand.[200,201]

The aim of the work in this chapter is to investigate and evaluate the properties of the DNAR-based nanocarrier system and its ability to specifically enter HER2+ human breast cancer cells and detect survivin mRNA transcript levels within the cells.

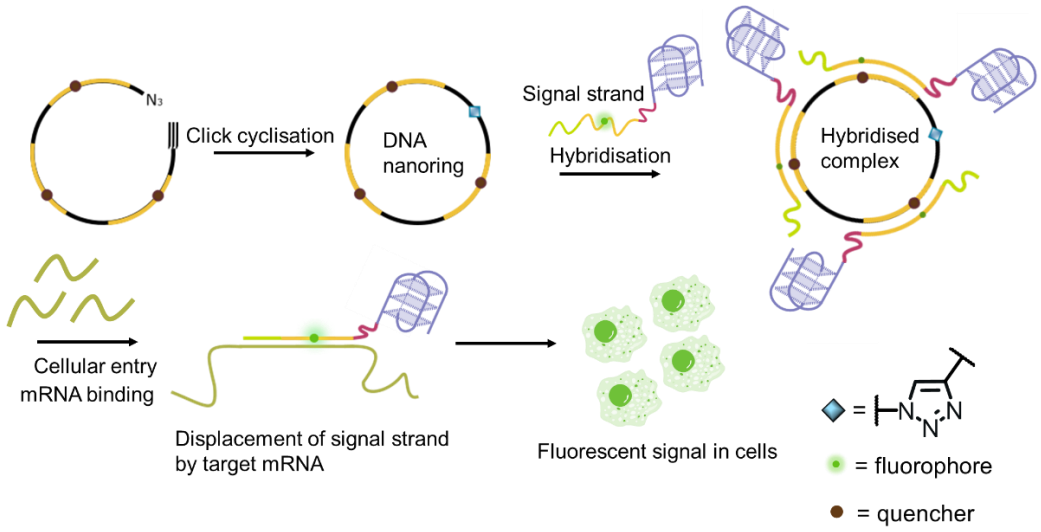


Figure 4.1. DNA nanoring (DNAR) is cyclised via click chemistry, introducing an artificial triazole backbone linkage. DNAR carrying multiple quenchers allows hybridisation of fluorophore-bearing signal strands, leading to fluorescence quenching. The signal strand is conjugated with a DNA G-quadruplex aptamer sequence to enable cell-specific recognition. Following cellular entry, the signal strand is displaced by the target mRNA, leading to fluorescence restoration within the cells.

4.2 Choice of oligonucleotide sequences

All DNA sequences used in this chapter are listed in Table **4.1**.

Oligo	Sequence (5′→3′)	Length (nt)
DNAR**1**	^{Z}TTGACCACCGCATCTTTCTTTTC^{K} Z = 5′-azide; K = 3′-propargyl; blue coloured bases represent the hybridisation site of signal strand.	23
DNAR**2**	^{Z}TTGACCACCGCATCTTTCTTGACCACCGCATCTTTC^{K} Z = 5′-azide; K = 3′-propargyl; blue coloured bases represent the hybridisation sites of signal strand.	36
DNAR**3**	^{Z}TTGACCACCGCATCTTTCTTGACCACCGCATCTTTCTT GACCACCGCATCTTTC^{K} Z = 5′-azide; K = 3′-propargyl; blue coloured bases represent the hybridisation sites of signal strand.	54
DNAR**4**	^{Z}TTGACCACCGCATCTTTCTTGACCACCGCATCTTTCTTGACCACCGCATCTTTCTTGACCACCGCATCTTTCT TGACCACCGCATCTTTC^{K} Z = 5′-azide; K = 3′-propargyl; blue coloured bases represent the hybridisation sites of signal strand.	90
DNAR**5**	^{Z}TTGACCACCGCAYCTTTCTTGACCACCGCAYCTTTCTT GACCACCGCAYCTTTC^{K} Z = 5′-azide; K = 3′-propargyl; Y = BHQ1-dT; blue coloured bases represent the hybridisation sites of signal strand.	54
DNAR**6**	^{Z}TTCACAYGCGACTCCTTCTTCACAYGCGACTCCTTCTTCACAYGCGACTCCTTC^{K} Z = 5′-azide; K = 3′-propargyl; Y = BHQ1-dT; blue coloured bases represent the hybridisation sites of signal strand.	54
DNAR**7**	^{Z}TTGACCACCGCAYCTTTCTYGACCACCGCAYCTTTCTT GACCACCGCAYCTTTC^{K} Z = 5′-azide; K = 3′-propargyl; Y = TAMRA-dT; blue coloured bases represent the hybridisation sites of signal strand.	54
Signal strand **1**	TCTTGAATGTAGAGATGCGGTGGTC Blue coloured bases represent the hybridisation site to the ring.	25
Signal strand **2**	TCTTGAATGTAGAGAYGCGGTGGTCXXGCAGCGGTGTGGGGGCAGCGGTGTGGGGGCAGCGGTGTGGGG X = HEG; Y = FAM-dT; blue coloured bases represent the hybridisation site to the ring; underlined bases represent the anti-HER2 aptamer sequence.	67
Signal strand **3**	GTGTACTTATGAGGAGTCGCAYGTGXXGCAGCGGTGTGGGGGCAGCGGTGTGGGGGCAGCGGTGTGGGG X = HEG; Y = FAM-dT; blue coloured bases represent the hybridisation site; underlined bases represent the anti-HER2 aptamer sequence.	67
Survivin target	CCUGCCUGGCAGCCCUUUCUCAAGGACCACCGCAUCUCUACAUUCAAGAACUGGCCCUUCU Blue coloured bases represent the hybridisation sites of the signal sequence.	61

Table 4.1. Sequences used in this chapter (mass spectra data are provided in the Appendix).

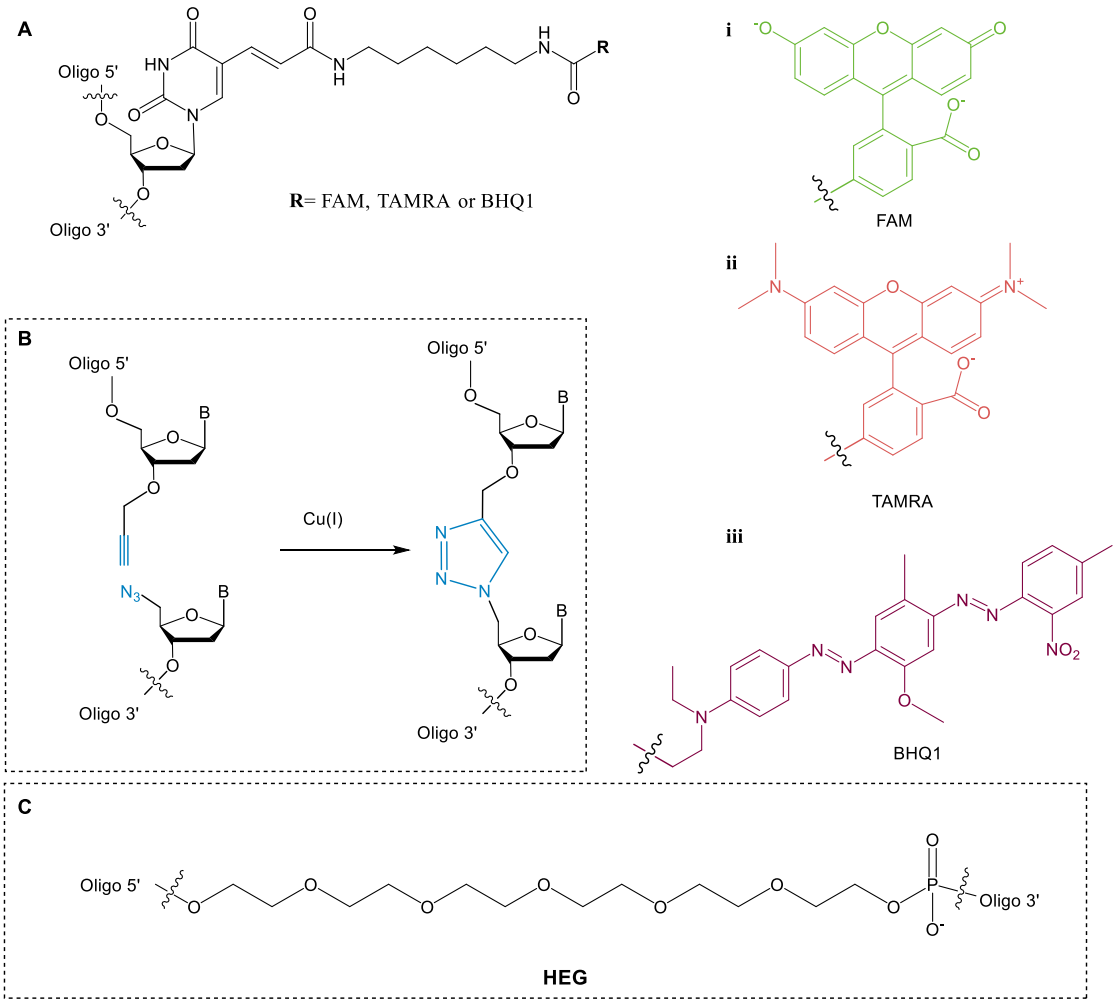


Figure 4.2. Chemical structures of oligonucleotides used in this chapter. **A**. FAM (i), TAMRA (ii) and BHQ1 (iii) modified oligonucleotides with the modifications on dT; **B**. 3′-propargyl and 5′-azide oligonucleotides and the triazole linkage formed after CuAAC; **C**. HEG spacer used in the signal strands.

From a structural point of view, cyclic DNA is possibly the simplest rigid nanometer-scaled DNA structure. It is more resistant to enzymatic degradation than linear DNA, making it suitable for in cells and *in vivo* applications.[243–245] In this study, we designed four cyclic DNA sequences with different sizes, accommodating one (DNAR**1**), two

(DNAR**2**), three (DNAR**3**) and five (DNAR**4**) hybridisation sites for the signal strand. With careful design, DNAR sequences do not possess complex secondary structures that could inhibit the hybridisation with the signal strand. To study the quenching upon hybridisation, DNAR**5** was made using the same sequence as DNAR**3**, with a BHQ1 quencher placed at each hybridisation site. Scrambled DNAR**6** was generated as a control version of DNAR**5,** with a random hybridisation sequence that does not overlap with any known target in cells. To study the cellular internalisation of the system, DNAR**7** was produced using the same sequence as DNAR**3,** with a fluorophore included at each hybridisation site.

The predicted secondary structures of DNARs are shown in Figure 4.3.

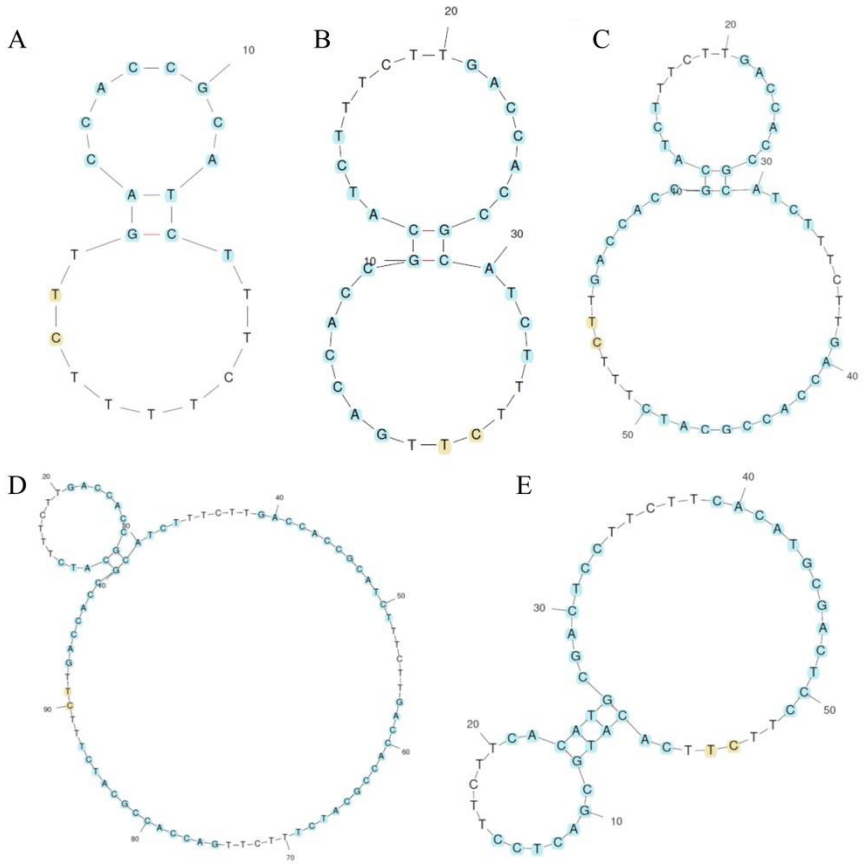


Figure 4.3. The predicted secondary structures of the DNA rings used in this chapter. (A) DNAR**1**; (B) DNAR**2**; (C) DNAR**3,** DNAR**5** and DNAR**7**; (D) DNAR**4** and (E) DNAR**6**. All structures were predicted by the Mfold web server software.[200] The yellow-coloured bases represent the point of ligation. The blue coloured bases are the hybridisation site of the signal strand.

We designed the signal strand to target a 25-base section of the survivin mRNA. Within this section, there is a 12-base region at the 5′ end of the sequence that does not bind to DNARs. This region is designed to facilitate the signal strand displacement by the target mRNA. Signal strand **1** is a simple version that contains no modifications or aptamer sequence on the 3'. It was used with DNAR**1**–**4** for the hybridisation study. Signal strand **2** carries a FAM within the hybridisation site, which is one base away

from the quencher on the DNARs upon hybridisation. The proximity between the quencher and the fluorophore enables efficient quenching. A trimeric anti-HER2 aptamer is attached to the 3′ of the sequence to serve as a recognition moiety to HER2 biomarkers. Between the aptamer and the targeting sequence, two HEGs were inserted to increase flexibility. Signal strand **2** was used with DNAR**5** and DNAR**7** for studies in cells. As a control, a signal strand with a random sequence complementary to DNR**6** was made. A synthetic survivin mRNA target complementary to the signal strand **1** and **2** was produced based on the survivin mRNA sequence (GenBank ID NM_001168, NM_001012270, NM_001012271).

4.3 CuAAC cyclisation of unmodified DNARs

DNAR**1–4** with different numbers of hybridisation sites were cyclised through a non-templated CuAAC reaction. To do this, the linear oligonucleotides were synthesised with 5′-azide and 3′-alkyne modifications and prepared as described in Section 1.1.3. The linear oligonucleotides were cyclised at 5 μM concentration in the presence of $CuSO_4$, THPTA and NaAsc. The crude reaction mixture of each sequence was analysed and purified by appropriate percentage of denaturing PAGE, and the products were characterised by LC-MS (Figure 4.4). In all cases, the linear oligonucleotides were cyclised in the absence of a splint oligonucleotide, with no polymeric by-products observed. However, when the length of the oligo increased, the efficiency of the

reaction decreased, leaving more uncyclised starting materials. This is probably because the increased size of the oligonucleotide makes it harder for the reactive ends to co-localise. The purified cyclic DNARs were used in subsequent hybridisation studies.

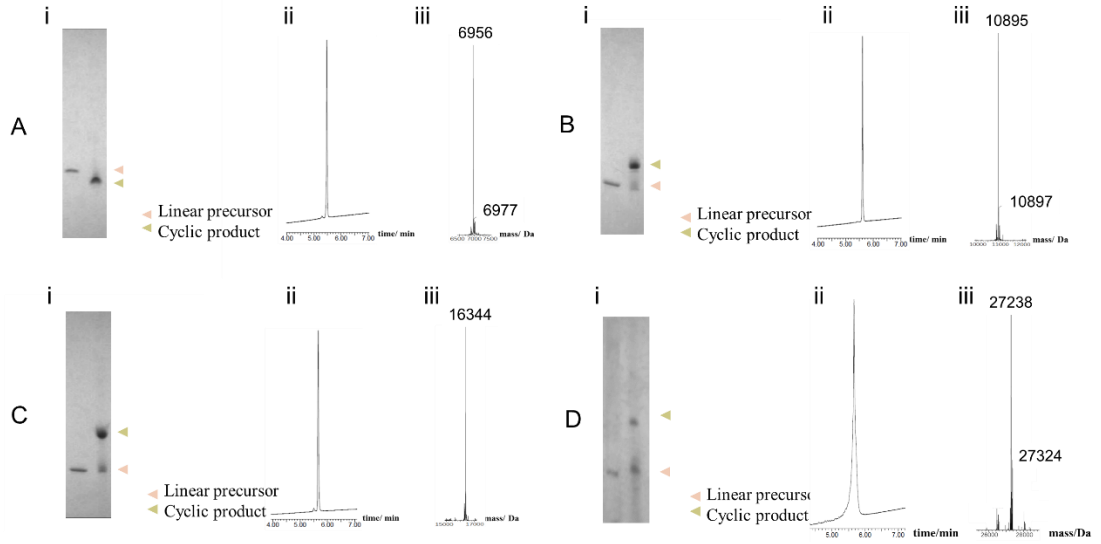


Figure 4.4. Non-templated CuAAC-mediated click cyclisation to give the cyclic DNAR**1-4**.

i: The crude reaction mixture was analysed by 15% denaturing PAGE for DNAR**1** (**A**), **3** (**C**) and **4** (**D**) and 20% denaturing PAGE for DNAR**2** (**B**). The gel was imaged under UV shadowing; **ii**: RP-HPLC trace (260 nm) of the purified cyclic templates; **iii**: Mass spectra (ES^-) of the purified cyclic templates. Mass for the templates are: **A**. DNAR**1** calculated 6954 Da, found 6956 Da; **B**. DNAR**2** calculated 10895 Da, found 10895 Da; **C**. DNAR**3** calculated 16343Da, found 16344 Da; **D**. DNAR**4** calculated 27238 Da, found 27238 Da.

4.4 Hybridisation study using unmodified DNARs and complementary signal strand

4.4.1 Investigation of the hybridisation property of unmodified DNARs and signal strand 1 on native PAGE

Having successfully obtained the DNARs through CuAAC cyclisation, the capability of cyclic DNAR**2**, DNAR**3** and DNAR**4** to accommodate the complementary signal strand **1** was investigated by native PAGE. DNAR**1** was not studied as it was unable to carry multiple signal strands.

Signal strand **1** was mixed with DNAR**2** at various molar ratios (signal strand **1** to DNAR**2** of 0.5:1, 1:1, 1.5:1 and 2:1) in 150 mM K^+ and 15 mM Na^+. The mixture was then annealed by heating to 95 °C for 5 min followed by cooling to RT at a rate of 0.5 °C/min. The hybridisation was determined by 10% native PAGE, which was performed at 4 °C.

The result indicated that the signal strand **1** successfully hybridised to DNAR**2** in precisely defined stoichiometry (Figure 4.5). Indeed, native PAGE analysis confirmed that when increasing the molar ratio of signal strand **1** to DNAR**2** up to 2:1, two hybridisation sites on DNAR**2** were fully occupied.

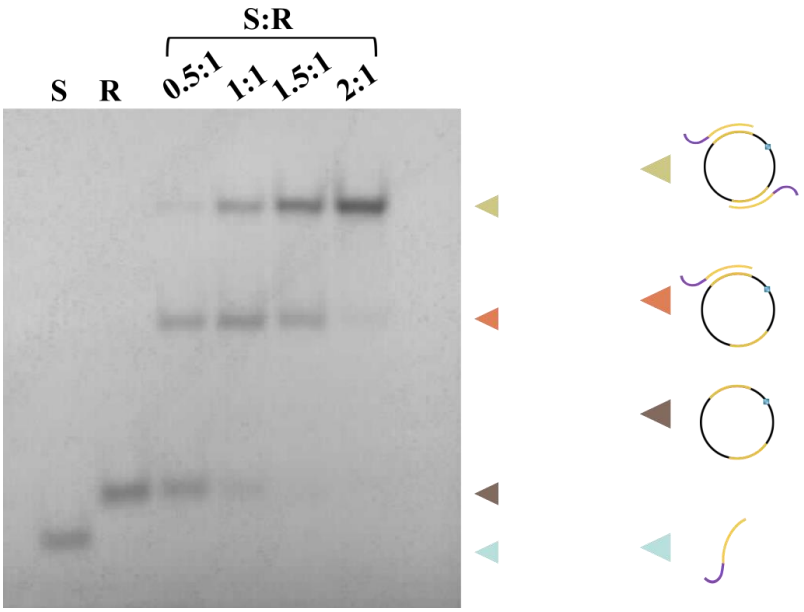


Figure 4.5. Native PAGE (10%) analysis of hybridisation between signal strand **1** and DNAR**2** at various molar ratios (signal strand: DNAR = 0.5:1, 1:1, 1.5:1 and 2:1) in 150 mM K^+ and 15 mM Na^+.. **S**: signal strand **1**; **R**: DNAR**2**.

The same trend was observed for signal strand **1** hybridising to DNAR**3** at various molar ratios (1:1, 2:1 and 3:1) under the same conditions (Figure 4.6). By altering the amount of the signal strand, occupancy of the hybridisation sites on the ring can be controlled. From the gel, DNAR**3** showed a clear band for the complex with all three binding sites fully accommodated by signal strand **1**.

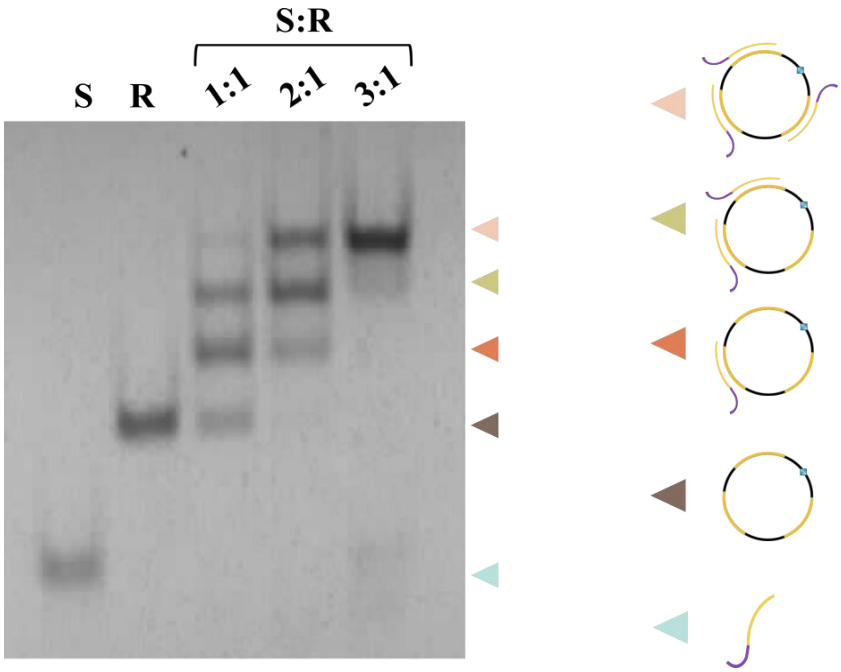


Figure 4.6. Native PAGE (8%) analysis of hybridisation between signal strand **1** and DNAR**3** at various molar ratios (signal strand:DNAR = 1:1, 2:1 and 3:1) in 150 mM K^+ and 15 mM Na^+. **S**: signal strand; **R**: DNAR**3**.

For DNAR**4** containing five hybridisation sites, two bands were present on the gel with a smear tail when five folds of signal strand **1** were added. The upper band represented the complex where all five hybridisation sites were fully occupied, and the lower band represented four hybridisation sites occupied. An obscure band was noted at the bottom of the lane, which was unbound signal strands (Figure 4.7). The observations indicated incomplete hybridisation between signal strand **1** and cyclic DNAR**4**, which might be due to the high flexibility of the large cyclic oligonucleotide.

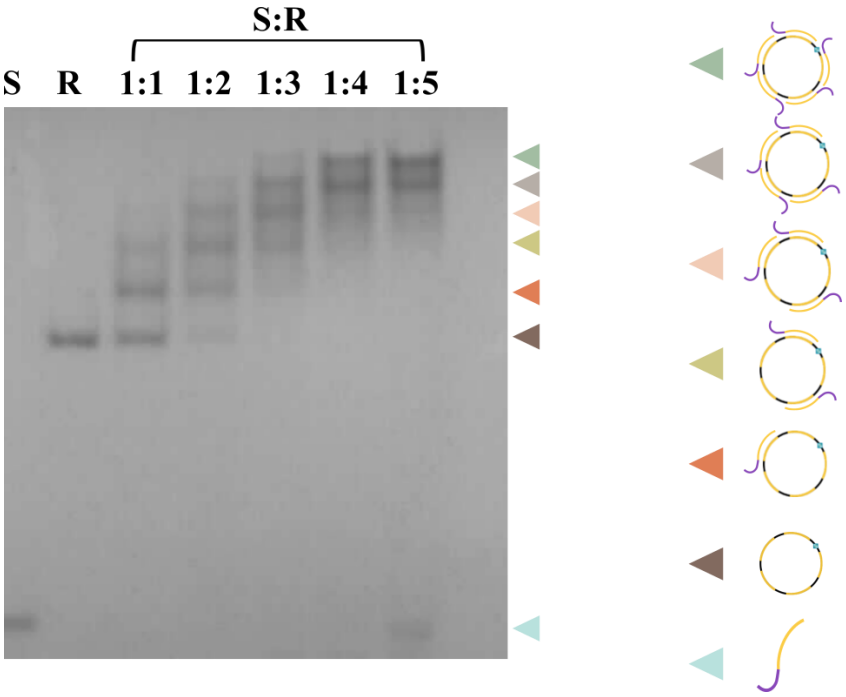


Figure 4.7. Native PAGE (8%) analysis of hybridisation complex generated from signal strand **1** and DNAR**4** at various molar ratios (signal strand:DNAR = 1:1, 2:1, 3:1, 4:1 and 5:1) in 150 mM K^+ and 15 mM Na^+. S: signal strand **1**; R: DNAR**4**.

DNA nanoring with proper sizes (DNAR**2**–**3**) showed their ability to accommodate the signal strands in precisely defined stoichiometry, suggesting the feasibility of accurate detection for target mRNA.

4.4.2 Thermal stability study of hybridised DNA nanocarriers using UV melting

Next, thermal stability of these constructs was evaluated. When DNA double strands unwind, the bases become unstacked and display an increased absorbance at 260 nm. Therefore, the absorbance of the constructs was recorded at 260 nm as a function of

temperature to obtain melting profiles.

The thermal stability of the DNA nanocarriers formed by both cyclic and linear DNAR**1**–**4** sequences and signal strand **1** was studied using UV melting assays at the presence of 150 mM K^+ and 15 mM Na^+. The melting temperature (T_m) was estimated using Cary Win UV thermal application software by the first derivative of absorption with respect to temperature (dA/dT).

As anticipated, the T_m of the complexes formed by linear DNAR**1**–**4** and signal strand **1** was higher than the cyclic counterparts (Figure 4.8). This is potentially due to the increased rigidity of the sequence after cyclisation, which destabilises the duplexes. As the size of the DNA increases, the cyclic DNAR becomes more flexible. The flexibility makes the hybridisation with the signal strand more thermally stable. This was reflected in the remarkable T_m change observed for short DNAR**1** and DNAR**2** sequences after cyclisation**,** while the difference was negligible for DNAR**3** and **4**.

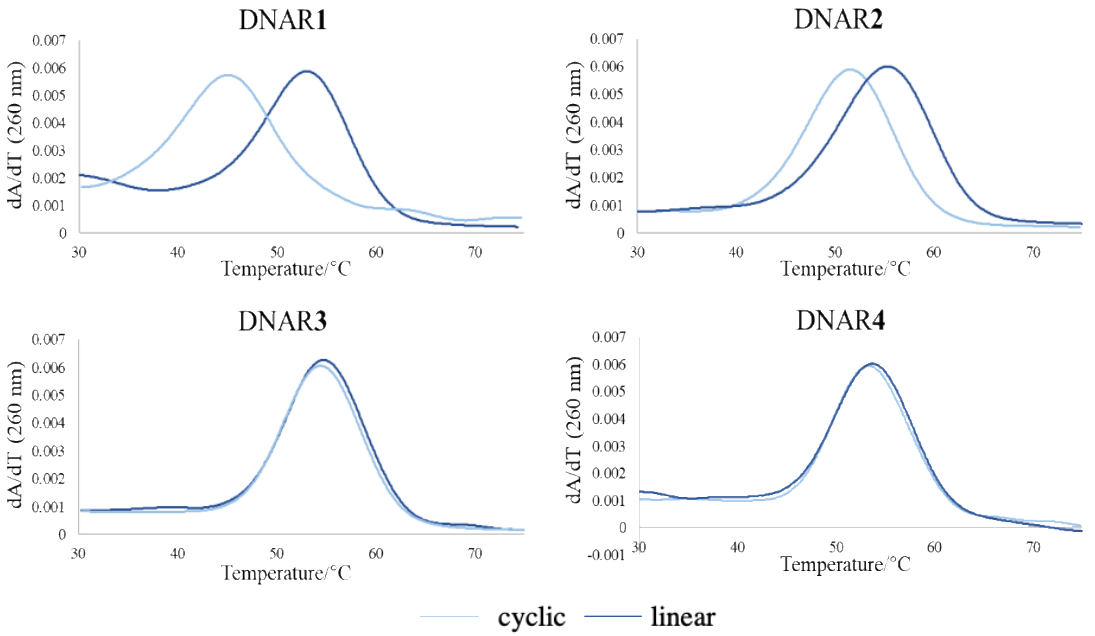


Figure 4.8. First melting derivatives obtained at 260 nm with a temperature gradient of 0.1 °C/min, for complexes formed by linear (dark blue) and cyclic (light blue) DNAR**1**–**4** with signal strand **1**. The measurements were done in triplicate.

Oligonucleotide	T_m linear/°C	T_m cyclic/°C	ΔT_m/°C
DNAR**1**	53.19	44.67	-8.52
DNAR**2**	55.37	51.70	-3.67
DNAR**3**	54.77	54.61	-0.16
DNAR**4**	53.62	53.34	-0.28

Table 4.2. T_m of complexes formed by linear/cyclic DNAR**1**–**4** and signal strand **1**.

The key conclusion from the experiment is that the T_m of all complexes formed was above 44 °C. Therefore, the complexes formed should be thermally stable when introduced into cells or *in vivo,* where the temperature is 37 °C, which is essential for

minimal background noise.

4.4.3 Investigation of signal strand displacement from DNARs by survivin RNA on native PAGE

To achieve target mRNA detection in cells, the signal strand hybridised to DNAR should dissociate in the presence of the target RNA. To investigate the dissociation *in vitro*, a target RNA strand complementary to the signal strand was synthesised based on the part of the survivin mRNA sequence. Displacement of the aptamer-functionalised signal strand **2** from DNAR**3** and DNAR**4** was investigated. To do this, the DNARs were first hybridised with 1.2 folds of signal strand **2** in 15 mM of Na^+ and 150 mM K^+ buffer. The K^+ was used to form the G-quadruplex aptamer, which is necessary for its binding ability. The synthetic survivin mRNA target strand was added to the complex 1.2 times to the signal strand, and the mixture was incubated for 10 min at 37 °C prior to loading onto an 8% native PAGE gel. After adding the RNA target, a new band appeared from the gel, representing the duplex formed by the signal strand **2** and the survivin RNA strand (Figure 4.9). At the same time, the bands representing the DNA nanocarrier complexes disappeared. This indicated that the signal strand was displaced by the survivin target RNA from DNARs.

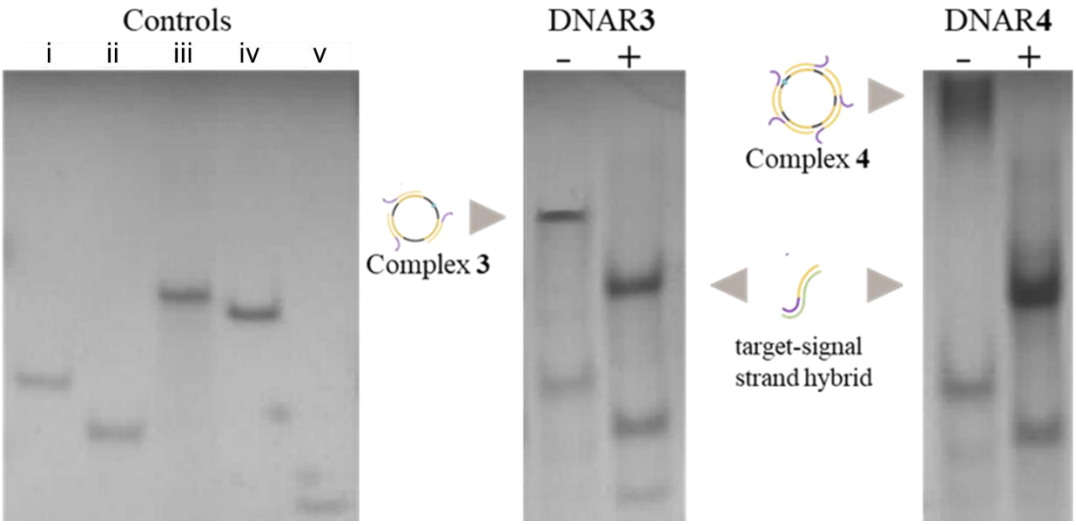


Figure 4.9. Native PAGE (8%) analysis of signal strand displacement by survivin mRNA target from DNARs. Complexes formed between DNARs and the signal strand **2** were loaded; −: without adding the target RNA strand; +: after adding the target RNA strand. Controls were **i**: signal strand **2**; **ii**: synthetic survivin mRNA target; **iii**: survivin mRNA target–signal strand **2** hybrid; **iv**: cyclic DNAR**4**; **v**: cyclic DNAR**3**.

4.5 Multivalent binding of the fluorescent DNA nanocarrier to target cells

Multivalent interactions in which multiple targeting ligands on one particle bind to multiple receptors on another are widely found in biological systems.[246–248] These interactions can lead to increased strength and selectivity compared to the corresponding monovalent interaction. The DNA nanocarrier formed by DNARs and aptamer-functionalised signal strands carries multiple targeting moieties on the same construct, endowing the system to bind to the target multivalently. To investigate the

multivalency of the DNA nanocarrier complex, the FAM-labelled signal strand **2** with 3' anti-HER2 aptamer was used to visualise its binding towards HER2 receptors on breast cancer cell surfaces.

Here, DNAR**3** and DNAR**4** were used as examples due to their ability to carry multiple signal strands, providing better insight into multivalency. SK-BR3 cells were used as they express a high level of HER2 receptors.[182] The DNA nanocarrier was formed between the signal strand **2** and DNARs at various molar ratios (signal strand **2** to DNAR**3** at 1:1, 2:1 and 3:1; signal strand **2** to DNAR**4** at 1:1, 2:1, 3:1, 4:1 and 5:1) in 15 mM Na^+ and 150 mM K^+ buffer by slow annealing to enable the formation of the G-quadruplex aptamer.

Previous studies in the group confirmed that higher concentration of aptamer leads to higher binding events with the cell and thus higher cell fluorescence by flow cytometry assay (J. Chen, unpublished). Similarly, for the DNA nanocarrier accommodating multiple aptamer-functionalised signal strands, we anticipated that the fluorescence intensity observed from the cells to increase with the signal strand loading. To investigate this, the DNA nanocarriers carrying different numbers of signal strand **2** were incubated with HER2+ SK-BR3 cells and HER2- MCF7 cells in the dark at 37 °C for 40 min. After incubation, the cells were washed repeatedly, and the fluorescence of the cells was measured by flow cytometry. The flow cytometry results showed stronger

cell fluorescence when DNARs bearing more signal strands were used. This suggested a positive correlation between the signal strand loading on DNA nanocarriers and their binding to target biomarkers (Figure 4.10. A, B).

The binding of the multivalent DNA nanocarriers to cells was compared with the binding of the monovalent probe (signal strand only) at the same molar concentrations. For example, when the DNA nanocarrier used was made by 1 μM of signal strand **2** hybridised with 0.2 μM of DNAR**4** (molar ratio of 5:1 between signal strand **2** and DNAR**4**), 1 μM of signal strand **2** was used for comparison.

The results from flow cytometry demonstrated that the multivalent DNA nanocarrier always exhibited stronger cell fluorescence than the monovalent signal strand. This is because the multivalent DNA nanocarrier has enhanced target affinity by simultaneously binding to more than one receptor on the cell surface (Figure 4.10.C and D**)**. From this point of view, the more signal strand the system carries, the better the binding towards the targets. However, to determine the proper size of the DNAR, other aspects such as cyclisation efficiency, thermal stability and hybridisation with signal strands should also be considered.

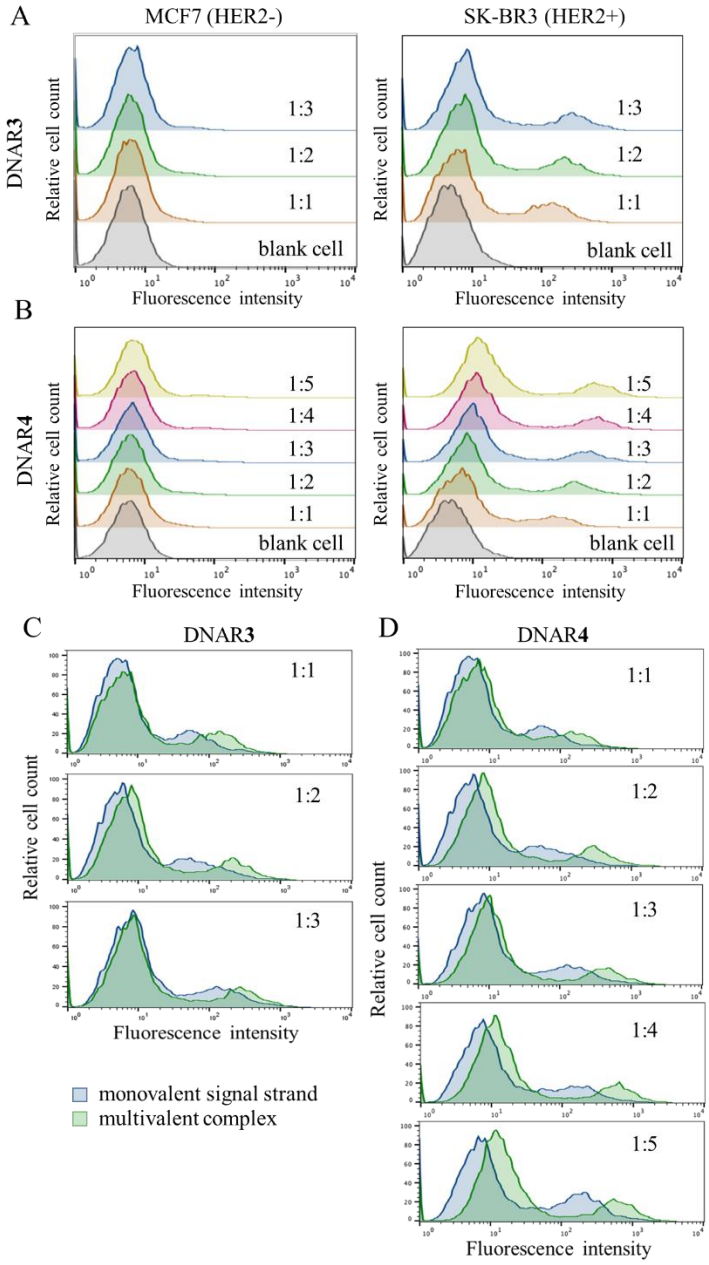


Figure 4.10. Flow cytometry results of the multivalent binding of the DNA nanocarriers to HER2+ and HER2- cell lines. **A**. Binding of the DNA nanocarriers formed by various ratios of DNAR**3** (3 binding sites) and signal strand **2** to cells; **B**. Binding of the DNA nanocarriers formed by various ratios of DNAR**4** (5 binding sites) and signal strand **2** to cells; Binding of the DNA nanocarriers formed by various ratios of **C**. DNAR**3** (3 binding sites), **D**. DNAR**4** (5 binding sites) and signal strand **2** to HER2+ SK-BR3 cells, compared with the same concentrations of monovalent signal strand **2**.

4.6 CuAAC cyclisation of quencher functionalised DNARs

From previous studies, the efficiency of CuAAC-mediated cyclisation decreased as the DNA size increased. Also, larger DNAR containing more hybridisation sites showed improved multivalent binding to specific cell surface receptors. Considering these two aspects, the DNAR**3** sequence with three hybridisation sites was chosen as the best model for the subsequent studies. To enable real-time detection of survivin mRNA target in cells, a BHQ1 quencher that can efficiently quench FAM was included in each hybridisation site of DNAR**3**. The sequence is termed DNAR**5**. As a control, DNAR**6** which had the hybridisation sequence randomised was designed.

We first investigated the CuAAC cyclisation efficiency of DNAR**5** and DNAR**6** to see whether BHQ1 modification affected the click efficiency. The reaction was carried out under the same conditions as in Section 4.3, and the products were purified by denaturing PAGE. Both reactions gave a clear band on the gel for the monomeric cyclised product (Figure 4.11). However, a few additional bands for polymeric by-products appeared on the gel, which were not observed for the cyclisation of unmodified DNARs. Considering rest of the conditions unchanged, the formation of polymeric products might be caused by the increased hydrophobicity after including the BHQ1, which aggregated the DNA and facilitated intermolecular ligations.

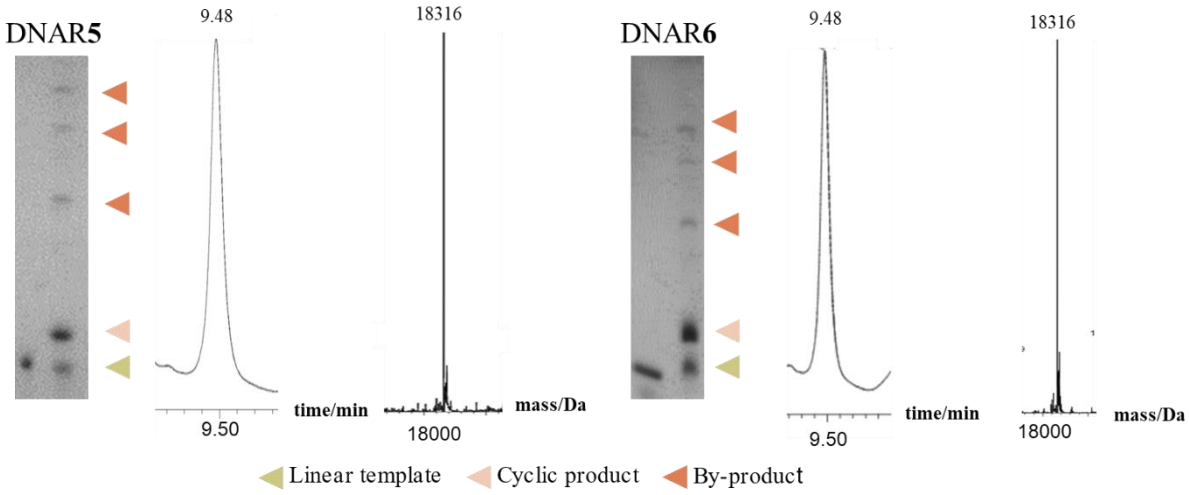


Figure 4.11. Non-templated CuAAC-mediated click cyclisation reactions to give the cyclic products of DNAR**5** and DNAR**6**. The crude reaction mixtures were analysed by 12% denaturing PAGE, and the gels were imaged under UV shadowing. RP-HPLC traces showed the high purity of the purified products. For both cyclised products, the calculated mass is 18314 Da, the found mass is 18316 Da.

4.7 The hybridisation of quencher-functionalised DNARs with fluorescent signal strands

4.7.1 Investigation of the hybridisation on native PAGE

After purification by PAGE, cyclised DNAR**5** and DNAR**6** were mixed with the FAM-labelled signal strands **2** and **3** respectively at various molar ratios (1:1, 1:1.5, 1:2, 1:2.5 and 1:3) in 15 mM Na^+ and 150 mM K^+. The mixture was heated first then annealed slowly to allow hybridisation before running on a 6% native PAGE at 4 °C. The gel showed that the fluorescent signal strand hybridised to the quencher-functionalised

DNAR in both cases (Figure 4.12). However, the bands in both gels were streaky, indicating incomplete hybridisation between the cyclised DNARs and the signal strands. The hybridisation was further investigated by the quenching of the fluorophore in Section 4.7.2.

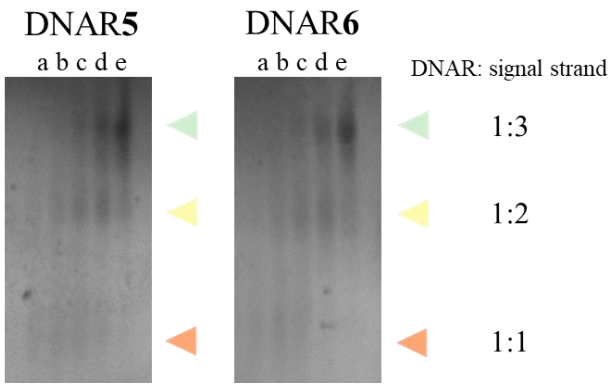


Figure 4.12. Hybridisation of cyclic DNAR**5** and DNAR**6** with signal strands **2** and **3,** in **a**.1:1, **b**.1:1.5, **c**.1:2, **e**.1:2.5 and **f**.1:3 ratio, respectively. Hybridisation was analysed by a 6% native PAGE gel and imaged under UV.

4.7.2 Investigation of the hybridisation by real-time fluorescence reading

To further investigate the hybridisation between the quencher embedded DNARs and their corresponding signal strands, fluorescence reading was conducted using a CFX real-time PCR detection system, giving continuous and real-time fluorescence signals during the heating/cooling cycles.

When the DNAR and the signal strand are hybridised at lower temperatures, the

fluorophore on the signal strand and the quencher on the DNAR come into the vicinity. As a consequence, the fluorophore is quenched, giving overall low fluorescence signals. When the hybridised complex is heated up during the melting steps, the duplex is unwinded, separating the quencher-fluorophore pair. Therefore the fluorophore is unquenched, resulting in an increase in the fluorescence signals. From the fluorescence change, the thermal stability of the duplex formed and the quenching efficiency can be understood.

To do this, DNAR**5** and DNAR**6** were mixed with their corresponding signal strands at a 1:3 ratio in different solutions, annealed and melted from 85°C to 10°C. Solutions with various K^+, Na^+ and Mg^{2+} concentrations were employed. The cations were added to stabilise the duplexes by neutralising the negative charge on the DNA phosphate backbone, while K^+ also helped form the G-quadruplex structure of the aptamer, which is crucial for the recognition of its biomarkers. The measurements were conducted using both linear and cyclised DNAR to compare the impact of the DNA structure on the hybridisation and quenching efficiency (Figure 4.13).

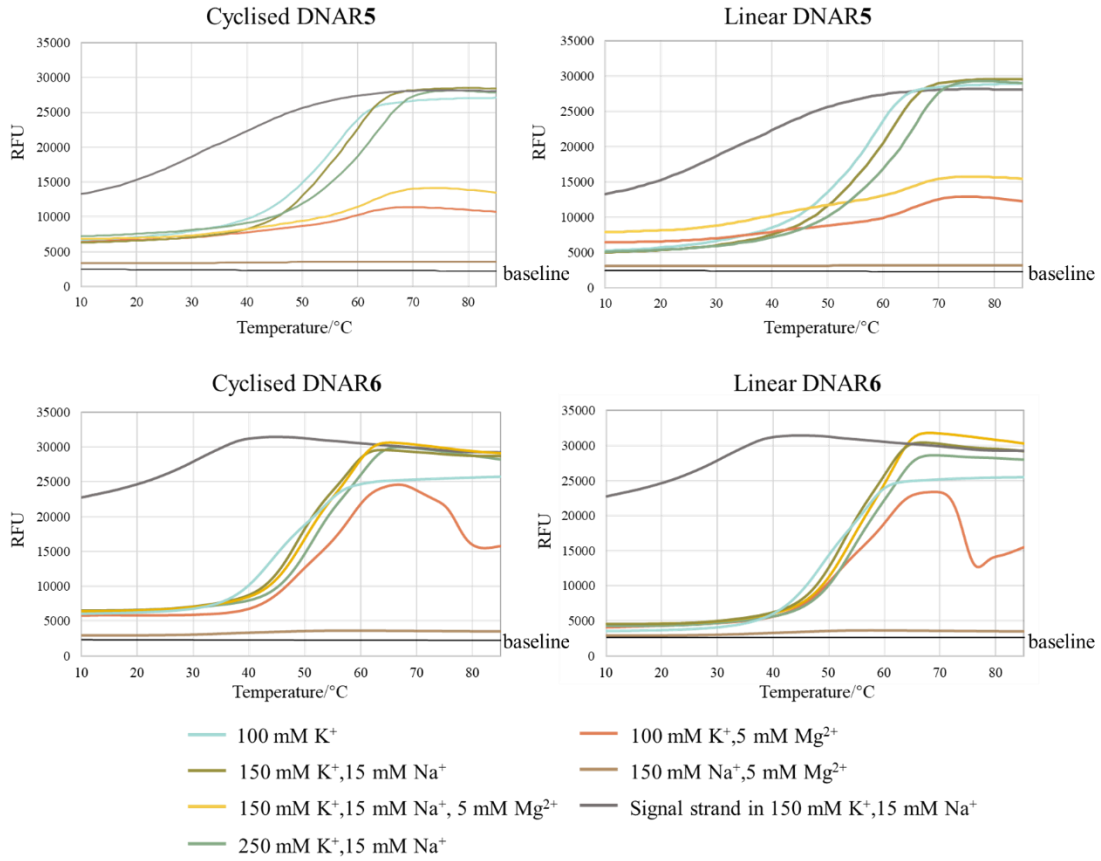


Figure 4.13. Fluorescence curves of complexes formed by DNAR**5** and DNAR**6** (0.33 μM) with signal strands **2** and **3** (1 μM) respectively in different solutions, before (labelled as linear) and after cyclisation (labelled as cyclised). The mixtures were melted from 10°C to 85°C at a rate of 0.5 °C/min. Baselines represent where no fluorescent oligonucleotides were added. All measurements were performed in triplicate.

The fluorescence curves showed that the DNARs quenched the fluorophore on the signal strands when the two DNA strands hybridised at low temperatures (Figure 4.13). However, the quenching efficiency was observed to vary before and after cyclisation of the DNAR under different salt concentrations. As the ultimate goal is to introduce

the nanocarrier system in living cells, we specifically studied quenching at 37 °C. For both sequences, the efficiency of quenching changed slightly after cyclisation (Table 4.3). In most cases, the quenching was more significant before cyclisation. As quenching by BHQ1 highly depends on the physical contact between the dye and the quencher, the reduced quenching observed after cyclisation of the DNAR sequences suggested inadequate hybridisation between the signal strands and the cyclic DNARs, which is consistent with the results observed from Section 4.7.1.

Oligo	100 mM K^+	150 mM K^+, 15 mM Na^+	150 mM K^+, 15 mM Na^+, 5 mM Mg^{2+}	250 mM K^+, 15 mM Na^+	100 Mm K^+, 5 mM Mg^{2+}	150 mM Na^+, 5 mM Mg^{2+}
C DNAR**5**	0.75	0.80	0.79	0.76	0.79	0.96
L DNAR**5**	0.80	0.83	0.67	0.84	0.80	0.98
C DNAR**6**	0.87	0.81	0.82	0.83	0.89	0.99
L DNAR**6**	0.92	0.89	0.90	0.91	0.92	0.99

Table 4.3. Quenching efficiency of the fluorescent signals strands by BHQ1 modified DNARs sequences in different solutions at 37 °C. C represents cyclic oligos, and L represents linear oligos.

For all salt concentrations used, T_m was consistently above 37 °C, suggesting that the complex should be thermally stable in living cells. Buffer composition was found to affect the thermal stability of the hybridised complexes significantly. We observed that the T_m increased at higher salt concentrations due to the stabilisation of the duplex by positively charged cations. The type of salt also substantially affected the fluorescence of the dye. One important observation from the experiment is that when K^+ was absent, the fluorescence was always quenched regardless of temperature. It is known that guanine quenches the dye adjacent.[249,250] As K^+ is essential for the formation of G-

quadruplex, we hypothesised that the lack of K^+ stopped the G-rich aptamer sequence from forming compacted G-quadruplex, leaving 'free' guanines which acted as quenchers. 150 mM K^+ with 15 mM Na^+ was used as it is similar to the component of mammalian intracellular fluid (139 mM K^+ and 12 mM Na^+).[251] Hybridisation in this solution showed the salt concentration and temperature in cells is sufficient to keep the complex hybridised as well as prevent undesired fluorescence quenching by guanines.

For DNAR**5**, when 5 mM Mg^{2+} was present, the fluorescence was significantly quenched. This is possibly due to the destabilisation of the G-quadruplexes by Mg^{2+}, which frees guanines.[252] However, such decrease in fluorescence was not significant for DNAR**6**. While the fluorescence dropped in 100 mM K^+ with 5 mM Mg^{2+}, at higher salt concentrations (150 mM K^+, 15 mM Na^+ and 5 mM Mg^{2+}), no fluorescence decrease was seen. This can be attributed to the addition of monovalent cations, which compensated for the destabilising effect.[252] The difference quenching observed for the complexes formed by DNAR**5-**signal strand **2,** and the control DNAR**6-**signal strand **3** indicated the sequences had different secondary structures, albeit with the same base composition. Further investigation is required to confirm the role of G-quadruplexes in the quenching process.

4.7.3 Investigation of signal strand displacement by synthetic survivin RNA

The key mechanism for mRNA detection in live cells is the signal strand hybridised with DNAR being displaced by specific mRNA to recover fluorescence. Following the hybridisation experiments in Section 4.7.2, 1.2-fold synthetic survivin mRNA target was added to the annealed mixture of DNAR**5** and signal strand **2** in 150 mM K^+ and 15 mM Na^+ to investigate the strand displacement by the target RNA *in vitro*. Complexes formed by random DNAR**6** sequences and signal strand **3** were used as control. The fluorescence was recorded at 37 °C by CFX over 100 min (5 min/cycle). The results showed that the fluorescence in the complex formed by DNAR**5**, which targeted survivin mRNA, recovered rapidly after adding the target RNA. For the control group that contained non-targeting sequences**,** the fluorophore remained low as the signal strand was not removed from the DNAR.

This RNA 'invasion process' was also analysed by native PAGE. After incubating the target RNA with the hybridised complexes for 10 min at 37 °C, the mixtures were run on a 6% native PAGE gel at 4 °C. The gel showed that for the DNAnaocarrier complex targeting survivin (DNAR**5**-signal strand **2** hybrid), the band representing the DNAR–signal strand complex disappeared after the addition of survivin RNA. In contrast, for the control, the band remained visible (Figure 4.14). The results suggested that the

displacement of the signal strand by the survivin target RNA sequence was specific, and the binding between them restored the fluorescence signal.

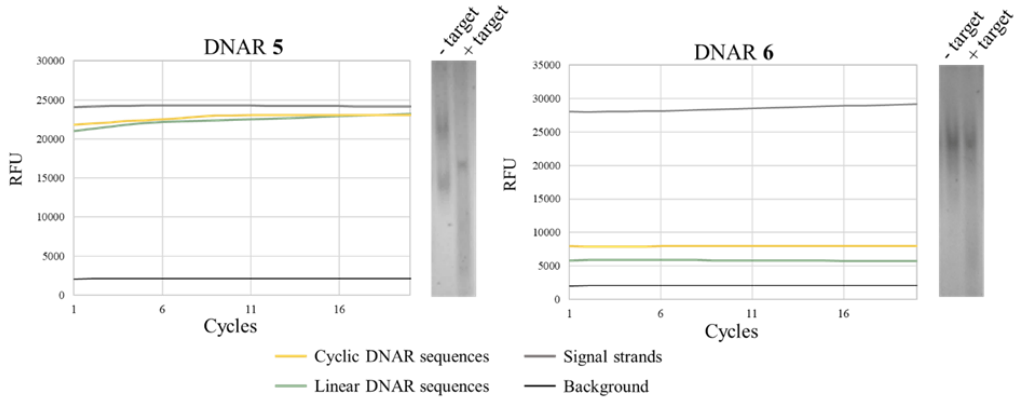


Figure 4.14. Fluorescence measurements of complexes with the addition of survivin RNA target sequence, at 37 °C in 150 mM K^+ and 15 mM Na^+, and the analysis on 6% native PAGE. For the fluorescence reading, each cycle is 5 min and the measurements were performed in triplicate.

4.8 Cellular binding and internalisation of DNA nanocarriers

The cellular binding and internalisation of the nanocarrier complexes is crucial to successful mRNA detection in cells and was investigated.

4.8.1 Investigation of the stability of DNA nanocarriers in serum by denaturing PAGE

To achieve specific mRNA detection, both the cyclic DNA and the signal strand must stay intact. Degradation of either will result in fluorescence recovery, leading to undesirable background signals. It was hence necessary to test their stability against

serum. Cyclic DNAR3 (unmodified), DNAR**5** (BHQ1-modified) and signal strand **2** (aptamer and FAM-modified) were incubated in cell culture medium supplemented with 10% fetal bovine serum (FBS) for 1, 6, 12 and 24 h, prior to analysis on 8% denaturing PAGE. The gel showed that the cyclised DNARs were completely degraded after 24 h incubation while a small amount of the signal strand remained (Figure 4.15). It is known that mammalian serum such as FBS contains a mixture of different nucleases, including exonucleases and endonucleases. Although cyclic DNA showed remarkable resistance against exonucleases, the endonucleases in the serum degraded such structure. The stability of the signal strand probably came from the compact G-quadruplex structure. When incubated for shorter times, both structures remained intact. This suggested that the experiment time needed to be strictly controlled. To achieve minimal DNA degradation, all experiments in cells were conducted and analysed within 1 h.

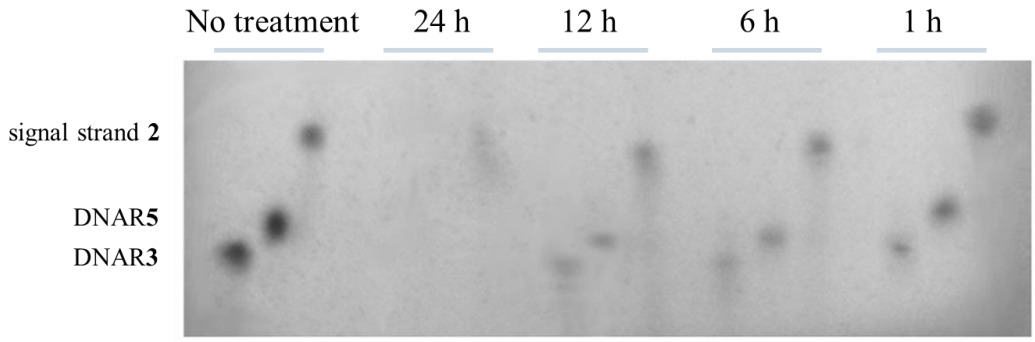


Figure 4.15. Serum stability of cyclic DNAR**3**, DNAR**5** and signal strand **2**. Samples were incubated at 37 °C in 10% FBS over 1, 6, 12 and 24 h and analysed on 8% denaturing PAGE.

4.8.2 Investigation of interactions between HER2+ cells and DNA nanocarriers by fluorescence microscopy

Cellular internalisation of nanostructures highly depends on their size and interactions with cell membranes.[197] To investigate the internalisation of DNA nanocarriers, DNAR**7** with a TAMRA dye placed within each of the hybridisation sites was synthesised. Labelling of DNAR with TAMRA enabled discrimination between the FAM-labelled signal strand and the DNAR. Cyclic DNAR**7** was hybridised with FAM-labelled signal strand **2,** which allowed tracking of both the DNAR and the signal strand during the binding process. The DNA nanocarrier hybrid was incubated with SK-BR3 cells in the dark at 37 °C for 40 min before imaging by confocal microscopy. The imaging showed that TAMRA (red) and FAM (green) fluorescence signals were co-localised in the perinuclear area, indicating that the DNA nanocarrier was internalised (Figure 4.16.A). The DNAR itself did not have affinity to the cells, meaning it was hybridised to the targeting signal strand under the 37 °C incubation condition. This is consistent with the results from the previously thermal stability study (Section 4.4.2). However, localised bright spots were observed, indicating such DNA structures entrapped in subcellular compartments. This could impede the DNA nanocarrier from binding with the target mRNA in the cytoplasm. For HER2- MCF-7 cells, low fluorescence was shown after incubation with the DNA nanocarrier, indicating the

recognition was specific (Figure 4.16.C).

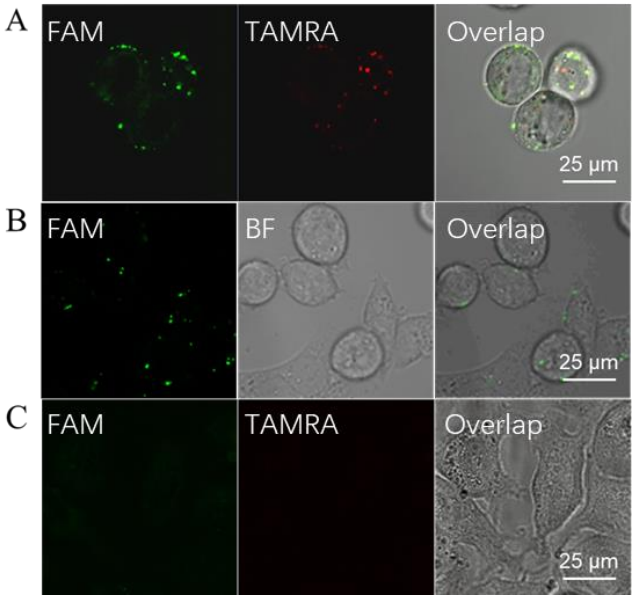


Figure 4.16. Fluorescence imaging of SK-BR3 cells **A.** under FAM and TAMRA channels, after incubation with the complex formed by TAMRA-modified DNAR**7** and FAM-modified signal strand **2** at 37 °C in the dark for 40 min; **B**. under FAM channel, after incubation with the complex formed by quencher-modified DNAR**5** and FAM-modified signal strand **2** at 37 °C in the dark for 40 min; **C**. Fluorescence imaging of MCF-7 cells under FAM and TAMRA channels, after incubation with the complex formed by TAMRA-modified DNAR**7** and FAM-modified signal strand **2** at 37 °C in the dark for 40 min.

The complex formed by quencher-modified DNAR**5** and signal strand **2** was also incubated with SK-BR3 cells to see if the quenched fluorophores were restored in the cytoplasm. The imaging showed that bright spots were observed inside the cells, with no apparent fluorescence observed in the cytoplasm. The bright spots indicated the complex was trapped in subcellular chambers and degraded, resulting in fluorescence leach. The weak fluorescence in the cytoplasm suggested a very low release of the

complex into the cytoplasm where the target mRNA was located (Figure 4.16.B).

The inefficient uptake of the complex could limit its chance of meeting mRNA in the cytoplasm, leading to failure in reflecting the mRNA level. Several methods were then attempted to improve the uptake efficiency.

4.8.3 Enhancing cellular uptake by cell-penetrating peptides (CPPs)

Different methods have been reported to promote the uptake and subcellular compartment escape of nanoparticles.[134,140,142] Cell-penetrating peptides (CPPs) are one of the most commonly used strategies. In this study, we used a 20-amino acid CPP, ppTG21, which has been reported to deliver CRISPR-Cas ribonucleoproteins into cells without covalent bonding efficiently.[253]

To achieve mRNA detection in HER2+ cells, the use of CPP must not interfere with the specific binding of the nanocarrier system. To investigate if ppTG21 improved cellular uptake without affecting the specific binding, it was added to SK-BR3 (HER2+) and MCF7 (HER2–) cells with FAM-labelled anti-HER2 aptamer. The internalisation was evaluated by confocal microscopy. Imaging showed that with the aptamer itself, SK-BR3 showed fluorescence around and inside the cells while MCF7 cells remained dark. With the addition of the CPP, the fluorescence in the HER2+ cells significantly increased, suggesting an improvement in the internalisation of the aptamer (Figure

4.17). Although MCF7 showed very low binding to the aptamer, after including the CPP, the fluorescence also increased (Figure 4.17). The mutated HER2 aptamer studied in Chapter 2, which showed reduced binding to the HER2 biomarker, was also added with the CPP. The cell imaging showed that the cellular uptake of the mutated aptamer increased in the presence of the CPP, resulting in fluorescence signals in both HER2+ and HER2- cell lines.

To examine if CPP improved the internalisation of the DNA nanocarrier, the complex formed by DNAR**3** and the FAM-labelled signal strand **2** mixed with the CPP was added to the cell lines. Fluorescence imaging showed that with the addition of the CPP, SK-BR3 cells exhibited very bright fluorescence, indicating improved cellular uptake. For MCF7, cells showed a much weaker fluorescence compared to SK-BR3. The results suggested that the ppTG21 CPP efficiently enhanced cellular uptake. However, non-specific uptake was also observed for HER2- cells, although not as substantial. Moreover, bright foci were visible, which could be attributed to DNA aggregation by the CPP. This could result in a high undesirable background signal, preventing accurate quantification of the target.

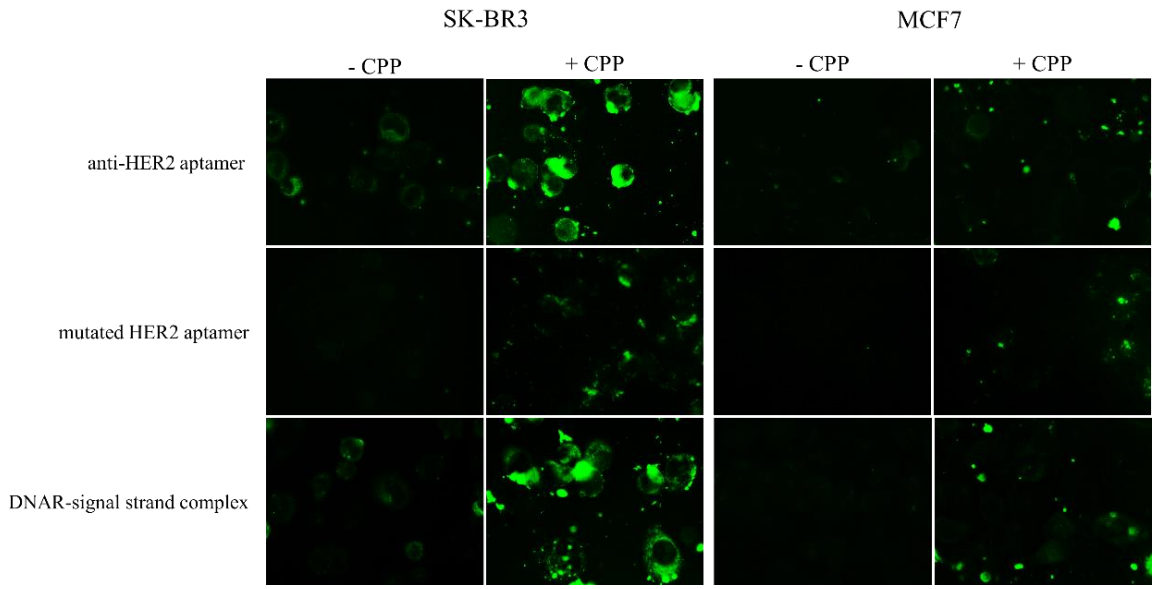


Figure 4.17. Fluorescence imaging of HER2+ SK-BR3 and HER2- MCF7 cells after incubation with FAM-labelled anti-HER2 aptamer, mutated HER2-aptamer and DNAR**3**-signal strand **2** complex, with and without the presence of the ppTG21 CPP.

4.8.4 Delivery of the DNA nanocarrier by lipid transfection

Transfection by lipid (lipofection) is commonly used for DNA delivery into cells. Mixing with a positively charged lipid allows DNAs to be encapsulated within a vesicle that can easily merge with negatively charged cell membranes and intracellular vesicles.[138,140] Although lipid transfection is not a cell-specific method, it delivers DNA efficiently without receptor-mediated internalisation. Considering the low efficiency of the spontaneous DNA internalisation, lipid transfection was used as a positive control. It could provide us with a perspective on how the fluorescence of the nanocarrier system restores in the cytoplasm.

We used Invitrogen™ Lipofectamine™ 2000 Transfection, which is commonly used for nucleic acid delivery to common cell lines. Quenched (DNAR**3**-signal strand **2**) and unquenched (DNAR**5**-signal strand **2**) DNA nanocarriers were pre-mixed with lipofectamine to form a DNA-lipid complex before adding to SK-BR3 cells. After transfection, the cells were imaged by confocal microscopy. From the imaging, strong fluorescence was observed all over the cells after the transfection of the unquenched complex, indicating successful internalisation (Figure 4.18). Some cells showed stronger fluorescence than others, suggesting an uneven distribution of transfection. The cell exhibited a weaker fluorescence for the quenched complex formed by DNAR5 and signal strand **2**, implying the fluorophore on the signal strand was still quenched. This meant the signal strand was not efficiently dissociated from the DNAR. In both cases, bright foci were observed indicating the aggregation of the lipid-DNA complex, which could obstruct precise mRNA detection.

Previously reported molecular beacon targeting the neighbouring region of survivin mRNA showed a bright signal in the same cell lines upon incubation.[254] The poor signal observed in our study could be due to the low abundance of the target mRNA in cells or inadequate access to the binding site on the mRNA. To address this, a control nanocarrier complex that targets a highly expressed housekeeping transcript should be studied in the future. It is also worth quantifying the mRNAs by currently existing

techniques, such as molecular beacon and reverse-transcription PCR, as comparisons.

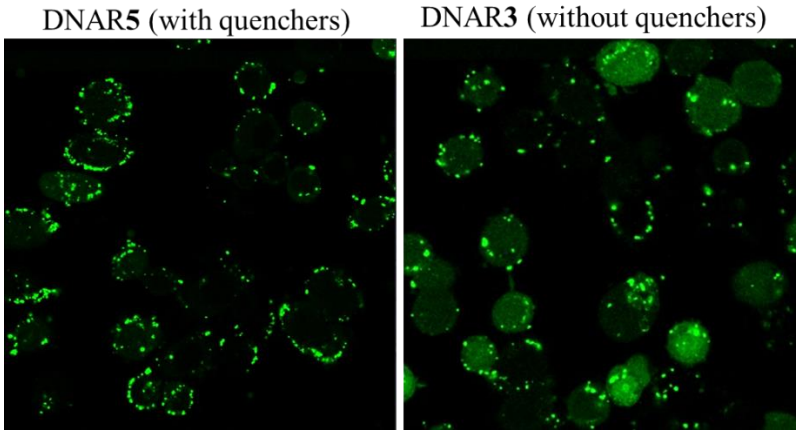


Figure 4.18. Fluorescence imaging of SK-BR3 cells after lipid transfection of complexes formed by DNAR**5**-signal strand **2** (with quenchers) and DNAR**3**-signal strand **2** (without quenchers).

4.9 Conclusions

In this chapter, a DNA nanocarrier system carrying multiple mRNA targeting signal strands was designed for mRNA detection in living cells.

DNA nanorings of different sizes were made. In all cases, the CuAAC cyclisation of linear oligonucleotides bearing 5′-azide/3′-alkyne modifications was efficient in the absence of a splint.

Hybridisation between the cyclic DNAR and the signal strands was investigated by native PAGE, UV-melting and real-time fluorescence measurement. It was demonstrated that the hybridisation sites of the unmodified DNARs reached saturation

by increasing the molar ratios of signal strands to DNARs up to maximum stoichiometry. The thermal stability and serum stability of the sequences satisfied the need for in cell and *in vivo* studies. In the presence of survivin mRNA target, the signal strand was successfully released from the DNAR, and its fluorescence was recovered, suggesting the feasibility of the design for mRNA quantification through the quenching mechanism. Encouragingly, the multivalency of the DNA nanocarrier system gave it an improved affinity to biomarkers on the cell surface.

However, several problems remain to be solved. The quenching efficiency of the fluorophore by the quenchers on the ring was not ideal, possibly due to the incomplete hybridisation between the two sequences. Quenching efficiency of current methods for mRNA *in-situ* hybridisation such as molecular beacon ranges from 85 to 97%, while with optimisation, it can reach 99.7%.[162] To increase the sensitivity of detection, it is necessary to improve the quenching efficiency. One solution to this is to attach multiple quenchers adjacent to the dye, which has been reported in molecular beacons to enhance the quenching effect greatly.[165] Gold nanoparticles have also been demonstrated as an excellent alternative to quenchers, sometimes performing more efficient quenching.[164] In addition, increasing the signal strand-DNAR hybridisation site sequences by a few bases can promote the binding to completion. However, the efficiency of the cyclisation might be affected due to the increased size.

To enable mRNA detection in living cells, it is important to deliver the complex into the cytoplasm. Our studies have shown that the spontaneous uptake of the DNA nanocarrier complex mediated by anti-HER2 aptamer was not efficient. Only very weak fluorescence was observed in cells, with a significant part trapped in subcellular vesicles. The delivery was boosted by ppTG21 CPP, with a greater fluorescent signal observed in the cytoplasm. However, delivery into HER2- cells was also increased, suggesting the specificity was compromised. In addition, fluorescence imaging showed aggregation of the CPP with DNA, leading to a brighter background. A possible solution is the covalent attachment of the CPP to the complex, which may minimise the non-specific uptake and reduce the aggregation.

Lipid transfection was also used for the delivery of the DNA nanocarrier into the cytoplasm as a control. However, the method was not ideal as the delivery was not selective. Furthermore, aggregation was observed as bright spots, leading to a high background signal. When the quenched complex was transfected into cells, very low fluorescence was observed. The cause for the poor signal needs to be further explored by using control sequences targeting housekeeping genes and quantifying mRNA level using existed methods such as reverse-transcription PCR.

In conclusion, with encouraging preliminary results, the system still needs to be improved in terms of detection sensitivity and cytoplasm delivery to achieve *in situ*

mRNA detection. Future work will include further improving the serum stability, optimising the quenching efficiency, quantifying the mRNA in cells using existing techniques as comparisons and improving cytoplasm releasing. In addition, the impact of introducing such complex into cells on cell behaviours and cell apoptosis is worth investigating.

Chapter 5. Conclusions

Multivalent DNA-based nanomaterials for diagnostic and therapeutic applications were designed and investigated in this study. First, a methodology to functionalised DNFs was developed. Nucleoside triphosphates with reactive chemical handles on the bases were incorporated during RCA, giving DNFs with reactive sites. The impact of these triphosphates on amplification rate and DNF morphology was first evaluated. It was discovered that bulky triphosphates hindered the amplification and consequently changed the structure of the DNFs. The labelling on the introduced chemical handles was then conducted through amine-NHS labelling, CuAAC or SPAAC. By varying the amount of modification, the extent of labelling was adjusted. In addition, orthogonal dual labelling of DNFs was accomplished by incorporating different reactive handles simultaneously. Amine-abundant protein BSA was encapsulated during RCA, providing reactive sites for NHS ester labelling. The application of the methodology was expanded by labelling DNFs with targeting groups that recognised biomarkers on cancer cells. In the study, HER2 targeting aptamer and peptide were attached to DNFs, and the binding ability of these DNFs was evaluated. By attaching targeting groups on DNFs, their binding towards specific cells was enhanced. Using this methodology, a wide variety of functionalities, including targeting groups, tagging groups and drugs, can be covalently linked to RCA generated materials.

The size of nanoparticles is crucial for their cellular recognition and uptake. To broaden their applications in cells, the size of DNFs was tuned using different conditions, including shortened reaction time, the addition of Mg^{2+} and the introduction of polymers. By decreasing the reaction time, less DNA and MgPP were generated, leading to smaller particle structures. The addition of Mg^{2+} increased nucleation sites, producing more crystals with smaller sizes. Polymers have been used to condense DNA and DNA micro/nanostructures. Among them, cationic polymers such as PLL were commonly used, which neutralised the negative charges on the DNA phosphate backbones, thus reducing the repulsion. When added to DNFs, positively charged PLL absorbed negatively charged DNA, replacing Mg^{2+} in the inorganic skeleton, deforming the flower-like structure. However, the potential cytotoxicity of PLL limited the application of this material. Condensation of DNFs by non-toxic neutral polymer PEG was then investigated. PEG in different sizes was added to RCA reactions. It was noted that PEG at high concentration or with high molecular weight hindered the reaction greatly. At the same time, the presence of PEG helped precipitate DNA and reduced the size of particles produced. This could be attributed to the crowding ability of PEG and its shielding of electrostatic repulsion. The stability of PEG-condensed particles in different solutions was improved compared to conventional DNFs, especially when exposed to chelating agent EDTA. Combined with the labelling

methodology developed in Chapter 2, PEGylated particles were successfully labelled with fluorescent dyes, implying potential biomedical applications. By involving neutral (i.e. uncharged) PEG, the HER2 aptamer sequenced particles gained an enhanced affinity towards cells, possibly due to the reduced repulsion between DNA and the cell membrane. To better understand the condensation process, the components and zeta-potential of the PEGylated materials need to be examined. Labelling with functionalities other than fluorescent dyes is also awaited to be explored.

In Chapter 4, DNA nanocarrier system was designed for real-time detection of mRNA in living cells. The DNA rings were synthesised using non-templated CuAAC, and the cyclisation efficiency reduced as the ring size increased. The hybridisation between the DNARs and signal strands was evaluated by UV-vis and native PAGE, showing that the loading of signal strands on DNARs could be controlled stoichiometrically, and the hybridisation between them was thermally stable for in cells and *in vivo* applications. DNARs with quencher BHQ1 were then prepared using the same condition, and the cyclic DNAs were obtained and purified successfully. These DNARs were hybridised with fluorophore-functionalised signal strands, and the quenching of the fluorophores upon hybridisation was studied by native PAGE and fluorescence reading. It showed that the fluorophore was quenched when duplexes were formed between the DNARs and the signal strands. When heated up, the fluorescence was restored as the two strands

separated. However, the quenching efficiency was not comparable to other existing detecting systems, such as molecular beacons. It was possibly due to the insufficient binding between the DNAR and the signal strand. Also, hybridisation in different solutions showed that the formation of the G-quadruplex was essential for fluorescence restoration, as mobile guanines also quenched the fluorophore.

The binding of the DNAR nanocarrier complexes to cells was evaluated. The complexes carrying multiple aptamer-functionalised signal strands showed an enhanced binding towards the target cells due to their multivalency. However, the internalisation of the complexes was found to be inefficient, which hindered their recognition of the subcellular mRNA. The internalisation was improved by CPP ppTG21. However, aggregations occurred, which induced a significant background signal. When the quenched complex was transfected using lipid, no evident fluorescence recovery was observed. To address the problems observed, it is required to use a housekeeping gene as a control. Furthermore, the internalisation of the complex needs to be improved by covalently modifying the complex with moieties such as CPP or by combining the complex with polymers such as PEG, which we found to promote cellular uptake.

Chapter 6. Experimental

6.1 General information

Reagents

Reagents were purchased from Sigma-Aldrich, Alfa Aesar and Fisher Scientific unless otherwise specified and were used without further purification.

Cell culturing

SKBR-3 (HER2+, human breast cancer) cell line was purchased from American Type Cell Culture (ATCC, USA). MDA-MB-468 (HER2-, human breast cancer), MCF-7 (HER2-, human breast cancer) and MDA-MB-231(HER2-, human breast cancer) cell lines were kindly provided by Prof. Robert Carlisle (The Institute of Biomedical Engineering, University of Oxford). All cell culture reagents, including medium, Dulbecco's Phosphate Buffered Saline (DPBS), fetal bovine serum (FBS) and trypsin, were purchased from Gibco.

Oligonucleotides

Oligonucleotides were synthesised by ATDBio or in the Brown group by Dr Afaf El-Sagheer. Oligonucleotides from ATDBio were used as received. In Tom Brown group, oligonucleotides were synthesised and purified as described in section 1.1.3.

T4 DNA ligase was purchased from Promega. NxGen Φ-29 DNA polymerase was purchased from Lucigen. Bst 2.0 DNA polymerase, deoxynucleotides (dNTPs) solution mix and Quick-Load® Purple 1 kb DNA ladder were purchased from New England Biolabs (UK).

NMR spectra were recorded on a Bruker AVIIIHD 400 spectrometer. Chemical shifts are given in ppm, and *J* coupling values are quoted in Hz. ^{1}H NMR spectra were internally referenced to the appropriate undeuterated solvent signal; ^{13}C NMR spectra were internally referenced to the appropriate undeuterated solvent signal.

Low-resolution mass spectra (LR-MS) were recorded using electrospray ionisation (ESI) on a Micromass platform 1 spectrometer in HPLC acetonitrile or methanol. Electrospray mass spectra of deoxynucleoside triphosphates were recorded in deionised water on a Bruker microTOF instrument in ES^- mode.

RP-HPLC column used for oligo purification is Phenomenex column Gemini-NX 10μm C18 110A AXIA, 250 × 21.2 mm.

General buffers

Buffer type	Components and pH
Ion exchange buffer 10X stock	1 M Triethylamine bicarbonate (TEAB) buffer stock: 1 M triethylamine, pH 7.5-8.0 at 25 °C; pH adjusted by bubbling with CO_2.
Ion exchange buffer A	10 mM triethylamine buffer, pH 7.5-8.0
Ion exchange buffer B	1 M triethylamine buffer, pH 7.5-8.0
RP-HPLC Buffer A	0.1 M triethylamine buffer, pH 7.5-8.0 at 25 °C
RP-HPLC Buffer B	0.1 M triethylamine buffer with 50% acetonitrile, pH 7.5-8.0 at 25 °C
Tris-borate-EDTA (TBE) buffer	89 mM Tris, 89 mM boric acid, 2 mM EDTA, pH 8.0 at 25 °C
PBS buffer	10 mM PO_4^{3-}, 137 mM NaCl, 2.7 mM KCl, pH 7.4 at 25 °C
Bicarbonate labelling buffer	0.5 M $NaHCO_3$, pH 8.5
HEPES labelling buffer	10 mM HEPES, pH 8.0, 10 mM MgSO4, 50% v/v DMSO
10× phi29 DNA Polymerase Reaction Buffer	500 mM Tris-HCl, 100 mM $MgCl_2$, 100 mM $(NH_4)_2SO_4$, 40 mM DTT, pH 7.5 at 25 °C
10× T4 DNA Ligase Reaction Buffer	500 mM Tris-HCl, 100 mM $MgCl_2$, 10 mM ATP, 100 mM DTT, pH 7.5 at 25 °C
10× Isothermal Amplification Buffer	200 mM Tris-HCl, 100 mM $(NH_4)_2SO_4$, 500 mM KCl, 20 mM $MgSO_4$, 1% Tween® 20, pH 8.8 at 25 °C
10× Potassium phosphate buffer	100 mM $PO4^{3-}$, 1 M potassium chloride (1 M), pH 7.2
Cell binding buffer	1% BSA (w/v) in DPBS
2× SDS-PAGE loading buffer	125 mM Tris-HCl pH 6.8, 30% glycerol, 2% SDS (w/v), 5% β-mercaptoethanol (v/v), 0.03% bromophenol blue (w/v)

6.2 DNA oligonucleotides synthesis

Standard DNA phosphoramidites, solid supports and all reagents were purchased from Link Technologies, Glen Research and Applied Biosystems Ltd. DNA oligonucleotides

were synthesised using an Applied Biosystems 394 automated DNA/RNA synthesiser with a standard 1.0 μmol scale phosphoramidite cycle of acid-catalysed detritylation, coupling, capping and iodine oxidation. Unless otherwise stated, the syntheses were performed using 1000 Å controlled pore glass (CPG) solid supports with a particle size of 110 μm and nucleoside loading of 25 - 40 μm/g, purchased from Link technologies. Except where stated, standard β-cyanoethyl phosphoramidite monomers (benzoyl-dA, isobutylryl-dG, benzoyl-dC and dT) were used throughout. β-cyanoethyl phosphoramidite monomers were dissolved in anhydrous acetonitrile to a concentration of 0.1 M immediately prior to use. The coupling time for standard A, G, C and T monomers was 60 s. The stepwise coupling efficiencies and overall yields were monitored by an automated trityl cation conductivity monitoring facility and in all cases, were higher than 98%. The cleavage from the solid support and the deprotection of oligonucleotides was achieved by exposing to concentrated aqueous ammonia solution at room temperature for 1 h followed by heating in a sealed glass vial at 55 ˚C for 5 h. The ammonia was evaporated, and the oligonucleotides were redissolved in deionised water for HPLC purification.

Synthesis of 5′-phosphate oligonucleotides

Terminal 5′ phosphate modifications were added using a commercially available 2-[2-(4,4-dimethoxytrityloxy)ethylsulfonyl]ethyl-(2-cyanoethyl)-(N,N-diisopropyl)-

phosphoramidite, purchased from Link technologies, using an extended coupling time of 600 seconds. The oligonucleotides were cleaved from the solid support, deprotected and purified as described above.

Synthesis of 5′-amino-3′-phosphate oligonucleotides

Oligonucleotides were synthesised on commercially available, pre-packed 3′ phosphate SynBaseTM CPG 1000/110 columns, purchased from Link technologies. The terminal 5′ amino dT modification was added using the commercially available phosphoramidite monomer 5′-monomethoxytritylamino-2′-deoxythymidine,3′-[(2-cyanoethyl)-(N, N-diisopropyl)]-phosphoramidite, purchased from Glen research, using an extended coupling time of 600 seconds. During the addition of the final 5′ amino dT nucleotide, the acetic anhydride capping step was omitted from the synthesis cycle in order to avoid acetylation of the amino group. The oligonucleotide was cleaved from the solid support, deprotected and purified according to the general procedure described above.

Synthesis of 3′-alkyne-5′-azide oligonucleotides.

5′-*O*-(4,4′-Dimethoxytrityl)-3′-*O*-propargyl- deoxycytidine or 5′-*O*-(4,4′-dimethoxytrityl)-3′-*O*-propargyl-5-methyldeoxycytidine on polystyrene solid support, prepared as described above, was packed into a twist column (Glen Research) and used

to synthesise the required sequences in the 3′- to 5′-direction (standard phosphoramidite oligonucleotide synthesis) with 5′-iodo-dT as the final nucleotide. The 5′-iodo-dT modification was introduced either using a commercially available 5′-iodo-2′-deoxythymidine, 3′-[(2-cyanoethyl) -(N,Ndiisopropyl)]-phosphoramidite, purchased from Glen research or through converting 5′-hydroxyl to 5′-iodo. For conversion of 5′-hydroxyl to 5′-iodo, a solution of methyltriphenoxyphosphonium iodide ($[MeP(OPh)3]^{+}I^{-}$，0.5 M) in dry DMF (1 mL) was prepared. Two 1 mL syringes were used to periodically pass 2 mL of the reagent solution through the oligonucleotide synthesis column over 30 min at RT. The column was then washed with dry DMF (5 × 1 mL) using new syringes. Then sodium azide (20 mg) was suspended in dry DMF (1 mL) in a glass vial and heated at 70 °C for 20 min with the lid loosely closed, followed by cooling down to RT. Another two 1 mL syringes were used to take up and pass the solution back and forth through the column. Then the column with the solution was incubated at 55 °C for 5 h. Next, the column was washed with DMF (5 × 1 mL) followed by acetonitrile (5 × 1 mL) and dried by blowing a stream of argon gas. The resultant 5′-azide oligonucleotide was cleaved from the solid support, deprotected and purified as described above.

6.3 RNA oligonucleotides synthesis

RNA oligonucleotides were synthesised on an Applied Biosystems 394 automated

DNA/RNA synthesiser using a standard 0.2 μmol or 1.0 μmol RNA phosphoramidite cycle of acid-catalysed detritylation, coupling, capping and iodine oxidation. The building blocks for RNA analogues were prepared using 2′-O-tert-butyldimethylsilyl (TBDMS) protected RNA phosphoramidite monomers with t-butylphenoxyacetyl protection of the A, C and G nucleobases and unprotected U. A solution of 0.3 benzylthiotetrazole in acetonitrile (Link Technologies) was used as the coupling agent, t-butylphenoxyacetic anhydride as the capping agent and 0.1 M iodine as the oxidising agent. All phosphoramidite monomers were dissolved in anhydrous acetonitrile to a concentration of 0.1 M immediately prior to use, and the coupling time for all monomers was 6 min. Stepwise coupling efficiencies and overall yields were monitored using the instrument's in-built automated trityl cation conductivity measurement facility, and in all cases, were >97%. Cleavage of oligonucleotides from the solid support was performed by exposure to 3:1 (v/v) concentrated aqueous ammonia: ethanol solution and heated at 55 °C for 2-4 h in a sealed glass vial. Most of the liquid was then evaporated. Any residual RNA was collected with acetonitrile, and then the RNA was lyophilised.

To deprotect, the dry RNA was dissolved in DMSO (300 μL) and triethylamine trihydrofluoride (300 μL) and incubated for 2.5 h at 65 °C. Then butanol precipitation was performed by adding sodium acetate (3 M, 50 μL) and butanol (3 mL). After

vortexing, the mixed solution was kept at -80 °C for at least 1 h, before being centrifuged for 30 min at 4 °C and 8500 rpm. The supernatant was discarded, and the RNA precipitate was washed twice with cold ethanol followed by freeze-drying prior to further purification.

6.4 Characterisation and purification of oligonucleotides

Reversed-phase high-performance liquid chromatography (RP-HPLC) purification

The purification of fully deprotected oligonucleotides was carried out by RP-HPLC on a Gibson system using a Luna 10 µm C8 100 Å pore Phenomenex 10 x 250 mm column with a gradient of acetonitrile in TEAB buffer (Buffer A: 0.1 M TEAB, buffer B: 0.1 M TEAB/ 50% MeCN) over 20 min with a flow of 4 mL/min. The elution of oligonucleotides was monitored by UV absorption at 298 nm. Collected fractions were freeze-dried and then re-dissolved in MilliQ water without further de-salting.

Denaturing polyacrylamide gel electrophoresis (PAGE)

Denaturing polyacrylamide gels were prepared by mixing acrylamide, urea, APS, TEMED in TBE buffer, and cast using an SE400 vertical slab gel electrophoresis unit from Hoefer Inc. (1.5 mm depth × 18 cm width × 24 cm height).

Prior to loading, the gels were pre-run for at least 30 min at constant power (20 W) using a PowerPac power supply (BioRad) with 1x TBE buffer, and the sample was mixed with an equal volume of formamide and denatured by heating to 95 ˚C for 5 min. The gels were then run in 1 × TBE buffer at 20 W for approximately 2 hr. Xylene cyanol and bromophenol blue were loaded as dye markers. The gels were then visualised using a UV transilluminator (GBOX SYNGENE).

The bands of interest were excised with a clean razor blade, crushed and transferred into a 15 mL falcon tube. Water (10 mL) was added and the mixture was incubated at 37 ˚C, 900 rpm for over 14 h. Then oligonucleotides were desalted using NAP - 25 and NAP - 10 columns (GE Healthcare) according to the manufacturer's protocol.

Native PAGE

Native polyacrylamide gels were prepared by mixing acrylamide, APS, TEMED in TBE buffer, and cast using an SE400 vertical slab gel electrophoresis unit from Hoefer Inc. (1.5 mm depth × 18 cm width × 24 cm height).

Prior to loading, the gels were pre-run for at least 1 hr at constant voltage (120 V) using a PowerPac power supply (BioRad) with 1x TBE buffer. The samples were mixed with 10% glycerol solution and added to samples before loading. Xylene cyanol and bromophenol blue were loaded as dye markers. The gels were run at 120 V for

approximately 12 h at 4 ˚C and visualised using a UV transilluminator (GBOX SYNGENE).

Agarose gel electrophoresis

For 0.8% agarose gel, 0.4 g of agarose was mixed with 50 mL 1× TBE buffer and the mixture was heated by microwave for 2 min until agarose fully dissolved. To stain the gel, 2.5 μL of SYBR gold was added before the gel was allowed to solidify. Before loading to the gel, all samples were mixed with 5× Green GoTaq® reaction buffer according to the commercial protocol. Gels were run in 1× TBE buffer at RT, using 130 V for 50 min. The gels were visualised using a UV transilluminator (GBOX SYNGENE).

Oligonucleotide mass spectrometry (MS)

Mass spectrometry samples of oligonucleotides were prepared as 20 μM solutions in deionised water and analysed by UPLC-mass spectrometry using a Waters XEVO G2-QTOF mass spectrometer (ESI negative mode) equipped with an Ethylene Bridged Hybrid (BEH) C18 column (130 Å pore, particle size 1.7 μm, 2.1 mm × 50 mm; Waters). A gradient of methanol in TEA and hexafluoroisopropanol (HFIP) was used (buffer A: 8.6 mM TEA, 200 mM HFIP in 5% methanol/water (v/v); buffer B: buffer A in 80% methanol): 0 to 70% buffer B over 8 minutes at a flow rate of 0.2 mL/min. Raw data

were deconvoluted using Waters MassLynx software.

Oligonucleotide quantification

The concentration of oligonucleotides was determined by measuring absorbance at 260 nm with a Varian Cary 50 Bio UV-Vis spectrophotometer (Agilent) in deionised water at RT, using the Beer-Lambert equation, c (concentration) = $A\varepsilon l$ (A = absorbance in OD, c = concentration, ε = molar extinction coefficient, l = cuvette length). The molar extinction coefficient was determined using the nearest neighbour method.

6.5 Preparation of cyclic DNA

Preparation of the cyclic oligonucleotide using T4 DNA ligase

The 5′-phosphorylated linear oligonucleotide (template **1**, **2** and **3**, Chapter **2**, Table **2.1**, 2.4 nmol) and the templating splint oligonucleotide (splint **1**, **2** and **3**, Chapter **2**, Table **2.1**, 4.8 nmol) were annealed in 3.9 mL of 1× T4 DNA ligase buffer (30 mM Tris-HCl, pH 7.8 at 25 °C, 10 mM $MgCl_2$, 10 mM DTT, and 1 mM ATP) by heating to 95 °C for 5 min before cooling to 25°C at a rate of 0.5°C/min. T4 DNA ligase (100 μL, 3U/μL) was added, and the solution was incubated at 25°C for overnight. The enzyme was denatured by heating to 95 °C for 5 minutes. The volume of the reaction mixture was reduced to 1 mL using a CentriVap centrifugal concentrator at 55 °C, and the cyclised oligonucleotides were purified by denaturing PAGE gel with appropriate

percentage (template **1**: 8%; template **2**: 15%; template **3**: 12%) as described above.

Preparation of the cyclic oligonucleotide using copper click

- **Preparation of Cu(I) click catalyst solution**

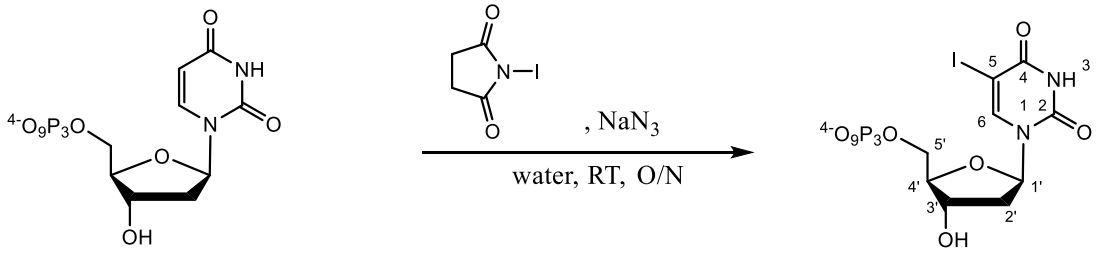
To prepare the catalyst solution for Cu(I) click, THPTA (3.6 mg) was dissolved into a solution of sodium ascorbate (12 μmol in MilliQ water, 24 μL). The solution was then degassed by bubbling with argon gas for 5 min. CuSO4 solution (1.2 μmol in MilliQ water, 12 μL) was added to the solution, and the mixture was degassed for another 5 min.

- **Preparation of the cyclic oligonucleotides through CuAAC click ligation**

Cu(I) click catalyst solution (36 μL, prepared as described above) was added to 2.364 mL of the linear 5′-azide-3′-propargyl oligonucleotide (linear DNAR**1-7**, Chapter **4**, Table **4.1**, 12 nmol in 0.2 M NaCl(aq)). The reaction mixture was kept at 25° for 2.5 h, and the reagents were removed by two NAP-25 columns. The volume of the reaction mixture was reduced to 1 mL using a CentriVap centrifugal concentrator at 55 °C, and the cyclised DNA products were analysed and purified by denaturing PAGE gel with appropriate percentage (DNAR**1**: 15% PAGE; DNAR**2**: 20% PAGE; DNAR**3**: 15% PAGE; DNAR**4**: 15% PAGE; DNAR**5**: 12% PAGE; DNAR**6**: 12% PAGE; DNAR**7**: 12% PAGE) as described above.

6.6 Chemical synthesis

5-iodo-2′-deoxyuridine-5′-O-triphosphate



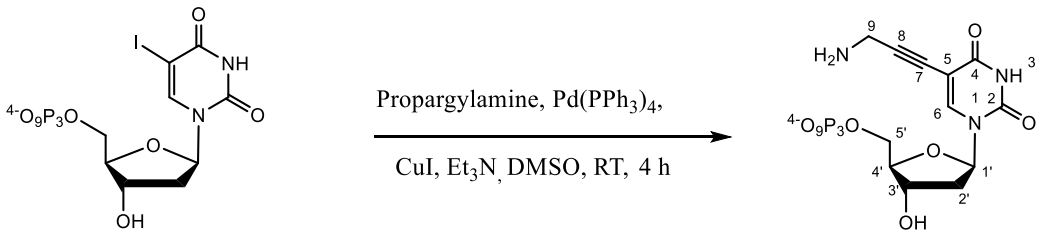
1 **2**

2′-Deoxyuridine-5′-triphosphate (99.4 mg, 0.21 mmol, 1 eq), sodium azide (68.25 mg, 1.06 mmol, 5 eq) and N-iodosuccinimide (144 mg, 0.64 mmol, 3eq) were dissolved in water (2 mL) in a 15 mL falcon tube and then incubated at room temperature, with shaking (500 rpm), O/N. Then the mixture was filtered through a syringe filter and diluted to 10 mL. The pH was adjusted with 0.1 M acetic acid to 6.5, and the solvent was removed in vacuo. The crude was re-dissolved in water and purified on a DEAE Sepharose column using a gradient of 0-80% ion-exchange buffer B in ion-exchange buffer A over 45 min. After lyophilisation, yellow solid was obtained (46.2 mg), with a yield of 44%.

^{1}H NMR (D_2O, 400 MHz) δ 8.24 (s, 1H, H-6), 6.36 – 6.11 (m, 1H, H-1′), 4.79 (s, 3H, D2O), 4.66 – 4.59 (m, 1H, H-3′), 4.23 – 4.11 (m, 3H, H-4′, 5′), 3.17 (q, J = 7.3 Hz, 26H, TEA), 2.35 (dd, J = 6.9, 4.9 Hz, 2H, H-2′), 1.25 (t, J = 7.3 Hz, 43H, TEA).

MS (m/z): 592[M-H]$^-$

5-(3-propargylamino)-2′-dexoyuridine-5′-O-triphosphate (NH_2-dUTP (3))



2 **3**

To a stirred solution of 5-iodo-2′-deoxyuridine-5′-triphosphate (5.1 mg, 8.6 µmol, 1.0 eq) in dry DMF (300 µL), palladium tetrakis triphenylphosphine (4.0 mg, 3.44 µmol, 0.4 eq), copper iodide (1.3 mg, 6.9 µmol, 0.8 eq), propargylamine (1.1 µL, 17.2 µmol, 2.0 eq), and triethylamine (3.6 µL, 25.8 µmol, 3.0 eq) were added and the reaction mixture was stirred under argon at room temperature O/N. The reaction was quenched by adding 2 mL of water, and the resulting mixture was filtered. The solvent was removed *in vacuo,* and the crude product was re-dissolved in 2 mL of water. The mixture was eluted on a DEAE Sepharose column using a gradient of 0-80% ion-exchange buffer B in ion-exchange buffer A over 45 min, and the fractions containing the product were pooled and lyophilised, followed by NaCl/EtOH precipitation. After precipitation, solid in pale yellow (1.34 mg) was obtained, with a yield of 30%.

^{1}H NMR (D_2O, 400 MHz) δ 8.45 (s, 1H, H-6), 6.27 (t, J = 6.0 Hz, 1H, H-1′), 4.65 (m,

1H, H-3′), 4.27–4.15 (m, 3H, H-4′, H-5′), 3.96 (s, 2H, H-9) 2.47-2.34 (m, 2H, H-2′); ^{31}P NMR (D_2O, 162 MHz) δ –6.40 (d, J = 21.0 Hz, 1P), –11.28 (d, J = 19.4 Hz, 1P), –22.23 (t, J = 19.8 Hz, 1P);

MS (m/z): 520[M-H]$^-$

5-(3-(6-azidohexanamido)prop-1-yn-1-yl)-2′-deoxyuridine-5′-O-triphosphate (AHP-dUTP (5))

To a stirred solution of NH_2-dUTP (3) (4.7 mg, 9.0 μmol, 1.0 eq) in in 1 M triethylammonium bicarbonate buffer (TEAB, 300 μL, pH 7.5) was added 6-azidohexonic acid NHS ester (5.8 mg, 23 μmol, 2.6 eq) in DMF (300 μL). The mixture was stirred at 55 ºC for 4 h and the solvent was removed *in vacuo.* The mixture was eluted by RP-HPLC (Column Gemini-NX 10u C18 110A AXIA, 250 × 21.2 mm) using a gradient of 15-60% RP-HPLC buffer B in RP-HPLC buffer A over 50 min, and the fractions containing the product were pooled and lyophilised, followed by NaCl/EtOH precipitation. AHP-dUTP (4.5mg, 6.9 μmol) was obtained in 77% yield.

^{1}H NMR (D_2O, 500 MHz,) δ 8.08 (s, 1 H, H-6), 6.24 (t, J = 6.6 Hz, 1 H, H-1′), 4.66 – 4.57 (m, 1 H, H-3′), 4.28 – 4.10 (m, 5 H, H-4′, H-5′, H-9), 3.26 (t, J = 6.9 Hz, 2 H, H-16), 3.15 (q, J = 7.3 Hz, $Et_2N^+C\boldsymbol{H}_2CH_3$), 2.39 – 2.29 (m, 2 H, H-2′), 2.26 (t, J = 7.3 Hz, 2 H, H-12), 1.65 – 1.49 (m, 4 H, H-13, H-15), 1.34 (tt, J = 9.1, 6.3 Hz, 2 H, H-14), 1.23 (t, J = 7.3 Hz, $Et_2N^+CH_2C\boldsymbol{H}_3$)

^{31}P NMR (D_2O, 202 MHz) δ -5.2 (d, *J* = 20 Hz, 1P), -10.1 (d, *J* = 20 Hz, 1P), -21.3 (app t, *J* = 20 Hz, 1P)

MS (m/z): 659.06$[M-H]^+$

NaCl/EtOH precipitation of triphosphates

To triphosphate water solution, NaCl (1 volume, 3M) solution was first added, followed with EtOH (9 volumes). The mixture was vortexed and stored at -80 ˚C for 1 h and centrifuged at 4000 rmp for 30 min. Supernatant was removed and the product was air dried.

6.7 Protocols for RCA

General protocols for RCA

For 20 mL reaction, a 10 mL solution containing cyclised template (6 pmol), splint (12 pmol), 2 mL of 10× NexGen phi29 reaction buffer (as supplied, 500 mM Tris-HCl, 100 mM $(NH_4)_2SO_4$, 40 mM DTT, 100 mM $MgCl_2$, pH 7.5 at 25°C) and $MgSO_4$ (1 mL, 100 mM) in MilliQ water was heated to 95 °C for 5 min before cooling to 25 °C at a rate of 0.5 °C/min. The dNTP mix (5 mL, 10 mM) was added to this solution, followed by phi29 (1 mL, 10 000 U/mL) and 4 mL of MilliQ water. The sample was incubated

at 30 °C for 20 h using a Bio-Rad T100TM thermocycler. The enzyme was then inactivated by heating the samples at 65 °C for 10 min before cooling to 4 °C.

After the RCA step, the samples were diluted with MilliQ water (280 mL). The DNFs were collected by centrifugation and the supernatant discarded. To remove the unencapsulated DNA, the resulting pellet was resuspended in MilliQ water (750 mL) and collected by centrifugation. The process was repeated 4 times, and the pellet was resuspended in 20 mL MilliQ water.

Preparation of functionalised DNFs

Functionalised DNFs were synthesised following the general RCA procedure described above. The dNTP mix was prepared using 100 mM stock solutions of dATP, dTTP, dGTP, dCTP, and modified dN*TP to ensure the reaction concentration of each triphosphate was 2 mM. For example, to prepare DNFs with 0-100% modified dUTP, the concentrations of dN*TP and dTTP added are:

% dUTP	Conc. of dN*TP	Conc. of dTTP/ mM
0%	0 mM	2 mM
25%	0.5 mM	1.5 mM
50%	1 mM	1 mM
75%	1.5 mM	0.5 mM
100%	2 mM	0 mM

Preparation of H_2N-DNFs using BSA

DNFs were prepared as described in section 6.5, including BSA (0.75 mg/mL) per 20 mL RCA volume.

6.8 Protocols for labelling

Strain promoted alkyne-azide cycloaddition (SPAAC) labelling of N_3-DNFs

DNFs were prepared using the appropriate N_3-dUTP as described in section 6.5. The DNFs were then suspended in 20 mL of labelling buffer (10 mM HEPES, pH 8.0, 10 mM $MgSO_4$, 50% v/v DMSO) containing 1 mM of bicyclo[6.1.0]nonyne (BCN)/dibenzocyclooctyne DBCO functionalised moiety and gently agitated at room temperature for 2 h. The DNFs were then collected by centrifugation and the supernatant discarded. Exceeded dye was removed by resuspending the pellet in 100 mL of labelling buffer, and the pellet was collected by centrifugation. The process was repeated twice with 50% v/v DMSO in MilliQ water and twice with MilliQ water. The resulting pellet was suspended in 20 mL MilliQ water.

Copper catalysed alkyne-azide cycloaddition (CuAAC) labelling of azide /alkyne functionalised DNFs

DNFs were prepared using the appropriate azide or alkyne dUTP as described in section 6.5. The DNFs were then suspended in 20 mL of labelling buffer (10 mM HEPES, pH 8.0, 10 mM $MgSO_4$, 50% v/v DMSO) containing 1 mM alkyne or azide

dye, 0.5 mM $CuSO_4$, 0.5 mM THPTA and 2.5 mM sodium ascorbate. The mixture was gently agitated at room temperature for 2 h. The DNFs were then collected by centrifugation and the supernatant discarded. Exceeded dye was removed by resuspending the pellet in 100 mL of labelling buffer, and the pellet was collected by centrifugation. The process was repeated twice with 50% v/v DMSO in MilliQ water and twice with MilliQ water. The resulting pellet was suspended in 20 mL MilliQ water.

N-Hydroxysuccinimide (NHS) ester labelling of H_2N-DNFs

DNFs were prepared using the appropriate amino dUTP as described in section 6.5. The DNFs were suspended in 20 mL of labelling buffer (10 mM HEPES, pH 8.0, 10 mM $MgSO_4$, 50% v/v DMSO) containing 1 mM of the NHS active ester was incubated at room temperature for 4 h with gentle agitation. The DNFs were then collected by centrifugation and the supernatant discarded. Exceeded dye was removed by resuspending the pellet in 100 mL of labelling buffer, and the pellet was collected by centrifugation. The process was repeated twice with 50% v/v DMSO in MilliQ water and twice with MilliQ water. The resulting pellet was suspended in 20 mL MilliQ water.

Dual labelling of DNFs using CuAAC and NHS active ester labelling

DNFs were prepared using the appropriate dN*TPs as described in section 6.5. The DNFs were then suspended in 20 mL of labelling buffer (10 mM HEPES, pH 8.0, 10

mM $MgSO_4$, 50% v/v DMSO) containing 1 mM alkyne or azide, 1 mM of NHS active ester, 0.5 mM $CuSO_4$, 0.5 mM THPTA and 2.5 mM NaAsc and the mixture was incubated at room temperature for 2 h with gentle agitation. The DNFs were then collected by centrifugation and the supernatant discarded. Exceeded dye was removed by resuspending the pellet in 100 mL of labelling buffer, and the pellet was collected by centrifugation. The process was repeated twice with 50% v/v DMSO in MilliQ water and twice with MilliQ water. The resulting pellet was suspended in 20 mL MilliQ water.

Dual labelling of DNFs using SPAAC and NHS active ester labelling

DNFs were prepared using the appropriate dN*TPs as described in section 6.5. The DNFs were then suspended in 20 mL of labelling buffer (10 mM HEPES, pH 8.0, 10 mM $MgSO_4$, 50% v/v DMSO) containing 2.5 mM of BCN/DBCO functionalised moiety and 1 mM of NHS active ester, and this was incubated at room temperature for 2 h with gentle agitation. The DNFs were then collected by centrifugation and the supernatant discarded. Exceeded dye was removed by resuspending the pellet in 100 mL of labelling buffer, and the pellet was collected by centrifugation. The process was repeated twice with 50% v/v DMSO in MilliQ water and twice with MilliQ water. The resulting pellet was suspended in 20 mL MilliQ water.

Labelling of phi29 and BSA with sulfoCy3-NHS

SulfoCy3-NHS (0.1 mg) in of DMF (25 mL) was added to phi29 (2 mL, 10 000 U/mL) or BSA (1.25 mL, 10 mg/mL) in protein labelling buffer (12.5 mL of 200 mM HEPES (pH 8.0), 1 mL of 1 M $MgSO_4$, 23 mL of MilliQ water) and the solution was incubated at 25 °C with agitation for 2 h. This was used for comparison without further purification.

6.9 Preparation of Con-DNFs

For 20 μL reaction, a 10 μL solution containing cyclised template **3** (6 pmol), splint **3** (12 pmol), 2 μL of 10× NexGen phi29 reaction buffer (as supplied, 500 mM Tris-HCl, 100 mM $(NH_4)_2SO_4$, 40 mM DTT, 100 mM $MgCl_2$, pH 7.5 at 25°C) and $MgSO_4$ (3 μL, 100 mM) in MilliQ water was heated to 95 °C for 5 min before cooling to 25 °C at a rate of 0.5 °C/min. To this solution was added the dNTP mix (0.4 μL of 100 mM dATP, 0.4 μL of 100 mM dGTP, 0.4 μL of 100 mM dCTP, 0.3 μL of 100 mM dTTP, 0.1 μL of 100 mM N_3-dUTP **1**) followed by phi29 (1 μL, 10 000 U/mL) and 7.4 μL of MilliQ water. The sample was incubated at 30 °C for 6 h using a Bio-Rad T100TM thermocycler. The enzyme was then inactivated by heating the samples at 65 °C for 10 min before cooling to 4 °C.

After the RCA step, the samples were diluted with MilliQ water (280 μL). The DNFs

were collected by centrifugation and the supernatant discarded. To remove the unencapsulated DNA, the resulting pellet was resuspended in MilliQ water (750 μL) and collected by centrifugation. The process was repeated 4 times, and the pellet was resuspended in 20 μL MilliQ water.

The DNFs were then suspended in 20 μL of labelling buffer (10 mM HEPES, pH 8.0, 10 mM $MgSO_4$, 50% v/v DMSO) containing 1 mM of FAM-BCN and gently agitated at room temperature for 2 h. The DNFs were then collected by centrifugation and the supernatant discarded. Exceeded dye was removed by resuspending the pellet in 100 μL of labelling buffer, and the pellet was collected by centrifugation. The process was repeated twice with 50% v/v DMSO in MilliQ water and twice with MilliQ water. The resulting pellet was suspended in 20 μL MilliQ water.

6.10 Preparation of Apt-DNFs

For 20 μL reaction, a 10 μL solution containing cyclised template **3** (6 pmol), splint **3** (12 pmol), 2 μL of 10× NexGen phi29 reaction buffer (as supplied, 500 mM Tris-HCl, 100 mM $(NH_4)_2SO_4$, 40 mM DTT, 100 mM $MgCl_2$, pH 7.5 at 25°C) and $MgSO_4$ (3 μL, 100 mM) in MilliQ water was heated to 95 °C for 5 min before cooling to 25 °C at a rate of 0.5 °C/min. To this solution was added the dNTP mix (0.4 μL of 100 mM dATP, 0.4 μL of 100 mM dGTP, 0.4 μL of 100 mM dCTP, 0.3 μL of 100 mM dTTP, 0.1 μL

of 100 mM N_3-dUTP **1**) followed by phi29 (1 μL, 10 000 U/mL) and 7.4 μL of MilliQ water. The sample was incubated at 30 °C for 6 h using a Bio-Rad T100TM thermocycler. The enzyme was then inactivated by heating the samples at 65 °C for 10 min before cooling to 4 °C.

After the RCA step, the samples were diluted with MilliQ water (280 μL). The DNFs were collected by centrifugation and the supernatant discarded. To remove the unencapsulated DNA, the resulting pellet was resuspended in MilliQ water (750 μL) and collected by centrifugation. The process was repeated 4 times, and the pellet was resuspended in 20 μL MilliQ water.

The DNFs were then suspended in 20 μL of labelling buffer (10 mM HEPES, pH 8.0, 10 mM $MgSO_4$, 50% v/v DMSO) containing 20 μM annealed 5'-alkyne-FAM-HER2 aptamer, 0.5 mM $CuSO_4$, 0.5 mM THPTA and 2.5 mM sodium ascorbate. The mixture was gently agitated at room temperature for 2 h. The DNFs were then collected by centrifugation and the supernatant discarded. Exceeded dye was removed by resuspending the pellet in 100 μL of labelling buffer, and the pellet was collected by centrifugation. The process was repeated twice with 50% v/v DMSO in MilliQ water and twice with MilliQ water. The resulting pellet was then treated with FAM-BCN to functionalise any remaining azides to improve the brightness of the DNFs.

6.11 Preparation of Tem-DNFs

For 20 μL reaction, a 10 μL solution containing cyclised template **2** (6 pmol), splint **2** (12 pmol), 2 μL of 10× NexGen phi29 reaction buffer (as supplied, 500 mM Tris-HCl, 100 mM $(NH_4)_2SO_4$, 40 mM DTT, 100 mM $MgCl_2$, pH 7.5 at 25°C) and $MgSO_4$ (3 μL, 100 mM) in MilliQ water was heated to 95 °C for 5 min before cooling to 25 °C at a rate of 0.5 °C/min. To this solution was added the dNTP mix (0.4 μL of 100 mM dATP, 0.4 μL of 100 mM dGTP, 0.4 μL of 100 mM dCTP, 0.3 μL of 100 mM dTTP, 0.1 μL of 100 mM N_3-dUTP **1**) followed by phi29 (1 μL, 10 000 U/mL) and 7.4 μL of MilliQ water. The sample was incubated at 30 °C for 6 h using a Bio-Rad T100TM thermocycler. The enzyme was then inactivated by heating the samples at 65 °C for 10 min before cooling to 4 °C.

After the RCA step, the samples were diluted with MilliQ water (280 μL). The DNFs were collected by centrifugation and the supernatant discarded. To remove the unencapsulated DNA, the resulting pellet was resuspended in MilliQ water (750 μL) and collected by centrifugation. The process was repeated 4 times, and the pellet was resuspended in 20 μL MilliQ water.

The DNFs were then suspended in 20 μL of labelling buffer (10 mM HEPES, pH 8.0, 10 mM $MgSO_4$, 50% v/v DMSO) containing 1 mM of FAM-BCN and gently agitated

at room temperature for 2 h. The DNFs were then collected by centrifugation and the supernatant discarded. Exceeded dye was removed by resuspending the pellet in 100 μL of labelling buffer, and the pellet was collected by centrifugation. The process was repeated twice with 50% v/v DMSO in MilliQ water and twice with MilliQ water. The resulting pellet was suspended in 20 μL MilliQ water.

6.12 Preparation of Pept-DNFs

For 20 μL reaction, a 10 μL solution containing cyclised template **3** (6 pmol), splint **3** (12 pmol), 2 μL of 10× NexGen phi29 reaction buffer (as supplied, 500 mM Tris-HCl, 100 mM $(NH_4)_2SO_4$, 40 mM DTT, 100 mM $MgCl_2$, pH 7.5 at 25°C) and $MgSO_4$ (3 μL, 100 mM) in MilliQ water was heated to 95 °C for 5 min before cooling to 25 °C at a rate of 0.5 °C/min. To this solution was added the dNTP mix (0.4 μL of 100 mM dATP, 0.4 μL of 100 mM dGTP, 0.4 μL of 100 mM dCTP, 0.3 μL of 100 mM dTTP, 0.1 μL of 100 mM Et-dUTP **2**) followed by phi29 (1 μL, 10 000 U/mL) and 7.4 μL of MilliQ water. The sample was incubated at 30 °C for 6 h using a Bio-Rad T100TM thermocycler. The enzyme was then inactivated by heating the samples at 65 °C for 10 min before cooling to 4 °C.

After the RCA step, the samples were diluted with MilliQ water (280 μL). The DNFs were collected by centrifugation and the supernatant discarded. To remove the

unencapsulated DNA, the resulting pellet was resuspended in MilliQ water (750 μL) and collected by centrifugation. The process was repeated 4 times, and the pellet was resuspended in 20 μL MilliQ water.

The DNFs were then suspended in 20 μL of labelling buffer (10 mM HEPES, pH 8.0, 10 mM $MgSO_4$, 50% v/v DMSO) containing 20 μM of FAM-labelled peptide 2 and gently agitated at room temperature for 2 h. The DNFs were then collected by centrifugation and the supernatant discarded. Exceeded dye was removed by resuspending the pellet in 100 μL of labelling buffer, and the pellet was collected by centrifugation. The process was repeated twice with 50% v/v DMSO in MilliQ water and twice with MilliQ water. The resulting pellets were then treated with FAM-azide to functionalise any remaining alkynes to improve the brightness of the DNFs.

6.13 Characterisation of DNFs

Scanning electron microscopy (SEM)

Scanning electron microscopy (SEM) analysis was performed using a Zeiss Sigma 300 Field Emission Gun Scanning Electron Microscope (FEG-SEM). DNFs were suspended in MilliQ water, and 10 μL of the suspension was added onto a silicon wafer chip which was dried at 50 °C for 15 min. Samples were sputter-coated with gold before imaging.

Fluorescence microscopy

Fluorescence microscopy was performed using an API DeltaVision Core Widefield Microscope. For FAM-labelled DNFs, FITC channel (l_{Ex} = 455 nm, bandwidth = 28nm; l_{Em} = 525 nm, bandwidth = 48) was used while for TAMRA/Cy3-labelled DNFs TRITC channel (l_{Ex} = 542 nm, bandwidth 27; l_{Em} = 597 nm, bandwidth = 45) was used. Before imaging, samples were prepared by loading a suspension of DNFs in MilliQ water into a glass haemocytometer.

Evaluating the ability of phi29 to incorporate modified dNTPs

RCA reactions were performed as described above in the general RCA procedure. The resultant mixtures (for 20 mL reaction) were diluted with 80 mL of water (5 × dilutions) and then thoroughly suspended with a pipette. The precipitate was isolated by centrifugation (20 min, 17 G), and the supernatant was carefully transferred. The precipitate was then washed with MilliQ water (3 × 100 mL) and stored in 100 mL of 1 × TBE buffer overnight, which broke down the DNFs and released the DNA. To a 96-well plate (F-bottom, black, Fluotrac, med. Binding Greiner), 100 mL of 1 × TBE buffer containing 1 × SYBR Gold and 0.1% Triton X-100 was loaded, and to the solution, 5 mL of either the supernatant solution or the particle solution was added. The plate was loaded into a CLARIOstar microplate reader and incubated for 20 min with

intermittent shaking (300 rpm, 1 min, 5 times) before taking a reading (Excitation: 495-8 nm; Dichroic filter: 514.2 nm). All experiments were performed in triplicate.

Measuring the fluorescence as a factor of % dN*TP

Labelled DNFs (for 20 mL RCA reaction, stored in 20 mL of MilliQ water) were stored with the addition of 20 mL of 2 × TBE buffer overnight to break down the particles and release the DNA. To a 96-well plate (F-bottom, black, Fluotrac, med. Binding Greiner), 40 mL of 1 × TBE buffer containing 1 × SYBR Gold and 0.1% Triton X-100 was loaded, and to the solution, 10 mL of the particle solution was added. The plate was loaded into a CLARIOstar microplate reader and incubated for 20 min with intermittent shaking (300 rpm, 1 min, 5 times) before taking a reading. The settings used for the FAM labelling were: Excitation 483-14 nm, Emission: 530-30 nm; For TAMRA Excitation: 535-20 nm; Emission: 585-20 nm; and for Coumarin: Excitation: 404-15 nm, Emission: 477-20 nm. All experiments were performed in triplicate, and three independent readings were taken for each sample.

Absorbance and emission spectra

Labelled DNFs (for 20 mL RCA reaction, stored in 20 mL of MilliQ water) were stored with the addition of 20 mL of 2 × TBE buffer overnight to break down the particles and release the DNA. To a 96-well plate (F-bottom, black, Fluotrac, med. Binding

Greiner), 40 mL of 1 × TBE buffer containing 1 × SYBR Gold and 0.1% Triton X-100 was loaded, and to the solution, 10 mL of the particle solution was added. The plate was loaded into a CLARIOstar microplate reader and incubated for 20 min with intermittent shaking (300 rpm, 1 min, 5 times) before taking a reading. The fluorescence spectra were obtained by scanning excitation and emission wavelength. The parameters used were Excitation: scanned from 420 to 520 nm, with a bandwidth of 10.0 nm; Emission: scanned from 500 to 600 nm, with a bandwidth of 10.0 nm. All experiments were performed in triplicate, and three independent readings were taken for each sample.

Size measurement of DNFs using DLS

DLS measurements were carried out using a Viscotek 802 Dynamic Light Scattering Instrument in a 1 mL glass cuvette. DNF samples were diluted 10 times by water to a final volume of 1 mL and measured at 20 °C, 50% power over 10 min. Data were analysed using OmniSIZE software.

6.14 Thermal stability study of DNA nanocarrier complex using UV melting

UV melting measurements were carried out on a Varian Cary 4000 UV-VIS spectrophotometer fitted with a Cary temperature controller using a 1 cm path length

(Hellma Precision cuvettes made of synthetic quartz glass, QG). Oligonucleotides were prepared at 1 μM in 150 mM potassium phosphate buffer with 15 mM NaCl at pH 7.2. The experiments were conducted by melting and annealing the temperature between 30 °C and 75 °C at a rate of 0.2 °C/min, with absorbance monitored at a wavelength of 260 nm every 0.5 °C. The *Tm* of oligonucleotides was determined using Cary Win UV thermal application software, and the first derivative of absorption with respect to temperature (dA/dT) of the melting curve was generated and used to calculate the value of *Tm*. The experiment was performed in four steps. The thermal protocol used was as follows:

Step	Data Interval (°C)	Rate (°C/min)	End Temp(°C)	Hold Time (min)
Melt 1	0.50	0.20	75.00	5.00
Anneal 1	0.50	0.20	30.00	5.00
Melt 2	0.50	0.20	75.00	5.00
Anneal 2	0.50	0.20	30.00	5.00

Table 6.5. The thermal protocol used for UV melting studies.

Thermal stability study of DNA nanocarrier complex using CFX96™ Real-Time PCR Detection System (Bio-Rad)

Cyclic oligonucleotides were prepared at 0.4 μM concentration in 10 mL of

corresponding buffers, with various amounts of the signal strand, heated and annealed between 10°C and 95°C at a rate of 1 °C/min. The fluorescence change was monitored using a CFX96^{TM} Real-Time PCR Detection System (Bio-Rad) every minute over the period.

Strand displacement of the signal strand by survivin target strand using CFX96^{TM} Real-Time PCR Detection System (Bio-Rad)

Cyclic oligonucleotides were prepared at 0.4 μM concentration in 10 mL of corresponding buffers, with 1.2 μM signal strand and annealed from 95°C to 10°C at a rate of 1 °C/min. The survivin target strand was added to the mixture to a final concentration of 1.2 μM, and the fluorescence was monitored every 5 min at 37°C after the addition for 2 h.

Strand displacement of the signal strand by survivin target strand using Native PAGE

Cyclic oligonucleotides were prepared at 0.4 μM concentration in corresponding buffers, with 1.2 μM signal strand and annealed from 95°C to 10°C at a rate of 1 °C/min. Survivin target strand was added to a final concentration of 1.2 μM, and the mixture was incubated at 37°C for 10 min before loading on 6% native PAGE. The gels were

run at 120 V for approximately 12 h at 4 ˚C and visualised using a UV transilluminator (GBOX SYNGENE).

Investigating serum stability of cyclic DNAR5 and signal strand 2 by denaturing PAGE

Cyclic DNAR**5** and signal strand **2 (**500 pmol of each**)** were incubated in 200 mL cell culture medium substituted with 10% fetal bovine serum (FBS) for time courses of 1 h, 6h, 12 h and 24 h at 37 °C, before loading on an 8% denaturing PAGE. The gel was run at 120 V for approximately 12 h at 4 ˚C and visualised using a UV transilluminator (GBOX SYNGENE).

6.15 Cell binding experiments

Tumour cell lines and cultivation

SKBR-3 (HER2+, human breast cancer) cell line was maintained in McCoy′s 5A medium supplemented with 15% (v/v) FBS, whereas MDA-MB-468 (HER2-, human breast cancer), MCF-7 (HER2-, human breast cancer) and MDA-MB-231 (HER2-, human breast cancer) cell lines were maintained in Dulbecco′s Modified Eagle Medium (DMEM) supplemented with 10% (v/v) FBS. The cell lines were incubated at 37 °C under a humidified atmosphere of 5% CO2.

Freezing, thawing and long-term storage of cell lines

Cells were harvested with the trypsin-EDTA solution in DPBS buffer and resuspended in

freezing medium containing 90% FBS and 10% DMSO. The cell suspension was immediately transferred into 1 mL cryovials, gradually cooled to -80 °C at a rate of -1 °C/min using an isopropanol container overnight and then kept in a liquid nitrogen tank for long-term storage. From frozen stock, cryovials containing cells were rapidly thawed in a 37 °C water bath and then added into 9 mL of growth medium dropwise to reduce exposure to DMSO during the process of thawing. Then cells were collected by centrifugation (1000 RPM, 5 min, RT), and the supernatant was removed. The cell pellet collected was resuspended in 15 mL of fresh complete growth medium and ready for counting and further culturing.

Flow cytometry general method

Flow cytometry experiments were carried out using a BD FACS Calibur cytometer. Prior to the experiments, the cell lines were incubated to confluent and harvested by trypsin-EDTA dissociation solution, non-enzymatic dissociation solution or scraping, as demanded. The cells were then resuspended in binding buffer (1% BSA(w/v) in DPBS) to give the desired cell suspension density (10^5 cells/mL). The mixture was then

incubated at 37°C for 5 min for blocking. Tested samples were then added to the cells, gently vortexed, and incubated at 37°C for the desired period in the dark. After, the cells were collected by centrifugation (2500 rpm, 5 min, RT), washed with DPBS (5 × 500 μL), and resuspended in 500 μL of DBPS for measurement. The fluorescence intensity was measured by counting 10000 events, and data were analysed using Flowjo software. All experiments for the binding assay were repeated at least three times.

Flow cytometry for DNFs binding

Into a 12-well plate, cells were seeded at a density of 5×10^5 and left overnight to attach. Then the cells were washed with DPBS before being blocked by incubation in 460μL DPBS with 1% BSA (w/v) at 37 °C for 5 min. 40 μL of labelled RCA product was then added to the blocking buffer. The cells were then incubated with RCA product at 37 °C for 40 min with agitation. The cells were then rinsed 5 times with DPBS and scraped off gently using a cell scraper. The cells were then suspended in 500 μL of DPBS for flow cytometry analysis.

Confocal microscopy general method for cell binding with aptamers and aptamer-containing DNA nanocarrier complexes

Cells were seeded in 35 mm glass-bottom culture dishes (Greiner Bio-One) at a density

of 5×10^4 cells/well and incubated for 24 h. The cells were washed with pre-warmed DPBS, then blocked by 1% BSA(w/v) DPBS at 37 °C for 5 min. To the cells, tested samples (1 μM) were added, and the cells were incubated at 37 °C for 40 min. After incubation, the cells were washed three times with 500 μL of ice-cold DPBS to remove the unbound aptamer, followed by adding 500 μL of DPBS. The cells were imaged immediately with a Zeiss LSM 780 confocal microscope using a 63× oil objective. The images were obtained using ZEN 2.1 acquisition software.

CPP Mediated cellular uptake of DNA nanocarrier Complexes

DNA complex was incubated with 20X CPP for 5 min before dispensed to cells. Cells were seeded in 35 mm glass-bottom culture dishes (Greiner Bio-One) at a density of 5×10^4 cells/well and incubated for 24 h. The cells were washed with pre-warmed DPBS, then blocked by 1% BSA(w/v) DPBS at 37 °C for 5 min. To the cells, tested samples (1 μM) were added, and the cells were incubated at 37 °C for 40 min. After incubation, the cells were washed three times with 500 μL of ice-cold DPBS to remove the unbound aptamer, followed by adding 500 μL of DPBS. The cells were imaged immediately with a Zeiss LSM 780 confocal microscope using a 63× oil objective. The images were obtained using ZEN 2.1 acquisition software.

Lipid Transfection of DNA nanocarrier Complexes

Cells were seeded on 35 mm glass-bottom culture dishes at a density of 10^5 cells/well. After 24 h, the growth media was removed, and the colourless Opti-MEM™ media (100 μL, Thermo Fisher Scientific, cat. no. 11058021) was added. The transfection mixture was prepared with Lipofectamine™ 2000 Transfection Reagent (2 μL in 100 μL colourless Opti-MEM™ media) and the tested nanocarrier complex (10 pmol in 100 μL colourless Opti-MEM™ media), which was pre-incubated for 5 min at room temperature. The transfection mixture was then added to the cells. After 6 h at 37 °C, the media was replaced with growth media and the cells were allowed to grow for a further 12 h before confocal microscopy.

Confocal microscopy general method for transfected cells

Transfected cells were seeded in 35 mm glass-bottom culture dishes (Greiner Bio-One) and incubated for 12 h. The cells were washed three times with pre-warmed DPBS and were imaged with a Zeiss LSM 780 confocal microscope using a 63× oil objective.

Chapter 7. Appendix

Mass spectra analysis of oligonucleotides and nucleoside triphosphates used.

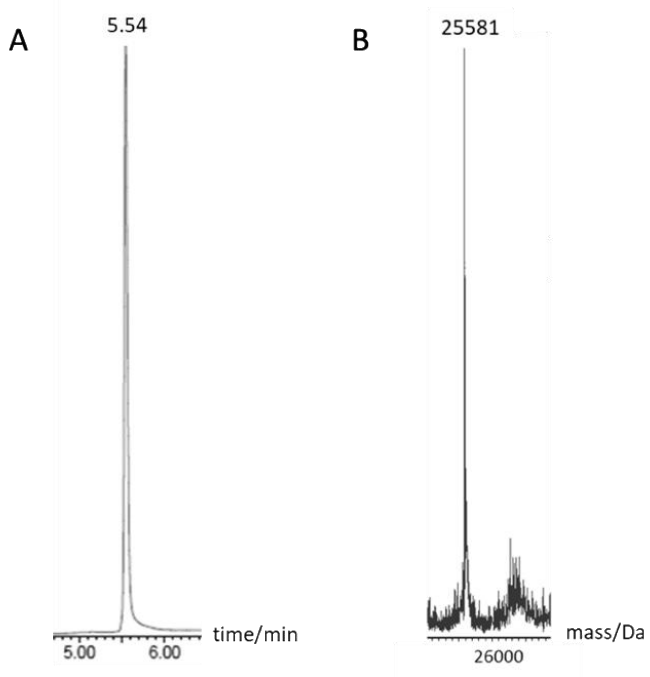


Figure 7.9. A. RP-UPLC (UV abs at 260 nm) and **B.** mass spectrum (ES^-) of cyclic template **1**, calculated 25579 Da, found 25581 Da.

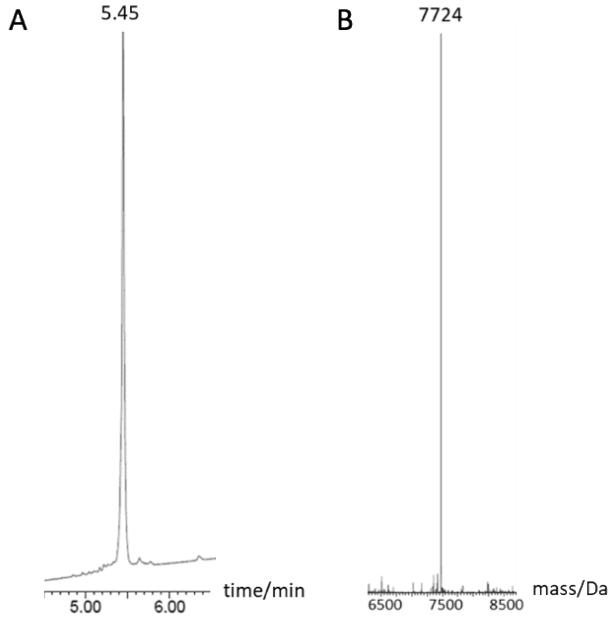


Figure 7.2. A. RP-UPLC (UV abs at 260 nm) and **B.** mass spectrum (ES^-) of splint 1, calculated 7724 Da, found 7724 Da.

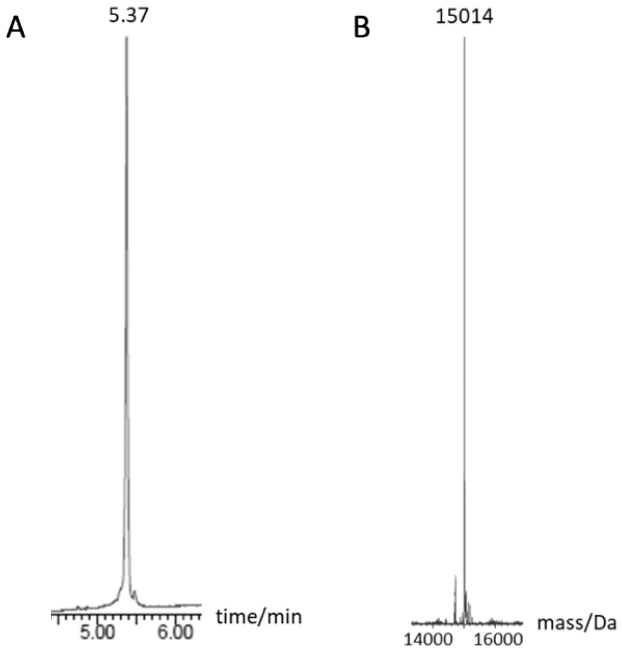


Figure 7.3. A. RP-UPLC (UV abs at 260 nm) and **B.** mass spectrum (ES^-) of template **2**, calculated 15012 Da, found 15014 Da.

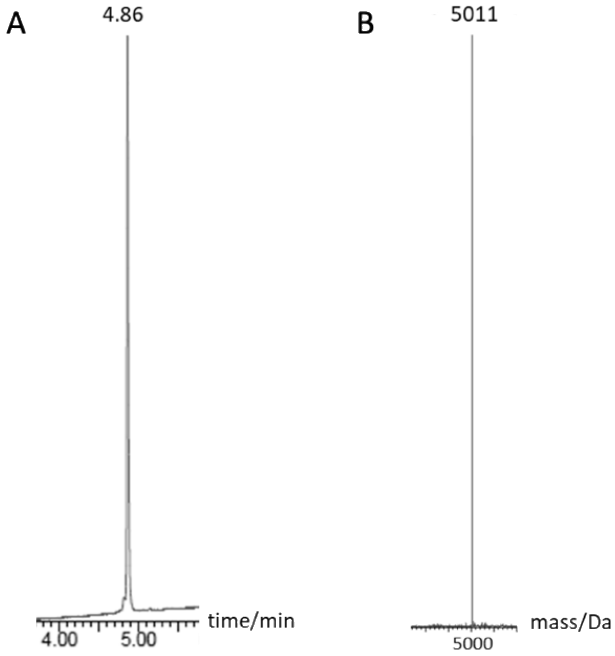


Figure 7.4. A. RP-UPLC (UV abs at 260 nm) and **B.** mass spectrum (ES^-) of splint **2**, calculated 5010 Da, found 5011 Da.

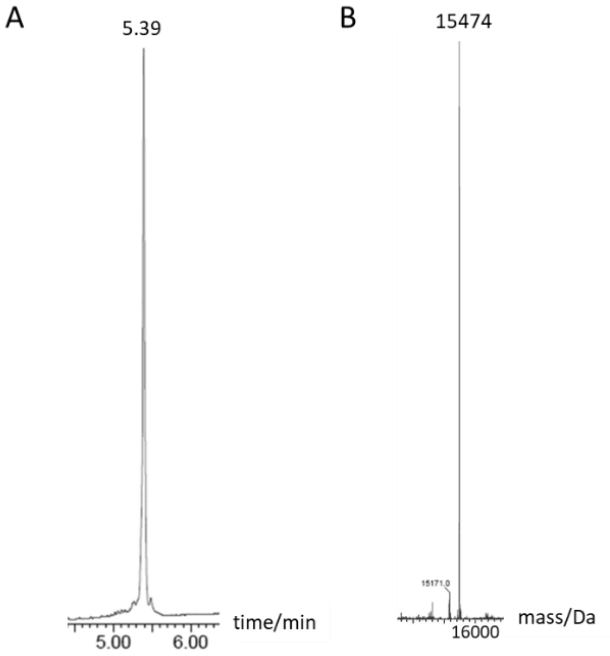


Figure 7.5. A. RP-UPLC (UV abs at 260 nm) and **B.** mass spectrum (ES-) of template 3, calculated 15473 Da, found 15474 Da.

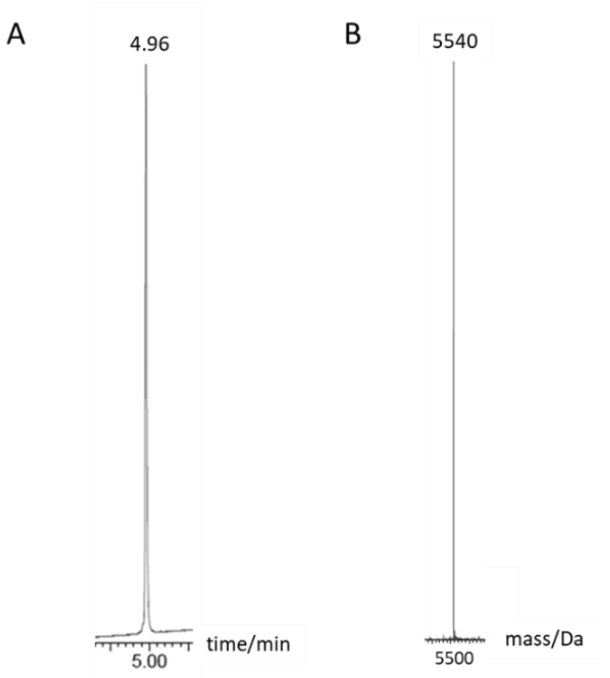


Figure 7.6. A. RP-UPLC (UV abs at 260 nm) and **B.** mass spectrum (ES-) of splint 3, calculated 5539 Da, found 5540 Da.

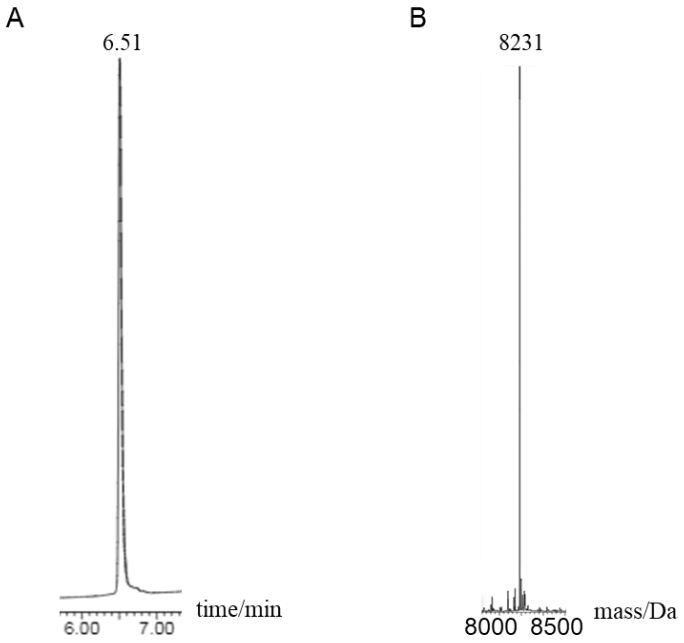


Figure 7.7. A. RP-UPLC (UV abs at 260 nm) and **B.** mass spectrum (ES-) of 5′-Cy3 anti-MUC1 aptamer, calculated 8231 Da, found 8231 Da.

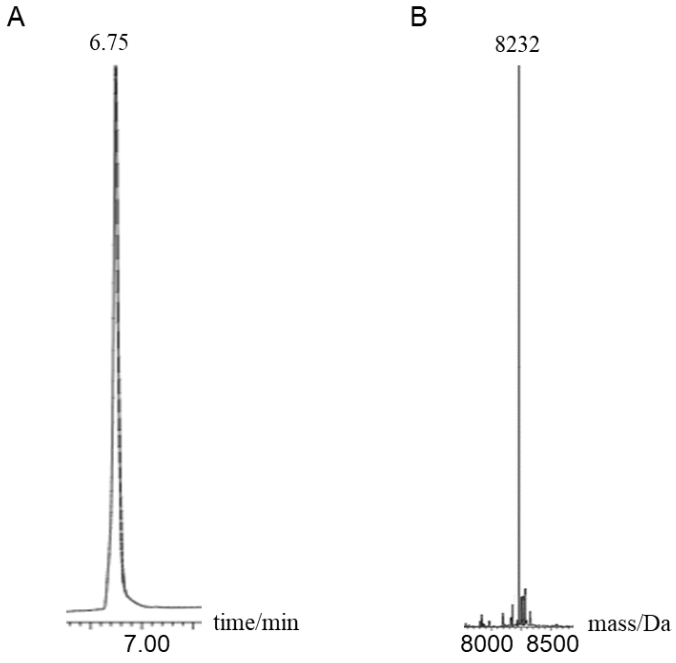


Figure 7.8. A. RP-UPLC (UV abs at 260 nm) and **B.** mass spectrum (ES-) of 5′-Cy3 scrambled MUC1 aptamer, calculated 8231 Da, found 8232 Da.

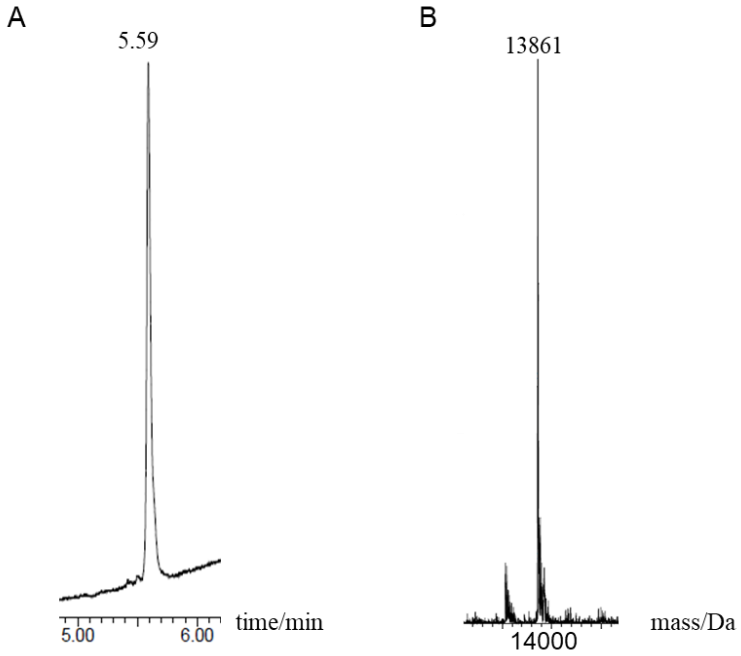


Figure 7.9. B. RP-UPLC (UV abs at 260 nm) and **B.** mass spectrum (ES-) of 5′-FAM anti-HER2 aptamer, calculated 13859 Da, found 13861 Da.

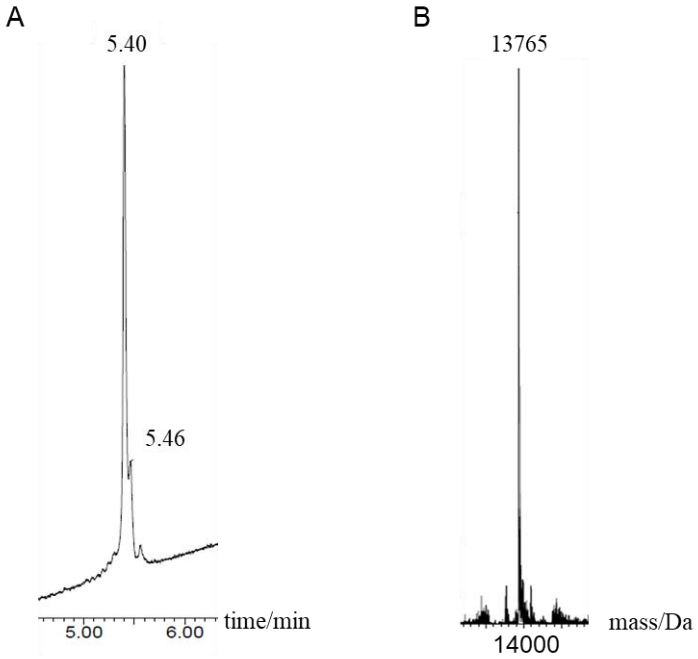


Figure 7.10. A. RP-UPLC (UV abs at 260 nm) and **B.** mass spectrum (ES-) of 5′-FAM mutated anti-HER2 aptamer, calculated 13763 Da, found 13765 Da.

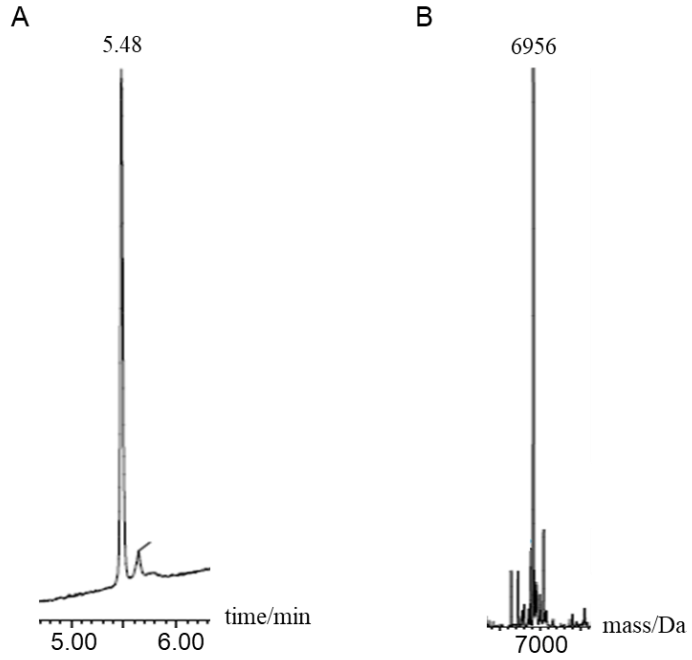


Figure 7.11. A. RP-UPLC (UV abs at 260 nm) and **B.** mass spectrum (ES-) of DNAR**1**, calculated 6954 Da, found 6956 Da.

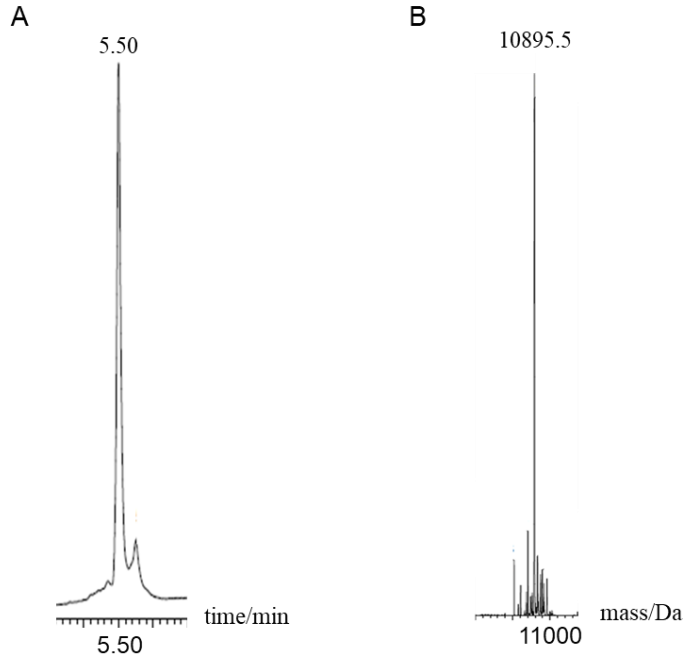


Figure 7.12. A. RP-UPLC (UV abs at 260 nm) and **B.** mass spectrum (ES-) of DNAR**2**, calculated 10895 Da, found 10895.5 Da.

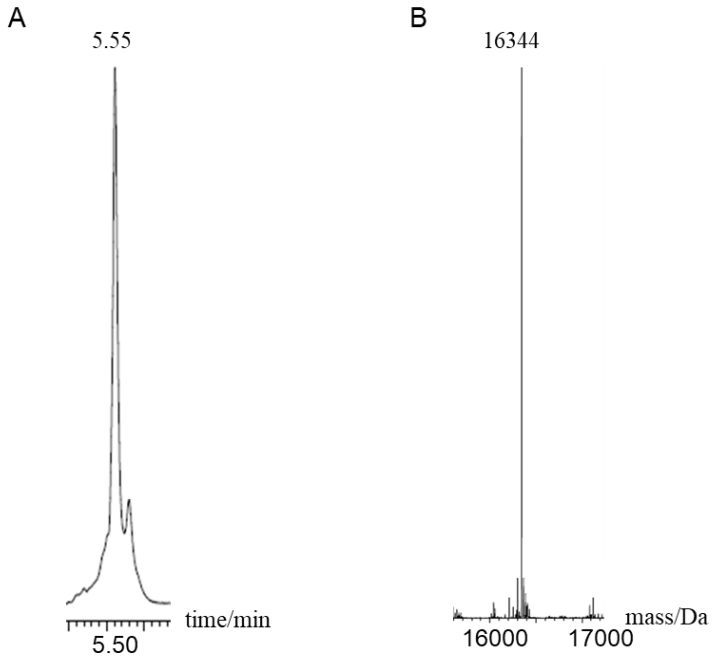


Figure 7.13. A.RP-UPLC (UV abs at 260 nm) and **B.** mass spectrum (ES-) of DNAR**3**, calculated 16343 Da, found 16344 Da.

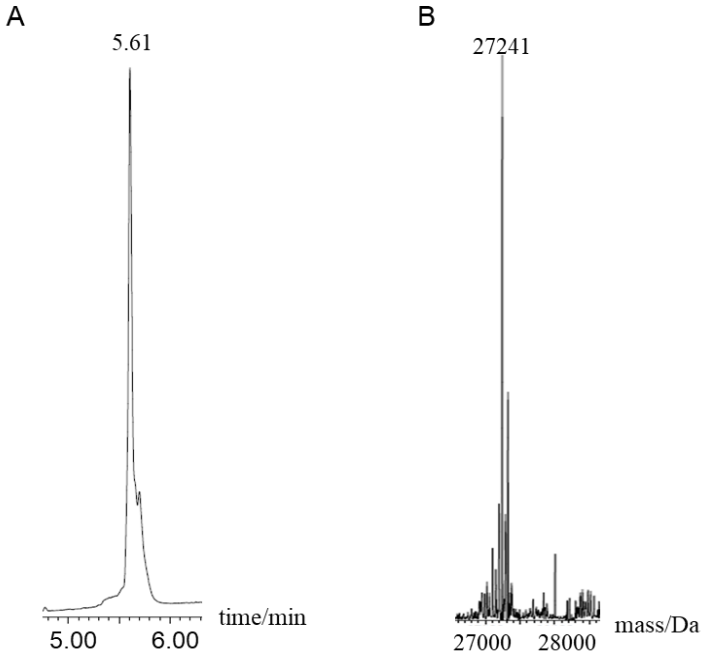


Figure 7.14. A. RP-UPLC (UV abs at 260 nm) and **B.** mass spectrum (ES-) of DNAR**4**, calculated 27238 Da, found 27241 Da.

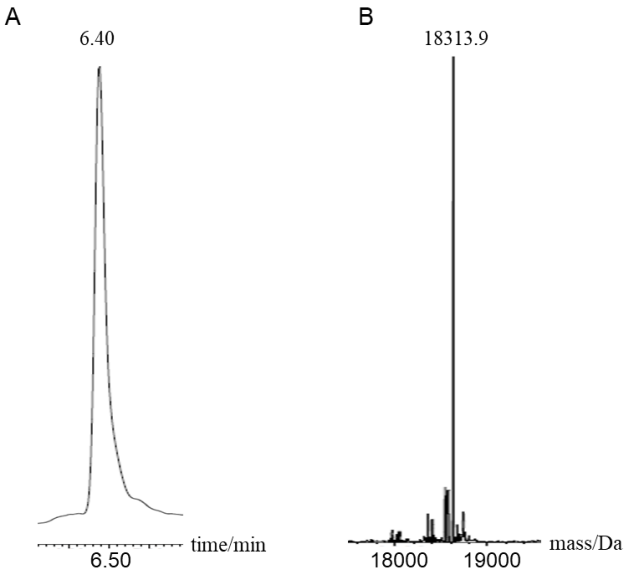


Figure 7.15. A. RP-UPLC (UV abs at 260 nm) and **B.** mass spectrum (ES-) of DNAR**5**, calculated 18314 Da, found 18313.9 Da.

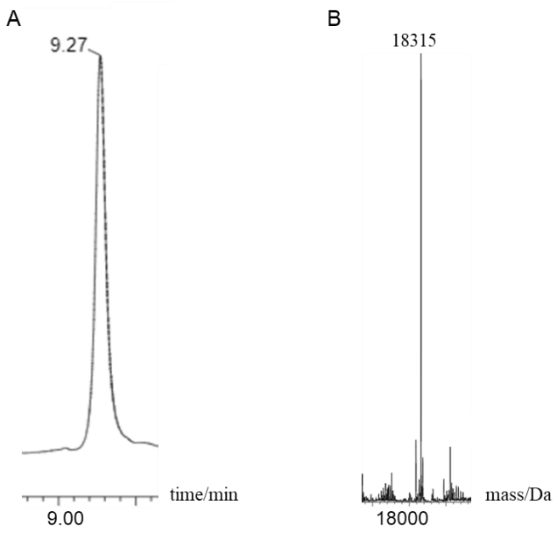


Figure 7.16. A. RP-UPLC (UV abs at 260 nm) and **B.** mass spectrum (ES-) of DNAR**6**, calculated 18314 Da, found 18315 Da.

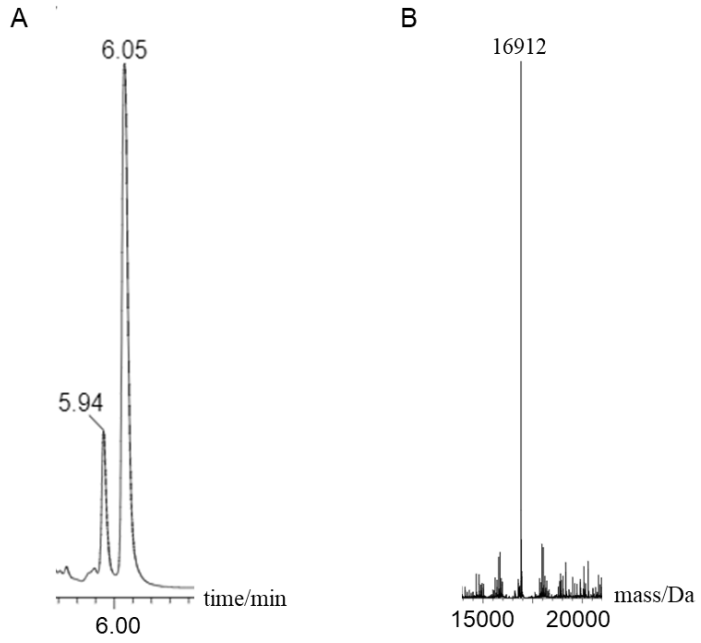


Figure 7.17. A. RP-UPLC (UV abs at 260 nm) and **B.** mass spectrum (ES-) of DNAR**7**, calculated 16912 Da, found 16912 Da. Two peaks are observed in the RP-UPLC trace due to a mixture of the 5 and 6 isomers of TAMRA

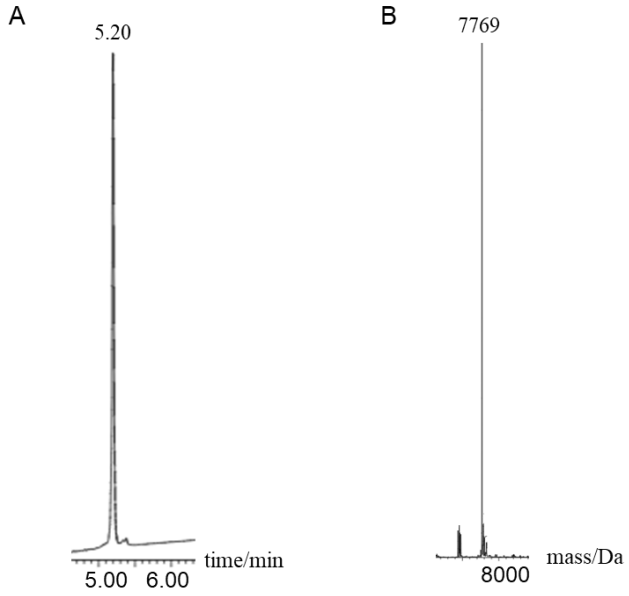


Figure 7.18. A. RP-UPLC (UV abs at 260 nm) and **B.** mass spectrum (ES-) of signal strand 1, calculated 7769 Da, found 7769 Da.

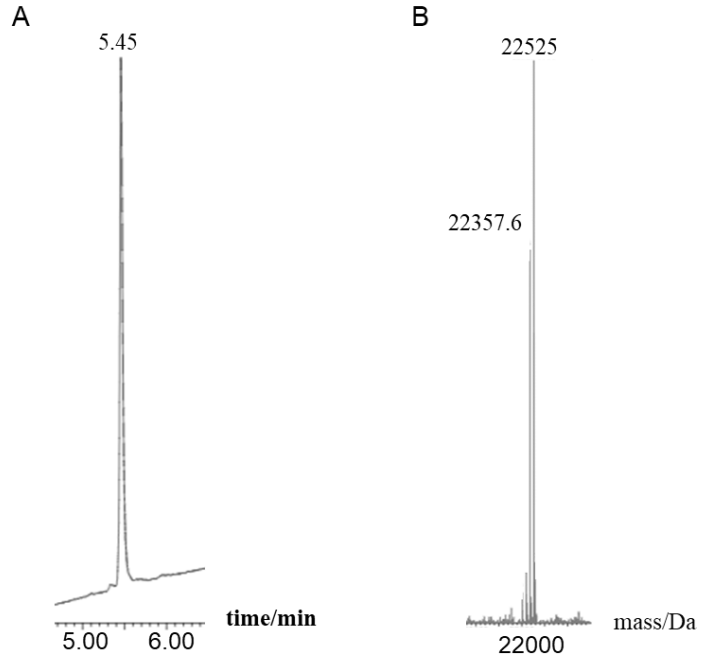


Figure 7.19. A. RP-UPLC (UV abs at 260 nm) and **B.** mass spectrum (ES-) of signal strand **2**, calculated 22358 Da, found 22357.6 Da and 22525 Da (+168 Da).

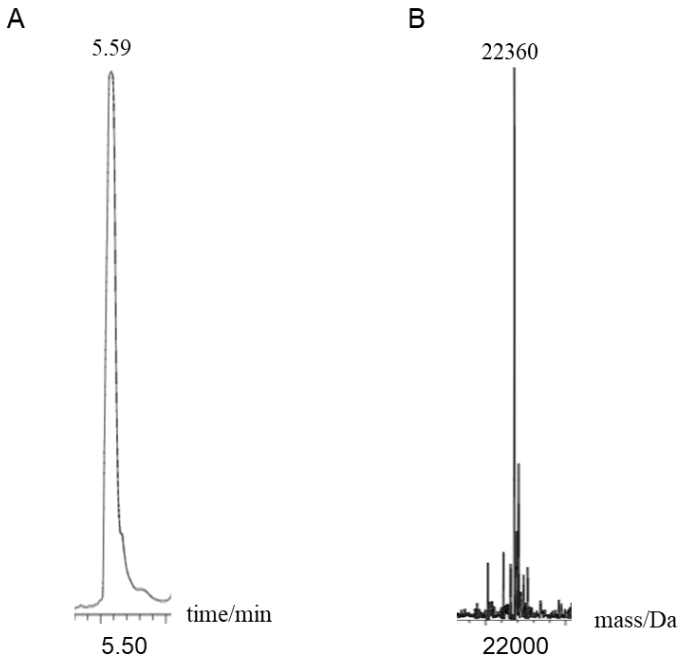


Figure 7.20. A. RP-UPLC (UV abs at 260 nm) and **B.** mass spectrum (ES-) of signal strand **3**, calculated 22358 Da, found 22360 Da.

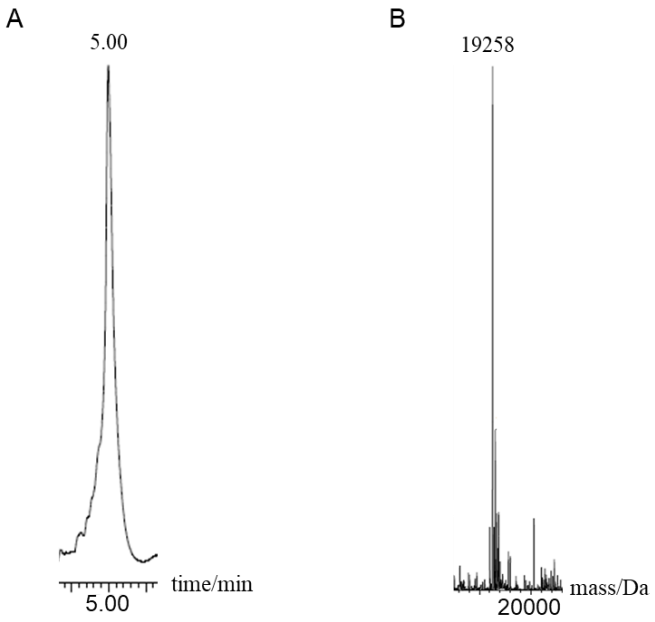


Figure 7.21. A. RP-UPLC (UV abs at 260 nm) and **B.** mass spectrum (ES-) of survivin mRNA target, calculated 19257 Da, found 19258 Da.

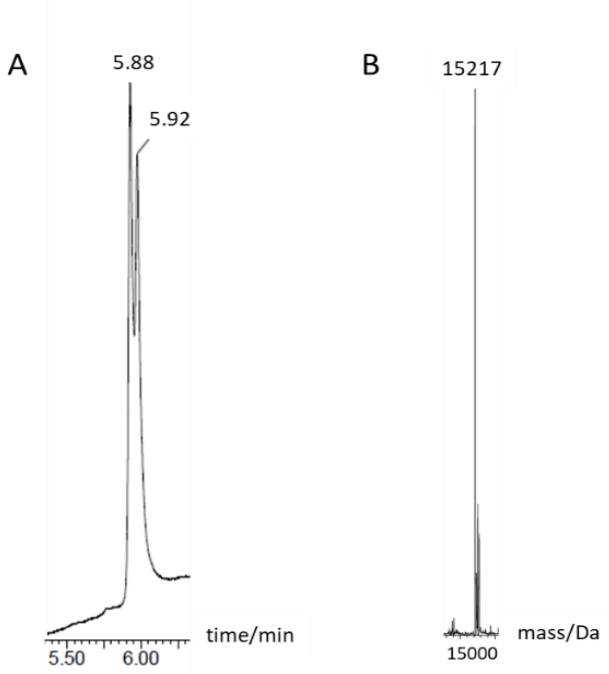


Figure 7.22. A. RP-UPLC (UV abs at 260 nm) and **B.** mass spectrum (ES-) of 5'-alkyne, FAM modified HER2 aptamer, calculated 15216 Da, found 15217 Da. Two peaks are observed in the RP-UPLC trace due to a mixture of the 5 and 6 isomers of FAM.

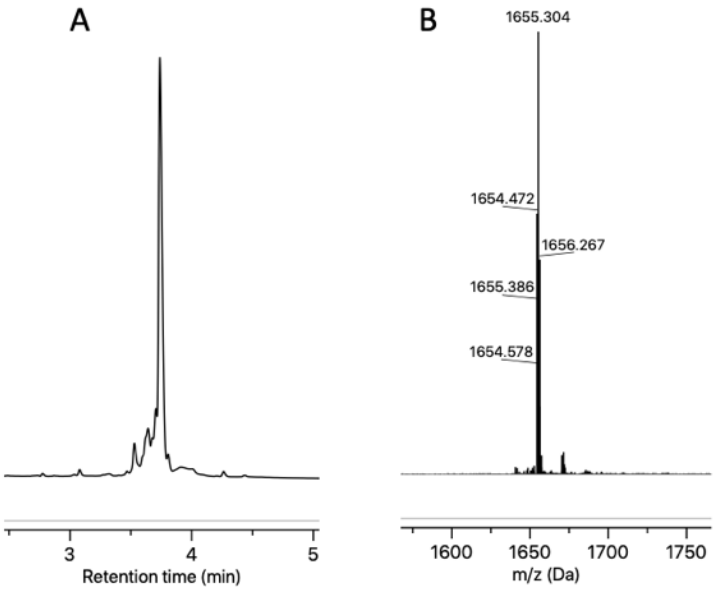


Figure 7.23. A. RP-UPLC (UV abs at 254 nm) and **B.** mass spectrum (ES^+) TAMRA labelled peptide **1**, calculated 1655.9 Da, found 1655.3 Da.

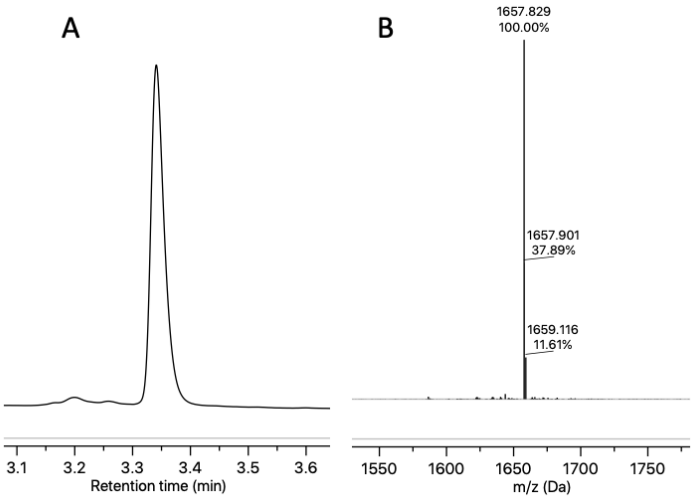


Figure 7.24. A. RP-UPLC (UV abs at 254 nm) and **B.** mass spectrum (ES^+) of FAM labelled peptide **2**, calculated 1658.7 Da, found 1657.8 Da.

Scanning electron microscopy

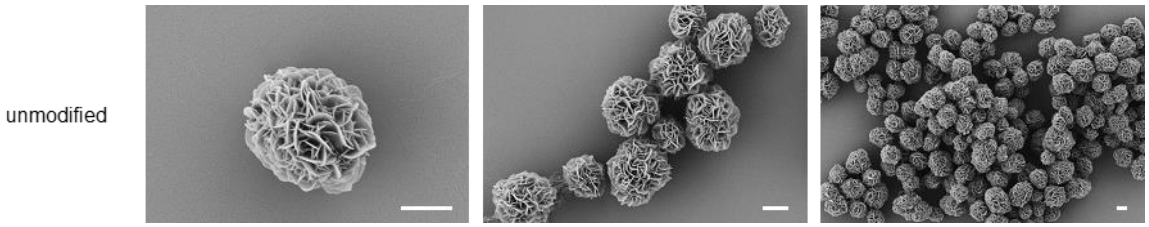


Figure **7.25.** SEM images of unmodified DNFs templated by template **1** at different magnifications. Scale bar represents 1 μm.

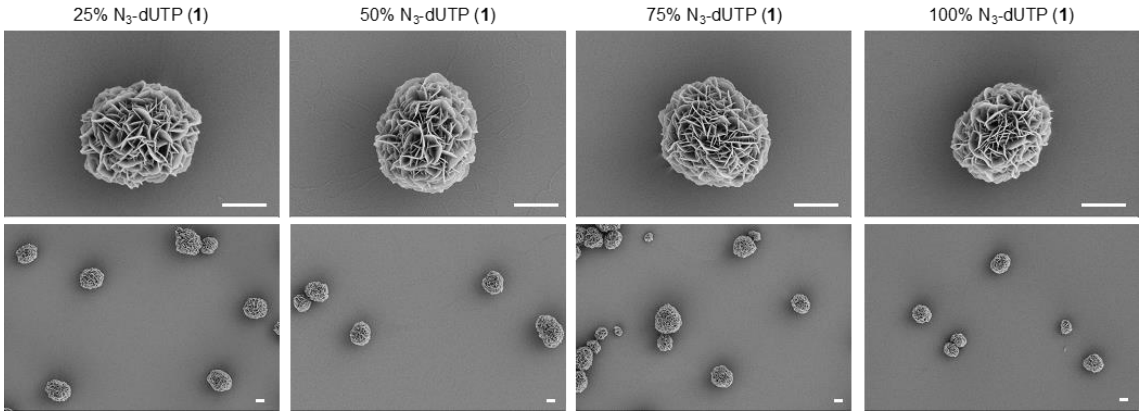


Figure **7.26.** SEM images of DNFs produced with different proportions of N_3-dUTP 1 to dTTP, templated by template **1**. In all cases, the total dNTP concentration was kept at 2 mM and the % dN*TP is indicated above the images. Scale bars represent 1 μm.

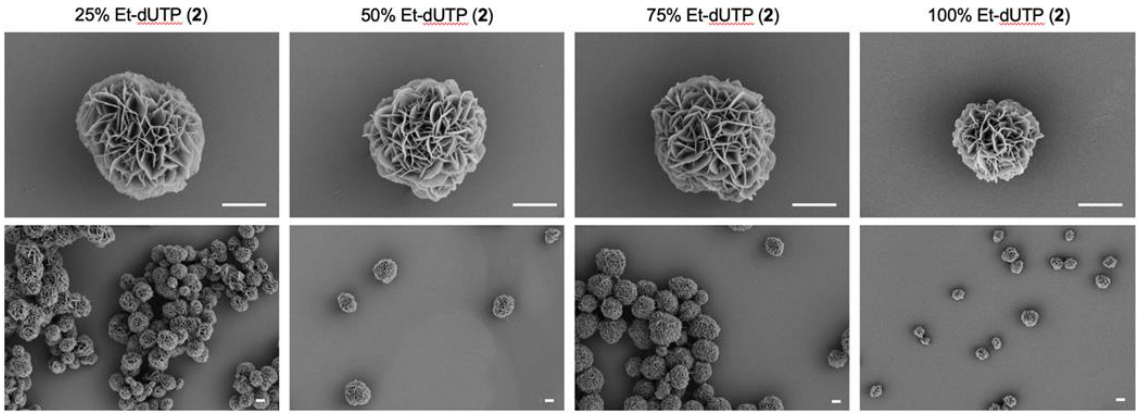


Figure 7.27. SEM images of DNFs produced with different proportions of Et-dUTP **2** to dTTP, templated by template **1**. In all cases, the total dNTP concentration was kept at 2 mM, and the % dN*TP is indicated above the images. Figure S7 shows a typical unmodified DNF. Scale bars represent 1 mm.

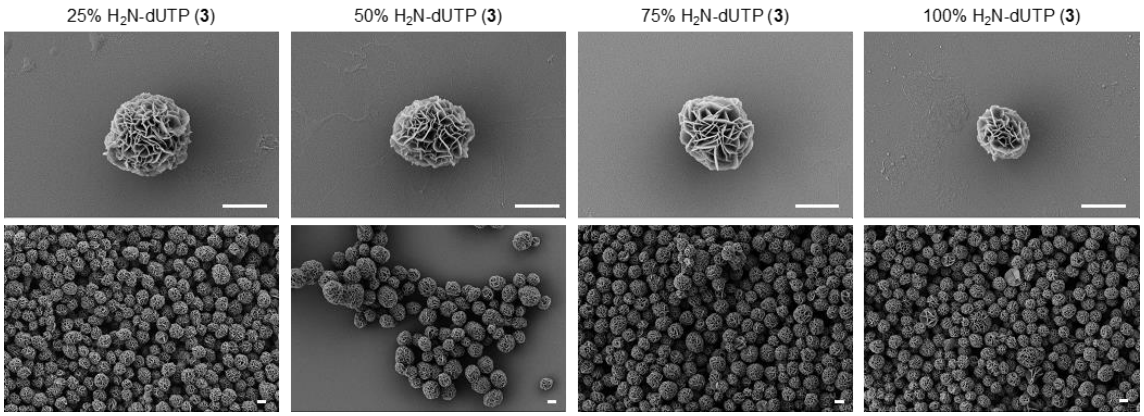


Figure 7.28. SEM images of DNFs produced with different proportions of H_2N-dUTP **3** to dTTP, templated by template **1**. In all cases, the total dNTP concentration was kept at 2 mM, and the % dN*TP is indicated above the images. Scale bars represent 1 mm.

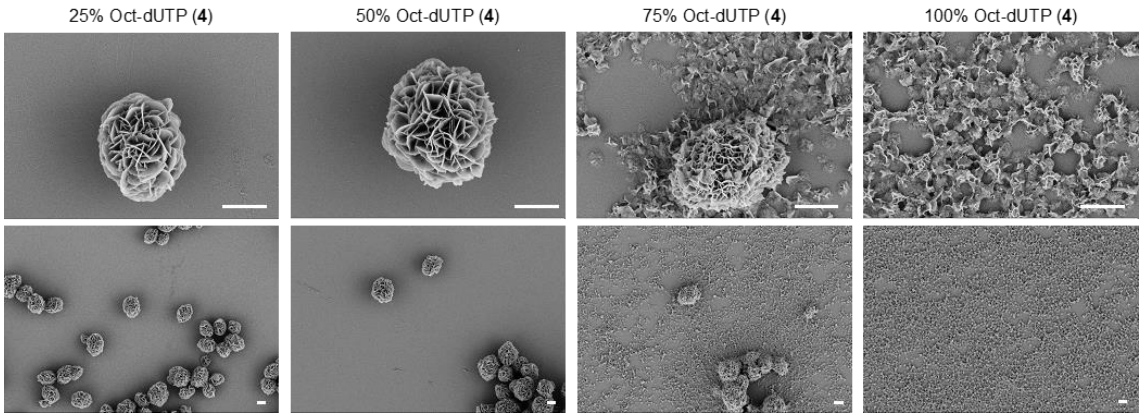


Figure 7.29. SEM images of DNFs produced with different proportions of Oct-dUTP 4 to dTTP, templated by template 1. In all cases, the total dNTP concentration was kept at 2 mM, and the % dN*TP is indicated above the images. Scale bars represent 1 mm.

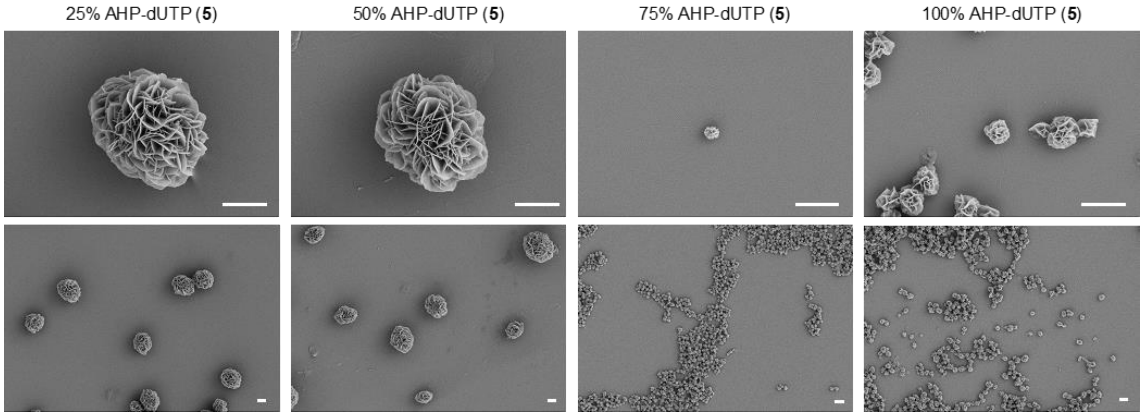


Figure 7.30. SEM images of DNFs produced with different proportions of AHP-dUTP **5** to dTTP, templated by template **1**. In all cases, the total dNTP concentration was kept at 2 mM, and the % dN*TP is indicated above the images. Scale bars represent 1 mm.

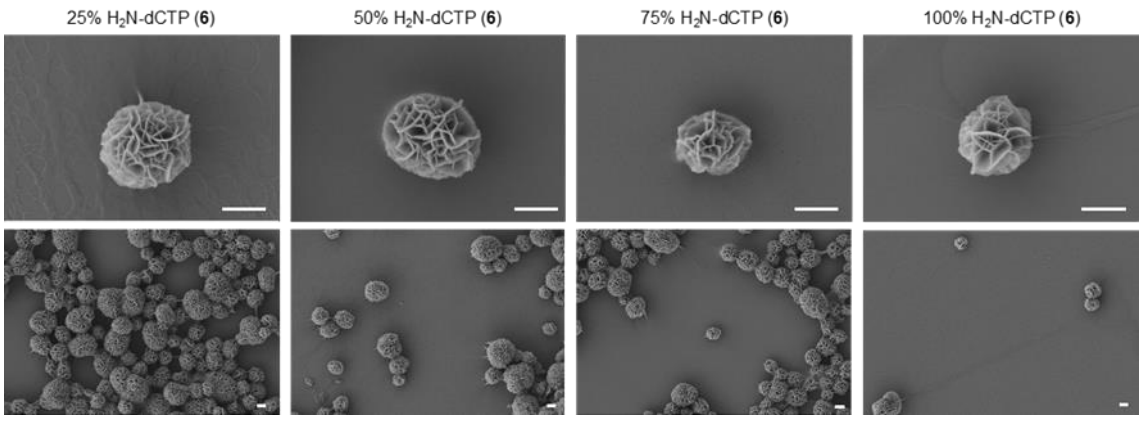


Figure 7.31. SEM images of DNFs produced with different proportions of H_2N-dCTP **6** to dTTP, templated by template **1**. In all cases, the total dNTP concentration was kept at 2 mM, and the % dN*TP is indicated above the images. Scale bars represent 1 mm.

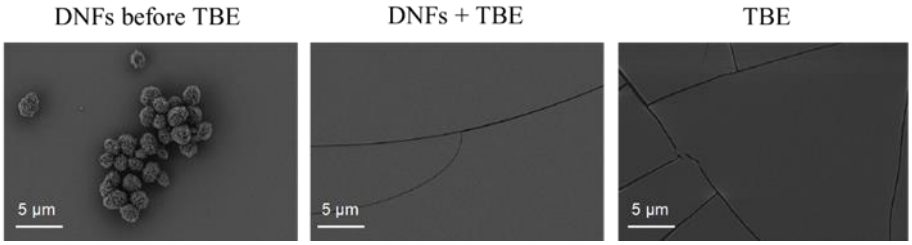


Figure 7.32. SEM images of a DNF before and after treatment with 1x TBE. No structures were observed following TBE treatment.

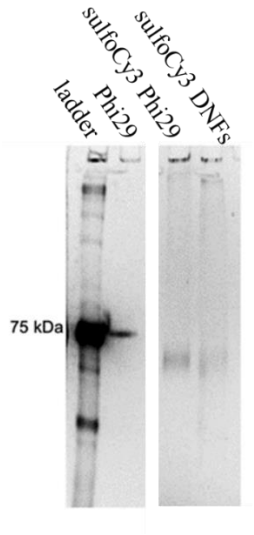


Figure 7.33. 8% SDS-PAGE analysis of the protein content of unmodified DNFs after NHS labelling with sulfoCy3-NHS. DNFs were dissolved in TBE buffer before SDS-PAGE, and the samples were compared to the Phi29 labelled with sulfoCy3-NHS. The experiment suggests that the non-specific labelling was occurring on Phi29. The experiment was done by Dr Ysobel Baker.

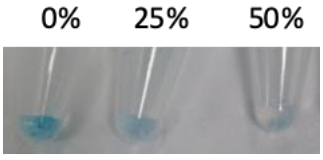


Figure 7.34. Non-specific labelling of N_3-DNFs by Cy5-BCN. DNFs prepared with varying ratios of N_3-dUTP **5** and incubated with Cy5-BCN. The Colour observed in 0% indicated non-specific interactions between DNFs and the dye. The experiment was done by Dr Ysobel Baker.

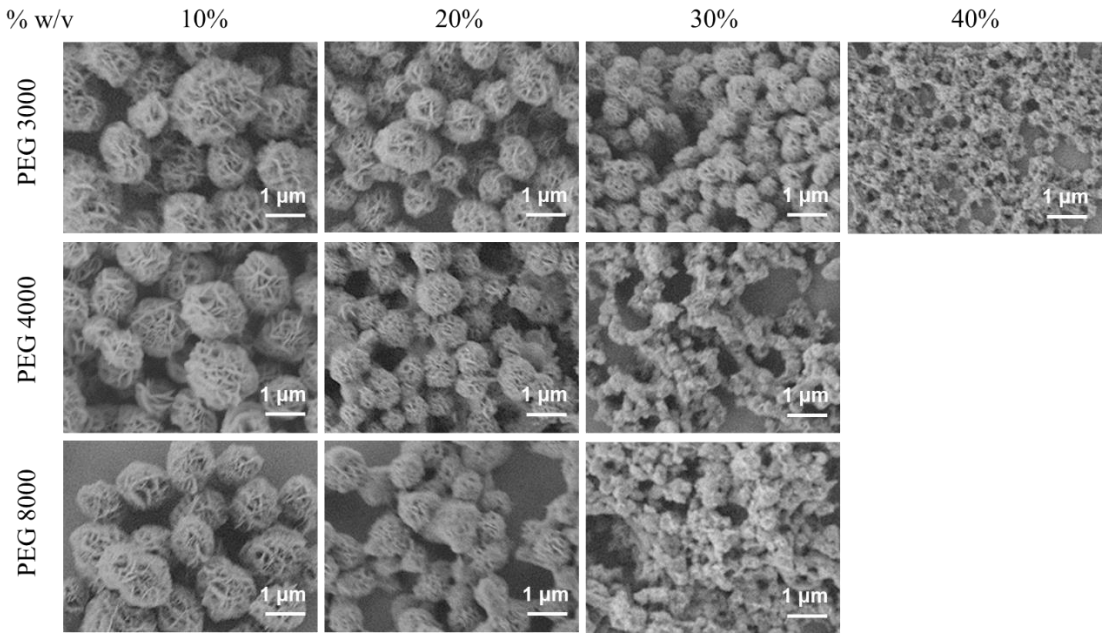
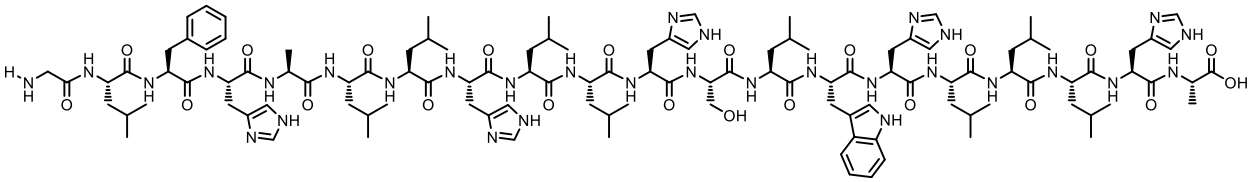


Figure 7.35. images of DNFs formed with different %w/v PEG in different sizes after 20 h RCA reaction. Scale bars represent 1 µm.



GLFHALLHLLHSLWHLLLHA

Figure 7.36. Structure and sequence of peptide ppTG21, synthesized by Biomatik Ltd.

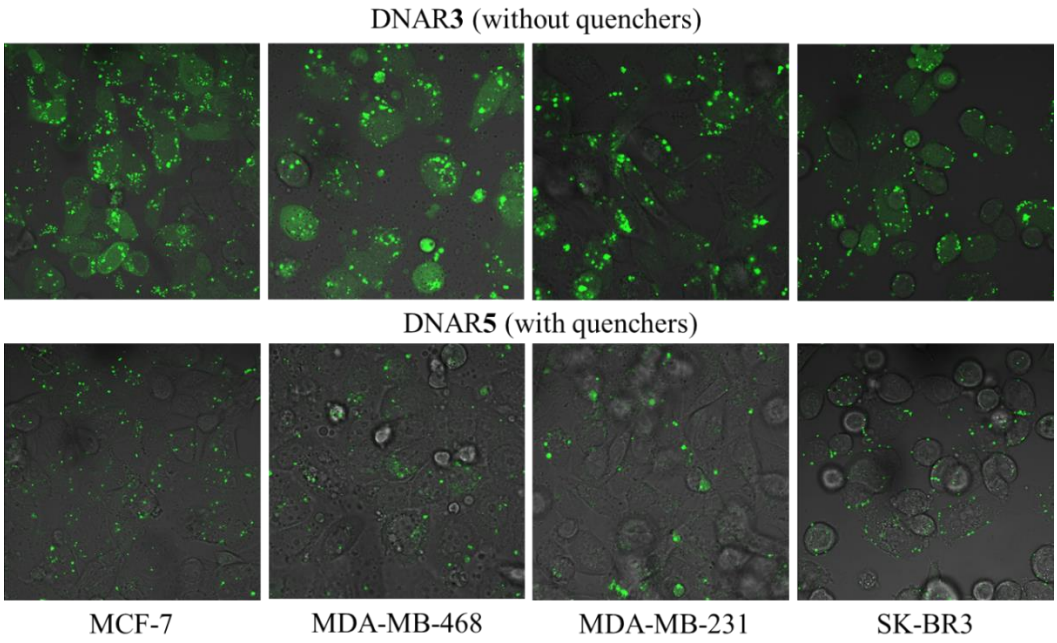


Figure 7.37. Fluorescence imaging of MCF-7, MDA-MB-468, MDA-MB-231 and SK-BR3 after lipid transfection of complexes formed by DNAR**3**-signal strand **2** (without quenchers) and DNAR**5**-signal strand **2** (with quenchers).

Chapter 8. References

1. Egli, M.; Flavell, A.; Pyle, A. M.; Wilson, W. D.; Haq, S. I.; Luisi, B.; Fisher, J.; Laughton, C.; Allen, S.; Engels, J. *Nucleic Acids in Chemistry and Biology*, Edition 3.; Blackburn, G. M., Gait, M. J., Loakes, D., Williams, D. M., Eds.; The Royal Society of Chemistry, 2006.

2. Chargaff, E. Chemical Specificity of Nucleic Acids and Mechanism of Their Enzymatic Degradation. *Experientia*. **1950**, *6* (6), 201–209.

3. Franklin, R. E.; Gosling, R. G. Molecular Configuration in Sodium Thymonucleate. *Nature*. **1953**, *171* (4356), 740–741.

4. Watson, J.; Crick, F. Molecular Structure of Nucleic Acids: A Structure for Deoxyribose Nucleic Acid. *Nature*. **1953**, *171* (4356), 737–738.

5. Hoogsteen, K. The Structure of Crystals Containing a Hydrogen-Bonded Complex of 1-Methylthymine and 9-Methyladenine. *Acta Crystallogr*. **1959**, *12*, 822–823.

6. Vasquez, K. M.; Wensel, T. G.; Hogan, M. E.; Wilson, J. H. High-Affinity Triple Helix Formation by Synthetic Oligonucleotides Within. *Biochemistry*. **1995**, *34*, 7243—7251.

7. James, P. L.; Brown, T.; Fox, K. R. Thermodynamic and Kinetic Stability of Intermolecular Triple Helices Containing Different Proportions of C+*GC and T*AT Triplets. *Nucleic Acids Res.* **2003**, *31* (19), 5598–5606.

8. Gellert, B. Y. I.; Lipsett, M. N.; Davies, D. R. Helix Formation by Guanylic Acid. *Proc. Natl. Acad. Sci. U. S. A.* **1962**, *48*, 2013–2018.

9. Parkinson, G. N.; Lee, M. P. H.; Neidle, S. Crystal Structure of Parallel Quadruplexes from Human Telomeric DNA. *Nature*. **2002**, *417* (June), 3–7.

10. Wang, Y.; Patell, D. I. Solution Structure of the Human Telomeric Repeat d[AG3(T2AG3)3] G-Tetraplex. *Structure*. **1993**, *1* (4), 263–282.

11. Ambrus, A.; Chen, D.; Dai, J.; Bialis, T.; Jones, R. A.; Yang, D. Human Telomeric Sequence Forms a Hybrid-Type Intramolecular G-Quadruplex Structure with Mixed Parallel / Antiparallel Strands in Potassium Solution. *Nucleic Acids Res.* **2006**, *34* (9), 2723–2735.

12. Yu, H.; Gu, X.; Nakano, S.; Miyoshi, D.; Sugimoto, N. Beads-on-a-String Structure of Long Telomeric DNAs under Molecular Crowding Conditions. *J. Am. Chem. Soc.* **2012**, *134*, 20060–20069.

13. Luu, K. N.; Kuryavyi, V.; Lacroix, L.; Patel, D. J.; Program, B.; Biophysique, D. Structure of the Human Telomere in K+ Solution: An Intramolecular (3 + 1) G-

Quadruplex Scaffold. *J. Am. Chem. Soc.* **2006**, *128* (30), 9963–9970.

14. Fadrna, E.; Spackova, N.; Stefl, R.; Koca, J.; Cheatham, T. E.; Sponer, J. Molecular Dynamics Simulations of Guanine Quadruplex Loops : Advances and Force Field Limitations. *Biophys. J.* **2004**, *87* (July), 227–242.

15. Fishel, R.; Griffith, J. D.; Kar, A.; Jones, N. Long Repeating (TTAGGG) n Single-Stranded DNA Self-Condenses into Compact Beaded Filaments Stabilized by G-Quadruplex Formation. *J. Biol. Chem*. **2018**, *293*, 9473–9485.

16. Venczel, E. A.; Sen, D. Parallel and Antiparallel G-DNA Structures from Complex Telomeric Sequence. *Biochemistry*. **1993**, *32*, 6220–6228.

17. Greidert, C. W.; Harley B., H.; Futcher, A. B. Telomeres Shorten during Ageing of Human Fibroblasts. *Nature*. **1990**, *345* (5429), 458–460.

18. Neidle, S.; Parkinson, G. Telomere Maintenance as a Target for Anticancer Drug Discovery. *Nat. Rev. Drug Discov.* **2002**, *1* (5), 383–393.

19. Hurley, L. H.; Wheelhouse, R. T.; Sun, D.; Kerwin, S. M.; Salazar, M.; Fedoroff, O. Y.; Han, F. X.; Han, H.; Izbicka, E.; Von Hoff, D. D. G-Quadruplexes as Targets for Drug Design. *Pharmacol. Ther.* **2000**, *85* (3), 141–158.

20. Seenisamy, J.; Bashyam, S.; Gokhale, V.; Vankayalapati, H.; Sun, D.; Siddiqui-jain, A.; Streiner, N.; Shin-ya, K.; White, E.; Wilson, W. D.; Hurley, L. H. Design and Synthesis of an Expanded Porphyrin That Has Selectivity for the C-MYC G-Quadruplex Structure. *J. Am. Chem. Soc.* **2005**, *127*, 2944–2959.

21. Ou, T.; Lu, Y.; Tan, J.; Huang, Z.; Wong, K. G-Quadruplexes :Targets in Anticancer Drug Design. *ChemMedChem.* **2008**, *3*, 690–713.

22. Caruthers, M. H. Chemical Synthesis of DNA and DNA Analogs. *Acc. Chem. Res.* **1991**, *24* (9), 278–284.

23. Beaucage, S. L.; Caruthers, M. H. Deoxynucleoside Phosphoramidites—A New Class of Key Intermediates for Deoxypolynucleotide Synthesis. *Tetrahedron Lett.* **1981**, *22* (20), 1859–1862.

24. Caruthers, M. H. Gene Synthesis Machines: DNA Chemistry and Its Uses. *Science*. **1985**, *230* (4723), 281–285.

25. Finn, P. J.; Gibson, N. J.; Fallon, R.; Hamilton, A.; Brown, T. Synthesis and Properties of DNA-PNA Chimeric Oligomers. *Nucleic Acids Res.* **1996**, *24* (17), 3357–3363.

26. Vongsutilers, V.; Daft, J. R.; Shaughnessy, K. H.; Gannett, P. M. A General Synthesis of C8-Arylpurine Phosphoramidites. *Molecules*. **2009**, *14* (9), 3339–3352.

27. Sproat, B. S. RNA Synthesis Using 2'-O-(Tert-Butyldimethylsilyl) Protection. *Methods Mol. Biol.* **2005**, *288*, 17–32.

28. Tuerk, C.; Gold, L. Systematic Evolution of Ligands by Exponential Enrichment : RNA Ligands to Bacteriophage El-T. *Science*. **1990**, *249* (4968), 505–510.

29. Ellington, A. D.; Szostak, J. W. In Vitro Selection of RNA Molecules That Bind Specific Ligands. *Nature*. **1990**, *346*, 818–822.

30. Han, K.; Liang, Z.; Zhou, N. Design Strategies for Aptamer-Based Biosensors. *Sensors*. **2010**, *10*, 4541–4557.

31. Kalra, P.; Dhiman, A.; Cho, W. C.; Bruno, J. G.; Sharma, T. K. Simple Methods and Rational Design for Enhancing Aptamer Sensitivity and Specificity. *Front. Mol. Biosci.* **2018**, *5*, 1–16.

32. Kaplon, H.; Reichert, J. M. Antibodies to Watch in 2019. *MAbs*. **2019**, *11* (2), 219–238.

33. Song, K.; Lee, S.; Ban, C. Aptamers and Their Biological Applications. *Sensors*. **2012**, *12*, 612–631.

34. Jayasena, S. D. Aptamers : An Emerging Class of Molecules That Rival Antibodies in Diagnostics. *Clin. Chem.* **1999**, *45* (9), 1628–1650.

35. Dollins, C. M.; Nair, S.; Sullenger, B. A. Aptamers in Immunotherapy. *Hum Gene Ther.* **2008**, *19* (5), 443–450.

36. Maier, K. E.; Levy, M. From Selection Hits to Clinical Leads : Progress in Aptamer Discovery. *Mol. Ther.* **2016**, *5*, 1–10.

37. Kanwar, J. R.; Roy, K.; Maremanda, N. G.; Subramanian, K. Nucleic Acid-Based Aptamers : Applications , Development And Clinical Trials Nucleic Acid-Based Aptamers : Applications , Development and Clinical Trials. *Curr. Med. Chem.* **2015**, 2539–2557.

38. Bunka, D. H. J.; Stockley, P. G. Aptamers Come of Age – at Last. *Nat. Rev.* **2006**, *4*, 588–596.

39. Pascal, J. M. DNA Ligases: Structures. In *Encyclopedia of Biological Chemistry*; Lennarz, W. J., Lane, M. D. B. T., Eds.; Academic Press: Waltham, 2013; pp 33–

39.

40. Eun, H.-M. Ligases. In *Enzymology Primer for Recombinant DNA Technology*; Eun, H.-M., Ed.; Academic Press: San Diego, 1996; pp 109–144.

41. Pawlowska, R.; Korczynski, D.; Nawrot, B.; Stec, W. J.; Chworos, A. The α-Thio and/or β-γ-Hypophosphate Analogs of ATP as Cofactors of T4 DNA Ligase. *Bioorg. Chem.* **2016**, *67*, 110–115.

42. Shi, K.; Bohl, T. E.; Park, J.; Zasada, A.; Malik, S.; Banerjee, S.; Tran, V.; Li, N.; Yin, Z.; Kurniawan, F.; Orellana, K.; Aihara, H. T4 DNA Ligase Structure Reveals a Prototypical ATP-Dependent Ligase with a Unique Mode of Sliding Clamp Interaction. *Nucleic Acids Res.* **2018**, *46* (19), 10474–10488.

43. Maloy, S. R. *Experimental Techniques in Bacterial Genetics*; Jones and Bartlett: Boston, Mass, 1990.

44. Ferretti, L.; Sgaramella, V.; Biochimica, G.; Epifanio, V. S. Temperature Dependence of the Joining by T4 DNA Ligase of Termini Produced by Type II Restriction Endonucleases. *Nucleic Acids Res.* **1981**, *9* (1), 85–93.

45. Suzuki, M.; Hayashi, H.; Mizuki, T.; Maekawa, T.; Morimoto, H. Efficient DNA Ligation by Selective Heating of DNA Ligase with a Radio Frequency Alternating Magnetic Field. *Biochem. Biophys. Reports*. **2016**, *8* (December 2015), 360–364.

46. Kolb, H. C.; Sharpless, K. B. The Growing Impact of Click Chemistry on Drug Discovery. *Drug Discov. Today*. **2003**, *8* (24), 1128–1137.

47. Kolb, H. C.; Finn, M. G.; Sharpless, K. B. Click Chemistry: Diverse Chemical Function from a Few Good Reactions. *Angew. Chem. Int. Ed.* **2001**, *40* (11), 2004–2021.

48. Rostovtsev, V. V.; Green, L. G.; Fokin, V. V.; Sharpless, K. B. A Stepwise Huisgen Cycloaddition Process: Copper(I)-Catalyzed Regioselective "Ligation" of Azides and Terminal Alkynes. *Angew. Chem. Int. Ed.* **2002**, *41* (14), 2596–2599.

49. Tornøe, C. W.; Christensen, C.; Meldal, M. Peptidotriazoles on Solid Phase: [1,2,3]-Triazoles by Regiospecific Copper(I)-Catalyzed 1,3-Dipolar Cycloadditions of Terminal Alkynes to Azides. *J. Org. Chem.* **2002**, *67* (9), 3057–3064.

50. Martell, J.; Weerapana, E. Applications of Copper-Catalyzed Click Chemistry in Activity-Based Protein Profiling. *Molecules*. **2014**, *19* (2), 1378–1393.

51. Bock, V. D.; Hiemstra, H.; Van Maarseveen, J. H. Cu I-Catalyzed Alkyne-Azide "Click" Cycloadditions from a Mechanistic and Synthetic Perspective. *European J.*

Org. Chem. **2006**, No. 1, 51–68.

52. Anilkumar, G.; Saranya, S. Ligand-Stabilized Cu(I)-Catalyzed Click Reaction. In *Copper Catalysis in Organic Synthesis*; Wiley-VCH: Weinheim, 2020; p 191.

53. Meldal, M.; Tomøe, C. W. Cu-Catalyzed Azide - Alkyne Cycloaddition. *Chem. Rev.* **2008**, *108* (8), 2952–3015.

54. Haque, M. M.; Peng, X. DNA-Associated Click Chemistry. *Sci. China Chem.* **2014**, *57* (2), 215–231.

55. El-Sagheer, A. H.; Brown, T. Click Chemistry with DNA. *Chem. Soc. Rev.* **2010**, *39* (4), 1388–1405.

56. Abel, G. R.; Calabrese, Z. A.; Ayco, J.; Hein, J. E.; Ye, T. Measuring and Suppressing the Oxidative Damage to DNA During Cu(I)-Catalyzed Azide–Alkyne Cycloaddition. *Bioconjug. Chem.* **2016**, *27* (3), 698–704.

57. El-Sagheer, A. .; Brown, T. New Strategy for the Synthesis of Chemically Modified RNA Constructs Exemplified by Hairpin and Hammerhead Ribozymes. *Proc. Natl. Acad. Sci.* **2010**, *107* (35), 15329–15334.

58. El-Sagheer, A. H.; Sanzone, A. P.; Gao, R.; Tavassoli, A.; Brown, T. Biocompatible Artificial DNA Linker That Is Read through by DNA Polymerases and Is Functional in Escherichia Coli. *Proc. Natl. Acad. Sci. U. S. A.* **2011**, *108* (28), 11338–11343.

59. El-Sagheer, A. H.; Brown, T. Efficient RNA Synthesis by in Vitro Transcription of a Triazole-Modified DNA Template. *Chem. Commun.* **2011**, *47* (44), 12057–12058.

60. Kukwikila, M.; Gale, N.; El-Sagheer, A. H.; Brown, T.; Tavassoli, A. Assembly of a Biocompatible Triazole-Linked Gene by One-Pot Click-DNA Ligation. *Nat. Chem.* **2017**, *9* (11), 1089–1098.

61. Birts, C. N.; Sanzone, A. P.; El-Sagheer, A. H.; Blaydes, J. P.; Brown, T.; Tavassoli, A. Transcription of Click-Linked DNA in Human Cells. *Angew. Chem. Int. Ed.* **2014**, *53* (9), 2362–2365.

62. Chen, J.; Baker, Y. R.; Brown, A.; El-Sagheer, A. H.; Brown, T. Enzyme-Free Synthesis of Cyclic Single-Stranded DNA Constructs Containing a Single Triazole, Amide or Phosphoramidate Backbone Linkage and Their Use as Templates for Rolling Circle Amplification and Nanoflower Formation. *Chem. Sci.* **2018**, *9* (42), 8110–8120.

63. Nallur, G.; Luo, C.; Fang, L.; Cooley, S.; Dave, V.; Lambert, J.; Kukanskis, K.; Kingsmore, S.; Lasken, R.; Schweitzer, B. Signal Amplification by Rolling Circle Amplification on DNA Microarrays. *Nucleic Acids Res.* **2001**, *29* (23), 118.

64. Yin, J.; Gan, P.; Zhou, F.; Wang, J. Sensitive Detection of Transcription Factors Using Near-Infrared Fluorescent Solid-Phase Rolling Circle Amplification. *Anal. Chem.* **2014**, *86* (5), 2572–2579.

65. Zhou, H.; Bouwman, K.; Schotanus, M.; Verweij, C.; Marrero, J. A.; Dillon, D.; Costa, J.; Lizardi, P.; Haab, B. B. Two-Color, Rolling-Circle Amplification on Antibody Microarrays for Sensitive, Multiplexed Serum-Protein Measurements. *Genome Biol.* **2004**, *5* (4), R28.

66. Wang, C.; Jia, X. M.; Jiang, C.; Zhuang, G. N.; Yan, Q.; Xiao, S. J. DNA Microarray Fabricated on Poly(Acrylic Acid) Brushes-Coated Porous Silicon by in Situ Rolling Circle Amplification. *Analyst*. **2012**, *137* (19), 4539–4545.

67. Dean, F. B.; Nelson, J. R.; Giesler, T. L.; Lasken, R. S. Rapid Amplification of Plasmid and Phage DNA Using Phi29 DNA Polymerase and Multiply-Primed Rolling Circle Amplification. *Genome Res.* **2001**, *11* (6), 1095–1099.

68. Lizardi, P. M.; Huang, X.; Zhu, Z.; Bray-Ward, P.; Thomas, D. C.; Ward, D. C. Mutation Detection and Single-Molecule Counting Using Isothermal Rolling-Circle Amplification. *Nat. Genet.* **1998**, *19* (3), 225–232.

69. Blanco, L.; Bernad, A.; Lazaro, J. M.; Martin, G.; Garmendia, C.; Salas, M. Highly Efficient DNA Synthesis by the Phage Φ29 DNA Polymerase. Symmetrical Mode of DNA Replication. *J. Biol. Chem.* **1989**, *264* (15), 8935–8940.

70. Tang, S.; Wei, H.; Hu, T.; Jiang, J.; Chang, J.; Guan, Y.; Zhao, G. Suppression of Rolling Circle Amplification by Nucleotide Analogs in Circular Template for Three DNA Polymerases. *Biosci. Biotechnol. Biochem.* **2016**, *80* (8), 1555–1561.

71. Smolina, I. V.; Cherny, D. I.; Nietupski, R. M.; Beals, T.; Smith, J. H.; Lane, D. J.; Broude, N. E.; Demidov, V. V. High-Density Fluorescently Labeled Rolling-Circle Amplicons for DNA Diagnostics. *Anal. Biochem.* **2005**, *347* (1), 152–155.

72. Yao, J.; Flack, K.; Ding, L.; Zhong, W. Tagging the Rolling Circle Products with Nanocrystal Clusters for Cascade Signal Increase in the Detection of MiRNA. *Analyst*. **2013**, *138* (11), 3121–3125.

73. Hollenstein, M. Generation of Long, Fully Modified, and Serum-Resistant Oligonucleotides by Rolling Circle Amplification. *Org. Biomol. Chem.* **2015**, *13* (38), 9820–9824.

74. Russell, C.; Roy, S.; Ganguly, S.; Qian, X.; Caruthers, M. H.; Nilsson, M. Formation of Silver Nanostructures by Rolling Circle Amplification Using Boranephosphonate-Modified Nucleotides. *Anal. Chem.* **2015**, *87* (13), 6660–6666.

75. Christian, A. T.; Pattee, M. S.; Attix, C. M.; Reed, B. E.; Sorensen, K. J.; Tucker, J. D. Detection of DNA Point Mutations and MRNA Expression Levels by Rolling Circle Amplification in Individual Cells. *Proc. Natl. Acad. Sci. U. S. A.* **2001**, *98* (25), 14238–14243.

76. Xu, W.; Xie, X.; Li, D.; Yang, Z.; Li, T.; Liu, X. Ultrasensitive Colorimetric DNA Detection Using a Combination of Rolling Circle Amplification and Nicking Endonuclease-Assisted Nanoparticle Amplification (NEANA). *Small*. **2012**, *8* (12), 1846–1850.

77. Dahl, F.; Banér, J.; Gullberg, M.; Mendel-Hartvig, M.; Landegren, U.; Nilsson, M. Circle-to-Circle Amplification for Precise and Sensitive DNA Analysis. *Proc. Natl. Acad. Sci. U. S. A.* **2004**, *101* (13), 4548–4553.

78. Dong, H.; Wang, C.; Xiong, Y.; Lu, H.; Ju, H.; Zhang, X. Highly Sensitive and Selective Chemiluminescent Imaging for DNA Detection by Ligation-Mediated Rolling Circle Amplified Synthesis of DNAzyme. *Biosens. Bioelectron.* **2013**, *41* (1), 348–353.

79. Mashimo, Y.; Mie, M.; Suzuki, S.; Kobatake, E. Detection of Small RNA Molecules by a Combination of Branched Rolling Circle Amplification and Bioluminescent Pyrophosphate Assay. *Anal. Bioanal. Chem.* **2011**, *401* (1), 221–227.

80. Cho, E. J.; Yanq, L.; Lew, M.; Ellinqton, A. D. Using a Deoxyribozyme Ligase and Rolling Circle Amplification to Detect a Non-Nucleic Acid Analyte, ATP. *J. Am. Chem. Soc.* **2005**, *127* (7), 2022–2023.

81. Ma, C.; Wang, W.; Yang, Q.; Shi, C.; Cao, L. Cocaine Detection via Rolling Circle Amplification of Short DNA Strand Separated by Magnetic Beads. *Biosens. Bioelectron.* **2011**, *26* (7), 3309–3312.

82. Yang, L.; Fung, C. W.; Eun, J. C.; Ellington, A. D. Real-Time Rolling Circle Amplification for Protein Detection. *Anal. Chem.* **2007**, *79* (9), 3320–3329.

83. Di Giusto, D. A.; Wlassoff, W. A.; Gooding, J. J.; Messerle, B. A.; King, G. C. Proximity Extension of Circular DNA Aptamers with Real-Time Protein Detection. *Nucleic Acids Res.* **2005**, *33* (6), 1–7.

84. Lee, J. B.; Peng, S.; Yang, D.; Roh, Y. H.; Funabashi, H.; Park, N.; Rice, E. J.;

Chen, L.; Long, R.; Wu, M.; Luo, D. A Mechanical Metamaterial Made from a DNA Hydrogel. *Nat. Nanotechnol.* **2012**, *7* (12), 816–820.

85. Zhao, W.; Cui, C. H.; Bose, S.; Guo, D.; Shen, C.; Wong, W. P.; Halvorsen, K.; Farokhzad, O. C.; Teo, G. S. L.; Phillips, J. A.; Dorfman, D. M.; Karnik, R.; Karp, J. M. Bioinspired Multivalent DNA Network for Capture and Release of Cells. *Proc. Natl. Acad. Sci. U. S. A.* **2012**, *109* (48), 19626–19631.

86. Ding, C.; Liu, H.; Wang, N.; Wang, Z. Cascade Signal Amplification Strategy for the Detection of Cancer Cells by Rolling Circle Amplification and Nanoparticles Tagging. *Chem. Commun.* **2012**, *48* (41), 5019–5021.

87. Maruyama, F.; Kenzaka, T.; Yamaguchi, N.; Tani, K.; Nasu, M. Visualization and Enumeration of Bacteria Carrying a Specific Gene Sequence by in Situ Rolling Circle Amplification. *Appl. Environ. Microbiol.* **2005**, *71* (12), 7933–7940.

88. Ma, Y.; Zheng, H.; Wang, C.; Yan, Q.; Chao, J.; Fan, C.; Xiao, S. J. RCA Strands as Scaffolds to Create Nanoscale Shapes by a Few Staple Strands. *J. Am. Chem. Soc.* **2013**, *135* (8), 2959–2962.

89. Zuccheri, G.; Samori, B. *DNA Nanotechnology: Methods and Protocols*; Walker, J. M., Ed.; Humana Press: New York, 2011.

90. Hamblin, G. D.; Carneiro, K. M. M.; Fakhoury, J. F.; Bujold, K. E.; Sleiman, H. F. Rolling Circle Amplification-Templated DNA Nanotubes Show Increased Stability and Cell Penetration Ability. *J. Am. Chem. Soc.* **2012**, *134* (6), 2888–2891.

91. Carneiro, K. M. M.; Hamblin, G. D.; Hänni, K. D.; Fakhoury, J.; Nayak, M. K.; Rizis, G.; McLaughlin, C. K.; Bazzi, H. S.; Sleiman, H. F. Stimuli-Responsive Organization of Block Copolymers on DNA Nanotubes. *Chem. Sci.* **2012**, *3* (6), 1980–1986.

92. Hamblin, G. D.; Hariri, A. A.; Carneiro, K. M. M.; Lau, K. L.; Cosa, G.; Sleiman, H. F. Simple Design for DNA Nanotubes from a Minimal Set of Unmodified Strands: Rapid, Room-Temperature Assembly and Readily Tunable Structure. *ACS Nano*. **2013**, *7* (4), 3022–3028.

93. Salata, O. V. Applications of Nanoparticles in Biology and Medicine. *J. Nanobiotechnology*. **2004**, *2* (1), 3.

94. De Jong, W. H.; Borm, P. J. A. Drug Delivery and Nanoparticles:Applications and Hazards. *Int. J. Nanomedicine*. **2008**, *3* (2), 133–149.

95. Khan, I.; Saeed, K.; Khan, I. Nanoparticles: Properties, Applications and

Toxicities. *Arab. J. Chem.* **2019**, *12* (7), 908–931.

96. Taton, T. A. Nanostructures as Tailored Biological Probes. *Trends Biotechnol.* **2002**, *20* (7), 277–279.

97. Youns, M.; Hoheisel, J. D.; Efferth, T. Therapeutic and Diagnostic Applications of Nanoparticles. *Curr. Drug Targets.* **2011**, *12* (3), 357–365.

98. Yameen, B.; Il, W.; Vilos, C.; Swami, A.; Shi, J.; Farokhzad, O. C. Insight into Nanoparticle Cellular Uptake and Intracellular Targeting. *J. Control. Release*. **2014**, *190*, 485–499.

99. Doherty, G. J.; Mcmahon, H. T. Mechanisms of Endocytosis. *Annu. Rev. Biochem.* **2009**, *78*, 857–902.

100. Behzadi, S.; Serpooshan, V.; Tao, W.; Hamaly, M. A.; Mahmoud, Y.; Dreaden, E. C.; Brown, D.; Alkilany, A. M.; Omid, C.; Mahmoudi, M.; Hospital, M. G.; Hospital, M. G.; Arabia, S. Cellular Uptake of Nanoparticles: Journey Inside the Cell Shahed. *Chem Soc Rev*. **2017**, *46* (14), 4218–4244.

101. Edidin, M. Lipids on the Frontier : A Century of Cell-Membrane Bilayers. *Nat. Rev. Mol. Cell Biol.* **2003**, *4*, 414–418.

102. McMahon, H. T.; Gallop, J. L. Membrane Curvature and Mechanisms of Dynamic Cell Membrane Remodelling. *Nature.* **2005**, *438*, 590–596.

103. Sabolid, I.; Katsura, T.; Verbavatz, J.-M.; Brown, D. The AQP2 Water Channel: Effect of Vasopressin Treatment, Microtubule Disruption, and Distribution in Neonatal Rats. *Journa Membr. Biol.* **1995**, *143*, 165–175.

104. Kelemen, L. E. The Role of Folate Receptor a in Cancer Development , Progression and Treatment : Cause , Consequence or Innocent Bystander ? *Int. J. Cancer*. **2006**, *119*, 243–250.

105. Rabinovitch, M. Professional and Non-Professional Phagocytes: An Introduction. *Trends Cell Biol.* **1995**, *5*, 85–87.

106. Rosales, C.; Uribe-querol, E. Phagocytosis : A Fundamental Process in Immunity. *Biomed Res. Int.* **2017**.

107. Gordon, S. Phagocytosis: An Immunobiologic Process. *Immunity*. **2016**, *44*, 463–475.

108. Flannagan, R. S.; Jaumouill, V.; Grinstein, S. The Cell Biology of Phagocytosis. *Annu. Rev. Pathol. Mech. Dis.* **2012**, *7*, 61–98.

109. Lim, J. P.; Gleeson, P. A. Macropinocytosis : An Endocytic Pathway for Internalising Large Gulps. *Immunity*. **2011**, *89*, 836–843.

110. Falcone, S.; Cocucci, E.; Podini, P.; Kirchhausen, T.; Clementi, E.; Meldolesi, J. Macropinocytosis : Regulated Coordination of Endocytic and Exocytic Membrane Traffic Events. *J. Cell Sci.* **2006**, *119*, 4758–4769.

111. Brown, C. M.; Petersen, N. O. Free Clathrin Triskelions Are Required for the Stability of Clathrin-Associated Adaptor Protein (AP-2) Coated Pit Nucleation Sites. *Biochem. cell Biol.* **1999**, *77* (5), 439–448.

112. Conner, S. D.; Schmid, S. L. Regulated Portals of Entry into the Cell. *Nature*. **2003**, *422*, 37–44.

113. Ehrlich, M.; Boll, W.; Oijen, A. Van; Hariharan, R.; Chandran, K.; Nibert, M. L.; Kirchhausen, T. Endocytosis by Random Initiation and Stabilization of Clathrin-Coated Pits. *Cell*. **2004**, *118*, 591–605.

114. Anderson, R. G. W. The Caveolae Membrane System. *Annu. Rev. Biochem.* **1998**, *67*, 199–225.

115. Carver, L. A.; Schnitzer, J. E. Caveolae : Mining Little Caves For New Cancer Targets. *Nat. Rev. Cancer*. **2003**, *3*, 23–28.

116. Yousuf, M. A.; Zhou, X.; Mukherjee, S.; Chintakuntlawar, A. V; Yoon, J.; Ramke, M.; Chodosh, J.; Rajaiya, J. Caveolin-1 Associated Adenovirus Entry into Human Corneal Cells. *PLoS One*. **2013**, *8* (10), 1–15.

117. Medina-Kauwe, L. K. "Alternative" Endocytic Mechanisms Exploited by Pathogens: New Avenues for Therapeutic Delivery? *Adv. Drug Deliv. Rev.* **2020**, *59*, 798–809.

118. Rodighiero, K.; Wolf, A. A.; Rodighiero, C.; Jobling, M.; Hirst, T. R.; Holmes, R. K.; Lencer, W. I. Floating Cholera Toxin into Epithelial Cells: Functional Association with Caveolae-like Detergent-Insoluble Membrane Microdomains. *Int. J. Med. Microbiol.* **2000**, *290*, 403–408.

119. Lencer, W. I.; Hirst, T. R.; Holmes, R. K. Membrane Traffic and the Cellular Uptake of Cholera Toxin. *Biochim. Biophys. Acta*. **1999**, *1450*, 177–190.

120. Pfeffer, S. R. Caveolae on the Move. *Nat. Cell Biol.* **2001**, *3*, 108–110.

121. Blanco, E.; Shen, H.; Ferrari, M. Principles of Nanoparticle Design for Overcoming Biological Barriers to Drug Delivery. *Nat. Biotechnol.* **2015**, *33* (9), 941–951.

122. Lu, Y.; Low, P. S. Folate-Mediated Delivery of Macromolecular Anticancer Therapeutic Agents. *Adv. Drug Deliv. Rev.* **2002**, *54*, 675–693.

123. Li, Z.; Zhang, Y.; Zhu, D.; Li, S.; Yu, X.; Ouyang, X.; Xie, Z.; Li, L. Transporting Carriers for Intracellular Targeting Delivery via Non-Endocytic Uptake Pathways. *Drug Deliv.* **2017**, *24*, 45–55.

124. Derossi, D.; Chassaing, G.; Prochiantz, A. Trojan Peptides : The Penetratin System for Intracellular Delivery. *Trends Cell Biol.* **1998**, *8*, 84–87.

125. Matsuzaki, K.; Yoneyama, S.; Murase, O.; Miyajima, K. Transbilayer Transport of Ions and Lipids Coupled with Mastoparan X. *Biochemistry*. **1996**, *35*, 8450–8456.

126. Wender, P. A.; Galliher, W. C.; Goun, E. A.; Jones, L. R.; Pillow, T. H. The Design of Guanidinium-Rich Transporters and Their Internalization Mechanisms. *Adv. Drug Deliv. Rev.* **2008**, *60*, 452–472.

127. Lee, M.-T.; Hung, W.-C.; Chen, F.-Y.; Huang, H. Many-Body Effect of Antimicrobial Peptides: On the Correlation Between Lipid's Spontaneous Curvature and Pore Formation. *Biophys. J.* **2006**, *89*, 4006–4016.

128. Gurney, L. R. I.; Taggart, J.; Tong, W.-C.; Jones, A. T.; Robson, S. C.; Taggart, M. J. Inhibition of Inflammatory Changes in Human Myometrial Cells by Cell Penetrating Peptide and Small Molecule Inhibitors of NFκB. *Front. Immunol.* **2018**, *9*, 2966.

129. Fu, L.-S.; Wu, Y.-R.; Fang, S.-L.; Tsai, J.-J.; Lin, H.-K.; Chen, Y.-J.; Chen, T.-Y.; Chang, M. D.-T. Cell Penetrating Peptide Derived from Human Eosinophil Cationic Protein Decreases Airway Allergic Inflammation. *Sci. Rep.* **2017**, *7* (1), 12352.

130. Ma, W.-Y.; Murata, E.; Ueda, K.; Kuroda, Y.; Cao, M.-H.; Abe, M.; Shigemi, K.; Hirose, M. A Synthetic Cell-Penetrating Peptide Antagonizing TrkA Function Suppresses Neuropathic Pain in Mice. *J. Pharmacol. Sci.* **2010**, *114* (1), 79–84.

131. Garcia-Caballero, A.; Gadotti, V. M.; Chen, L.; Zamponi, G. W. A Cell-Permeant Peptide Corresponding to the CUBP Domain of USP5 Reverses Inflammatory and Neuropathic Pain. *Mol. Pain*. **2016**, *12*.

132. Peng, J.; Rao, Y.; Yang, X.; Jia, J.; Wu, Y.; Lu, J.; Tao, Y.; Tu, W. Targeting Neuronal Nitric Oxide Synthase by a Cell Penetrating Peptide Tat-LK15/SiRNA Bioconjugate. *Neurosci. Lett.* **2017**, *650*, 153–160.

133. Jia, L.; Gorman, G. S.; Coward, L. U.; Noker, P. E.; McCormick, D.; Horn, T. L.;

Harder, J. B.; Muzzio, M.; Prabhakar, B.; Ganesh, B.; Das Gupta, T. K.; Beattie, C. W. Preclinical Pharmacokinetics, Metabolism, and Toxicity of Azurin-P28 (NSC745104) a Peptide Inhibitor of P53 Ubiquitination. *Cancer Chemother. Pharmacol.* **2011**, *68* (2), 513–524.

134. Betts, C. A.; Wood, M. J. A. Cell Penetrating Peptide Delivery of Splice Directing Oligonucleotides as a Treatment for Duchenne Muscular Dystrophy. *Curr. Pharm. Des.* **2013**, *19* (16), 2948–2962.

135. Koutsokeras, A.; Purkayastha, N.; Rigby, A.; Subang, M. C.; Sclanders, M.; Vessillier, S.; Mullen, L.; Chernajovsky, Y.; Gould, D. Generation of an Efficiently Secreted, Cell Penetrating NF-KB Inhibitor. *FASEB J. Off. Publ. Fed. Am. Soc. Exp. Biol.* **2014**, *28* (1), 373–381.

136. Gurbel, P. A.; Bliden, K. P.; Turner, S. E.; Tantry, U. S.; Gesheff, M. G.; Barr, T. P.; Covic, L.; Kuliopulos, A. Cell-Penetrating Pepducin Therapy Targeting PAR1 in Subjects With Coronary Artery Disease. *Arterioscler. Thromb. Vasc. Biol.* **2016**, *36* (1), 189–197.

137. Nasrollahi, S. A.; Fouladdel, S.; Taghibiglou, C.; Azizi, E.; Farboud, E. S. A Peptide Carrier for the Delivery of Elastin into Fibroblast Cells. *Int. J. Dermatol.* **2012**, *51* (8), 923–929.

138. Kleusch, C.; Hersch, N.; Hoffmann, B.; Merkel, R.; Csiszár, A. Fluorescent Lipids: Functional Parts of Fusogenic Liposomes and Tools for Cell Membrane Labeling and Visualization. *Molecules*. **2012**, *17* (1), 1055–1073.

139. Kube, S.; Hersch, N.; Naumovska, E.; Gensch, T.; Hendriks, J.; Franzen, A.; Landvogt, L.; Siebrasse, J. P.; Kubitscheck, U.; Hoffmann, B.; Merkel, R.; Csiszár, A. Fusogenic Liposomes as Nanocarriers for the Delivery of Intracellular Proteins. *Langmuir* . **2017**, *33* (4), 1051–1059.

140. He, S.; Fan, W.; Wu, N.; Zhu, J.; Miao, Y.; Miao, X.; Li, F.; Zhang, X.; Gan, Y. Lipid-Based Liquid Crystalline Nanoparticles Facilitate Cytosolic Delivery of SiRNA via Structural Transformation. *Nano Lett.* **2018**, *18*, 2411–2419.

141. Xie, X.; Xu, A. M.; Leal-Ortiz, S.; Cao, Y.; Garner, C. C.; Melosh, N. A. Nanostraw-Electroporation System for Highly Efficient Intracellular Delivery and Transfection. *ACS Nano*. **2013**, *7* (5), 4351–4358.

142. Cao, Y.; Chen, H.; Qiu, R.; Hanna, M.; Ma, E.; Hjort, M.; Zhang, A.; Lewis, R. S.; Wu, J. C.; Melosh, N. A. Universal Intracellular Biomolecule Delivery with Precise Dosage Control. *Sci. Adv.* **2018**, *4*, 1–9.

143. Chang, L.; Bertani, P.; Gallego-Perez, D.; Yang, Z.; Chen, F.; Chiang, C.; Malkoc, V.; Kuang, T.; Gao, K.; Lee, L. J.; Lu, W. 3D Nanochannel Electroporation for High-Throughput Cell Transfection with High Uniformity and Dosage Control. *Nanoscale*. **2016**, *8*, 243–252.

144. Chow, Y. T.; Chen, S.; Wang, R.; Liu, C.; Kong, C. W.; Li, R. A.; Cheng, S. H.; Sun, D. Single Cell Transfection through Precise Microinjection with Quantitatively Controlled Injection Volumes. *Sci. Rep.* **2016**, *6* (January), 1–9.

145. Zhang, Y.; Yu, L. C. Single-Cell Microinjection Technology in Cell Biology. *BioEssays*. **2008**, *30* (6), 606–610.

146. Bertrand, E.; Chartrand, P.; Schaefer, M.; Shenoy, S. M.; Singer, R. H.; Long, R. M. Localization of ASH1 MRNA Particles in Living Yeast. *Mol. Cell*. **1998**, *2* (4), 437–445.

147. Fusco, D.; Accomero, N.; Lavoie, B.; Shenoy, S. M.; Blanchard, J. M.; Singer, R. H.; Bertrand, E. Single MRNA Molecules Demonstrate Probabilistic Movement in Living Mammalian Cells. *Curr. Biol.* **2003**, *13* (2), 161–167.

148. Ozawa, T.; Natori, Y.; Sato, M.; Umezawa, Y. Imaging Dynamics of Endogenous Mitochondrial RNA in Single Living Cells. *Nat. Methods*. **2007**, *4* (5), 413–419.

149. Daigle, N.; Ellenberg, J. ΛN-GFP: An RNA Reporter System for Live-Cell Imaging. *Nat. Methods*. **2007**, *4* (8), 633–636.

150. Molenaar, C.; Abdulle, A.; Gena, A.; Tanke, H. J.; Dirks, R. W. Poly(A)+ RNAs Roam the Cell Nucleus and Pass through Speckle Domains in Transcriptionally Active and Inactive Cells. *J. Cell Biol.* **2004**, *165* (2), 191–202.

151. Paillasson, S.; Van De Corput, M.; Dirks, R. W.; Tanke, H. J.; Robert-Nicoud, M.; Ronot, X. In Situ Hybridization in Living Cells: Detection of RNA Molecules. *Exp. Cell Res.* **1997**, *231* (1), 226–233.

152. Bao, G.; Won, J. R.; Tsourkas, A. Fluorescent Probes for Live-Cell RNA Detection. *Annu. Rev. Biomed. Eng.* **2009**, *11*, 25–47.

153. Tyagi, S.; Kramer, F. R. Molecular Beacons: Probes That Fluoresce upon Hybridization. *Nat. Biotechnol.* **1996**, *14* (3), 303–308.

154. Lee, J. H.; Kim, J. A.; Kwon, M. H.; Kang, J. Y.; Rhee, W. J. In Situ Single Step Detection of Exosome MicroRNA Using Molecular Beacon. *Biomaterials*. **2015**, *54*, 116–125.

155. Yao, Q.; Sun, J. G.; Ma, H.; Zhang, A. M.; Lin, S.; Zhu, C. H.; Zhang, T.; Chen, Z.

T. Monitoring Micrornas Using a Molecular Beacon in CD133+/CD338+ Human Lung Adenocarcinoma-Initiating A549 Cells. *Asian Pacific J. Cancer Prev.* **2014**, *15* (1), 161–166.

156. Tsourkas, A.; Behlke, M. A.; Xu, Y.; Bao, G. Spectroscopic Features of Dual Fluorescence/Luminescence Resonance Energy-Transfer Molecular Beacons. *Anal. Chem.* **2003**, *75* (15), 3697–3703.

157. Santangelo, P. J.; Nix, B.; Tsourkas, A.; Bao, G. Dual FRET Molecular Beacons for MRNA Detection in Living Cells. *Nucleic Acids Res.* **2004**, *32* (6), 1–9.

158. Meaking, W. S.; Edgerton, J.; Wharton, C. W.; Meldrum, R. A. Electroporation-Induced Damage in Mammalian Cell DNA. *Biochim. Biophys. Acta*. **1995**, *1264* (3), 357–362.

159. Batista Napotnik, T.; Polajžer, T.; Miklavčič, D. Cell Death Due to Electroporation – A Review. *Bioelectrochemistry*. **2021**, *141*, 107871.

160. Kim, T. K.; Eberwine, J. H. Mammalian Cell Transfection: The Present and the Future. *Anal. Bioanal. Chem.* **2010**, *397* (8), 3173–3178.

161. Liu, F.; Wu, D.; Wu, X.; Chen, K. Analyses of the Cell Mechanical Damage during Microinjection. *Soft Matter*. **2015**, *11* (7), 1434–1442.

162. Marras, S. A. E.; Kramer, F. R.; Tyagi, S. Efficiencies of Fluorescence Resonance Energy Transfer and Contact-Mediated Quenching in Oligonucleotide Probes. *Nucleic Acids Res.* **2002**, *30* (21), 1–8.

163. Uddayasankar, U.; Krull, U. J. Analytical Performance of Molecular Beacons on Surface Immobilized Gold Nanoparticles of Varying Size and Density. *Anal. Chim. Acta*. **2013**, *803*, 113–122.

164. Dubertret, B.; Calame, M.; Libchaber, A. J. Erratum: Single-Mismatch Detection Using Gold-Quenched Fluorescent Oligonucleotides. *Nat. Biotechnol.* **2001**, *19* (7), 680–681.

165. Yang, C. J.; Lin, H.; Tan, W. Molecular Assembly of Superquenchers in Signaling Molecular Interactions. *J. Am. Chem. Soc.* **2005**, *127* (37), 12772–12773.

166. Paige, J. S.; Wu, K. Y.; Jaffrey, S. R. RNA Mimics of Green Fluorescent Protein. *Science.* **2011**, *333* (6042), 642–646.

167. Chen, X.; Zhang, D.; Su, N.; Bao, B.; Xie, X.; Zuo, F.; Yang, L.; Wang, H.; Jiang, L.; Lin, Q.; Fang, M.; Li, N.; Hua, X.; Chen, Z.; Bao, C.; Xu, J.; Du, W.; Zhang, L.; Zhao, Y.; Zhu, L.; Loscalzo, J.; Yang, Y. Visualizing RNA Dynamics in Live

Cells with Bright and Stable Fluorescent RNAs. *Nat. Biotechnol.* **2019**, *37* (11), 1287–1293.

168. Strack, R. L.; Disney, M. D.; Jaffrey, S. R. A Superfolding Spinach2 Reveals the Dynamic Nature of Trinucleotide Repeat-Containing RNA. *Nat. Methods*. **2013**, *10* (12), 1219–1224.

169. Song, W.; Filonov, G. S.; Kim, H.; Hirsch, M.; Li, X.; Moon, J. D.; Jaffrey, S. R. Imaging RNA Polymerase III Transcription Using a Photostable RNA-Fluorophore Complex. *Nat. Chem. Biol.* **2017**, *13* (11), 1187–1194.

170. Swetha, P.; Fan, Z.; Wang, F.; Jiang, J.-H. Genetically Encoded Light-up RNA Aptamers and Their Applications for Imaging and Biosensing. *J. Mater. Chem. B.* **2020**, *8* (16), 3382–3392.

171. Briley, W. E.; Bondy, M. H.; Randeria, P. S.; Dupper, T. J.; Mirkin, C. A. Quantification and Real-Time Tracking of RNA in Live Cells Using Sticky-Flares. *Proc. Natl. Acad. Sci. U. S. A.* **2015**, *112* (31), 9591–9595.

172. Wu, Q.; Liu, Z.; Su, L.; Han, G.; Liu, R.; Zhao, J.; Zhao, T.; Jiang, C.; Zhang, Z. Sticky-Flares for in Situ Monitoring of Human Telomerase RNA in Living Cells. *Nanoscale*. **2018**, *10* (19), 9386–9392.

173. Wu, X. A.; Choi, C. H. J.; Zhang, C.; Hao, L.; Mirkin, C. A. Intracellular Fate of Spherical Nucleic Acid Nanoparticle Conjugates. *J. Am. Chem. Soc.* **2014**, *136* (21), 7726–7733.

174. Radovic-Moreno, A. F.; Chernyak, N.; Mader, C. C.; Nallagatla, S.; Kang, R. S.; Hao, L.; Walker, D. A.; Halo, T. L.; Merkel, T. J.; Rische, C. H.; Anantatmula, S.; Burkhart, M.; Mirkin, C. A.; Gryaznov, S. M. Immunomodulatory Spherical Nucleic Acids. *Proc. Natl. Acad. Sci. U. S. A.* **2015**, *112* (13), 3892–3897.

175. Lv, Y.; Hu, R.; Zhu, G.; Zhang, X.; Mei, L.; Liu, Q.; Qiu, L.; Wu, C.; Tan, W. Preparation and Biomedical Applications of Programmable and Multifunctional DNA Nanoflowers. *Nat. Protoc.* **2015**, *10* (10), 1508–1524.

176. Zhu, G.; Hu, R.; Zhao, Z.; Chen, Z.; Zhang, X.; Tan, W. Noncanonical Self-Assembly of Multifunctional DNA Nanoflowers for Biomedical Applications. *J. Am. Chem. Soc.* **2013**, *135* (44), 16438–16445.

177. Kevin E. Shopsowitz, Young Hoon Roh, Zhou J. Deng,Stephen W. Morton, P. T. H. Composite RNAi-Microsponges Form through Self-Assembly of the Organic and Inorganic Products of Transcription. *Small*. **2014**, *10* (8), 1623–1633.

178. Lv, J.; Dong, Y.; Gu, Z.; Yang, D. Programmable DNA Nanoflowers for Biosensing, Bioimaging, and Therapeutics. *Chem. - A Eur. J.* **2020**, 1–14.

179. Linck, L.; Reiß, E.; Bier, F.; Resch-Genger, U. Direct Labeling Rolling Circle Amplification as a Straightforward Signal Amplification Technique for Biodetection Formats. *Anal. Methods*. **2012**, *4* (5), 1215–1220.

180. Kim, K. R.; Röthlisberger, P.; Kang, S. J.; Nam, K.; Lee, S.; Hollenstein, M.; Dae-Ro, A. Shaping Rolling Circle Amplification Products into DNA Nanoparticles by Incorporation of Modified Nucleotides and Their Application to in Vitro and in Vivo Delivery of a Photosensitizer. *Molecules*. **2018**, *23* (7).

181. Taylor-Papadimitriou, J.; Burchell, J.; Miles, D. W.; Dalziel, M. MUC1 and Cancer. *Biochim. Biophys. Acta - Mol. Basis Dis.* **1999**, *1455* (2–3), 301–313.

182. Mitri, Z.; Constantine, T.; O'Regan, R. The HER2 Receptor in Breast Cancer: Pathophysiology, Clinical Use, and New Advances in Therapy. *Chemother. Res. Pract.* **2012**, *2012*, 1–7.

183. Marano, L.; Roviello, F.; Jeong, H.; Kim, J.; Lee, Y.; Seo, J. H.; Hong, S. R.; Kim, A.; Faltus, T.; Yuan, J.; Zimmer, B.; Krämer, A.; Loibl, S.; Kaufmann, M.; Strebhardt, K.; Collins, D. M.; O'donovan, N.; Mcgowan, P. M.; O'sullivan, F.; Duffy, M. J.; Crown, J. The Distinctive Nature of HER2-Positive Gastric Cancers. *Oncol. Rep.* **2015**, *41* (3), 1788–1795.

184. Zuker, M. Mfold Web Server for Nucleic Acid Folding and Hybridization Prediction. *Nucleic Acids Res.* **2003**, *31* (13), 3406–3415.

185. Hu, R.; Zhang, X.; Zhao, Z.; Zhu, G.; Chen, T.; Fu, T.; Tan, W. DNA Nanoflowers for Multiplexed Cellular Imaging and Traceable Targeted Drug Delivery. *Angew. Chem. Int. Ed.* **2014**, *53* (23), 5821–5826.

186. Mei, L.; Zhu, G.; Qiu, L.; Wu, C.; Chen, H.; Liang, H.; Cansiz, S.; Lv, Y.; Zhang, X.; Tan, W. Self-Assembled Multifunctional DNA Nanoflowers for the Circumvention of Multidrug Resistance in Targeted Anticancer Drug Delivery. *Nano Res.* **2015**, *8* (11), 3447–3460.

187. Alsmadi, O.; Alkayal, F.; Monies, D.; Meyer, B. F. Specific and Complete Human Genome Amplification with Improved Yield Achieved by Phi29 DNA Polymerase and a Novel Primer at Elevated Temperature. *BMC Res. Notes*. **2009**, *2*, 1–7.

188. Konigsberg, W. Reduction of Disulfide Bonds in Proteins with Dithiothreitol. *Methods Enzymol.* **1964**, *11* (2), 185–188.

189. Kim, E.; Zwi-Dantsis, L.; Reznikov, N.; Hansel, C. S.; Agarwal, S.; Stevens, M. M. One-Pot Synthesis of Multiple Protein-Encapsulated DNA Flowers and Their Application in Intracellular Protein Delivery. *Adv. Mater.* **2017**, *29* (26).

190. Lee, S. Y.; Kim, K. R.; Bang, D.; Bae, S. W.; Kim, H. J.; Ahn, D. R. Biophysical and Chemical Handles to Control the Size of DNA Nanoparticles Produced by Rolling Circle Amplification. *Biomater. Sci.* **2016**, *4* (9), 1314–1317.

191. Zhang, L.; Abdullah, R.; Hu, X.; Bai, H.; Fan, H.; He, L.; Liang, H.; Zou, J.; Liu, Y.; Sun, Y.; Zhang, X.; Tan, W. Engineering of Bioinspired, Size-Controllable, Self-Degradable Cancer-Targeting DNA Nanoflowers via the Incorporation of an Artificial Sandwich Base. *J. Am. Chem. Soc.* **2019**, *141* (10), 4282–4290.

192. Kore, A. R.; Senthilvelan, A.; Shanmugasundaram, M. Highly Regioselective C-5 Iodination of Pyrimidine Nucleotides and Subsequent Chemoselective Sonogashira Coupling with Propargylamine. *Nucleosides, Nucleotides and Nucleic Acids*. **2015**, *34* (2), 92–102.

193. Ren, X.; El-Sagheer, A. H.; Brown, T. Efficient Enzymatic Synthesis and Dual-Colour Fluorescent Labelling of DNA Probes Using Long Chain Azido-DUTP and BCN Dyes. *Nucleic Acids Res.* **2016**, *44* (8), e79.

194. Sato, K.; Sasaki, A.; Matsuda, A. Highly Fluorescent 5-(5,6-Dimethoxybenzothiazol-2-Yl)-2'-Deoxyuridine 5'-Triphosphate as an Efficient Substrate for DNA Polymerases. *Chembiochem.* **2011**, *12* (15), 2341–2346.

195. Simeonov, A. A Chemical Method for Fast and Sensitive Detection of DNA Synthesis in Vivo: Commentary. *Assay Drug Dev. Technol.* **2008**, *6* (2), 157–158.

196. Montagu, A.; Roy, V.; Balzarini, J.; Snoeck, R.; Andrei, G.; Agrofoglio, L. A. Synthesis of New C5-(1-Substituted-1,2,3-Triazol-4 or 5-Yl)-2′- Deoxyuridines and Their Antiviral Evaluation. *Eur. J. Med. Chem.* **2011**, *46* (2), 778–786.

197. Hoshyar, N.; Gray, S.; Han, H.; Bao, G. The Effect of Nanoparticle Size on in Vivo Pharmacokinetics and Cellular Interaction. *Nanomed. J.* **2016**, *11* (6), 673–692.

198. Takagi, S.; Takahashi, Y.; Sugimura, K.; Nishikawa, M.; Takakura, Y. Application of Magnesium Pyrophosphate-Based Sponge-Like Microparticles to Enhance the Delivery Efficiency and Adjuvant Effects of Polyriboinosinic-Polyribocytidylic Acid in Immune Cells. *J. Pharm. Sci.* **2016**, *105* (2), 766–772.

199. Chen, H.; Zhao, J.; Zhang, M.; Yang, H.; Ma, Y.; Gu, Y. MUC1 Aptamer-Based Near-Infrared Fluorescence Probes for Tumor Imaging. *Mol. Imaging Biol.* **2014**, *17* (1), 38–48.

200. Mahlknecht, G.; Maron, R.; Mancini, M.; Schechter, B.; Sela, M.; Yarden, Y. Aptamer to ErbB-2/HER2 Enhances Degradation of the Target and Inhibits Tumorigenic Growth. *Proc. Natl. Acad. Sci. U. S. A.* **2013**, *110* (20), 8170–8175.

201. Mahlknecht, G.; Maron, R.; Schechter, B.; Yarden, Y.; Sela, M. Multimerization of ERBB2/HER2 Specific Aptamer Leads to Improved Receptor Binding. *Biochem. Biophys. Res. Commun.* **2015**, *465* (2), 218–224.

202. Collins, D. M.; O'donovan, N.; Mcgowan, P. M.; O'sullivan, F.; Duffy, M. J.; Crown, J. Trastuzumab Induces Antibody-Dependent Cell-Mediated Cytotoxicity (ADCC) in HER-2-Non-Amplified Breast Cancer Cell Lines. *Ann. Oncol.* **2012**, *23* (7), 1788–1795.

203. Faltus, T.; Yuan, J.; Zimmer, B.; Krämer, A.; Loibl, S.; Kaufmann, M.; Strebhardt, K. Silencing of the HER2/Neu Gene by SiRNA Inhibits Proliferation and Induces Apoptosis in HER2/Neu-Overexpressing Breast Cancer Cells. *Neoplasia*. **2004**, *6* (6), 786–795.

204. Jeong, H.; Kim, J.; Lee, Y.; Seo, J. H.; Hong, S. R.; Kim, A. Neuregulin-1 Induces Cancer Stem Cell Characteristics in Breast Cancer Cell Lines. *Oncol. Rep.* **2014**, *32* (3), 1218–1224.

205. Shadidi, M.; Sioud, M. Identification of Novel Carrier Peptides for the Specific Delivery of Therapeutics into Cancer Cells. *FASEB J.* **2003**, *17* (2), 256–258.

206. Calce, E.; Monfregola, L.; Sandomenico, A.; Saviano, M.; De Luca, S. Fluorescence Study for Selecting Specific Ligands toward HER2 Receptor: An Example of Receptor Fragment Approach. *Eur. J. Med. Chem.* **2013**, *61*, 116–121.

207. Zhao, J.; Stenzel, M. H. Entry of Nanoparticles into Cells: The Importance of Nanoparticle Properties. *Polym. Chem.* **2018**, *9* (3), 259–272.

208. Roh, Y. H.; Lee, J. B.; Shopsowitz, K. E.; Dreaden, E. C.; Morton, S. W.; Poon, Z.; Hong, J.; Yamin, I.; Bonner, D. K.; Hammond, P. T. Layer-by-Layer Assembled Antisense DNA Microsponge Particles for Efficient Delivery of Cancer Therapeutics. *ACS Nano*. **2014**, *8* (10), 9767–9780.

209. Bielinska, A. U.; Kukowska-Latallo, J. F.; Baker, J. R. The Interaction of Plasmid DNA with Polyamidoamine Dendrimers: Mechanism of Complex Formation and Analysis of Alterations Induced in Nuclease Sensitivity and Transcriptional Activity of the Complexed DNA. *Biochim. Biophys. Acta - Gene Struct. Expr.* **1997**, *1353* (2), 180–190.

210. Boussif, O.; LezoualC'H, F.; Zanta, M. A.; Mergny, M. D.; Scherman, D.;

Demeneix, B.; Behr, J. P. A Versatile Vector for Gene and Oligonucleotide Transfer into Cells in Culture and in Vivo: Polyethylenimine. *Proc. Natl. Acad. Sci. U. S. A.* **1995**, *92* (16), 7297–7301.

211. Behr, J. P. Synthetic Gene-Transfer Vectors. *Acc. Chem. Res.* **1993**, *26* (5), 274–278.

212. Mislick, K. A.; Baldeschwieler, J. D. Evidence for the Role of Proteoglycans in Cation-Mediated Gene Transfer. *Proc. Natl. Acad. Sci. U. S. A.* **1996**, *93* (22), 12349–12354.

213. March, H. U. M. A. N. G. T.; Felgner, P. L.; Barenholz, Y.; Behr, J. P.; Cheng, S. H.; Cullis, P.; Huang, L.; Jessee, J. A.; Seymour, L.; Szoka, F.; Thierry, A. R.; Wagner, E.; Behr, J. P. Nomenclature for Synthetic Gene Delivery Systems. *Hum. Gene Ther.* **1997**, *8*, 511–512.

214. Kadlecova, Z.; Baldi, L.; Hacker, D.; Wurm, F. M.; Klok, H. A. Comparative Study on the in Vitro Cytotoxicity of Linear, Dendritic, and Hyperbranched Polylysine Analogues. *Biomacromolecules*. **2012**, *13* (10), 3127–3137.

215. Symonds, P.; Murray, J. C.; Hunter, A. C.; Debska, G.; Szewczyk, A.; Moghimi, S. M. Low and High Molecular Weight Poly(L-Lysine)s/Poly(L-Lysine)-DNA Complexes Initiate Mitochondrial-Mediated Apoptosis Differently. *FEBS Lett.* **2005**, *579* (27), 6191–6198.

216. Moghimi, S. M.; Symonds, P.; Murray, J. C.; Hunter, A. C.; Debska, G.; Szewczyk, A. A Two-Stage Poly(Ethylenimine)-Mediated Cytotoxicity: Implications for Gene Transfer/Therapy. *Mol. Ther.* **2005**, *11* (6), 990–995.

217. Liu, Z.; Robinson, J. T.; Sun, X.; Dai, H. PEGylated Nanographene Oxide for Delivery of Water-Insoluble Cancer Drugs. *J. Am. Chem. Soc.* **2008**, *130* (33), 10876–10877.

218. Tsilfidis, C.; Mackenzie, A. E.; Mettler, G.; Barcell, J.; Robert, G. Polyethylene Glycol Enhanced Protein Refolding. *Nat. Biotechnol.* **1992**, *10* (june), 192–195.

219. D'souza, A. A.; Shegokar, R. Polyethylene Glycol (PEG): A Versatile Polymer for Pharmaceutical Applications. *Expert Opin. Drug Deliv.* **2016**, *13* (9), 1257–1275.

220. Lee, J. H.; Lee, H. B.; Andrade, J. D. Blood Compatibility of Polyethylene Oxide Surfaces. *Prog. Polym. Sci.* **1995**, *20* (6), 1043–1079.

221. Walsh, M.; Tangney, M.; O'Neill, M. J.; Larkin, J. O.; Soden, D. M.; McKenna, S. L.; Darcy, R.; O'Sullivan, G. C.; O'Driscoll, C. M. Evaluation of Cellular Uptake

and Gene Transfer Efficiency of Pegylated Poly-L-Lysine Compacted DNA: Implications for Cancer Gene Therapy. *Mol. Pharm.* **2006**, *3* (6), 644–653.

222. Rimann, M.; Lühmann, T.; Textor, M.; Guerino, B.; Ogier, J.; Hall, H. Characterization of PLL-g-PEG-DNA Nanoparticles for the Delivery of Therapeutic DNA. *Bioconjug. Chem.* **2008**, *19* (2), 548–557.

223. Männistö, M.; Vanderkerken, S.; Toncheva, V.; Elomaa, M.; Ruponen, M.; Schacht, E.; Urtti, A. Structure-Activity Relationships of Poly(L-Lysines): Effects of Pegylation and Molecular Shape on Physicochemical and Biological Properties in Gene Delivery. *J. Control. Release*. **2002**, *83* (1), 169–182.

224. Cheng, C.; Jia, J. L.; Ran, S. Y. Polyethylene Glycol and Divalent Salt-Induced DNA Reentrant Condensation Revealed by Single Molecule Measurements. *Soft Matter*. **2015**, *11* (19), 3927–3935.

225. Lerman, L. S. A Transition to a Compact Form of DNA in Polymer Solutions. *Proc. Natl. Acad. Sci. U. S. A.* **1971**, *68* (8), 1886–1890.

226. Ojala, H.; Ziedaite, G.; Wallin, A. E.; Bamford, D. H.; Hæggström, E. Optical Tweezers Reveal Force Plateau and Internal Friction in PEG-Induced DNA Condensation. *Eur. Biophys. J.* **2014**, *43* (2–3), 71–79.

227. Kim, H. R.; Baek, A.; Lee, I. J.; Kim, D. E. Facilitation of Polymerase Chain Reaction with Poly(Ethylene Glycol)-Engrafted Graphene Oxide Analogous to a Single-Stranded-DNA Binding Protein. *ACS Appl. Mater. Interfaces*. **2016**, *8* (49), 33521–33528.

228. Minton, A. P. The Effect of Volume Occupancy upon the Thermodynamic Activity of Proteins: Some Biochemical Consequences. *Mol. Cell. Biochem.* **1983**, *140*, 119–140.

229. Ellis, R. J. Macromolecular Crowding: Obvious but Underappreciated. *Trends Biochem. Sci.* **2001**, *26* (10), 597–604.

230. Eggers, D. K.; Valentine, J. S. Crowding and Hydration Effects on Protein Conformation: A Study with Sol-Gel Encapsulated Proteins. *J. Mol. Biol.* **2001**, *314* (4), 911–922.

231. Kim, Y. J.; Lee, W. N.; Yoo, H. J.; Baek, C.; Min, J. Direct Buffer Composition of Blood Pre-Process for Nucleic Acid Based Diagnostics. *Biochip J.* **2017**, *11* (4), 255–261.

232. Sasaki, Y.; Miyoshi, D.; Sugimoto, N. Effect of Molecular Crowding on DNA

Polymerase Activity. *Biotechnol. J.* **2006**, *1* (4), 440–446.

233. Batchelor, J. D.; Olteanu, A.; Tripathy, A.; Pielak, G. J. Impact of Protein Denaturants and Stabilizers on Water Structure. *J. Am. Chem. Soc.* **2004**, *126* (7), 1958–1961.

234. Qiu, X.; Hill, A.; Packer, J.; Lin, D.; Ma, Y.-A.; Trapnell, C. Single-Cell MRNA Quantification and Differential Analysis with Census. *Nat. Methods*. **2017**, *14* (3), 309–315.

235. Kays, I.; Chen, B. E. Protein and RNA Quantification of Multiple Genes in Single Cells. *Biotechniques*. **2019**, *66* (1), 15–21.

236. Kedmi, R.; Ben-Arie, N.; Peer, D. The Systemic Toxicity of Positively Charged Lipid Nanoparticles and the Role of Toll-like Receptor 4 in Immune Activation. *Biomaterials*. **2010**, *31* (26), 6867–6875.

237. Leonetti, J. P.; Mechti, N.; Degols, G.; Gagnor, C.; Lebleu, B. Intracellular Distribution of Microinjected Antisense Oligonucleotides. *Proc. Natl. Acad. Sci.* **1991**, *88* (7), 2702–2706.

238. Seferos, D. S.; Giljohann, D. A.; Hill, H. D.; Prigodich, A. E.; Mirkin, C. A. Nano-Flares: Probes for Transfection and MRNA Detection in Living Cells. *J. Am. Chem. Soc.* **2007**, *129* (50), 15477–15479.

239. Czarnek, M.; Bereta, J. SmartFlares Fail to Reflect Their Target Transcripts Levels. *Sci. Rep.* **2017**, *7* (1), 1–10.

240. Jaiswal, P. K.; Goel, A.; Mittal, R. D. Survivin: A Molecular Biomarker in Cancer. *Indian J. Med. Res.* **2015**, *142* (April), 389–397.

241. Ju, J. H.; Yang, W.; Oh, S.; Nam, K. S.; Lee, K. M.; Noh, D. Y.; Shin, I. HER2 Stabilizes Survivin While Concomitantly Down-Regulating Survivin Gene Transcription by Suppressing Notch Cleavage. *Biochem. J.* **2013**, *451* (1), 123–134.

242. Wang, H.; Ye, Y. F. Effect of Survivin SiRNA on Biological Behaviour of Breast Cancer MCF7 Cells. *Asian Pac. J. Trop. Med.* **2015**, *8* (3), 225–228.

243. Mao, Y.; Gu, J.; Chang, D.; Wang, L.; Yao, L.; Ma, Q.; Luo, Z.; Qu, H.; Li, Y.; Zheng, L. Evolution of a Highly Functional Circular DNA Aptamer in Serum. *Nucleic Acids Res.* **2020**, *48* (19), 10680–10690.

244. Di Giusto, D. A.; King, G. C. Construction, Stability, and Activity of Multivalent Circular Anticoagulant Aptamers. *J. Biol. Chem.* **2004**, *279* (45), 46483–46489.

245. Tang, X. J.; Su, M.; Yu, L. L.; Lv, C.; Wang, J.; Li, Z. J. Photomodulating RNA Cleavage Using Photolabile Circular Antisense Oligodeoxynucleotides. *Nucleic Acids Res.* **2010**, *38* (11), 3848–3855.

246. Lee, C.; Lee, T. Carbohydrate-Protein Interactions: Basis of Glycobiology. *Acc. Chem. Res.* **1995**, *28* (8), 321–326.

247. Kiessling, L. L.; Gestwicki, J. E.; Strong, L. E. Synthetic Multivalent Ligands in the Exploration of Cell-Surface Interactions. *Curr. Opin. Chem. Biol.* **2000**, *4* (6), 696–703.

248. Mammen, M.; Choi, S. K.; Whitesides, G. M. Polyvalent Interactions in Biological Systems: Implications for Design and Use of Multivalent Ligands and Inhibitors. *Angew. Chem. Int. Ed.* **1998**, *37* (20), 2754–2794.

249. Seidel, C. A. M.; Schulz, A.; Sauer, M. H. M. Nucleobase-Specific Quenching of Fluorescent Dyes. 1. Nucleobase One-Electron Redox Potentials and Their Correlation with Static and Dynamic Quenching Efficiencies. *J. Phys. Chem.* **1996**, *100* (13), 5541–5553.

250. Mao, H.; Luo, G.; Zhan, Y.; Zhang, J.; Yao, S.; Yu, Y. The Mechanism and Regularity of Quenching the Effect of Bases on Fluorophores: The Base-Quenched Probe Method. *Analyst*. **2018**, *143* (14), 3292–3301.

251. Lodish, H.; Berk, A.; Zipursky, S. Intracellular Ion Environment and Membrane Electric Potential. In *Molecular Cell Biology*; W. H. Freeman: New York, 2000; Vol. 15.4.

252. Bhattacharyya, D.; Arachchilage, G. M.; Basu, S. Metal Cations in G-Quadruplex Folding and Stability. *Front. Chem.* **2016**, *4*, 1–14.

253. Rouet, R.; Christ, D. Efficient Intracellular Delivery of CRISPR-Cas Ribonucleoproteins through Receptor Mediated Endocytosis. *ACS Chem. Biol.* **2019**, *14* (3), 554–561.

254. Peng, X.-H.; Cao, Z.-H.; Xia, J.-T.; Carlson, G. W.; Lewis, M. M.; Wood, W. C.; Yang, L. Real-Time Detection of Gene Expression in Cancer Cells Using Molecular Beacon Imaging: New Strategies for Cancer Research. *Cancer Res.* **2005**, *65* (5), 1909–1917.